Study of Titan's Upper and Lower Atmosphere : An Experimental Approach

David Dubois

To cite this version:

David Dubois. Study of Titan's Upper and Lower Atmosphere : An Experimental Approach. Planetology. Université Paris Saclay (COmUE), 2018. English. NNT : 2018SACLV049 . tel-01925462v2

HAL Id: tel-01925462
https://theses.hal.science/tel-01925462v2

Submitted on 19 Mar 2019

université
PARIS-SACLAY

UNIVERSITÉ DE
VERSAILLES
ST-QUENTIN-EN-YVELINES
université PARIS-SACLAY

BNNT: 2018SACLV049

Study of Titan’s Upper and Lower Atmosphere: An Experimental Approach

Thèse de doctorat de l’Université Paris-Saclay
préparée à l’Université de Versailles Saint-Quentin-en-Yvelines

École doctorale n° 579 Sciences mécaniques et énergétiques, matériaux et géosciences (SMEMAG)
Spécialité de doctorat: Structure et Évolution de la Terre et des autres Planètes

Thèse présentée et soutenue à Guyancourt, le 1 octobre 2018, par

David Dubois

Composition du Jury:

Cyril Szopa Professeur, UVSQ — LATMOS	Président
Véronique Vuitton Chargée de Recherche CNRS, UJF-Grenoble — IPAG	Rapportrice
Nicolas Fray Maître de Conférences, UPEC — LISA	Rapporteur
Sandrine Vinatier Chargée de Recherche CNRS, Obs. Paris-Meudon — LESIA	Examinatrice
François Leblanc Directeur de Recherche, UVSQ — LATMOS	Examinateur
Nathalie Carrasco Professeure, UVSQ — LATMOS	Directrice de thèse
Murthy Gudipati Research Scientist – JPL/Caltech	Invité

Thèse de doctorat

"The beauty of a living thing is not the atoms that go into it, but the way those atoms are put together."

Carl Sagan

Preface

Titan is the only moon in the Solar System to possess its own dense and gravitationally bound atmosphere, and is even larger than planet Mercury. Its rocky diameter is a mere $\sim$117 km shy of Ganymede's. If we were to scoop up a 1 cm^3 sample from Titan's upper atmosphere, we would find two dominant molecules: molecular nitrogen N_2 and methane CH_4. Should we look a bit more carefully, we would find many neutral molecules and positive and negative ion compounds. These chemical species are the outcome of processes resulting from energetic radiation reaching Titan's upper atmosphere, breaking apart the initial N_2 and CH_4. A cascade of subsequent reactions will trigger the formation of new gas phase products more and more complex. Eventually, these products mainly containing hydrogen, carbon and nitrogen will form large fractal aggregates composing the opaque haze enshrouding the surface of Titan. This haze is what gives Titan such a unique brownish hue. Most of the photochemically-produced volatiles will eventually condense in the lower atmosphere, where they may aggregate to form micrometer-sized icy particles and clouds.

During my PhD, I have focused my studies on (i) the gas phase reactivity of aerosol precursors in experimental conditions analogous to Titan's upper atmosphere, and (ii) the end of life of some of the products as they condense in the lower and colder atmosphere. I was able to use two experiments to address these respective issues: the PAMPRE plasma reactor, located at LATMOS, UVSQ, Guyancourt, France, and the Acquabella chamber at the Jet Propulsion Laboratory, NASA-Caltech, Pasadena, USA. A paper related to the neutral gas phase reactivity using the PAMPRE experiment has been accepted for publication in Icarus, and a second paper on the positive ion chemistry is to be submitted. In this current manuscript, I present my work on the neutral and cation reactivity in the PAMPRE plasma discharge, as well as ice photochemistry results using laser irradiation.

In Chapter 1, I present the context of my object of interest: Titan. The historical context and scientific discoveries is presented in scope of how our knowledge led to building the Cassini-Huygens Mission. A summary of recent results related to the gas phase upper atmosphere and cold lower atmosphere is also detailed. In light of these findings, I explain how laboratory simulations can provide insight into Titan's atmospheric chemistry.

A brief past and current review of laboratory experiments aimed at reproducing gas and solid phase processes is given in Chapter 2, accompanied with the two experiments that I used during this PhD.

Chapter 3 consists of an investigation of the neutral precursors to tholins present in the PAMPRE plasma discharge. In this chapter I present results using coupled mass spectrometry and an infrared analysis on the main neutral precursors. These measurements were made possible thanks to a cryotrap system developed inside the reactor.

For the first time using our PAMPRE experiment, it was possible to probe inside the plasma and measure the positive ion compounds. Their coupling to neutral species is indeed important (Chapter 1). These results are detailed in Chapter 4. Moreover, I compared these first results with spectra taken by the INMS instrument onboard Cassini.

In complement to these gas phase study, I had the opportunity of carrying out ice spectroscopy experiments in conditions analogous to Titan's lower atmosphere. Near the tropopause, most of the volatiles undergo a gas-solid phase change and icy particles rich in hydrocarbons and nitrogenous species may form. In particular, HCN clouds have been detected and monitored, and spectral signatures of other more complex icy particles likely to be nitrogen-rich are still not fully understood. Our current understanding of how these particles evolve in the lower atmosphere and how they interact with near-UV-vis wavelengths is relatively limited. This project, led at the Jet Propulsion Laboratory, focused on HCN and HCN-C_4H_2 ice mixtures which I irradiated at near-UV wavelengths. The spectral evolutions of these ices are presented in Chapter 5 and put in context of what these results suggest in characterizing the potential solid-state photochemistry in Titan's lower atmosphere.

Over the centuries, our understanding of Titan's atmosphere has drastically expanded, with the help of observations, laboratory measurements and theoretical modeling. The exploration of Titan will certainly flourish over the decades to come, hopefully aided by future robotic missions probing further into its atmosphere, surface and liquid hydrocarbon lakes.

"[...] I am a part of the whole that is governed by nature; next, that I stand in some intimate connection with other kindred parts."

Marcus Aurelius (Stoic philospher and emperor), Meditations Book X (II A.D.)

"[...] And that the other Planets are round like it, and like it receive all the Light they have from the Sun, theres no room (since the Discoveries made by Telescopes) to doubt, Another thing they are like it in is, that they are moved round their own Axis; for since tis certain that Jupiter and Saturn are, who can doubt it of the others? Again, as the Earth has its Moon moving round it, so Jupiter and Saturn have theirs."

Christiaan Huygens, Cosmotheoros (1698)

"The nitrogen in our DNA, the calcium in our teeth, the iron in our blood, the carbon in our apple pies were made in the interiors of collapsing stars. We are made of star stuff."

Carl Sagan, Cosmos (1980)

Acknowledgements

Mentorship

While I attended a lecture on Titan's atmospheric chemistry during my first year of Master's in 2013, I was thoroughly inspired by this organics-rich world. The lecture was given by Pr. Nathalie Carrasco, who would a few years later become my PhD advisor. Nathalie, I wish to thank you endlessly for the opportunities and trust you have given me. Your constant positivity and team-spirit influenced me daily and inspired me throughout the last three years. These were the best 3 years of my life, and you always made sure I was working in the best conditions possible. You always gave me a lot of freedom in my work, while also following it closely. I could not have asked for anything better. I also thank Murthy Gudipati (bahut dhanyavaad!) for having guided me and inspired me. I thoroughly enjoyed working at the ISL, and being an ISLer during the summers. Research is a team effort and would never have been possible alone. Above anything else, I feel humbled and extremely grateful for this long journey, which came to fruition with the help of family, close friends, colleagues and mentors. Because much like in martial arts, this is not an ending but an open door to new beginnings. I encourage every student to pursue their dreams, brush off the negativity, turn obstacles into opportunities and work hard towards daring mighty things. Again, thank you Nathalie and Murthy to Titan and back for being awesome mentors, and giving me the opportunity to work in two amazing labs. I very much look forward to collaborating with you again, pursuing our current work and meeting you at conferences. You have taught me how to be critical of my results, while still giving me enough freedom in my work to make my own path. Murthy, I also thank you (and your family) for the wonderful hiking, camping and biking trips and moments spent altogether in the beautiful California wilderness. These occasional escapades were very resourceful.

I also wish to thank my jury members, for having accepted to be on my committee, thoroughly read my thesis and provided very useful comments on the manuscript: Pr. Cyril Szopa, Dr. Véronique Vuitton, Dr. Nicolas Fray, Dr. Sandrine Vinatier and Dr. François Leblanc. I immensely enjoyed the productive discussion entertained for almost 2h during my defense with all of you. I also thank Ella Sciamma-O'Brien and Farid Salama for greeting me soon in their lab to start new and exciting Titan adventures.

I am grateful to the LATMOS and JPL laboratories, and Philippe Keckhut for having greeted me at LATMOS.

I am of course indebted to all my previous teachers at the OSUC, University of Orléans, in particular Yan Chen and Christian Di Giovanni for their knowledge and classes I always enjoyed.

This research was made possible by funding from the European Research Council Starting Grant PrimChem, grant agreement No. 636829. This research was also partially carried out at the Jet Propulsion Laboratory, California Institute of Technology, and was sponsored by the JPL Visiting Student Research Program (JVSRP) and the National Aeronautics and Space Administration.

Family

My heartfelt gratitude goes to my family for their continuous support and unconditional love. You have given me strength in pursuing my dreams and given me the opportunity to study. Everything I have done is thanks to you, and I especially want to thank my mother for her love, support and inspiration (and for always laughing at all my jokes). Thanks also to my father for his support and interest in my research, and for the tasty buffet. Many thanks to Angèle, Louis, Anas, and Garima for your love, your patience with me especially when I was writing this thesis, and your presence!

This thesis is for all of you!

Friends

I wish to thank all of my close friends with whom I have shared so many memorable moments, especially during the past 3 years: Arnaud, Tiago, Apurva, Charles, Eddie, Nacer, Tanguy and the Bhangra team. Tiago, I am so humbled that we met more than 10 years ago, shared some of our university years and then went on to our theses. Thank you for your presence and all the laughs all of these years. Not to mention our movie premieres in Paris that were interstellar highlights of our lives! I also can't wait to expand our video editing and filming skills to new horizons... Arnaud, since we met, we have spent nothing but amazing moments together, both personally and scientifically. Working all night with you on so many occasions, interspersed with teas, songs, Matlab debuggings or simply talking about chemistry and geophysics was rewarding in so many ways. My PhD would certainly not have been the same without your presence, and I am so thankful that we met. I will fondly cherish all these memories, and may we share more moments like these in the future. Thank you Apurva for your great friendship, for introducing me to Bhangra, for all the dancing, and all the deep discussions about Europa and exomoons. Let us go on many more adventures and create more memories to enjoy in the following new chapters. I also thank Serigne for inspiring me to get a PhD and being my Kung Fu mentor.

Colleagues

Science is never a lone endeavor – teamwork is essential and includes strong social harmony and coordination. Therefore, I wish to thank all my colleagues at LATMOS and JPL for their amazing help: Ludovic, for your incredible knowledge, expertise and kindness which I took so much pleasure from and made working with you a smooth and wonderful adventure. I learned a lot from you, and our mutual optimism participated in the success of many tasks. Future PhD students will surely appreciate immensely working with you, too. Thank you for everything. Many thanks to Sarah, Benjamin, Marie, Lora, Audrey, Jeremy, Bryana, Laura, Demian, Sumya for bringing joy (and new results) to the team. I wish you all the best and will miss you. Thanks to Lisseth for being a great office mate, and bearing with my many posters in our office. Thanks to Pierre for your help in designing new parts for PAMPRE. HCN synthesis and photochemistry analyses would not have been possible without Isabelle's great help and kindness. Thank you for everything.

I also wish to thank admin personnel both at LATMOS and JPL who dealt with tedious tasks in a very supportive and professional way: our staff assistants Karine, Nouria and Valérie, Education Office personnel Arpine and Kim, and ou staff assistants Maria and Gloria. Many thanks to Patrick Galopeau for always stopping by the office and sharing thoughtful discussions with me. I extend these acknowledgements to Bob and Alex, who greeted me at JPL before I started my PhD, whom I had great pleasure working with. I have always heeded your advice.

Resources

I could not go about these acknowledgements without recognizing the impact that *Sci-hub* has had in my life and work. I strongly believe that having the opportunity to have free and open access to all research is crucial for inclusiveness and the progress of science. *Removing all barriers in the way of science* is the way to go. Thank you *Sci-hub*, and its founder Alexandra Elbakyan.

Inspirations

Finally, I thank all of my other inspirations from near and afar, who have had some kind of impact in my life. Carl Sagan, J. S. Bach and Chopin, Ariane, Martha, my Karate Sensei Michel, Efthymios Nicolaidis, Colt, nighttime,, the security agents at JPL and LATMOS for entertaining many discussions, my surgeon for taking care of my lung while writing my thesis, all of my students I tutored in the past 3 years, for your interest and great questions, and for continuously and indirectly making me work on creating a productive and happy working environment for you and I. Lastly, I thank you, the reader, for taking the time to open and read this thesis. I hope you will find it interesting and want to learn more about Titan!

"It was always me vs the world
Until I found it's me vs me"
– Kendrick Lamar, DUCKWORTH (2017)

Contents

Chapter 1

Titan's Atmosphere: An Organic Chemistry Laboratory

"There is not perhaps another object in the heavens that presents us with such a variety of extraordinary phenomena as the planet Saturn: a magnificent globe, encompassed by a stupendous double ring: attended by seven satellites: ornamented with equatorial belts: compressed at the poles: turning upon its axis: mutually eclipsing its ring and satellites, and eclipsed by them: the most distant of the rings also turning upon its axis, and the same taking place with the farthest of the satellites: all the parts of the system of Saturn occasionally reflecting light to each other: the rings and moons illuminating the nights of the Saturnian: the globe and satellites enlightening the dark parts of the rings: and the planet and rings throwing back the sun's beams upon the moons, when they are deprived of them at the time of their conjunctions. (1805)"

Sir William Herschel

"On Titan the molecules that have been raining down like manna from heaven for the last 4 billion years might still be there largely unaltered deep-frozen awaiting the chemists from Earth."

Carl Sagan, Pale Blue Dot: A Vision of the Human Future in Space

1.1 The Saturnian System

The Outer Solar System contains some of the most mesmerizing and castaway worlds that we know. Floating adrift between the asteroid and Kuiper Belts, Jupiter, Saturn, Uranus and Neptune stand tall among the planetary bodies of our Solar System. Each of these planets contains at least 14 moons in the case of Neptune, up to 69 for Jupiter. They are circled by systems of multiple rings, the most impressive one belonging to Saturn. Located beyond those rings, Titan orbits at R_S ~20.3[1] from Saturn (i.e. ~1,223,000 km). It is Saturn's largest moon, and second only largest of the Solar System behind Ganymede. Saturn's subsolar magnetosphere extends to ~17-24 R_S (~1,205,360 km), immersing most of its natural satellites (Bagenal, 2005). There are 62 known satellites orbiting Saturn, 53 of them having official names. They range in sizes from the smallest Aegaeon (~500 m) to Titan, the largest, with a diameter of ~5,151 km (excluding moonlets and icy ring particles).

With its moons, moonlets and icy rings, Saturn seems to have formed a planetary system of its own. The rings extend non-continuously, with two major gaps: the Cassini and Encke Divisions. The A, B, C and D rings are closest to Saturn's cloud top, the F and G are thinner, and the outer E ring is more diffuse and extends all the way to Titan. This extended E ring is being created by the outgassing of icy particles and water vapor. This, and other plasma sources (rings, ionospheres, Titan) contributes to the internal complexity and variability of Saturn's Kronian magnetosphere (Garnier et al., 2007). The induced magnetic field surrounding Titan is caused by the plasma flow and Titan's own atmosphere (Béghin, 2015). This creates an ion tail that can reach a few Titan radii downstream (Snowden et al., 2007). Located near the magnetopause in the sunward direction, Titan can also be outside the magnetosphere (e.g. Bertucci et al., 2015) and cause temperature and chemical changes in the upper atmosphere.

The Saturnian system is far from being a quiet and dormant place: Enceladus' plumes spew out icy particles and water molecules unremittingly (Waite et al., 2017), tidal forces causing heating by interior friction (Běhounková et al., 2017), tidal winds at Titan (Tokano, 2002), shepherd moons causing gravitational instabilities within the rings (Hyodo and Ohtsuki, 2015) and aurorae at Saturn (Pryor et al., 2011), all make it a very dynamic environment. In particular, the diverse moon portrait exhibiting various exo(atmo)spheric phenomena are calling for further investigation. Some of these satellites, dubbed *Ocean Worlds*, may hide global water oceans below the icy surface, potentially interacting with rocky mantle material, such as on Enceladus, Titan, Mimas and Dione (Lunine, 2017; Vance et al., 2017). These worlds may hold conditions suitable for life with the organics, liquid water and heat triad, defining their own "habitable zones" in remote freezing environments orbiting giant planets.

---

[1] Saturn's radius $R_S = 60,268$ km

1.2 The Discovery of Titan and First Explorations

In early 17th century Europe, the Scientific Revolution was already underway. Following the legacy of earlier observations and cosmological models from Islamic and Chinese civilizations, Western Europe was transforming our perception of the workings of the Solar System. Italian astronomer Galileo Galilei pointed the newly invented telescope towards Jupiter in January 1610, and then Saturn, in July of that same year. He was astonished by what he saw: the planet Saturn, with what appeared to be two annexed bodies on either side (Figure 1.1). He wrote, "The fact is that the planet Saturn is not one alone but is composed of three, which almost touch one another and never move nor change with respect to one another." Galileo thought they were "handles" of planetary companions about Saturn. Later observations two years later, the surprise was even greater when these "moons" disappeared. Little did he know that he was the first person to witness Saturn's ring plane crossing. Over the years, many astronomers attempted similar observations with improved lenses, only to come with different interpretations (e.g. see three interpretations in Figure 1.1). About 45 years after Galileo's first observations, Dutch astronomer Christiaan Huygens provided an answer to this mysterious configuration in 1655.

Huygens was born in 1629 and died in 1695 at The Hague, Netherlands. He was a polymath, and excelled at mathematics, physics, astronomy, and optics in particular. In late 1652, with the help of his brother, he started grinding and polishing his own lenses. On March 25, 1655, he pointed one of his first telescopes (which does not exist anymore, only the objective lens does) over the Hague skies in direction of Saturn. That night marked the discovery of Saturn's largest moon, now called Titan. For this observation, he used a plano-convex lens now commonly referred to "*Admovere*", with a 57 mm diameter and 336.7 cm focal length. Along the outer edge of the lens can be read *"Admovere oculis distantia sidera nostris"* ("They brought the distant stars closer to our eyes") dated to February 3, 1655, a mere two months before the titanic discovery (Louwman, 2004). Huygens wanted to keep this discovery secret, until further repeatable observations. He hid, however, in missives, a clue as to what this discovery could be, by the means of the following anagram: *Admovere oculis distantia sidera nostris vvvvvvv ccc rr h n b q x*. He only revealed its true meaning a year later, disclosing not only the discovery of a moon around the farthest planet away known at that time, but also accurate indications about its orbit "*Saturno luna sua circunducitur diebus sexdecim horis quatuor*", i.e. *"A moon revolves around Saturn in 16 days and 4 hours"*.

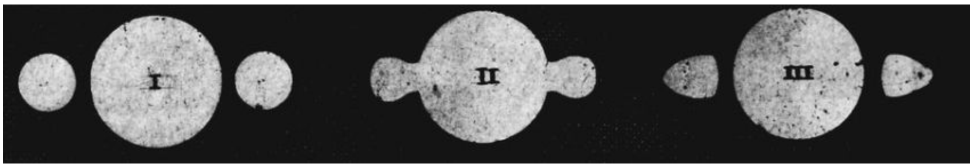

FIGURE 1.1: Drawings of the first observations of Saturn with a telescope. I: Galileo (1610), II: Scheiner (1614), III: Riccioli (1641). From *Systema Saturnium*, Huygens (1659).

He followed the same secretive pattern months later, when he concluded that the oddly-shaped figures around Saturn could be nothing else than a ring plane encircling Saturn (Figure 1.2). In *Systema Saturnium* (1659), he noted that Saturn was "*encircled by a ring, thin and flat, nowhere touching, inclined to the ecliptic*". Therefore, this was the first plausible explanation for the shape of this object. As a consequence, this also provided an answer as to the rings' appearance/disappearance patterns: the planet's (and the ring plane) movement about the ecliptic caused the ring plane to some times be seen from above, some times from down under, and as determined by Huygens, once every ∼15 years (1/2 Saturn year, i.e. every equinoxes), the Earth passes by the ring plane. In other words, the apparent ring tilt changed. The edge-on configuration enables detection of new moons, and was finally confirmed by Huygens' ring-plane hypothesis.

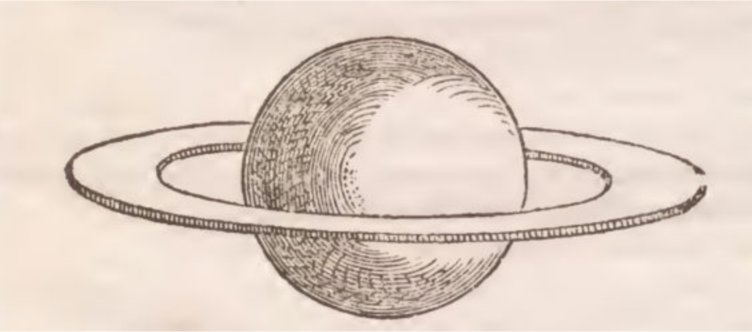

FIGURE 1.2: Sketch drawn by Huygens, taken from *Systema Saturnium*, Huygens (1659).

Huygens pursued observations of Saturn and its large moon for several months, and precisely noted down his observations. Figure 1.3 shows a sketch of his first observation with Titan (noted "*a"), to the right of Saturn. That night, Saturn and Titan had magnitudes of 0.74 and 8.40, respectively. Starting on March 25 1655, Huygens tracked the position of Titan for over two weeks, and subsequently determined a very accurate value for its orbital period, which he found to be a little over 16 days (Figure 1.4). Each numeral corresponds to Huygens' estimate on Titan's position about Saturn after each following day. Note that the orbit was assumed to be perfectly circular in shape, as was thought for all orbits and planetary motion at that time.

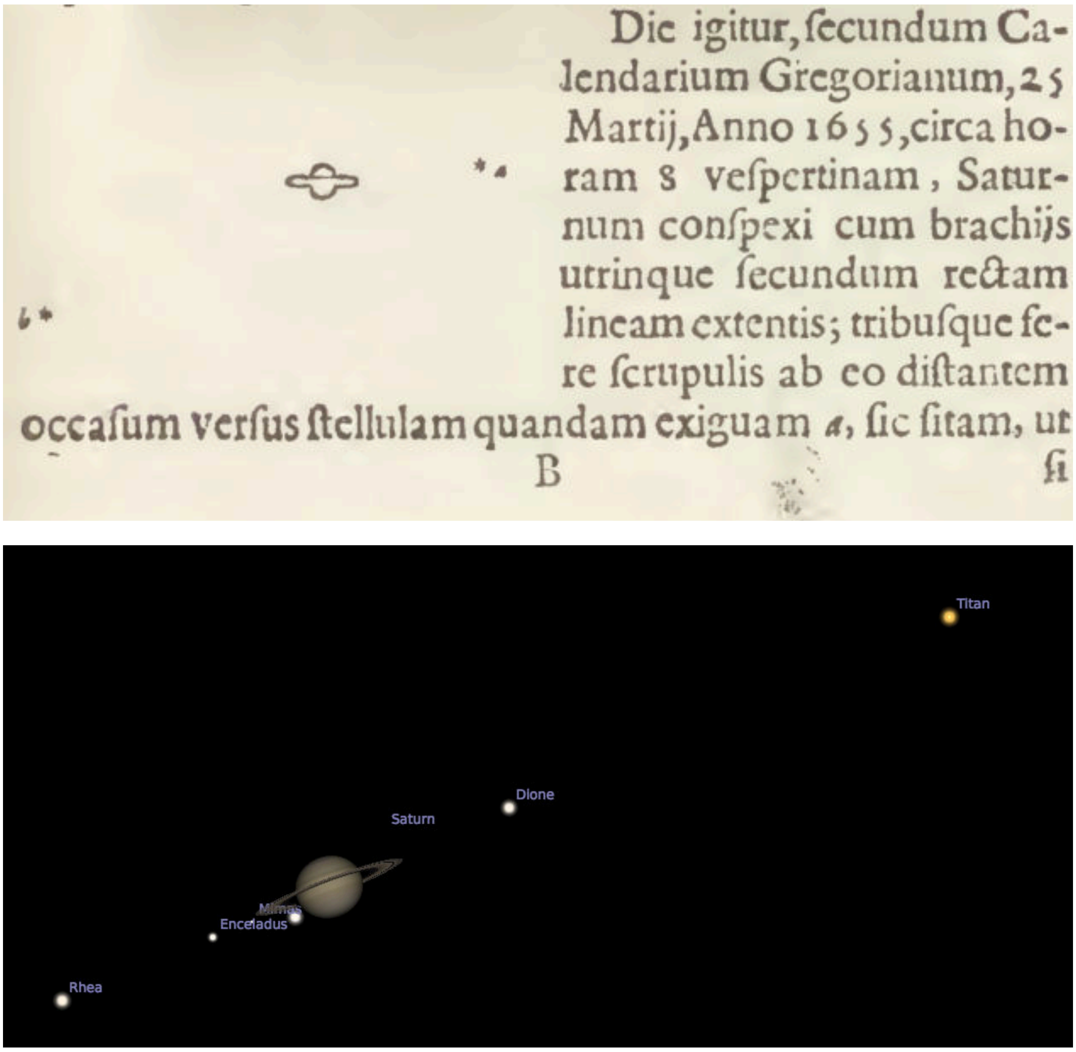

Die igitur, ſecundum Calendarium Gregorianum, 25 Martij, Anno 1655, circa horam 8 veſpertinam, Saturnum conſpexi cum brachijs utrinque ſecundum rectam lineam extentis; tribuſque fere ſcrupulis ab eo diſtantem occaſum verſus ſtellulam quandam exiguam *a*, ſic ſitam, ut

B ſi

FIGURE 1.3: Top: Sketch by Huygens of Saturn (center) along with Titan (right, labeled "*a") taken from *Systema Saturnium*, Huygens (1659). The date indicates March 25, 1655, at 8 in the evening. Bottom: Simulation of this observation and moon configuration, as what would have been seen from The Hague at 8 p.m. on March 25, 1655. This matches almost perfectly the top sketch, with the under-view of Saturn, and Titan on the right-hand side being slightly above the alignment of the ring plane. Unbeknownst to Huygens at that time, Rhea, Enceladus, Mimas and Dione were also aligned in the field.

Titan did not get its namesake until English astronomer Herschel coined it in 1847. Until then, Titan would only be named "Huygens' moon". In the years 1671-1672, Giovanni Domenico Cassini went on to discover Iapetus (1671) and Rhea (1672), the second two largest moons after Titan. He published his discoveries in *Decouverte de deux nouvelles planètes autour de Saturne* in 1673, and then discovered Tethys and Dione in 1684.

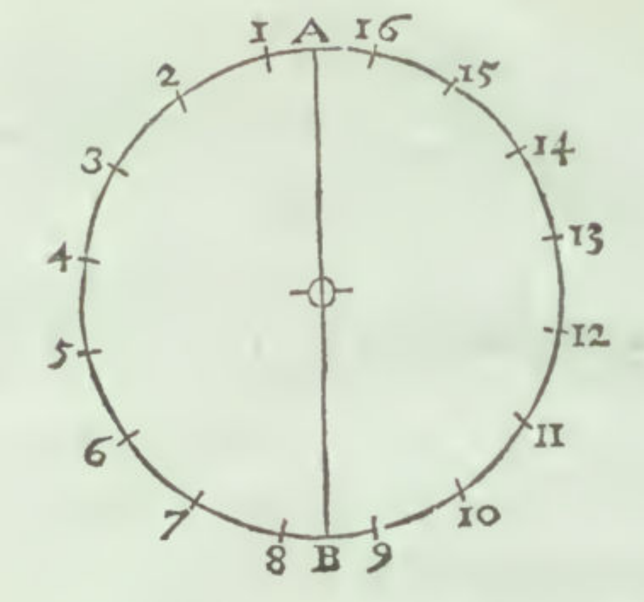

FIGURE 1.4: Sketch of Titan's perfectly circular orbit, by Huygens, determined to be slightly over 16 days, in *Systema Saturnium*, Huygens (1659). Saturn is at the center.

Titan and the Saturn system have remained in the scope of astronomers ever since (Herschel, Laplace, Encke, Maxwell, Pickering...), and further discoveries were awaiting astronomers in the early 20th century.

1.2.1 Titan's atmospheric discoveries

Between the late 17th century and early 20th, telescopic observations and the understand of thermodynamic processes had made great leaps. In 1906, José Comas Solá claimed to have observed limb darkening around Titan, in the summer of 1907 (Solá Comas, 1908), comparing it to similar observations of the Neptune disk. He concluded that Titan must possess a thick absorbing atmosphere. James Jeans further elaborated on this putative atmosphere and escape processes in 1925 (Jeans, 1925; Owen, 1982). The true, indisputable evidence for an atmosphere at Titan *and* the first detection of one of its major constituents came from Gerard Kuiper in 1944 (Kuiper, 1944). Using photographic plates and infrared spectroscopy, he examined Titan (and other Jovian planets) at the McDonald Observatory. His observations revealed the presence of methane CH_4, which has strong absorption bands in the infrared. Now that methane had been found on Titan, the question was whether it was the sole constituent in the atmosphere or if it was only a minor one. The answer came from the combination of observations, experiments and theoretical predictions. The search started with Trafton (1972b) and Trafton (1972a), which searched for H_2 lines, but also showed saturations of the methane bands. Laboratory results indicated methane contamination near those H_2 lines (Giver, 1976). More laboratory measurements of CH_4 absorption and band strength calibration were needed, while matching some of methane's weak absorption bands seen in Titan spectra with the known ones at Jupiter or Saturn could provide abundances. Lutz, Owen, and Cess (1976) used this method by calibrating the pressure-dependent methane $3\nu_3$ weak band. There was a factor of 20 discrepancy with Trafton (1972b). So, by using some of the methane visible bands, Lutz, Owen, and Cess (1976) concluded that methane would have a pressure of only 0.9 mbar. Therefore, some other constituent had to complement the atmospheric pressure in large amounts. They offered two candidates: neon or nitrogen. Both are common gases found in cold environments and spectroscopically transparent. However, the pure-methane atmosphere model vs. the one where methane is a minor constituent still persisted. With the help of laboratory photochemistry of N_2-CH_4 (see also Chapter 2), Chang et al. (1979) remarked that in order to produce stratospheric haze, one needed to account for an N_2-CH_4 atmospheric composition, in particular for the highly sought-for product HCN (Mizutani et al., 1975).

By the end of 1980 however, the Voyager 1 spacecraft provided much insight into Titan's atmospheric composition. It conclusively determined whether Titan was methane-rich with a 20 mbar surface pressure (Danielson, Caldwell, and Larach, 1973) or nitrogen-rich (Hunten, 1973). In particular, Hanel et al. (1981) showed how combined infrared and radio science observations resulted in knowing both the temperature profile and molecular weight content. They found a temperature minimum of $\sim$70 K at the tropopause and a mean molecular weight of 28. Further complementary dayglow and solar occultation experiments by the UltraViolet Spectrometer (UVS) on board Voyager clearly showed the presence of abundant N_2 (Broadfoot et al., 1981). Consequently, the atmosphere had to be dominated by molecular nitrogen, methane being a relatively minor constituent.

About 73 years elapsed between the first speculative guesses that Titan possessed a thick atmosphere by Comas Solá (Solá Comas, 1908) to the actual detection of molecular compounds by the Voyager flyby of the Saturn system in 1980 (Owen, 1982). These remarkable discoveries were just beginning.

1.2.2 Pioneer 11 and Voyager 1 flybys

Between 1979 and 1980, two spacecraft flew by Saturn, Pioneer 11 and Voyager 1. The twin Pioneer and Voyager spacecraft were the first designed to explore the Outer Solar System. On September 1, 1979, Pioneer 11 was at closest approach of Saturn. One day later, it made a far encounter with Titan 363,000 km away (Figure 1.5). Altogether, it was the first manmade object to enter the Saturnian system, 369 years after Galileo first saw it through his telescope. Although Pioneer 11 was not designed for imagery or spectroscopic measurements, it paved the way for Voyager 1, expected to arrive a year later.

The Voyager 1 probe launched in 1977 and arrived at Saturn in November 1980. Inspired by Pioneer a year earlier, Voyager took the daring task of exploring Titan a step further: it flew by Titan on November 11, 1980 at 6,969 km, just 9 months after Northern Spring Equinox (Figure 1.5). Voyager 1 helped decipher Titan's atmospheric chemistry (Hanel et al., 1981) scale height (Tyler et al., 1981) and surface pressure and temperature (Hanel et al., 1981; Tyler et al., 1981), among other things. Photochemical models were refined (e.g. Strobel, 1982; Yung, Allen, and Pinto, 1984 with N_2 being the dominant nitrogen source.

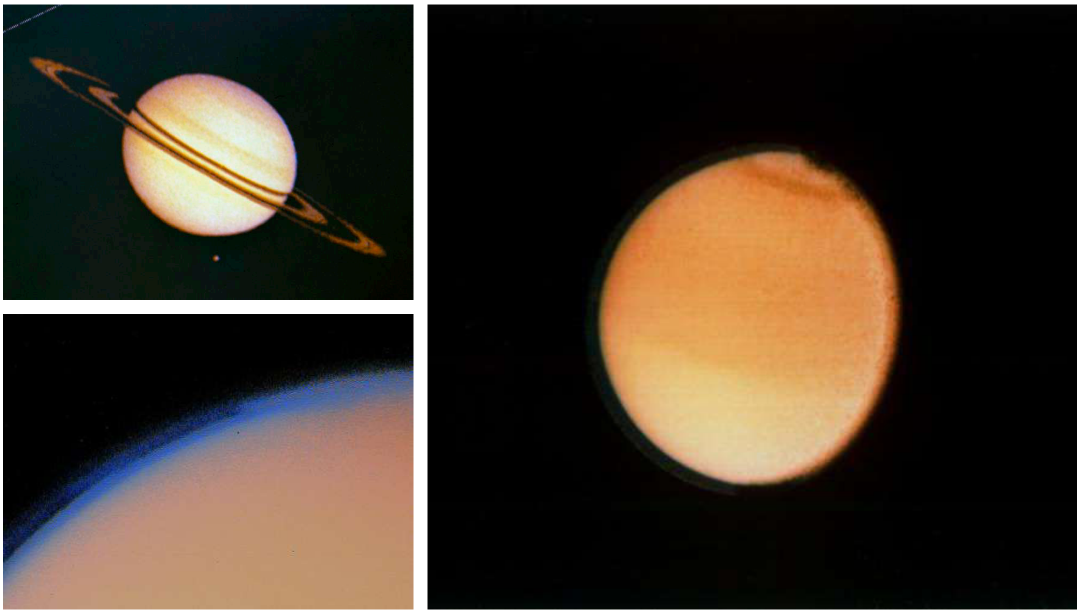

FIGURE 1.5: Some of the first pictures taken of Saturn and Titan up-close. Top-left: Picture taken by Pioneer 11 upon arrival in September, 1979, about 2.8×10^6 km from Saturn. Titan is seen below Saturn. Credit: NASA Ames. Bottom-left: Titan's hazy limb as seen from Voyager 1 on November 12, 1980, on the outbound leg of Titan's closest approach. The thick layered haze is clearly visible, merging into the North polar clouds. Credit: NASA/JPL (PIA02238). Right: Two days before closest encounter with Saturn, Voyager 2 took this picture of Titan on August 23, 1981. A north polar collar is visible, with a brightness dichotomy between the southern and northern hemisphere. These observations indicated potential cloud circulation. Credit: NASA/JPL (PIA01532).

Following the Voyager 2 flyby in August 1981, one thing remained evident: Titan, with its thick N_2 rich atmosphere concealing an uncharted surface, its interactions with Saturn's magnetic field, and plethora of hydrocarbons that was just beginning to be unveiled, required a new mission dedicated to this world. Such a mission was already envisaged in the pre-Voyager era in Carl Sagan's *The Origin of Life in a Cosmic Context* (Sagan, 1974):

"Because of their atmospheric structures and high gravitational accelerations, the Jovian planets are not easy objectives for in situ organic chemistry by space vehicle. Titan is a much more accessible objective. Moreover the carbon-to-hydrogen ratio on Titan is likely to be larger than for any of the Jovian planets. [...] However the pace of plans for examination of Titan is not breathless. Apparently the earliest time for flyby spectroscopic examination of Titan from a distance of a few tens of thousands of kilometers is 1981, and a Titan landing mission probably not until many years after that. But by the late 1980's or early 1990's direct investigations of the organic chemistry of the outer solar system - the clouds of Jupiter, the surface of Titan, the heads and comas of comets - may be expected, and the results of 5×10^9 *yr of prebiological organic chemistry uncovered for the first time."*

1.3 The Cassini-Huygens Mission

1.3.1 Inception, development and launch

The Cassini-Huygens Project started in response to a regular call for missions issued by the European Space Agency (ESA) in 1982, after the remarkable Voyagers encounters of the Saturn system. Many questions remained: what was the surface of Titan like? Was there more to the several hydrocarbons detected in its atmosphere? What were the interactions between Saturn's ring, its moons and magnetosphere? The response was a mission called *Cassini* consisting of a Saturn orbiter transporting a Titan landing probe. The consortium backing this project was lead by three lead scientists: Daniel Gautier (Observatoire de Paris, Meudon), Wing Ip (Max Planck Institute für Aeronomie, Germany) and Toby Owen (State University of New York, Stony Brook, USA). They proposed that the mission be in collaboration with NASA. In the Fall of 1988, ESA released its Phase A study report[2], and in 1988, NASA and ESA validated the *Cassini* orbiter and *Huygens* landing probe for funding, as a joint international mission. By 1989, U.S. Congress approved the mission. In late 1990, the Huygens scientific payload was selected, followed by Cassini's. Huygens was given 6 experiments, and Cassini was to carry a total of 12 instruments (detailed in Section 1.3.3. See also the very detailed review by Ralph Lorenz and Jacqueline Mitton in *Titan Unveiled*, Lorenz et al., 2008).

This was the most advanced and diverse set of instruments onboard a spacecraft at the time. On the one hand, Cassini would be able to perform optical and spectroscopic measurements covering a wide range of the spectrum (IR, optical and UV), plasma field, particle and wave analyses and microwave remote sensing. It combined complementary instruments capable of seeing where others could not[3].

In terms of navigation, this was also an ambitious mission. The voyage to Saturn would last about 7 years, with a launch planned between 1994 and 1997 to accommodate the planetary alignment of Jupiter. The spacecraft was indeed set to use the gravity assist of Venus (x2), Earth and then Jupiter (Lebreton and Matson, 1992). The Jupiter flyby was critical to ensure an arrival at Saturn in 2004 and a cruise of about 7 years[4]. As detailed in ESA's 1988 report, the mission scientific objectives were five-fold (the Saturnian System, primary target), Titan, Saturn, rings, icy satellites and magnetosphere of Saturn. Other targets of opportunity included asteroids, Jupiter and cruise science.

The Titan IVB/Centaur rocket spectacularly launched at nighttime from Cape Canaveral carrying the Cassini-Huygens spacecraft, on October 15, 1997 at 8:43 UTC (Figure 1.6). Saturn Orbit Insertion (SOI) occurred nearly 7 years later, on June 30, 2004.

---

[2] `https://ntrs.nasa.gov/search.jsp?R=19910008874`

[3] See JPL's excellent interactive 3D tool to visualize the Cassini-Huygens spacecraft: `https://saturn.jpl.nasa.gov/mission/spacecraft/cassini-orbiter/`

[4] Detailed timeline of the mission: `https://saturn.jpl.nasa.gov/the-journey/timeline/`

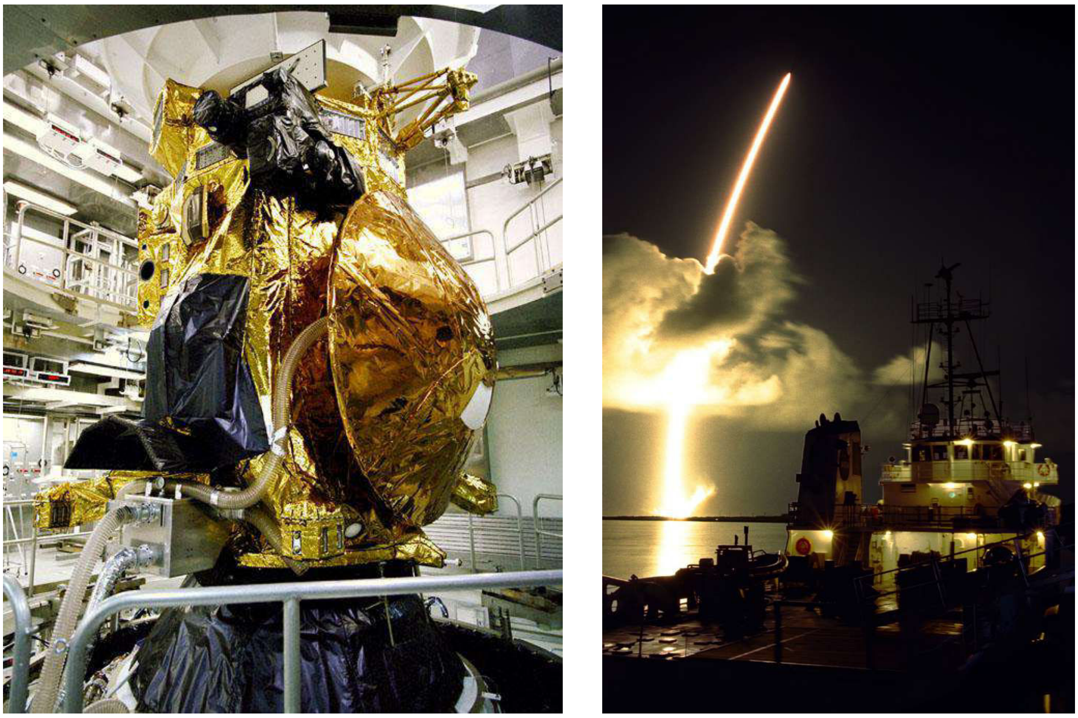

FIGURE 1.6: Left: The Cassini spacecraft with the Huygens probe to the right, atop the Titan IVB/Centaur rocket, awaiting its final shielding, weeks before launch. Credit: NASA. Right: Long exposure of the launch from Launch Pad 40, Cape Canaveral Air Station. Credit: NASA.

The Cassini spacecraft was ahead of its time. It was one of the heaviest and largest spacecraft ever built. Up to now, no spacecraft has ever orbited another planet as far as Saturn as Cassini did. The orbiter (Figure 1.7) measured 6.7x4 m and weighed 5,600 kg at launch, the approximate size and weight of an empty school bus. The total cost of the mission amounted to $3.9 billion. On its way to Saturn, it traveled 3.5 billion kilometers and 7.9 billion kilometers in total over the entire mission. Considering its planned journey to the Outer Solar System, the spacecraft's 885 W of power were supplied by three radioisotope thermoelectric generators (RTGs). The initial mission was planned for 4 years, until 2008, after arrival at Saturn in 2004 (Lebreton and Matson, 1992). It 2008, the Primary Mission being done, it was extended once. This part of the mission was called the Cassini Equinox Mission. The second extension in 2010 that lasted until 2017 was called the Cassini Solstice Mission.

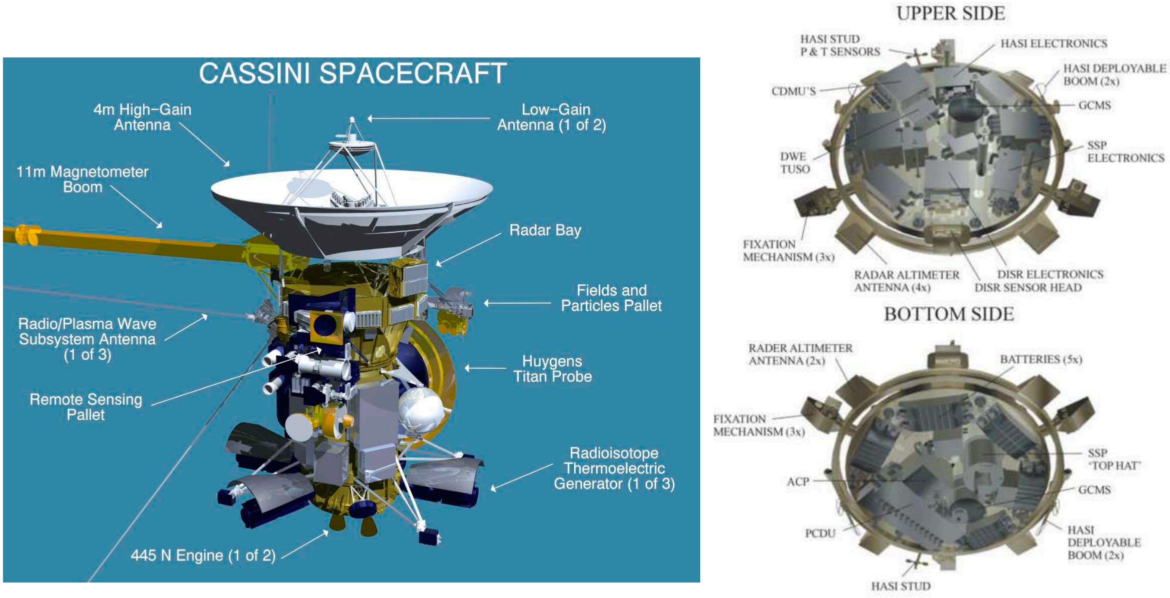

FIGURE 1.7: Left: Cassini spacecraft diagram with its suite of 12 instruments (Section 1.3.3). Credit: NASA. Right: Two views of the Huygens probe (Section 1.3.4 with its 6 experiments (Lebreton et al., 2005).

1.3.2 The Grand Finale

The ending of this fantastic mission, after having spent almost 20 years in space, was grandiose in itself. Dubbed "Grand Finale", the daring final sequences started in April, 2017. Thanks to the final close Titan flyby on April 22, 2017, the gravity assist enabled Cassini to dramatically change its trajectory, bound to plunge in the gap between Saturn's cloud deck and inner part of the rings. Henceforth, it was to dive in this uncharted inner gap every week for five months. Cassini's fate was sealed: there was nothing to do about it, the ship was bound to zip by Saturn's cloud tops, until it eventually disintegrated and united with the planet, on September 15, 2017. The last bittersweet signals received by Cassini at 4:55 a.m. PDT, eagerly awaited, marked the End of Mission (Figure 1.8). Until the very end, Cassini pointed its radio antenna at Earth, communicating with the Deep Space Network.

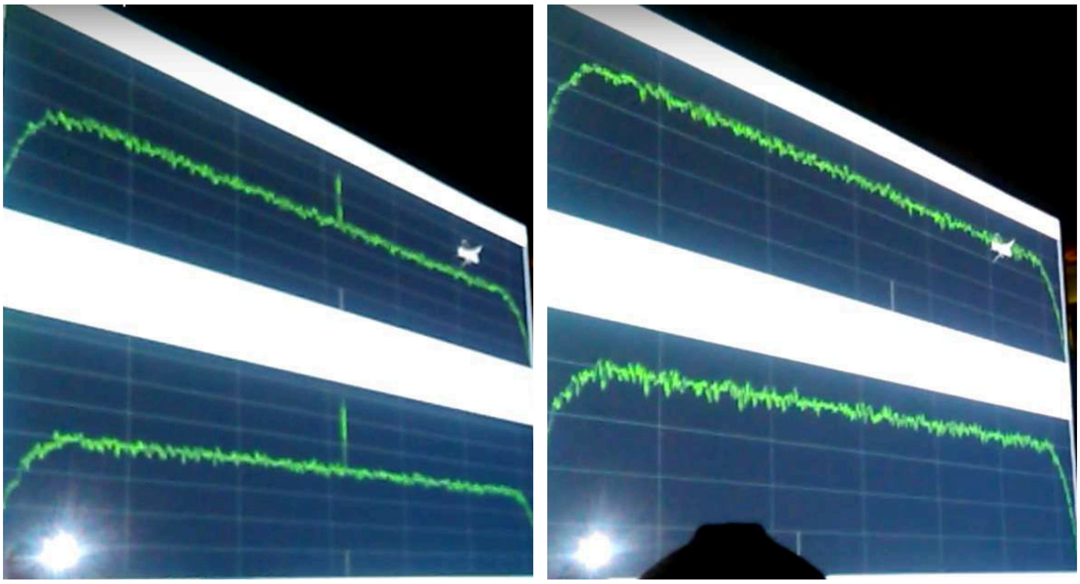

FIGURE 1.8: The final grand moments of Cassini. Left: the X-band up and down link radio signal (top) and the longer wavelength S-band downlink (bottom). The X-band signal started to drop at 4:55:39 a.m. By 4:55:46 a.m. (right), the bottom S-band signal had also dropped. Cassini was now part of Saturn's atmosphere. Pictures taken at the California Institute of Technology, Pasadena, September 15, 2017.

1.3.3 The Cassini Orbiter Payload

The Cassini orbiter had 12 instruments, distributed among the fields and particles pallet and the remote sensing pallet (Figure 1.7 and Lebreton et al., 2005). Pertaining to the upper atmosphere gas phase chemistry, I will put particular emphasis on the INMS and CAPS instruments, as they revolved around studying the upper atmosphere chemistry, to which Chapters 3 and 4 pertain.

The Ion and Neutral Mass Spectrometer (INMS)

The Ion Neutral Mass Spectrometer (INMS) was built by a team of engineers and scientists from NASA'S Goddard Space Flight Center and the University of Michigan (Waite et al., 2004a). Its duty was to analyze the neutral and charged compounds present in Saturn's magnetosphere and Titan's upper atmosphere ($\sim$1000 km). Its mass range was 1u to 99u, and could detect neutral species and low energy ions <100 eV. It had two modes of operation: closed source and open source. The closed source mode was used for neutral species, which consisted in enhancing the neutral gas density in an antechamber before ionizing the gas. In open source mode, the detection was straightforward. The positive ions would be directly deflected and guided through a series of lenses and eventually focused towards a quadrupole mass analyzer (Figure 1.9). Reactive neutral species could also be measured in this mode. Depending on the working mode, the switching quadrupole switching lens can either guide the ions coming from closed-source measurements, or as a 90ž deflector for incoming ions in open source mode. INMS had a $M/\Delta M = 100$ at 10% of mass peak height.

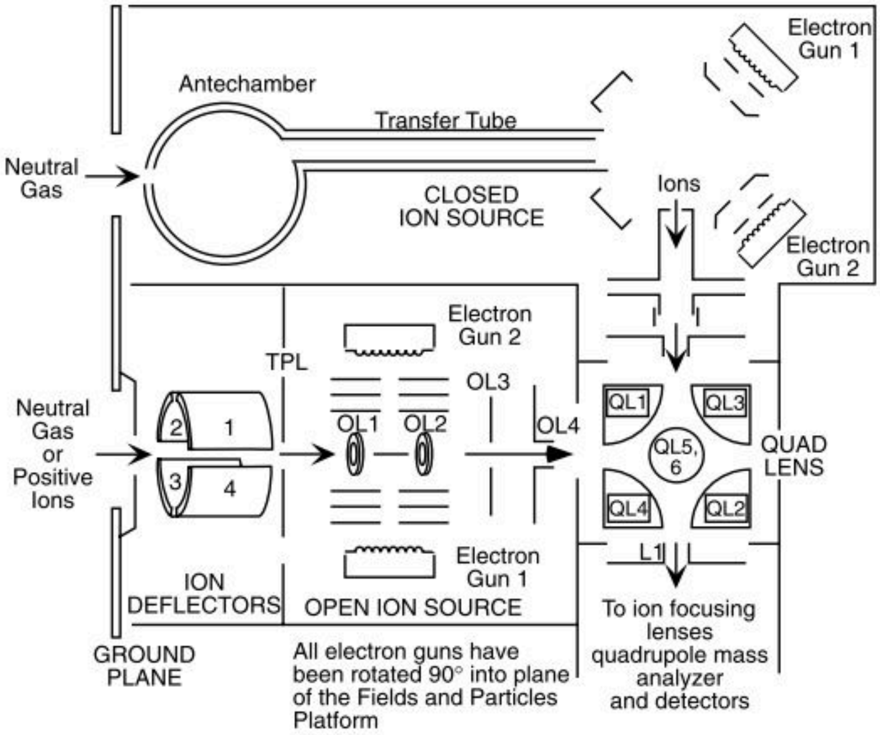

FIGURE 1.9: INMS schematic diagram from Waite et al. (2004a). INMS enabled *in situ* analysis of neutrals and positive ions. The closed-source mode (upper) analyzed non-reactive neutrals (e.g. N_2, CH_4, while the open source configuration (lower) enabled measurements of reactive neutrals and positive ions with energies <100 eV.

The Cassini Plasma Spectrometer (CAPS)

Another instrument which measured *in situ* plasma within and near Saturn's magnetosphere" (Lebreton and Matson, 1992) was the Cassini Plasma Spectrometer, also mounted on the Fields and Particles Pallet (Young, 2004). It consisted of three sensors mounted on a motor-driven actuator: the Electron Spectrometer (ELS), the Ion Beam Spectrometer (IBS) and the Ion Mass Spectrometer (IMS). All three worked harmoniously to detect thermal and more energetic electrons near Titan, ion velocity distributions and the composition of low-concentrated species. CAPS has been an interesting comparison companion to INMS, in that it was able to detected ions beyond the INMS range, although at a lower resolution. At Titan, IBS detected positive ions up to m/z 350 (Crary et al., 2009), ELS negative ions up to m/z ~14,000 (Coates et al., 2007). CAPS went through a series of short-circuits in 2011 and 2012 and had to be turned off.

Other instruments such as the Cosmic Dust Analyzer (CDA), magnetometer (MAG), magnetospheric imaging instrument (MIMI) and the Radio and plasma wave science (RPWS) were also mounted on the Fields and Particles Pallet. CDA analyzed icy and dust particles present in the Saturn system (Srama et al., 2004). MAG and MIMI studied Saturn's magnetic field, and RPWS studied plasma waves and radio emissions coming from Saturn. Furthermore, microwave remote sensing was performed by the radar and by the Radio Science Subsystem (RSS). The radar particularly imaged the surface and altimetry of Titan (Elachi et al., 2004). RSS measured gravity waves and ring structure.

The Composite Infrared Spectrometer (CIRS)

The Composite Infrared Spectrometer (CIRS) was one of four complementary optical remote sensing instruments mounted on the remote sensing pallet (Figure 1.7 and Kunde et al., 1996). It is a better resolution and more advanced version of Voyager's IRIS (Infrared Interferometer Spectrometer) instrument, and sensed thermal emission from e.g. Saturn's rings, icy satellite surfaces, Titan's atmosphere. By design, CIRS was to measure "thermal emission from atmospheres, rings and surfaces" (Kunde et al., 1996). It would also analyze gas composition and aerosol particles. It consisted of a Cassegrain 50 cm fitted with two interferometers, a Far-IR polarizing one ranging from 10 - 600 cm^{-1} (16.67 μm to 1000 μm), the other sensitive to mid-infrared was a Michelson with a 600 - 1400 $^{-1}$ (7.16-16.67 μm). The spectral resolution ranged from 0.5 to 20 cm^{-1}. As seen in Figure 1.10, the Far-IR interferometer had one focal plane (FP1) while the Mid-IR Michelson interferometer had two (FP3 and FP4). CIRS provided enormous contributions to constraining mixing ratios, temporal temperature variations and spectral characteristics of Titan's stratosphere. These will be presented further into this chapter.

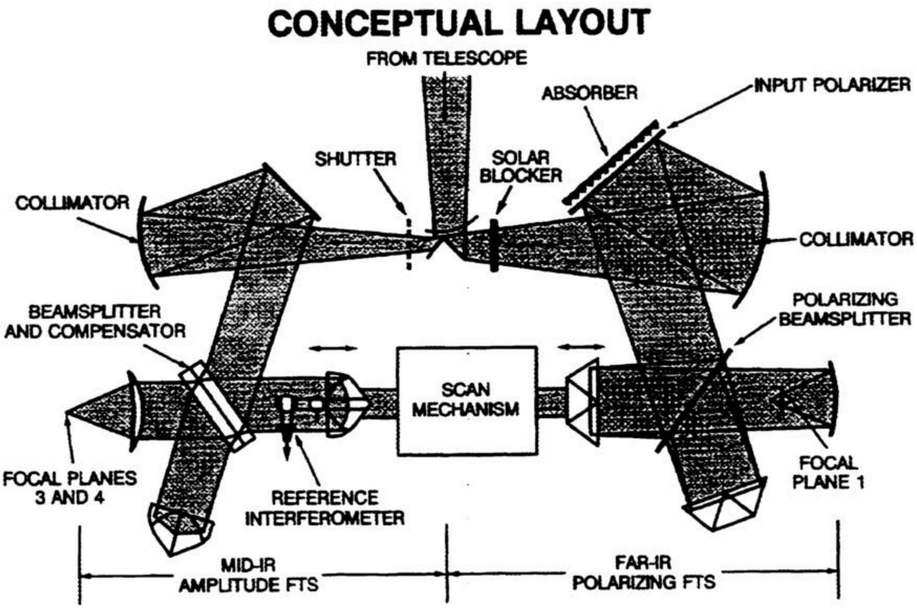

FIGURE 1.10: Schematic diagram of CIRS, with its interferometers and light trajectories coming from the Cassegrain telescope (Kunde et al., 1996).

Visible and Infrared Mapping Spectrometer (VIMS)

VIMS covered the visible and near-IR wavelengths (0.35-5.1 μm, Brown et al., 2004). This was decomposed into the visible channel (0.35-1.07 μm) and the infrared channel (0.85-5.1 μm). While operating, VIMS measured the scattered and emitted light from solid planetary surfaces and atmospheres. At Saturn, VIMS emphasized observations of Titan (aerosol and gas distributions), Saturn, icy satellites and rings. In particular, given some infrared windows reaching down the surface of Titan, VIMS was also able to peak and map its surface.

Ultraviolet Imaging Spectrograph (UVIS)

Ultraviolet spectral imaging aboard the orbiter was led by UVIS, built by the Laboratory for Atmospheric and Space Physics in Boulder, Colorado (Esposito et al., 2004). UVIS had two far and extreme UV spectrographs (55.8-190 nm), which measured the UV light reflected off aerosols. In particular, it helped constrain chemical abundances (e.g CH_4) while looking at specific absorption bands, as well as Titan's limb through solar and stellar occultations, and inferred horizontal, vertical distributions and circulation processes. The solar and stellar occultations were of particular interest for the mesosphere, which measured CH_4 profiles and composition of species such as C_2H_2, C_2H_4, C_4H_2 and HCN.

Imaging Science Subsystem (ISS)

The fourth instrument fitted to the remote sensing pallet was ISS, a multispectral camera, imaging Saturn, rings, Titan and other icy satellites (Porco et al., 2004). It was divided into a narrow-angle camera (reflecting telescope with a 2m focal length) and a 0.2m focal length refractor wide-angle camera. The detector was a charged coupled device (CCD). The spectral filters altogether enabled imaging from 200 to 1100 nm. ISS also took some of the most spectacular images of Saturn's rings, icy satellites and Titan, and tiny moons located within the ring plane.

1.3.4 The Huygens Probe

Huygens was composed of six experiments: the gas chromatograph/mass spectrometer (GCMS), the Descent Imager/Spectral Radiometer (DISR), the Huygens Atmospheric Structure Instrument (HASI), the Aerosol Collector and Pyrolyzer (ACP), the Doppler Wind Experiment (DWE) and finally the Surface Science Package (SSP). In particular, the ACP, HASI and the GCMS performed analyses on Titan's atmosphere. HASI measured the pressure and temperature during the probe's descent, and helped locate Titan's boundary layer at 300 m (Fulchignoni et al., 2005). HASI also carried sensors such as the Permittivity and Electromagnetic Wave Analyzer (PWA) measuring the conductivity of the atmosphere. The ACP directly sampled aerosol particles from the atmosphere, which were then sent to a pyrolyzer to heat them. The organic volatiles released from the pyrolysis were then sent to the GCMS for mass analysis (Israel et al., 2005). Some of these instruments will be put in perspective of their results in later sections of this chapter.

The probe is about 2.7m wide. Its descent in Titan's atmosphere lasted 2h27min. The Entry Assembly Module carried the heat shield and thermal protection during descent, while the scientific payload is located in the Descent Module. On December 25, 2004, the probe jettisoned from Cassini, and started its 22-day descent towards Titan. It then started its plunge towards the surface of Titan on January 14, 2005. The landing was soft, and occurred at 10.3ž S latitude, 167.6ž E longitude, on a frozen riverbed with rocky and icy material. Science operations at the surface lasted for 1h10min, before the probe's batteries turned off. The DISR (Karkoschka et al., 2007) took 376 images during the descent (~2.5 captions/min) and 224 during its surface activity (~3.2 captions/min).

1.3.5 Impact of the Mission

The Cassini-Huygens Mission got extended twice (2008 and then 2010) and was a pioneer of Solar System exploration in many ways. Over the course of its mission, it discovered six new named moons, nearly 8 billion kilometers were traveled in outer space, Saturn's icy moons were flown by 162 times, and last but not least, the overall mission included 27 nations and thousands of scientists worldwide to imagine, design, assemble, send, manage, study, and publish papers (Figures 1.11 and 1.12). But such a feat did not happen overnight. It was a natural continuum of observations, experiments, predictions and missions, from ancient observers to Huygens all the way to the Voyager missions that propelled the interest in exploring the Saturn system and daring mighty things. These limits may hopefully be pushed farther in the coming decades, with more orbiters circling Saturn, and probes hovering over Titan's surface and diving in its lakes, unlocking more organic mysteries kept hidden under its shrouding haze.

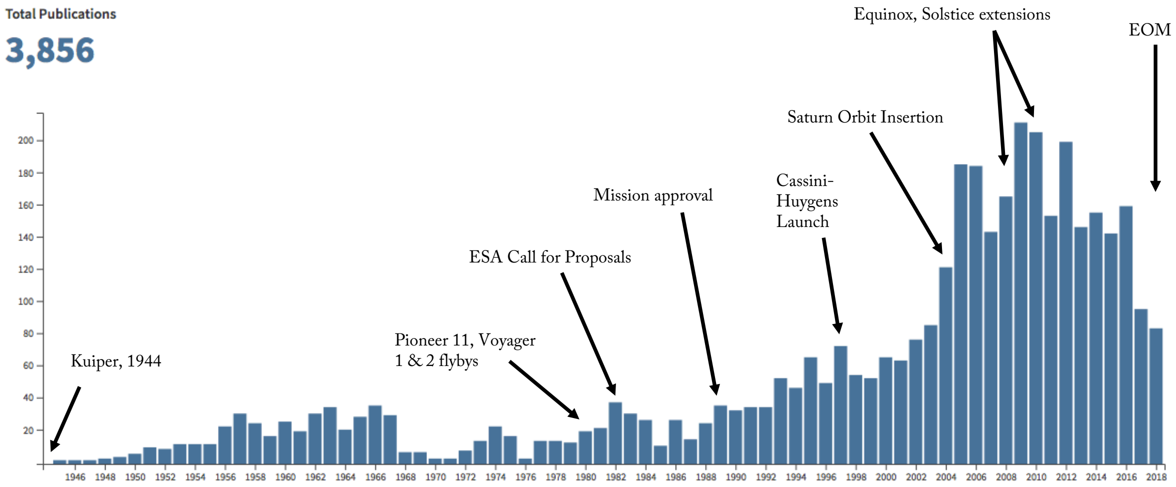

FIGURE 1.11: Total number of publications including the word "Titan" in their title (from Web of Science) from 1945 (1 year after Kuiper, 1944) until Cassini-Huygens EOM (End Of Mission). Also labeled are trailblazing events that enabled further exploration and understand of Titan and the Saturn system.

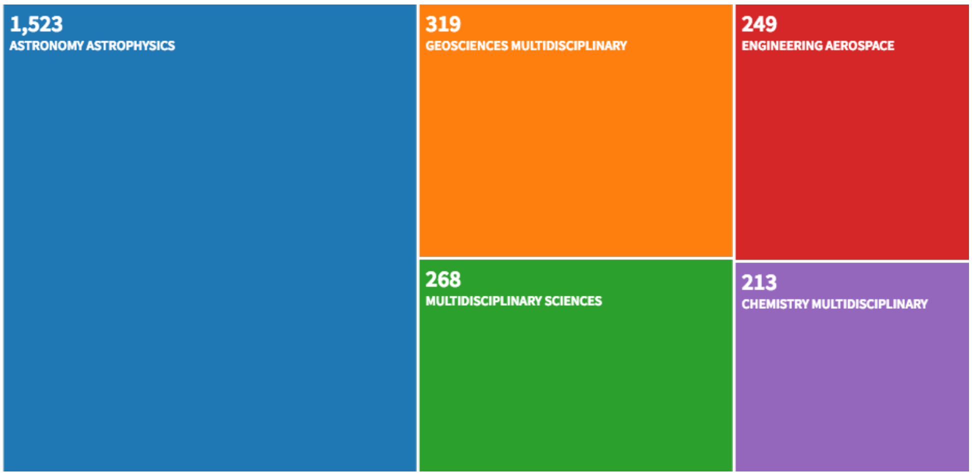

FIGURE 1.12: The five main fields of research implicated in the list of publications from Figure 1.11, showing the multidisciplinary resulting aspect of the mission.

1.4 Titan's Atmospheric Structure

The atmospheric vertical structure has been fairly well constrained by the Cassini-Huygens mission. In addition, the unique descent by the Huygens probe provided us *in situ* measurements of the temperature and pressure vertical profiles at one latitudinal and longitudinal point (Fulchignoni et al., 2005).

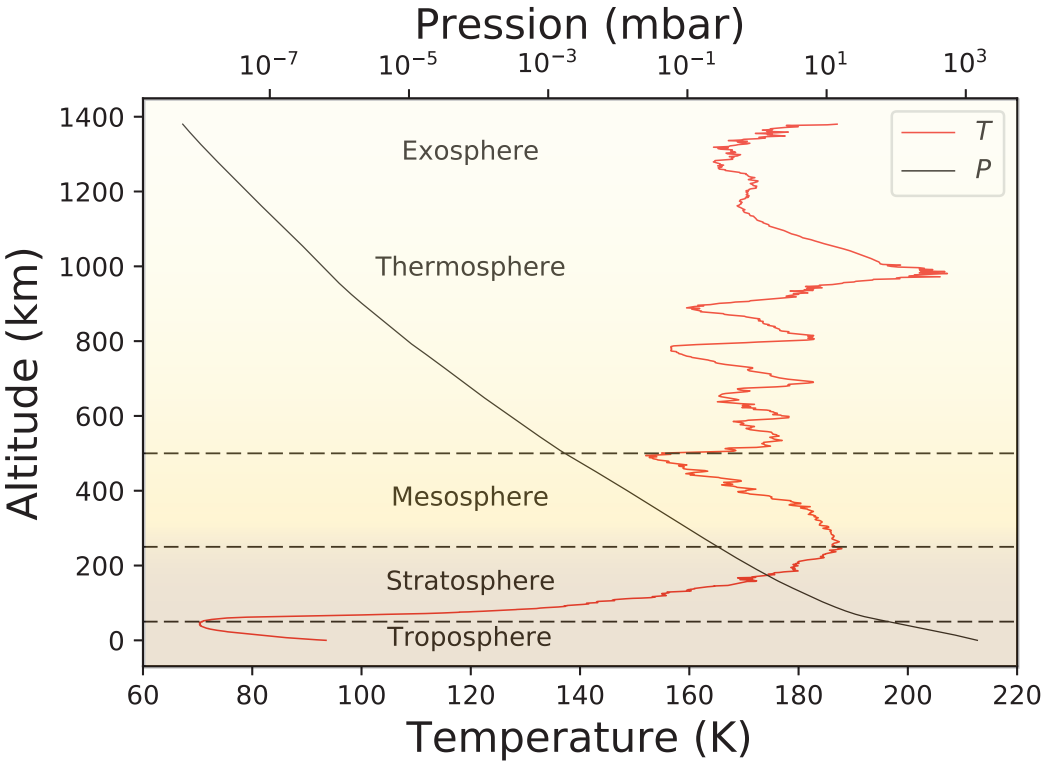

FIGURE 1.13: HASI vertical temperature (red line) and pressure (black line) profiles measured during the Huygens descent.

In Figure 1.13, I plotted the temperature and pressure profiles, as measured by HASI during the Huygens descent. Similar to Earth's, the atmosphere is divided in five layers which each present characteristics in terms of pressure, temperature, and notably in chemistry.

Titan's thermosphere, starting just above the mesopause (∼550 km), is interrupted by the exobase, located at ∼1,200-1,500 km. This limit marks the threshold where the scale height is small against the molecular mean free path. So, light species such as H_2 with escape velocities greater than $\sim 2\ km \cdot s^{-1}$ (Strobel, 2008) can escape. Subsequent ionization of these species can contribute to Saturn's plasma magnetosphere. Plasma-induced sputtering in these top layers may even form a light N and N_2 torus around Titan, gravitationally bound to Saturn (Smith, Johnson, and Shematovich, 2004). The ionized region of the thermosphere is called the ionosphere. The ionospheric peak is located at ∼1,150 km (Nagy and Cravens, 1998; Cravens et al., 2009). Overall, temperatures in the thermosphere increase upward, and are slightly higher than in the mesosphere. This heating occurs due to molecular absorption of short-UV wavelengths. Here, photodissociation and ionization of N_2 and CH_4 occurs, initiating the first steps of Titan's organic chemistry. The mesosphere (∼300-550 km) undergoes a sharp temperature decrease as a consequence of radiative cooling (∼185 to 155 K). Titan's seasonally-dependent detached haze layer is also located in this layer (West et al., 2018). From the "cold trap" tropopause (∼70K, 40 km) up to the stratopause (∼180K, 300 km), haze and methane increasingly absorb UV photons, radiating in the IR, causing heating in the stratosphere. The stratosphere is also an abundant reservoir of hydrocarbon and nitrile species, originating from their formation by the photodissociation of N_2 and CH_4 higher up. Where the temperature profile reaches its lowest value (70K) at the tropopause, most of these species will condense (see Section 1.8). Finally, the tropospheric layer's thermal conditions are controlled by convection processes, explaining the upward decreasing temperature.

1.5 Methane Abundance

The methane mixing ratio ranges from ∼4.5 % (Schröder and Keller, 2008) in the troposphere near the surface. With increasing altitude, near the tropopause, methane starts condensating (e.g. formation of CH_4 clouds) and its gas phase mixing ratio thus decreases. Therefore, methane being the second most abundant species in the atmosphere is not as well mixed in the stratosphere as it is in the troposphere because of this cold trap. Flasar et al. (2005) derives a stratospheric methane mole fraction of 1.6 %, and similar amounts are found in the mesosphere, 1-3 % up to 550 km (Vervack, Sandel, and Strobel, 2004). In the thermosphere, upward CH_4 molecular diffusion causes the methane mixing ratio to reach ∼10 % near 1,500 km (Waite et al., 2005).

Overall, the methane mixing ratio is ∼ 5 %, or less. These constraints are important for experiments in the laboratory, as we inject methane with nitrogen. As explained in Chapter 2, most of the experiments carried out with the PAMPRE reactor use a 1-10% CH_4 mixing ratio (Sciamma-OBrien et al., 2010). Therefore, we use these values to be consistent with the proportions found in Titan's upper atmosphere.

1.6 The Upper Atmosphere

1.6.1 Thermosphere: Energy Sources

The gas phase chemistry in Titan's upper atmosphere is initiated by the photodissociation and ionization of N_2 and CH_4, driven by solar UV, EUV and FUV radiation, energetic particles (electrons, protons) from Saturn's magnetosphere (Figure 1.14). The energy threshold for dissociation of N_2 (Thissen et al., 2009) is 12.4 eV (100 nm, Reaction 1), ionization is 15.6 eV (79.5 nm, Reaction 2) and dissociative ionization is 24.3 eV (51 nm, Reaction 3).

$$\mathrm{N_2 + h\nu \longrightarrow N(^4S) + N(^2S)\,(12.4\,eV)} \qquad \{1\}$$

$$\mathrm{N_2 + h\nu \longrightarrow {N_2}^+ + e^-\,(15.6\,eV)} \qquad \{2\}$$

$$\mathrm{N_2 + h\nu \longrightarrow N^+ + N(^4S) + e^-\,(24.3\,eV)} \qquad \{3\}$$

Figure 1.14 taken from Krasnopolsky (2009) shows the different ionizing sources. We can see that solar EUV photons are the main driver for ionization, about an order of magnitude greater than electrons near 1,000 km, just below the ionospheric peak. Solar radiation is the main driver for ionization of N_2 (Lavvas et al., 2011; Hörst, 2017). Nonetheless, dayside ionization is driven by solar radiation, nightside ionization by the Kronian magnetospheric electrons (Ågren et al., 2009). Other exogenic energy sources contributing to the ionization of the neutral molecules are energetic protons (e.g. H^+, O^+) present in the magnetosphere and torus, galactic cosmic rays (GCRs) and ions created by micrometeorite ablation in the mesosphere.

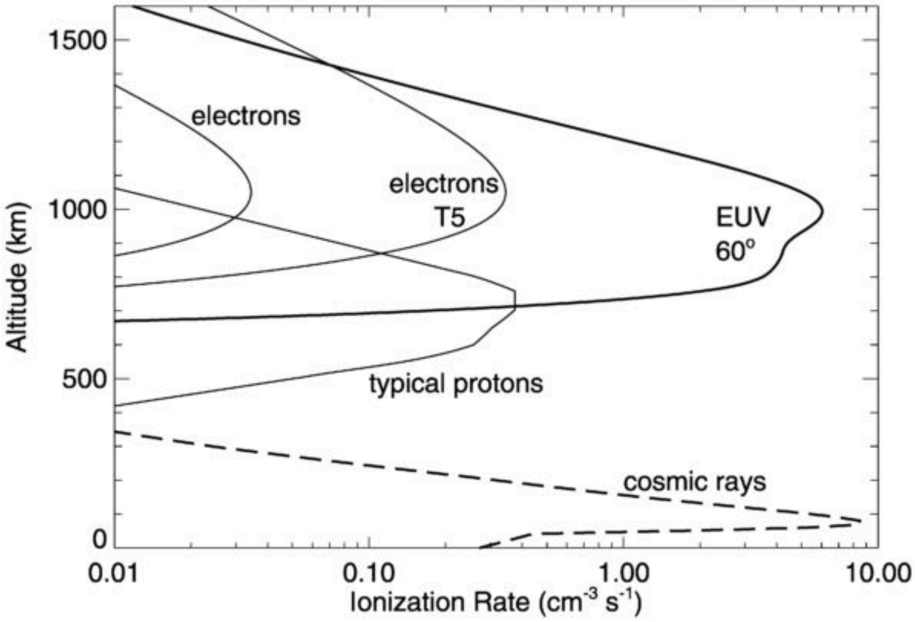

FIGURE 1.14: Different ionization energy sources from the thermosphere to the surface, taken from Krasnopolsky (2009), with an ionizing peak at 1060 km (Solar Zenith Angle 60ž).

Note that GCRs are not absorbed in the upper layers, but may reach deeper down in the atmosphere near the surface. Their presence at these altitudes can create another ionospheric layer, peaking near 60 km (Fulchignoni et al., 2005). GCRs may also play an important role in the HCN/solid-state chemistry (Lavvas, Griffith, and Yelle, 2011) and further ionization deeper down, just after the condensation of the volatiles. Photodissociation and photoionization of CH_4 can also lead to a number of products (see e.g. Krasnopolsky, 2009), such as direct ionization and dissociation of CH_4 (Reactions 4 and 5).

$$\mathrm{CH_4 + h\nu \longrightarrow {CH_4}^+ + e^-}\ (\lambda < 93\,\mathrm{nm}) \tag*{\{4\}}$$

$$\mathrm{CH_4 + h\nu \longrightarrow {CH_3}^+ + H + e^-}\ (\lambda < 86\,\mathrm{nm}) \tag*{\{5\}}$$

As we can see, the production of the primary ion products are directly linked to the presence and abundance of neutral N_2 and CH_4. Their photodissociation and photoionization produce immediate primary ions and radicals, readily available to react with other neutral and charged compounds. This growth, coupling neutral and ion chemistry, is at the core of the further evolution and complexity of the gas phase products.

1.6.2 Neutral Gas Phase Chemistry

Since the first detection of a compound (i.e. CH_4) in the atmosphere by Kuiper (1944), a plethora of neutrals have been additionally detected. After the Voyager 1 encounter in 1980, a large quantity of trace hydrocarbons such as C_2H_2, C_2H_4, C_2H_6, C_4H_2, C_3H_8 were cataloged (Owen, 1982). The first N-containing photochemical product detected was HCN by Hanel et al. (1981). HCN not only was its first detection at Titan, but also in any planetary atmosphere (Hanel et al., 1981). Thanks to INMS measurements, we now know that HCN is the most abundant N-containing photochemically-produced species (Vuitton, Yelle, and Anicich, 2006; Vuitton, Yelle, and McEwan, 2007; Waite et al., 2007; Magee et al., 2009) with a mole fraction on the order of 10^{-4} near the ionospheric peak. Other photochemical products involving nitrogen include NH_3, C_2N_2, CH_3CN and HC_3N, just to name a few. Ground-based observations have also helped constrain their mixing ratios or detect new N-bearing species (e.g. Tanguy et al., 1990; Bezard and Paubert, 1993; Hidayat et al., 1997; Cordiner et al., 2014a; Molter et al., 2016; Palmer et al., 2017).

The neutral gas phase inventory mainly relies on hydrocarbon and nitrile compounds (and to a lesser extent Ar and H_2). However, many other neutral species in the lower or upper atmosphere have also been detected. Some of which, including oxygen, phosphorous or sulfur-bearing compounds have had their upper limits inferred (Cottini et al., 2012; Cui et al., 2009b; Nixon et al., 2013; Teanby et al., 2018).

Figure 1.15 shows the neutral and positive ion correspondences, as measured by INMS during T19 between 950 and 1,000 km. The neutral spectrum (Figure 1.15, bottom panel) is dominated by the presence of light hydrocarbons, N_2 and HCN. Waite et al. (2007) suggested the key role in ion-neutral coupling for the production and growth of heavier and more complex species as precursor to the aerosols.

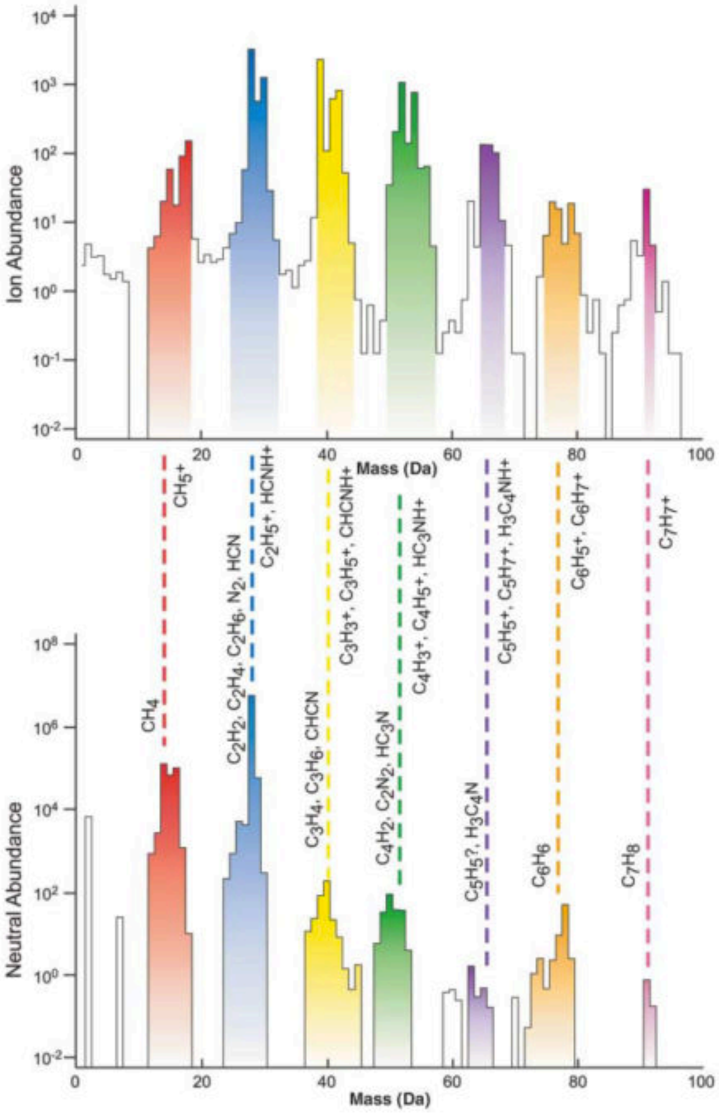

FIGURE 1.15: T19 INMS spectra from Waite et al. (2007), taken between 950 and 1000 km. Lower panel: neutral spectrum. Upper panel: positive ion correspondences.

1.6.3 Positive Ion Chemistry

Early photochemical models (e.g. Keller, Cravens, and Gan, 1992; Fox and Yelle, 1997) started including positive ion chemistry for Titan's ionosphere. Earlier models were using coupled ion-neutral chemistry for the outer giant planets (Atreya, 1986), after the Voyager encounters. With the arrival of Cassini at Saturn and increasing INMS measurements, it became clear that the positive ion reactivity involved a long list of species that could react with their neutral counterparts. Vuitton, Yelle, and McEwan (2007) provided an updated photochemical model based on one of the first Titan encounters (Figure 1.16). Some complex ions up to m/z 100 were detected. In particular, they derived mole fractions of 19 neutral species, which included polyynes and cyanopolyynes, and presented a thorough analysis of ion production and loss mechanisms, directly dependent on the neutral composition. $HCNH^+$ was the dominant ion with a density of 4.6×10^2 cm^{-1} and was mainly produced by proton attachment with the following Reaction 6.

$$C_2H_5^+ + HCN \longrightarrow HCNH^+ + C_2H_4 \qquad \{6\}$$

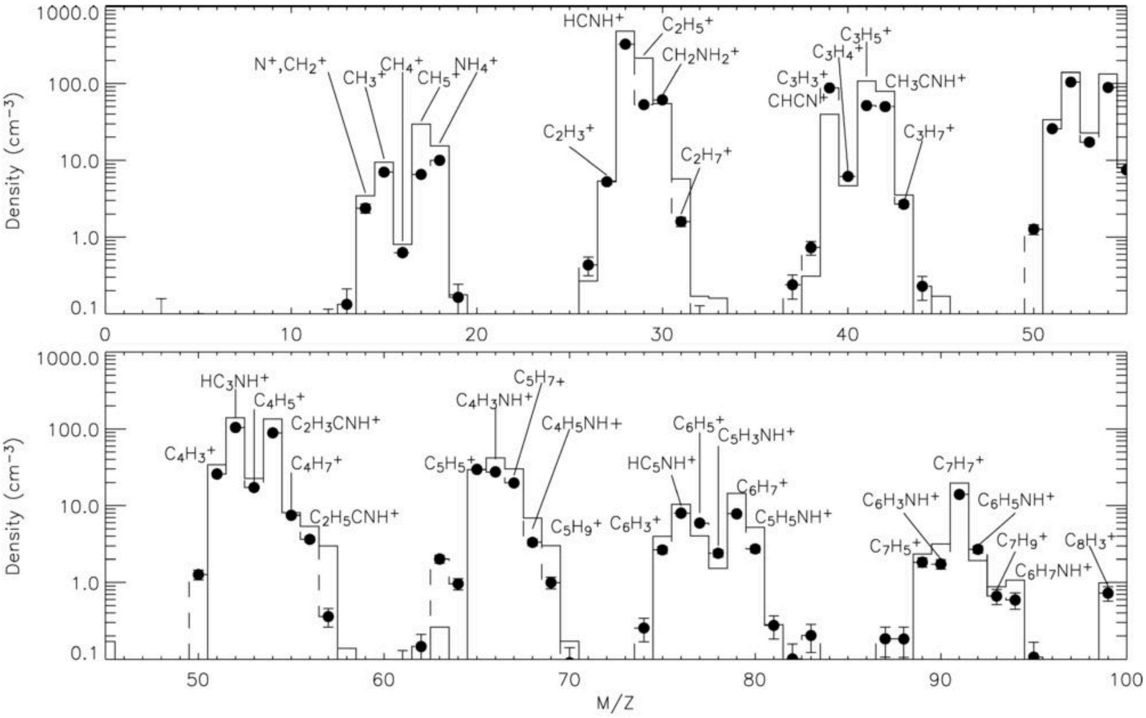

FIGURE 1.16: T5 INMS nighttime spectrum, from Vuitton, Yelle, and McEwan (2007), showing the densities of ions inferred from the neutral densities. The spectrum shown is averaged from spectra taken between 1027 and 1200 km. Closest approach occurred at 75ž N.

CAPS-IBS also demonstrated its capabilities and covered a wider mass range. It could sample up to m/z ~300 (Figure 1.17). Comprehensively combining INMS and CAPS-IBS data enabled characterizing masses >100 *m/z* using the derived INMS densities (e.g. Crary et al., 2009; Westlake et al., 2014). Crary et al. (2009) attributed ion species for heavy aliphatic (N-bearing and hydrocarbon) as well as aromatic compounds.

Furthermore, Cravens et al. (2009) modeled the neutral and positive ion chemistry involving the primary ions and some of the heavier ion species (e.g. $HCNH^+$, $C_2H_5{}^+$) compared with INMS measurements on Titan's nightside ionosphere taken during the T5 and T21 flybys. They correlated these results with CAPS ELS measurements of the Kronian magnetospheric electron fluxes reaching the upper atmosphere. Their results indicated a temporal and spatial (altitudinal) variation of some ion density profiles in Titan's nightside ionosphere. Such variations were shown to be likely due to the distribution and composition of major and minor neutral species (N_2, CH_4, HCN...), as well as the primary ion production rates determined by the electron fluxes originating from the Kronian magnetosphere. For example, the distribution of $CH_5{}^+$ was shown to be strongly associated with the incident electron flux, and its density near the ionospheric peak better fitted with models incorporating a more abundant C_2H_2 and C_2H_4 reservoir (Cravens et al., 2009). ${CH_5}^+$ is indeed subsequently converted into ${C_2H_5}^+$ via reaction with C_2H_4 (Reaction 7 and Vuitton, Yelle, and McEwan, 2007). Overall, the nightside vs. dayside ion density profiles are different in intensity, although similar in distribution (Cravens et al., 2009; Robertson et al., 2009). Ågren et al. (2009) found that the dayside plasma electron density was ∼4x larger than on the nightside.

$$\mathrm{CH_5}^+ + \mathrm{C_2H_4} \longrightarrow \mathrm{C_2H_5}^+ + \mathrm{CH_4} \qquad \{7\}$$

The neutral and positive ion chemistry is intimately intertwined in Titan's upper atmosphere. Both display an unsuspected complexity, suggesting higher and larger compounds rely on the production of lighter ones, threading the way to aerosol growth. This ion-neutral coupling needs further investigation in the laboratory. A review of these experiments is made in Chapter 2.

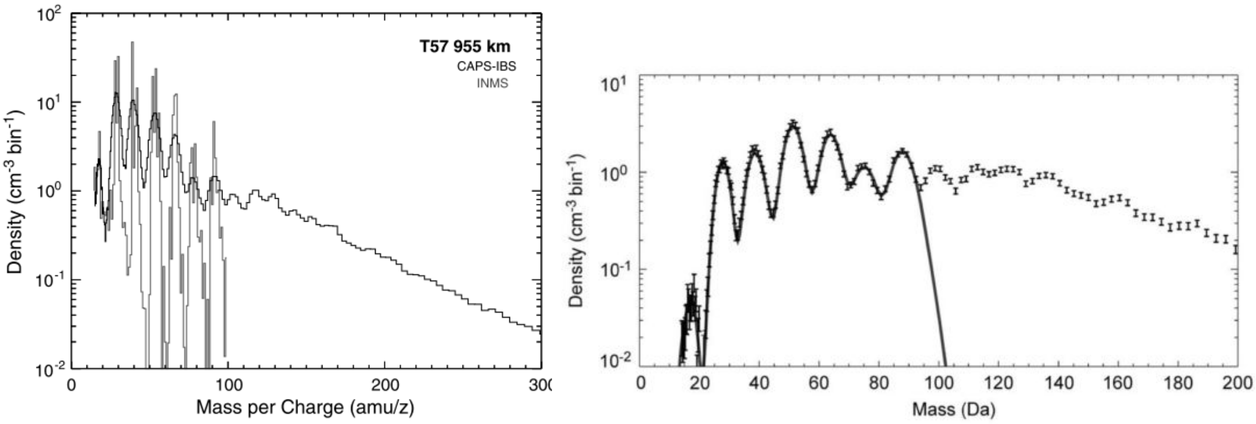

FIGURE 1.17: Left: T57 CAPS-IBS spectrum with m/z up to 300 compared with an INMS spectrum, both taken at 955 km (Westlake et al., 2014). Right: CAPS-IBS and INMS fit model spectrum, taken at T26 at 1,025 km (Crary et al., 2009).

Positive ion laboratory studies are further needed to characterize these precursors, whether in plasma or UV discharges. INMS and CAPS both unveiled cation compounds at high altitudes (Figures 1.16 and 1.17), that suggest the ion-neutral chemistry is initiated at higher altitudes than previously thought. In the post-Cassini era, laboratory experiments can probe at higher masses with a higher resolution, and reveal or confirm compounds with varying gas mixing ratios and/or wavelengths.

1.6.4 Negative Ion Chemistry

An important and unsuspected discovery at Titan's upper atmosphere was the evidence for abundant and large negative ions. Their existence was revealed by Coates et al. (2007) using CAPS-ELS measurements from 16 passes from 950 km to 1174 km. In one case (T16, 950 km), negative ions up to m/z 10,000 were observed.

They were detected regardless of the position of the spacecraft, both at daytime and nighttime (Coates et al., 2007). Coates et al. (2009) provided a more systematic study as to the latitude and altitude dependencies of these negative ions. In Desai et al. (2017), they found a consistent growth from small anions to larger ones, with decreasing altitude (1300-950 km). These trends are consistent with CN^-/C_3N^- and C_2H^-/C_4H^- growth patterns (at m/z ~26 and m/z ~50, respectively).

There are currently three published papers accounting for the anion chemistry in Titan's ionosphere using photochemical modeling (Vuitton et al., 2009; Dobrijevic et al., 2016; Mukundan and Bhardwaj, 2018). The model by Vuitton et al. (2009) was the first to include negative ion chemistry, and focused on 11 low-mass ions. In spite of poor mass resolution (ELS was designed to detect electrons, not negative ions, Coates et al., 2007), CN^-, C_3N^-/C_4H^- and C_5N^- were predicted to be the three most abundant negative ions, with densities ranging from 10^{-2} to 10^{0} cm^{-3} and slightly more intense at 900-1100 km altitudes (Figure 1.18). Among their production pathways (ion-pair formation, dissociative electron attachment, radiative electron attachment), dissociative electron attachment of supra-thermal electrons with nitriles such as HCN was found to be significant in the first steps of the anion chemistry. Dobrijevic et al. (2016) provided updated density profiles of the major anions. Recently, Mukundan and Bhardwaj (2018) revisited these density profiles for Titan's dayside T40 flyby with updated cross-sections and reaction rate coefficients. In agreement with prior studies, CN^- was found to be the most abundant anion ($\sim 5 \times 10^{-1}$ cm^{-3} at ~1015 km). However, the second most abundant anion was either H^- or C_3N^-, with an inversion near the ionospheric peak (Figure 1.19).

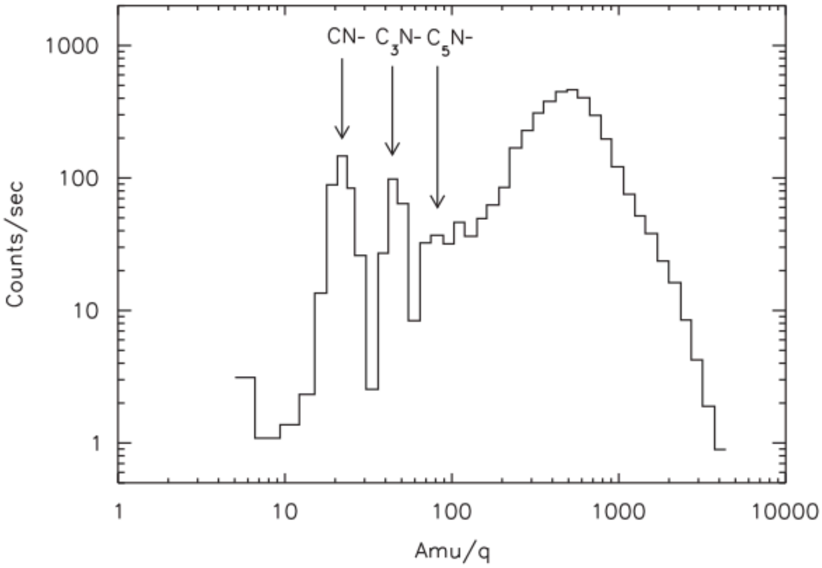

FIGURE 1.18: The CAPS-ELS negative ion spectrum, from Vuitton et al. (2009), taken during T40 at 1015 km. The three most abundant ions CN^-, C_3N^- and C_5N^- derived from the photochemical model are indicated.

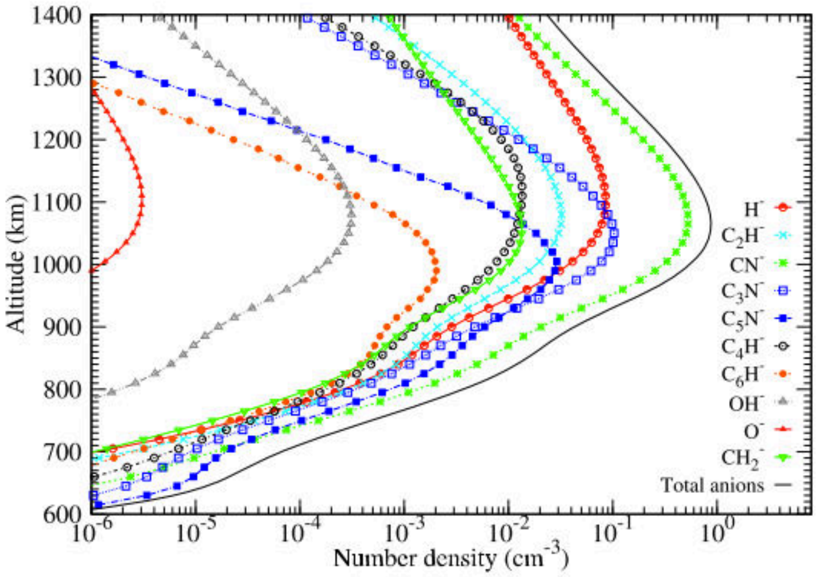

FIGURE 1.19: 10 dominant anion abundances found by Mukundan and Bhardwaj (2018) using updated cross-sections and reaction rate coefficients, of the same flyby as Figure 1.18.

At present, only one laboratory simulation has preliminarily detected negative ions in a plasma discharge of Titan-like ionosphere conditions (Horvath et al., 2009). Their detection in plasma discharges is challenging (Chapter 2), yet crucial in order to better characterize the tholin precursors in N_2-CH_4 mixtures.

1.7 The Ionosphere: A Dusty Plasma

The gas-to-solid conversion in the upper atmosphere is still poorly understood. Laboratory work such as probing the precursor gas phase or analyzing specific chemical channels in Titan-like conditions can help in understanding particle inception, coagulation, sticking and surface growth, as well as structural patterns that may be found in laboratory tholins.

Lavvas et al. (2013) modeled the chemical and physical growth of the aerosols, and their interaction with positive ions. Negatively-charged aerosols may react with positive ions and grow. This growth revolves around ion-neutral reactions and can explain observations by CAPS-ELS and CAPS-IBS of negative ions and positive ions, respectively. For particles ranging in radii from 0.35 nm to 1.6 nm (i.e. 100 Da. to 10,000 Da.), they find the total particle density to be greater than the charge balance, and conclude that the plasma is dusty. Therefore, an efficient ion-neutral chemistry in the ionosphere may occur and participate in the organic growth.

1.8 The Lower Atmosphere

As we saw in the previous section, the chemistry initiated in the upper atmosphere relies on the coupling between neutral, positive and negative ion gas phase precursors. These compounds diffuse downward, and eventually condense near the tropopause. Using a cloud microphysics and radiative transfer model, Barth (2017) recently reviewed the condensation profile and cloud formation of several trace species present in the stratosphere (Figure 1.20). Interestingly, C_2H_4 is the only species here to not reach saturation and so does not condense. CH_4 condenses the lowest, just below the tropopause (Wang, Atreya, and Signorell, 2010). According to Barth (2017) condensation nuclei radii are the largest for C_2H_6 ($\sim$10 μm).

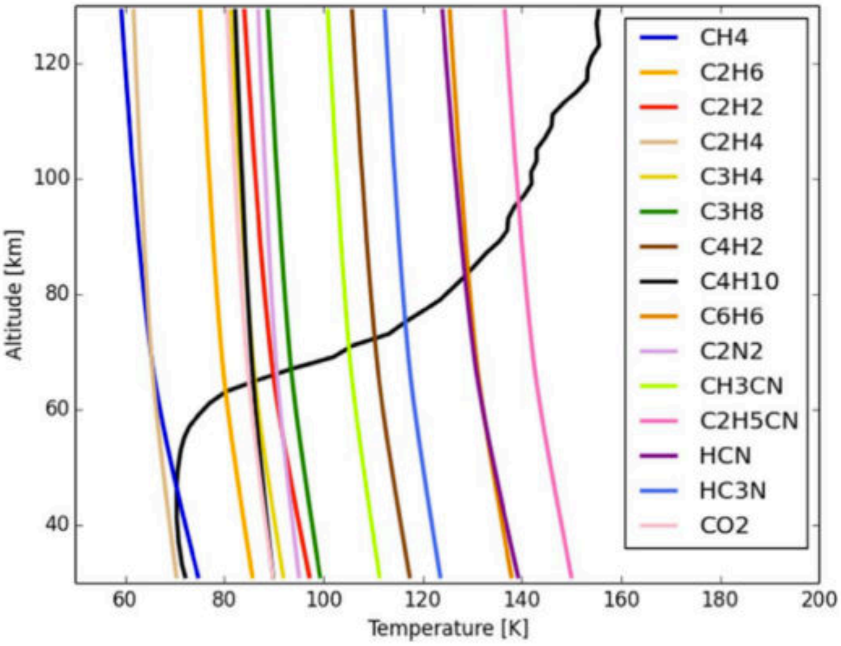

FIGURE 1.20: Condensation curves obtained for 15 neutrals, intersecting the temperature profile (black line), by Barth (2017).

HCN, the most abundant photochemical nitrile product (Section 1.6.2) reaches its condensation point at $\sim$80-90 K. Episodic seasonally-driven dynamics can however perturb these clouds and their formation, such as vertical dramatic cooling episodes. For example, using VIMS, De Kok et al. (2014) detected an HCN cloud at an altitude of 300 km (i.e. three times higher than its expected condensation altitude) at the south pole, coinciding with the winter polar vortex. Such clouds can be a strong source of opacity in the atmosphere (e.g. Anderson and Samuelson, 2011).

Another interesting unresolved feature seen in the far-IR by CIRS in high northern latitudes is shown in Figure 1.21. At 220 cm^{-1}, a broad absorption feature clearly separated from the continuum has been detected (Anderson et al., 2014; Muller-Wodarg et al., 2014), and named the *haystack* feature (also seen in IRIS/Voyager data by Kunde et al., 1981). The band, has been interpreted as a composite ice absorption. This feature was indeed continuously tracked from 2004 to 2012, where its intensity decreased by a factor of of four (Jennings et al., 2012). Trends in other gaseous nitriles showed similar evolutions in the stratosphere (e.g. Vinatier et al., 2010), making a complex nitrile mixture a good candidate resulting in such a broad absorption feature.

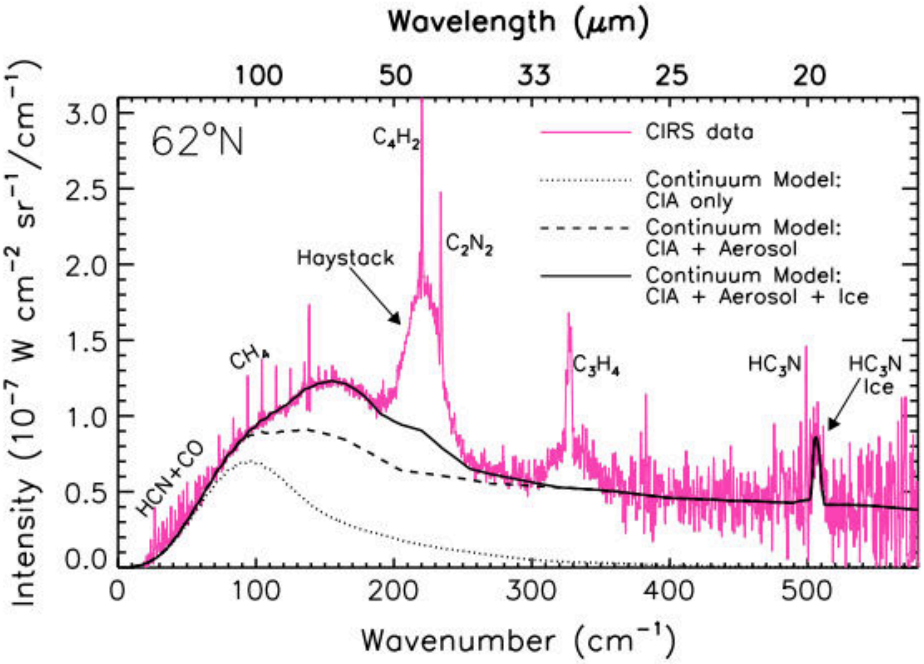

FIGURE 1.21: CIRS limb spectrum (pink) at a 0.48 cm^{-1} spectral resolution, at a limb tangent height of ~125 km (Anderson et al., 2014). The broad *haystack* feature at 220 cm^{-1} is attributed to an ice cloud absorption, potentially nitrile-rich.

The rich gaseous chemistry, condensation and dynamical processes in the stratosphere and lower stratosphere, controlled by seasonal effects, shown by CIRS, indicate a very different chemistry from that of the upper atmosphere. The icy particles and cloud condensation nuclei forming aggregates near the cold trap tropopause are under the influence of long-UV radiation. That is, while the gas phase photochemistry diminishes at these lower altitudes, ice particles may experience solid-state chemistry.

Figure 1.22 shows the depth of penetration of photos in the lower atmosphere (Lavvas, Coustenis, and Vardavas, 2008). Lesser energetic UV-vis photons (>300 nm) may reach the lower stratosphere below ~100-110 km.

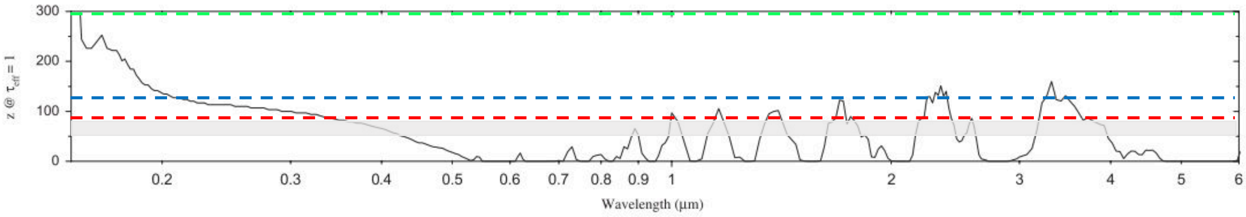

FIGURE 1.22: Adapted from Lavvas, Coustenis, and Vardavas (2008), the depth of penetration of photons in the lower atmosphere. The green dashed line corresponds to the altitude of the HCN cloud detected at 300 km (De Kok et al., 2014). The *haystack* feature detected by Anderson et al. (2014) at ∼125 km is shown as the blue dashed line. The red dashed line corresponds to the approximate HCN condensation altitude region as given by Barth (2017), and the gray shaded area below it is the saturation point of most other volatiles (Barth, 2017).

Experimental work has been carried out to simulate these distinct conditions (e.g. Gudipati et al., 2013; Couturier-Tamburelli et al., 2014; Anderson et al., 2016; Couturier-Tamburelli et al., 2018; Nna-Mvondo, Anderson, and Samuelson, 2018 and are detailed in Chapter 2.

Current Questions and Objectives of this PhD thesis

The chemical reactivity in Titan's atmosphere implies many underlying processes involving neutral and ion species, in the gas and solid phases. These processes are controlled by energy deposition and ionization mechanisms, as well as by dynamical and seasonal effects. The Cassini-Huygens mission, coupled with laboratory and theoretical simulation, and state-of-the-art ground-based and space-based observations have all participated in making a clearer picture of the chemistry at work in Titan's atmosphere. The next mission to Titan might not happen before another few decades. Cassini data although is likely to reveal many aspects of Titan's atmosphere and surface hitherto hidden.

However, many questions pertaining to the chemical activity in Titan's atmosphere remain. Here are a few important ones, which include laboratory comprehensive work to be carried out synergistically, to shed light on the organic mysteries of this unique hazy world. Questions directly related to the topics addressed in this thesis are also listed.

The gas phase chemistry of the upper atmosphere

- How can laboratory experiments constrain the neutral gas phase chemistry? Chapter 2 and 3 will address this topic. In particular, Chapter 3 presents work that I carried out in our PAMPRE plasma discharge (see also Chapter 2) and investigated the neutral precursor products formed in the plasma. Following previous work by Gautier et al. (2011) where they analyzed the gas phase products by mass spectrometry and gas chromatography, I will present therein a quantification approach using infrared spectroscopy coupled with mass spectrometry on the major neutral products with a newly cryogenic setup developed inside the reactor.
- What is the coupling between ion compounds and neutral species in plasma discharges? What are the main positive ion precursors used for the growth of tholins? As see in the previous sections of this chapter and in Chapter 4, the positive ion chemistry is directly dependent on the neutral species. Until now, there had not been a study focused on the gas phase positive ion precursors produced in our plasma discharge, and how they are coupled with the neutral species. An ion mass spectrometer was fitted to the plasma reactor for this purpose. I will present these first results in Chapter 4, and discuss the distributions observed with changing methane concentrations. Further, I will also compare these spectra with INMS measurements with m/z up to 100.
- Do negative ions participate substantially to the growth of organic aerosols? If so, to what extent? What are the main anion precursors in a cold plasma discharge? As explained in Section 1.6.4, the presence of anions was an important discovery by Cassini, and laboratory simulations have yet to further constrain their nature as tholin precursors. Work focusing on the negative ion chemistry is currently in progress.

- What is the influence of trace species on the precursor chemistry to tholin formation? Experimental work can achieve gas mixtures in the laboratory in a very constrained way to estimate the influence of trace species on the volatile products. For example, Sciamma-O'Brien, Ricketts, and Salama (2014) examined the influence of C_2H_2 and C_6H_6 on the initial steps of the chemistry.

- How can a theoretical approach predict new stable species or help in evaluating better constraints to inferred trace species? The soaring applications of quantum chemical methods to astrochemistry have enabled new potential venues and routes for the gas phase reactivity and molecular strucutres (e.g. Rahm et al., 2016; Fortenberry et al., 2017; Fortenberry, 2017). Such studies can help laboratory experiments and our general understanding of the gas phase chemistry by predicting new species and pathways to model.

- What is the composition of Titan's haze? How can laboratory measurements constrain the composition of the haze? The use of plasma discharges is a valuable tool for efficient tholin production and analyses (Chapter 2). Imanaka et al. (2004) for instance, studied the effect of pressure during tholin production on the nitrogen incorporation into the solid phase. They found that nitrogen incorporation as nitrogen-containing polycyclic aromatic compounds was facilitated at lower pressures. The gas phase reactivity has yet to be further explored by comprehensively studying the neutral-ion interactions, as well as specific pathways. These pathways are necessary in aiding photochemical models by providing rate constants and branching ratios of ion-molecule reactions (Thissen et al., 2006), controlled cation-molecule reactions (Romanzin et al., 2018) or specific anion routes (Žabka et al., 2012; Biennier et al., 2014; Bourgalais et al., 2016; Joalland et al., 2016).

The solid-state chemistry of the lower, colder atmosphere

- How do the aerosols and condensed ices evolve in Titan's lower atmosphere? What effect does the radiation have on them? Most of the gas phase products eventually condensate and form cloud nuclei near the tropopause. Cassini has provided much insight into the chemical reservoir and temporal variability of these clouds in this region of the atmosphere. In terms of the radiation reaching these low altitudes, their photochemical effect on the icy particles is poorly understood. Laboratory cryogenic experiments can help investigate the potential photochemical role that these condensed nuclei experience. In this context, I will present results pertaining to HCN and C_4H_2 solid-state chemistry in Chapter 5. This work is also currently being carried out further.

Chapter 2

Experimental Methodology

"Now, with no directing signals to orientate it, the shallow dish had automatically set itself in the neutral position. It was aimed forward along the axis of the ship –and, therefore, pointing very close to the brilliant beacon of Saturn, still months away. Poole wondered how many more problems would have arisen by the time Discovery reached her still far-distant goal. If he looked carefully, he could just see that Saturn was not a perfect disk; on either side was something that no unaided human eye had ever seen before the slight oblateness caused by the presence of the rings. How wonderful it would be, he told himself, when that incredible system of orbiting dust and ice filled their sky, and Discovery had become an eternal moon of Saturn! But that achievement would be in vain, unless they could reestablish communication with Earth."

Arthur C. Clarke, 2001: A Space Odyssey

Titan is a cold, organic-rich world far away from the Sun, yet subject to active radiation (solar photons, energetic particles from Saturn's magnetosphere, GCRs and X-rays) as seen in the previous chapter. Finding suitable complementary laboratory experiments to simulate specific chemical processes occurring in Titan's atmosphere is both challenging and necessary to tackle the questions related to this world. In this chapter, I present a multi-approach review of experimental simulations used to study Titan's atmospheric reactivity and amongst those, the ones I used during my PhD. I also describe how they are considered good analogs for specific conditions in the atmosphere of Titan.

2.1 Historical context for the simulation of Titan's atmospheric chemistry

As we saw in the previous chapter, complementary techniques are needed to simulate the chemical reactivity of Titan's atmosphere. A wide range of more or less energetic radiation reaches Titan's ionosphere and thermosphere; from galactic cosmic rays (GCRs), EUV and FUV, all the way to infrared wavelengths. Most of these are stopped in the upper and middle layers of the atmosphere, while GCRs, near-UV and certain IR windows may reach the troposphere and surface.

Historically, the appeal to simulate Titan's atmosphere chemistry was driven by the first Voyager observations of Titan, which prompted laboratory investigations to characterize the nature of the hazy material. The Urey-Miller experiments by Miller (1953) simulating early Earth conditions instigated new venues in the quest for reproducing planetary atmosphere here on Earth. Species such as N_2, NH_3, CH_4, CO_2 and H_2O were all part of various mixtures, to either study the Jovian and outer Solar System reducing atmospheres (e.g. Sagan and Miller, 1960; Woeller and Ponnamperuma, 1969; Chadha et al., 1971; Sagan and Khare, 1971a; Molton and Ponnamperuma, 1974; Scattergood, Lesser, and Owen, 1975), or prebiotic syntheses (e.g. Dodonova, 1966; Khare and Sagan, 1971; Sagan and Khare, 1971b; Chang et al., 1979). During the decade following the works by Sanchez, Ferris, and Orgel (1966), Woeller and Ponnamperuma (1969), and Khare and Sagan (1971), UV irradiations and electrical discharges were becoming common ground for studying CH_4/N_2-based mixtures and their hydrocarbon and nitrogen-rich products. The organic colored material observed was finally given the name of *tholins* in 1978 (See Chapter 1), and detailed their nature in Sagan and Khare (1979). They distinguished between "UV tholins" and "spark discharge tholins", but noted their chemical similarities in spite of the two different sources of energy. Two of those experiments are shown in Figure 2.1). Thanks to these techniques and in complement of gas chromatography-mass spectrometry, they found that tholins were not a successive repetition of a monomeric unit, i.e. a polymer, but a more complex material. In the context of Titan, the primitive Earth and the Jovian atmospheres, discharge-induced tholins in the laboratory started getting a lot of interest for their prebiotic implications (Sagan and Khare, 1979).

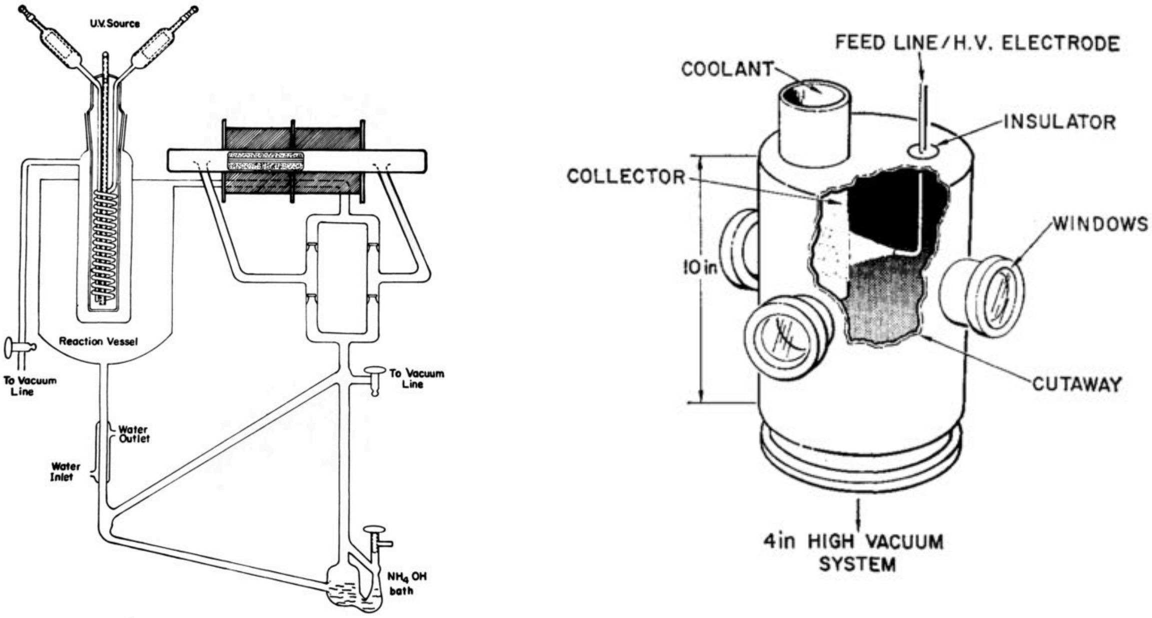

FIGURE 2.1: Examples of seminal experiments simulating the reducing Jovian atmosphere. Left: Apparatus from Sagan and Khare (1971a) for UV photochemistry of the lower Jovian clouds. The experiment uses an Hg discharge lamp irradiating the gas precursors at 2537 Å. Right: Example of an electric discharge from Woeller and Ponnamperuma (1969). It uses both a semicorona and arc discharge, and was also able to trap products with a cold finger.

2.2 Panorama of past and current laboratory investigations

Since Sagan and Khare (1979), a variety of experimental apparatuses have been developed to reproduce different and complementary phenomena and analyze the gas and solid phase of Titan organic chemistry conditions (see review by Coll et al. (1999)). Cable et al. (2012) gave an updated review of complementary methods used to produce Titan tholins in the Cassini era. Among all of these, plasma discharges and UV irradiation are most commonly used. Cold plasma discharges can reproduce exogenic sources affecting the chemistry in the upper layers and initiating the production of aerosols. These sources include Saturn's magnetospheric protons, electrons, cosmic rays and VUV solar photons as a fraction of the electrons in a cold plasma discharge have an energy high enough to dissociate and ionize N_2 and CH_4 (e.g. Szopa et al., 2006). In addition, corona processes using cold plasma discharges at low pressure can simulate potential electrical activity present in the methane clouds (Navarro-González and Ramírez, 1997; Lammer et al., 2001).

Typically, UV photochemistry can be initiated by selectively using wavelengths below the $\lambda < 100$ nm (12.4 eV) threshold for N_2 photodissociation and starting the coupled N_2-CH_4 chemistry. Ionization of N_2 requires more energetic irradiation with $\lambda < 79.5$ nm (15.6 eV). Light sources able to produce those wavelengths are varied (e.g. hydrogen, deuterium or mercury lamps); some of them are listed in Table 2.1. Such experiments have the advantage of selectively initiating photolysis at specific UV wavelengths, which are key, given the significance of solar UV radiation as the main source of ionization between 700-1600 km in Titan's atmosphere

(Krasnopolsky, 2009). UV irradiation techniques can therefore probe some of the primordial photodissociative ionizing steps of the N_2-CH_4 photochemistry. However, other complementary techniques such as plasma discharges operating over a broader energy spectrum continuum can investigate further, more elaborate chemistry. A number of experiments working closely with photochemical studies also investigate specific pathways, low-temperature kinetics and ion-molecule interactions using UV beam lines (e.g. Berteloite et al., 2008; Žabka et al., 2012; Bourgalais et al., 2016; Romanzin et al., 2018). Finally, other experiments aimed at simulating Titan's surface lakes, methane clathrates and hydrocarbon solubility are also shown in Table 2.1 for reference.

TABLE 2.1: List of some historical and current complementary experimental methods with their corresponding references, aimed at simulating (i) the gas phase volatile chemistry in N_2/CH_4 mixtures using complementary energy sources (plasma discharges, UV lamps, synchrotron beam lines...), (ii) specific neutral and ion reaction pathways and low-temperature kinetics, (iii) tholin solid-state photochemistry in the lower atmosphere and cloud nucleation in the lower atmosphere, and (iv) the interaction between tholin material and hydrocarbon liquids, and lacustrine evaporation rates. References are: [1]Sanchez, Ferris, and Orgel (1966),[2]Khare et al. (1981),[3]McDonald et al. (1994),[4]Coll et al. (1995),[5]Szopa et al. (2006),[6]Sagan and Khare (1971a),[7]Carrasco et al. (2013),[8]Gupta, Ochiai, and Ponnamperuma (1981), [9]Scattergood et al. (1989),[10]Thompson et al. (1991),[11]Ramírez et al. (2005),[12]Tigrine et al. (2016),[13]Dodonova (1966),[14],Chang et al. (1979),[15]Imanaka et al. (2004),[16]Imanaka and Smith (2009),[17]Ferris et al. (2005),[18]Hörst and Tolbert (2013),[19]Sciamma-O'Brien, Ricketts, and Salama (2014),[20]Mahjoub et al. (2016),[21]Loveday et al. (2001),[22]Curtis et al. (2008),[23]Gudipati et al. (2013),[24]Nna-Mvondo, Anderson, and Samuelson (2018),[25]Couturier-Tamburelli et al. (2014),[26]Barnett and Chevrier (2016),[27]Luspay-Kuti et al. (2015), [28]Singh et al. (2017),[29]Gupta, Ochiai, and Ponnamperuma (1981),[30]Khare et al. (1984),[31]Pilling et al. (2009),[32]Scattergood, Lesser, and Owen (1975),[33]Vuitton et al. (2006),[34]Berteloite et al. (2008),[35]Žabka et al. (2012),[36]Bourgalais et al. (2016),[37]Alcaraz et al. (2004),[38]Miranda et al. (2015)

	Energy source/altitude	References
Volatiles	Plasma discharges	1, 2, 3, 4, 5, 8, 9, 10, 11, 15, 18, 19
	UV photochemistry	6, 7, 12, 13, 14, 16, 17, 18, 33
	Soft X-rays and γ rays	29, 30, 31
	Proton/electron beam irradiation	29, 32
Kinetics/pathways		34, 35, 36, 37, 38
Tholins	Lower atmosphere	22, 23, 24, 25
Liquid/clathrates	Surface/subsurface	20, 21, 26, 27, 28

In order to investigate the neutral gas phase chemistry and its coupling with positive ion compounds, I used the PAMPRE plasma discharge. With PAMPRE, I was able to study the gas phase reactivity and its precursors to the formation of tholins. The PAMPRE experiment with its ion and neutral mass spectrometer, as well as a cold trap and infrared spectrometer, make it a useful tool to simulate the gas phase reactivity of Titan's upper atmosphere. Simulating the colder lower atmosphere of

Titan requires a cryogenic chamber where gas deposition is possible, coupled with an irradiation system to irradiate the ice samples. In this context, the Acquabella experiment (JPL) enabled me to investigate the ageing of the aerosols in Titan's lower atmosphere. Results pertaining to the PAMPRE studies are presented in Chapters 3 and 4, Acquabella's are in Chapter 5. For more detailed descriptions of their respective applications, the reader is referred to the Experimental sections in said chapters. In the following sections, I will describe the PAMPRE and Acquabella experiments.

2.3 The PAMPRE Plasma Experiment, LATMOS, France

2.3.1 The versatility of PAMPRE

The PAMPRE reactor was developed in the early 2000's. It demonstrated its capability of efficiently producing Titan tholins first in Szopa et al. (2006). It was the first study of Titan aerosol analogs using PAMPRE. Figure 2.2 shows the suite of instruments fitted to the reactor, adapted from Szopa et al. (2006).

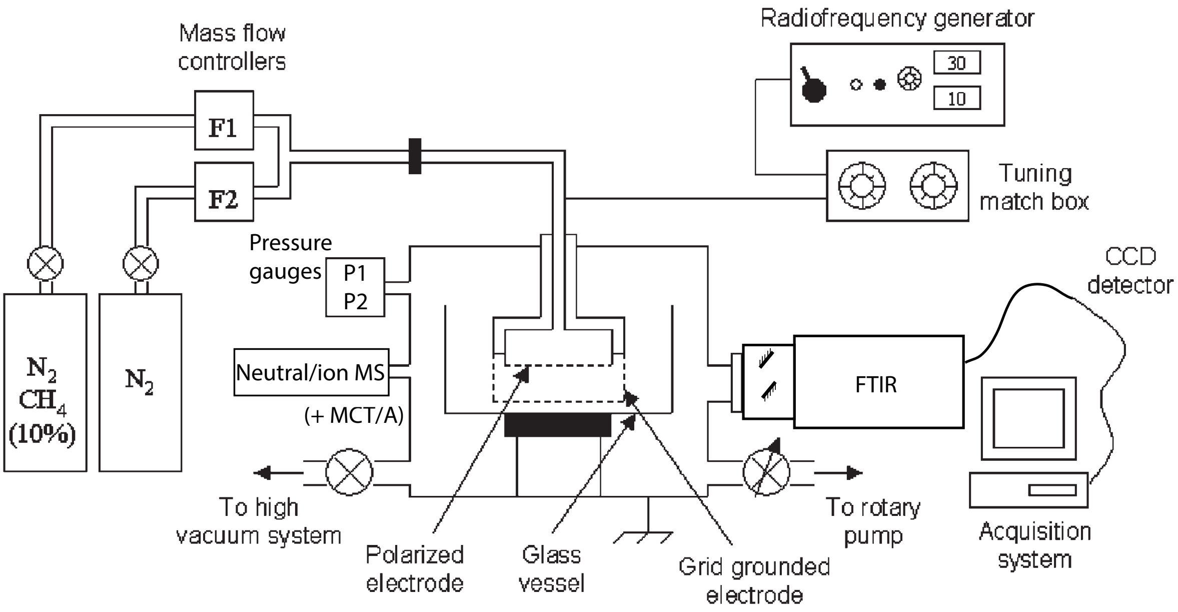

FIGURE 2.2: Schematic diagram of the PAMPRE experiment, adapted from Szopa et al. (2006).

Over the years, the gas phase analysis abilities have multiplied, coupled with *ex situ* analyses of the tholin product. They include optical emission spectroscopy (OES) analyzing UV-vis emission from the plasma (Szopa et al., 2006; Alcouffe et al., 2010; Carrasco et al., 2012), mass spectrometry to study the *in situ* neutral, positive and/or negative ion composition (Sciamma-OBrien et al., 2010; Gautier et al., 2011; Carrasco et al., 2012; Gautier et al., 2013; Fleury et al., 2014; Fleury et al., 2015; Dubois et al., 2019; Dubois et al., *work in progress*), Fourier-transform IR spectroscopy with Attenuated Total Reflectance (ATR) to study solid tholin samples and an MCT/A for gas phase absorption (Gautier et al., 2012; Gautier et al., 2013; Fleury et al., 2014; Fleury et al., 2015; Dubois et al., 2019), and a cryogenic system (Figure 2.3) cooled with liquid nitrogen to directly trap the gas phase products to analyze and quantify them (Gautier et al., 2011; Fleury et al., 2015; Dubois et al., 2019). *Ex situ* analyses of the tholin material produced by PAMPRE have ranged from optical constants measurements to microscopic observations and synchrotron irradiations (Szopa et al., 2006; Carrasco et al., 2009; Hadamcik et al., 2009; Pernot et al., 2010; Sciamma-OBrien et al., 2010; Gautier et al., 2012; Mahjoub et al., 2012; Sciamma-O'Brien et al., 2012; Hadamcik et al., 2013; Gautier et al., 2014; Mahjoub et al., 2014; Carrasco et al., 2016; Mahjoub et al., 2016; Gavilan et al., 2017; Carrasco et al., 2018; Lethuillier et al., 2018).

Figure 2.3 shows the cryogenic system that I used to study the neutral precursors (Chapter 3). Liquid nitrogen is regulated by a solenoid valve which controls the electrode temperature with a ± 1žC precision. The PAMPRE polarized electrode temperature can thus be regulated from -180žC to +20žC, and trap the volatiles in the discharge.

FIGURE 2.3: A close-up view of the polarized electrode montage, with the cryocooling system which consists of a soft copper pipe circulated by liquid N_2. A solenoid valve regulates the liquid N_2 rate in order to reach the set temperature value at a ± 1žC precision. Its external and internal diameters are 6 mm and 2.5 mm, respectively. This cold trapping tube comes in contact with the electrode to trap the gas phase products. Note the gate VAT valve at the back, placed between the reactor and the mass spectrometer (MS) chamber to isolate the MS when the reactor is at atmospheric pressure.

2.3.2 The plasma discharge

The capacitively coupled plasma (CCP) discharge is supplied by a radiofrequency SAIREM GRP01KE generator (13.56 MHz), through a tuning match box. This match box works as an impedance adapter, regulating the incident and reflected RF power. With it, we can measure the incident delivered power and the fraction of it absorbed by the plasma. It essentially controls the power to match with the exiting 50Ω impedance of the RF generator. Inelastic collisions between the electrons and the neutral gas initiates the chemistry, and depend on the pressure. In addition, the discharge typically functions with pressures from $\sim$0.1 to $\sim$3 mbar. The plasma expands between a showerhead-shaped powered electrode and a grounded electrode, and can also be confined with a cylindrical metallic box with grid openings (Figure 2.2). This box can be used for electron density measurements, using the microwave resonant cavity effect. Gas injection is done vertically and downward. Mass flow controllers regulate the laminar gas flow at a rate of 55 sccm in standard conditions leading to a pressure of 0.9 mbar. As the neutral gas is injected, the negatively charged aerosols are in levitation due to electrostatic forces within the plasma and experience a neutral drag force, ejecting them out of the plasma (Figure 2.4).

The discharge itself can either be configured in continuous or pulsed mode (Figure 2.5). Working in pulsed mode may be of interest in at least two cases, (i) given a certain modulated frequency below the time threshold it takes to initiate tholin formation, studying the gas phase in pulsed mode can facilitate the detection of the first light products, preventing further formation of more complex compounds, (ii) also enable the detection in certain cases of short-lived ions decaying in the afterglow (e.g. Howling et al., 1994). I have only worked in continuous mode, although pulsing the plasma was also used in complement of detecting negative ions (results not presented in this thesis). In pulsed plasma mode, the Electrostatic Quadrupole Plasma (EQP) acquisition must be adjusted to the pulsed discharge. This can be done with a Transistor-transistor logic (TTL) signal, linked to a pulsed generator. To adapt the EQP's measurement frequency to the generator's, a gate delay value is adjusted to the extractor. This delay has to match the output signal sent by the generator so that the acquisition is synchronized with the boxcar plasma on/off signal (Figure 2.5).

FIGURE 2.4: Top left: Glowing N_2-CH_4 plasma in the PAMPRE reactor. Bottom left: The tholin product collected in a glass vessel. Right: Holding the collected tholins, available for *ex situ* analyses, storage and preservation. The color and morphologies of tholins produced by PAMPRE have been detailed in Hadamcik et al. (2009).

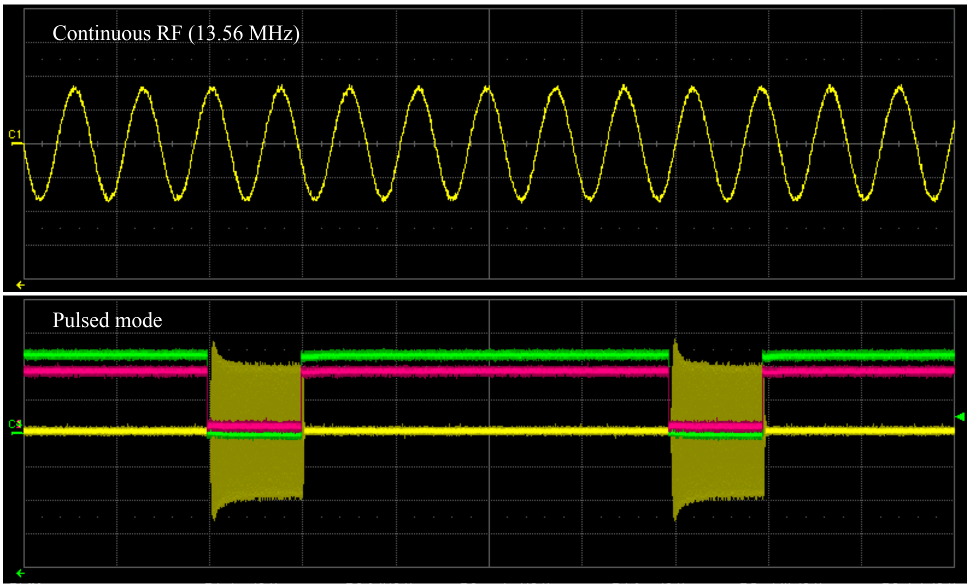

FIGURE 2.5: Top: 13.56 MHz RF modulation of the plasma discharge in continuous mode. Bottom: Power-modulated frequency corresponding to a 800/200 μs cycle; the plasma is turned on for 200 μs every 800 μs in this example. The green and red curves follow a boxcar function where the edge-triggered falling corresponds to an impulse to turn the plasma on. Both plots are not to scale.

For *in situ* gas phase mass analysis, I used the Hiden Analytical Standard System (Electrostatic Quadrupole Plasma) EQP. This EQP analyzes neutrals (in Residual Gas Analysis mode), positive and negative ions, and radicals. The measurement of the neutrals and radicals uses an electron-impact ion source and is driven by a twin filament. Ions (positive and negative) extracted directly from the plasma (Figure 2.6), are directly focused into an electrostatic field energy filter after their transit in the extraction tube. Subsequently, the ions are directed to a triple-section quadrupole mass filter for a mass-to-charge (m/z) ratio sampling. About 20 fully-tunable electrodes are located throughout the EQP. The first, and likely most important one, is located at the extractor, just behind the bore orifice in contact with the plasma. The potential applied to this lens will determine the efficiency at which the ions will be extracted. The tuning of each electrode is a crucial step before analyzing ions and neutrals, thus providing the best signal-over-noise ratio. The following remaining electrode potentials are also of importance in that they will help guide the ions to the energy filter. For a more detailed description of this apparatus in ion mode, applied to N_2-CH_4 mixtures, the reader is referred to Chapter 4.

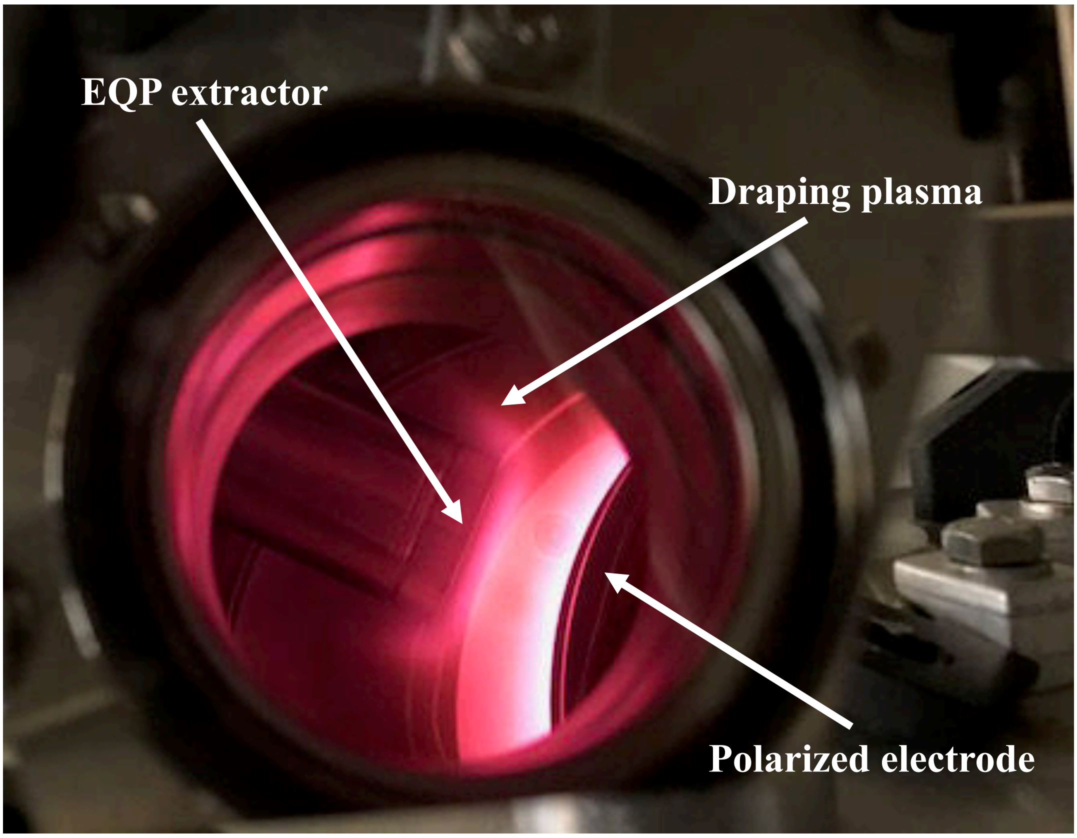

FIGURE 2.6: Close-up view through one of PAMPRE's porthole windows, showing the Electrostatic Quadrupole Plasma (EQP) extractor head in contact with the plasma volume, forming a drape around the head. The extraction orifice comes in three different diameters: 100, 200 and 300 μm.

2.4 The Acquabella Chamber, JPL, USA

The experimental interest in simulating Titan's lower atmosphere (Table 2.1), was mainly catalyzed by the Cassini-Huygens Mission. The chemical variability that Cassini-Huygens unveiled at Titan was not restricted only to the upper atmosphere – it was in all atmospheric layers.

In complement of the gas phase analyses carried out with PAMPRE, I used the Acquabella (*beautiful water* cryogenic chamber at NASA's Jet Propulsion Laboratory, in Pasadena, CA. This experiment is aimed at simulating the lower, cold atmosphere of Titan, where most of the gas phase species condense and may interact with the longer UV wavelengths and less energetic photons that penetrate into these low altitudes (see Chapter 1 and Chapter 5 for more details). To obtain analogous conditions to those found on Titan, it is necessary to carry out such experiments at low temperatures and relatively low pressures (Figure 2.7).

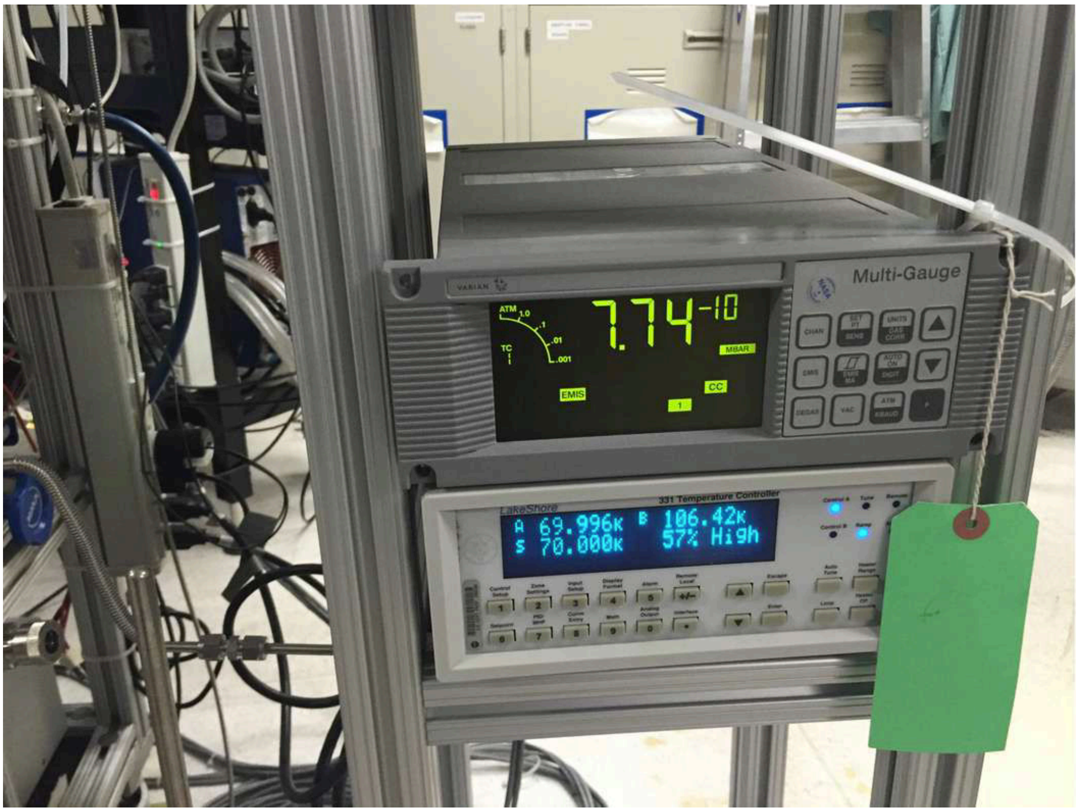

FIGURE 2.7: Penning pressure gauge displaying 7.74 $\times$ 10^{-10} mbar, while the chamber is being pumped by a turbomolecular Pfeiffer pump. The cryostat, regulated thanks to a Helium closed-cycle system, here set at 70K, can go down to 10K. Working at these low pressures and temperatures is important to simulate Titan-relevant conditions (Chapter 1 and 5).

The samples inside the chamber are cooled to low temperatures thanks to a closed-cycle helium Advanced Research System cryostat. A sample-holder holds the substrate (e.g. sapphire) onto which volatile deposition through a spray nozzle is made possible, either directly on the substrate, or on tholin films made with PAMPRE. Irradiation of those ices is provided by either a tunable Opotek laser or a continuum Nd-Yag laser for higher energies. During irradiation, the chamber is evacuated thanks to a turbomolecular pump, to limit contamination of atmospheric species. Finally, samples are directly measured with FTIR and UV-vis spectroscopy post-irradiation.

For a more detailed description of the experimental setup, the reader is invited to peruse Chapter 5.

Part I

The Volatile Upper Atmosphere

Chapter 3

In Situ Investigation of Neutrals Involved in the Formation of Titan Tholins

The content of this chapter was accepted for publication in Icarus on July 6, 2018

Abstract

The Cassini Mission has greatly improved our understanding of the dynamics and chemical processes occurring in Titans atmosphere. It has also provided us with more insight into the formation of the aerosols in the upper atmospheric layers. However, the chemical composition and mechanisms leading to their formation were out of reach for the instruments onboard Cassini. In this context, it is deemed necessary to apply and exploit laboratory simulations to better understand the chemical reactivity occurring in the gas phase of Titan-like conditions. In the present work, we report gas phase results obtained from a plasma discharge simulating the chemical processes in Titans ionosphere. We use the PAMPRE cold dusty plasma experiment with an N_2-CH_4 gaseous mixture under controlled pressure and gas influx. An internal cryogenic trap has been developed to accumulate the gas products during their production and facilitate their detection. The cryogenic trap condenses the gas-phase precursors while they are forming, so that aerosols are no longer observed during the 2h plasma discharge. We focus mainly on neutral products NH_3, HCN, C_2H_2 and C_2H_4. The latter are identified and quantified by in situ mass spectrometry and infrared spectroscopy. We present here results from this experiment with mixing ratios of 90-10% and 99-1% N_2-CH_4, covering the range of methane concentrations encountered in Titans ionosphere. We also detect in situ heavy molecules (C_7). In particular, we show the role of ethylene and other volatiles as key solid-phase precursors.

Keywords: Ionosphere, Neutral chemistry, Volatiles, Plasma discharge

3.1 Introduction

Titan is Saturn's largest moon and second largest in the Solar System after Ganymede. It has a mean radius of 2,575 km. One major interest in Titan is its uniquely dense (a 1.5-bar ground pressure) and extensive (≈1,500 km) atmosphere, primarily made of N_2 and CH_4. In fact, the extent of the atmosphere alone accounts for about 58% in size of Titans radius. Titan's first flyby by Pioneer 11 (1979) revealed the moon as being a faint brownish dot orbiting Saturn. The subsequent Voyager 1 (1980), Voyager 2 (1981), Cassini (2004 - 2017) and Huygens (2005) spacecraft have uncovered physicochemical processes unique in the solar system occurring both in the atmosphere and surface. Early seminal studies (Khare and Sagan, 1973; Sagan, 1973; Hanel et al., 1981) showed that Titans reducing atmosphere is also composed of complex and heavy organic molecules and aerosols, their laboratory analogous counterparts named tholins. This chemistry is initiated at high altitudes and participates in the formation of solid organic particles (Khare et al., 1981; Waite et al., 2007; Hörst, 2017 for a more recent and holistic review of Titan's atmospheric chemistry). At altitudes higher than 800 km, the atmosphere is under the influence of energy deposition such as solar ultraviolet (VUV) radiation, solar X-rays, Saturns magnetospheric energetic electrons and solar wind (Krasnopolsky, 2009; Sittler et al., 2009). Cosmic dust input is also thought to chemically interact with volatiles in the middle atmosphere (English et al., 1996; Frankland et al., 2016). To wit, Titan is presumably one of the most chemically complex bodies in the solar system. Some of the techniques used to better understand the processes occurring in Titans atmosphere are detailed hereafter.

Earth-based observations of Titan have been used to determine the atmospheric composition and structure, as well as surface and subsurface features. For example, direct monitoring of seasonal tropospheric clouds from Earth-based observations helped us infer their transient locations (Brown, Bouchez, and Griffith, 2002). Ground-based submillimeter observations were used to infer the stratospheric composition with for example, the determination of hydrogen cyanide (HCN) and acetonitrile (CH_3CN) mixing ratios (Tanguy et al., 1990; Bezard and Paubert, 1993; Hidayat et al., 1997), and with the rise of ground-based observation techniques such as the Atacama Large Millimeter Array (ALMA) (Cordiner et al., 2014a; Cordiner et al., 2014b; Molter et al., 2016; Serigano et al., 2016; Palmer et al., 2017). The use of other space-based telescopes such as the Infrared Space Observatory (ISO) and the Herschel Space Observatory has additionally provided information on the stratospheric composition and neutral abundances (Coustenis, 2003; Courtin et al., 2011; Rengel et al., 2014). Early on, atmospheric studies obtained by the Voyager 1 mission were able to identify several organic molecules (Hanel et al., 1981; Kunde et al., 1981; Maguire et al., 1981). Later, the Cassini-Huygens (NASA/ESA) mission provided us with a more precise atmospheric characterization of the composition (Teanby et al., 2012; Vinatier et al., 2015; Coustenis et al., 2016), wind (Flasar et al., 2005; Achterberg et al., 2011) and upper atmosphere thermal profiles (Snowden et al., 2013), while the Huygens lander (ESA) was able to provide insight on the in situ composition (Israel et al., 2005) and optical properties of the aerosols (Doose et al., 2016). Cassinis Composite Infrared Spectrometer (CIRS) limb spectral imaging (Vinatier et al., 2007) examined the role of volatiles in Titans chemistry and atmospheric dynamics. Many hydrocarbons and nitriles were shown to have wide latitudinal variations of vertical mixing ratios (sometimes contradicting Global Circulation Models, e.g. De Kok et al., 2014), emphasizing the importance of understanding the complex coupling between gas phase chemistry and global dynamics. Both polar enrichments of nitriles (Teanby et al., 2009) as well as the presence of heavy ions (Crary et al., 2009; Wellbrock et al., 2013) have also been suggested to participate in Titan's aerosol production. Thus, ground- and space-based observations have and will be especially important in the post-Cassini era (Nixon et al., 2016).

Photochemical models have been complementarily used to predict the thermal, compositional and structural evolution of Titans atmospheric column (e.g. Atreya, Donahue, and Kuhn, 1978; Carrasco et al., 2007; Carrasco et al., 2008). Furthermore, these models offer us testable hypotheses for experiments and predictions for chemical pathways leading to the formation of aerosols (Waite et al., 2007; Yelle et al., 2010).

Lastly, experimental techniques have also been used to simulate Titans atmospheric conditions (Khare et al., 1984; Sagan and Reid Thompson, 1984; Pintassilgo et al., 1999; Cable et al., 2012; Carrasco et al., 2013; Sciamma-O'Brien et al., 2015; Tigrine et al., 2016; Hörst et al., 2018) and determine chemical mechanisms that are otherwise out of Cassinis reach. A wide range of laboratory simulations have been used to complementarily investigate Titans atmospheric chemistry and different energy inputs (see Cable et al., 2012 for a thorough review of these experiments). Typically in our lab, plasma discharges (Szopa et al., 2006; Sciamma-OBrien et al., 2010; Carrasco et al., 2012) or UV irradiation (Peng et al., 2013) have been used to achieve Titan-like ionospheric conditions. In this context, it is deemed necessary to apply and exploit such a technique to better understand the chemical reactivity occurring in Titan-like upper atmospheric conditions. Hence, the gas phase which we know to be key to the formation of aerosols on Titan (Waite et al., 2007), is emphasized. Indeed, chemical precursors that are present in the gas phase (Carrasco et al., 2012) follow certain chemical pathways that still need to be investigated. For instance, Sciamma-OBrien et al. (2010) showed how the production of atomic hydrogen coming from CH4 was anti-correlated with aerosol formation, by changing the initial methane amount in the discharge. They argued that the presence of molecular and atomic hydrogen in overabundance in the gas mixture may have an inhibiting effect on the production of atomic nitrogen, thus on the incorporation of N-bearing species into the tholins. To reproduce these ionosphere conditions, we used the PAMPRE cold dusty plasma experiment (Szopa et al., 2006) with an N_2-CH_4 gas mixture under controlled gas influx and pressure. Cold plasma discharges have been shown to faithfully simulate the electron energy range of magnetospheric electrons and protons, and UV irradiation deposited at Titans atmosphere within a range of $\approx$ 10 eV 5 keV (Sittler, Ogilvie, and Scudder, 1983; Chang, Lawless, and Yamamoto, 1991; Maurice et al., 1996; Brown, Lebreton, and Waite, 2009; Johnson, Tucker, and Volkov, 2016).

A first study (Gautier et al., 2011) dealt with the identification of gas products in the PAMPRE reactor and used an external cold trap to study the gas phase. Analyses were made by gas-chromatography coupled with mass spectrometry. More than 30 reaction products were detected and a semi-quantitative study was performed on nitriles, the most abundant molecules collected. However, one of the limitations to this technique is how the products are transported ex situ, and may allow for loss or bias in their chemical reactivity and measurements. In situ detections were then made by mass spectrometry with no cryogenic trapping (Carrasco et al., 2012). Unfortunately, the only use of mass spectrometry prevented any univocal identification of large organic molecules likely involved as precursors for aerosol formation.

Since then, setup improvements such as an internal cryogenic trap and infrared spectroscopy have been made in order to study the gas phase in situ using these different complementary techniques. The purpose of the cryotrap is to act as a cold finger enabling the volatiles to condensate and preventing them from being evacuated from the chamber. This has allowed us to avoid any volatile loss and to take on a quantitative approach on volatile products. Thus, to better characterize the initial volatile products precursors to aerosols, we used a coupled analysis of mass and infrared spectrometry. The presence of an internal cold trap made the condensation of these volatiles possible, allowing for in situ measurements.

We will first describe our experimental chamber, which was designed to be relevant to simulate Titans ionosphere conditions. Mass spectrometry results of volatiles at two methane concentrations will be then presented, as well as their infrared spectroscopic analyses with a quantitative approach carried out on four major neutral volatiles (NH_3, C_2H_2, C_2H_4, and HCN) acting as precursors to the formation of aerosols. Finally, we will discuss the discrepancies between both methane conditions, ethylene and ammonia chemistry and hydrogen cyanide chemistry.

3.2 Experimental

3.2.1 The PAMPRE experiment and *in situ* cryogenic analysis

The PAMPRE cold plasma reactor used in this study aims, by design, at reproducing exogenic energy sources, for example Saturns magnetosphere particles, UV radiation, cosmic rays and coronal processes impacting Titans atmosphere (Szopa et al., 2006; Alcouffe et al., 2010). The reactor delivers a capacitively coupled plasma discharge, produced by a 13.56 MHz radiofrequency generator via a tuning match box (Chapter 2). The gas influx is held constant and monitored with mass flow controllers. The latter can tune an N_2-CH_4 mixing ratio from 0% to 10% of CH_4 from highly pure N_2 (>99.999%) and 90-10% N_2-CH_4 (>99.999%) bottles. An in situ mass spectrometer (MS) and Fourier-Transform Infrared (FT-IR) spectrometer are also integrated in the system. To simulate Titans atmospheric conditions, 90-10% and 99-1% N_2-CH_4 ratios were considered. Both correspond to a 55 sccm flow in standard conditions. Pressure gauges are set at 0.9 mbar of constant pressure in the reactor while the plasma power is constant at 30W.

In order to detect, analyze and preserve all of the products during our experiments, we need a trapping mechanism to capture these compounds, and thus prevent them from being evacuated. Gautier et al., 2011 used an external cryogenic trap system, shaped as a cylindrical coil, immersed in liquid nitrogen. Then, they isolated the coiled trap and analyzed the gas phase ex situ. Here, the setup is different, and we believe more efficient as the trapping and subsequent analyses are performed in situ and avoid any transfer line bias. Moreover, this cryo-trap mainly traps the gas-phase chemistry in the preceding stages to the formation of solid organic aerosols, preventing their production. In the absence of such a cryo-trap, the plasma is dusty and several mg/h of solid particles are produced. As a result, this enables us to effectively study in detail these gas-phase precursors of tholins, trapped and accumulated during a 2h plasma discharge. Figure 3.1 shows the 3D schematics of our cryogenic trap. An external liquid nitrogen tank extends as a copper circuit into the chamber for cooling. This cooling circuit goes through the upper lid of the chamber, and spirals down onto and lays flat on the polarized electrode. This cooling system is semi-closed, in that the remaining liquid nitrogen is stored in another container outside the reactor. The electrode temperature is controlled with a temperature regulator (Cryo-Diffusion Pt100 probe) which controls the liquid nitrogen circulation in the cooling circuit with a solenoid valve. The initial temperature is adjusted to -180 ±2°C prior to the experiment.

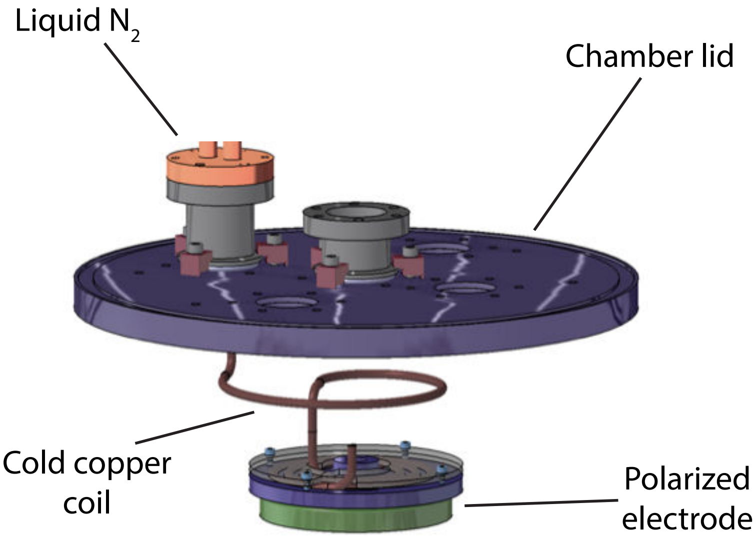

FIGURE 3.1: 3D schematics of the cryogenic trap. The cold trap goes through the top lid of the reactor and coils down into the chamber, which is then in contact with the polarized electrode. The electrode is thus cooled to low-controlled temperatures and the liquid nitrogen goes out through an exit system. This cryogenic trap enables the in situ condensation of the produced volatiles within the plasma.

Using the cryogenic trap set at T = -180 ±2°C, the protocol used was the following: The plasma discharge and cooling system are turned on and the electrodes are kept for 2h at T = -180°C. The duration of the plasma discharge was chosen to trap and accumulate the gas phase products, and improve their detection. The discharge reaches a steady state after a few minutes, as shown in Alcouffe et al., 2010. A similar 2h trapping was previously performed in Gautier et al., 2011 with an external cold trap, which was then analyzed by GC-MS. For consistency, we have chosen the same discharge duration. During this time, the products formed in the N_2-CH_4 plasma are accumulated and adsorbed onto the chamber walls still at low-controlled temperatures thanks to the cryogenic system. After 2h, the plasma is switched off, the chamber is pumped down from 0.9 mbar to 10^{-4} mbar, and the cold trap is stopped. The volatile products are gradually released under vacuum. We then proceed to do in situ gas phase measurements as the chamber goes back to room temperature (Figure 3.1). During this temperature increase, it is possible that some additional neutral-neutral chemistry could occur. Our analytical capacity enables us to address the most abundant and therefore stable molecules, which are not expected to vary strongly apart from the sublimation process.

3.2.2 Mass Spectrometry

QMS quadrupole mass spectrometers were used (Pfeiffer and Hiden Analytics) for in situ measurements inside the chamber. Once the neutral gas is ionized within the MS chamber (SEM voltage of 1000V), each mass is collected by the detector. The MS samples near the reactive plasma with a 0.8 mm-diameter capillary tube, long enough to keep a high-pressure gradient between the MS and plasma chambers. Thus, an effective 10^{-5}–10^{-6} mbar resident pressure in the MS chamber is maintained throughout the experiment. This vacuum background was thoroughly checked before each simulation. The experiments were done using a 1u resolution, covering a 1-100 mass range, at a speed of 2s/mass with a channeltron-type detection. Finally, a baseline noise filter was applied to each spectrum.

3.2.3 Infrared Spectroscopy

A ThermoFisher Nicolet 6700 Fourier Transform Infrared (FT-IR) spectrometer was used for in situ analysis of the gas phase in transmission mode. The spectrometer uses a Mercury Cadmium Telluride (MCT/A) high sensitivity detector with a KBr beamsplitter. During each measurement, 500 scans were taken at a resolution of 1 cm^{-1} for 650–4000 cm^{-1} corresponding to a short-wavelength mid-IR (15.4 – 2.5 μm) range. The optical path length is 30 cm.

3.3 Results

We will now present results from two sets of experiments done at two initial methane concentrations, 1% and 10% (three and two replicates, respectively), representative of the methane concentration range found in Titans ionosphere (Waite et al., 2005). The effect of the cold trap on the plasma can be appreciated by comparing the mass spectra in the same conditions with and without the cold trap (Figure 3.2).

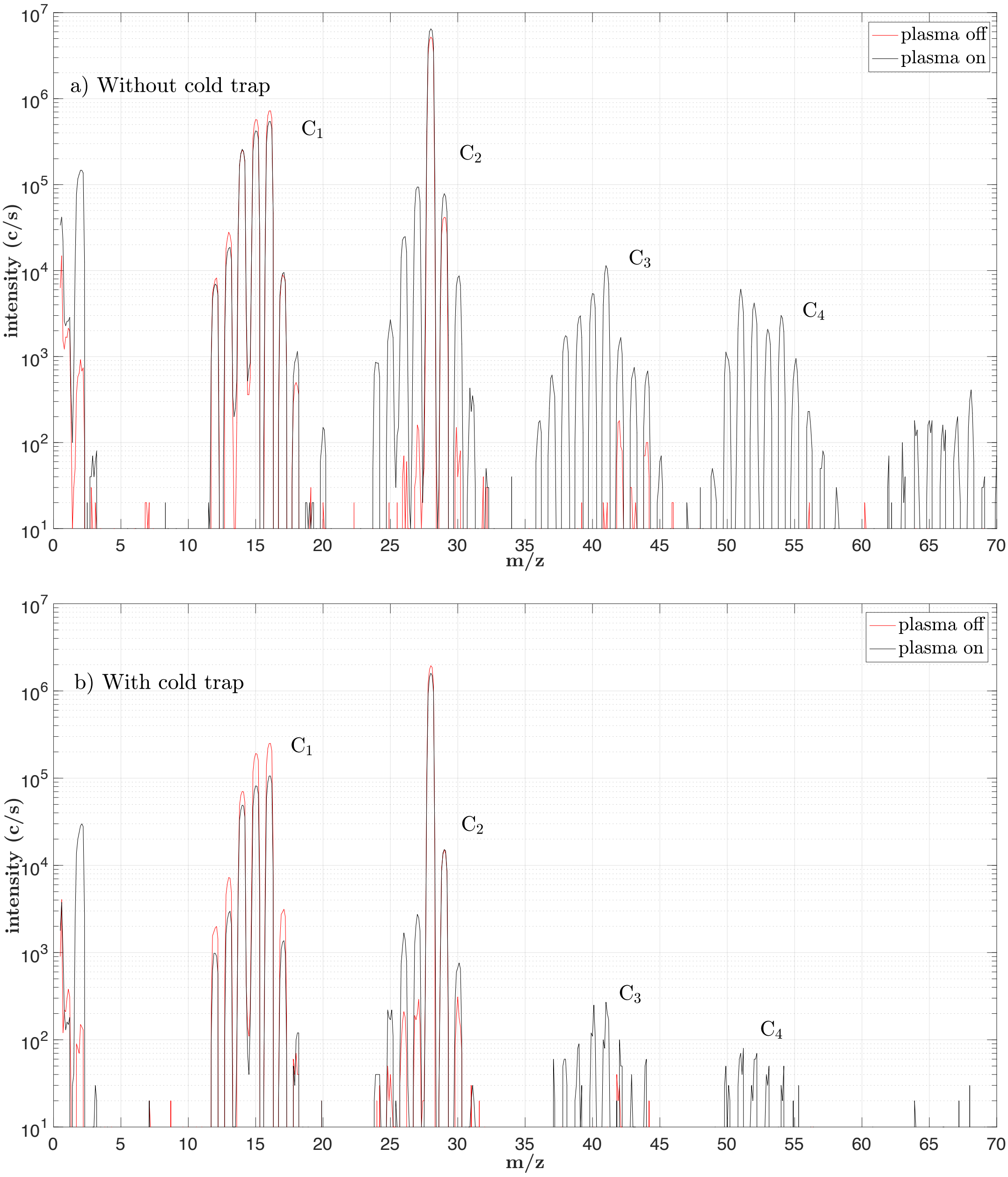

FIGURE 3.2: (a) Upper panel: No cryogenic trap. Mass spectra of a 90-10% N_2-CH_4 mixture with plasma off (red) and plasma on (black). The consumption of methane at m/z 16 and its fragments m/z 15, 13, 12 is visible after the plasma is switched on. (b) Lower panel: With cold trap. Mass spectra of a 90-10% N_2-CH_4 mixture with plasma off (red) and plasma on (black). The main products seen in the top plot (C_2, C_3 and C_4) decrease by about two orders of magnitude in intensity in the bottom figure. This shows the efficient role of the cryotrap, which is to trap (albeit not completely here) the gas products formed in the plasma.

Figure 3.2 shows two sets of N_2-CH_4 mass spectra, one (in red) taken before the plasma is switched on, the other (in black) taken 5 min after plasma ignition, thus making sure methane dissociation and the plasma have reached their equilibrium state (Sciamma-OBrien et al., 2010; Alves et al., 2012). The m/z 29 and 30 peaks are the isotopic signatures of N_2. Under usual conditions, without cold-trap, several mg/h of solid particles are produced in the plasma volume in steady state conditions after the very first minutes of the discharge (Sciamma-OBrien et al., 2010). Now, with the cold-trap, solid particles are no longer produced even after a 2h plasma duration: the aerosol formation is prevented. So, we must investigate how far the gas-phase chemistry goes in the presence of the cold trap. The plasma is out of thermodynamical equilibrium and hosts fast ion-neutral reactions. If the entrapment is faster than the chemistry, then the absence of aerosols might be explained by the fact that any product larger than CH_4 would be removed from the reaction space. But, if the chemical kinetics of the gas phase chemistry is competitive with the entrapment, then complex molecules are produced before their entrapment on the cold reactor walls. In this case, the absence of aerosols is caused by the low amount of gas-phase precursors in the discharge, thus preventing the gas-to-solid conversion. The analysis of the mass spectra obtained in situ during the plasma discharge with and without cold-trap (Figure 3.2) informs us on this effect regarding the cold-trap on the gas-phase chemistry.

The methane consumption can be estimated with m/z 15 and m/z 16 on Figure 3.2 corresponding to the CH_3^+ and CH_4^+ fragments. Following the method described in Sciamma-OBrien et al. (2010), we quantify the methane consumption with the CH_3^+ (m/z 15) fragment at a pressure of 0.9 mbar. With the current cold trap setup, we found this consumption to be of 52% and 60% at 10% and 1% $[CH_4]_0$, respectively. Without the current cryotrap system, Sciamma-OBrien et al. (2010) found methane consumption efficiencies of 45% and 82% at 10% and 1% $[CH_4]_0$. The behavior of methane consumption obtained with and without cold trap are comparable, even if an effect of the different electrode temperature cannot be discarded.

In the following sections, we define C_n families as molecular classes using a $C_xH_yN_z$ nomenclature for N-bearing and hydrocarbon species, where x + z = n. As such, C_n blocks detected using mass spectrometry can be traced, where n is related to the presence of heavy aliphatic and N-bearing compounds. In the C_1 block, in addition to the methane ion peaks, we can notice the signature of the residual water of the mass spectrometer at m/z 17, 18. Other compounds due to the residual air in the mass spectrometer can be seen at m/z 32 (O_2) and m/z 44 (CO_2). The role of the cryotrap has a substantive effect on trapping organic volatile products. Heavy compounds such as the C4 block (Figure 3.2 a) vanish with the cold trap (Figure 3.2 b), despite similar methane consumptions. This shows the role of the cryo-trap, which is to efficiently condense and accumulate in situ the organic products on the cold walls of the reactor instead of being evacuated out as volatiles during the discharge. Methane is consumed in similar quantities in the plasma discharge with and without the cryotrap. Some large and complex molecules are still detected during the discharge by mass spectrometry (Figure 3.2 b), up to the upper mass limits of our instrument (m/z 100) with the cold trap, showing that the gas phase chemistry ensuring their formation is still occurring. Their concentration in the gas phase is drastically reduced, by two orders of magnitude (Figure 3.2 b), suggesting that they are efficiently trapped on the plasma walls while they are forming. The cold trap does not prevent the formation of complex gas-phase molecules, but mainly blocks the gas-to-solid conversion step. The cryogenic trap stops the gas-phase chemistry in the stage preceding the formation of solid organic aerosols. It condenses the gas-phase precursors while they are forming, and no aerosols are observed during the 2h plasma discharge.

3.3.1 Release of volatiles back to room temperature

We leave the cold trap continuously on during a 2h plasma discharge. After 2h, the plasma and cryo-trap are stopped, the chamber is pumped down to 10^{-4} mbar, isolated, and left to go back to room temperature. Hence, all the species condensed on the cold walls are progressively desorbed according to their vaporization temperatures and analyzed in situ. We define MS1, MS2 and MS3 (Figures 3.3 and 4) as three mass spectra for 10% $[CH_4]_0$ taken at three different pressures ($\sim$ 0.38, 0.74 and 1.84 mbar) and temperatures (-130žC, -79žC and +22žC) during volatile release, respectively. The temperature heat-up rate initially increases relatively fast ($\sim$ 7 žC/min between t = 0 min and the acquisition of the MS1 spectrum), then decreases to $\sim$ 0.3 žC/min near MS2 and finally reaches a temperature decrease rate of $\sim$ 0.1 žC/min above -50žC (MS3). This desorption is recorded with a pressure gauge within the isolated chamber as the temperature increases. Figure 3.3 (top) shows the pressure of the gas products being released and the temperature of the electrode (bottom) according to time, both at $[CH_4]_0$ = 10% and $[CH_4]_0$ = 1%, in blue and red, respectively. Both pressures increase, owing to the volatiles sublimating though in different behaviors. Most of the volatiles have been released at 6h of release (Figure 3.3, top) and the curve starts to reach an asymptotic limit in the case of 10% methane, (i) the release starts immediately with the temperature increase until 0.74 mbar at -79žC where it reaches a small plateau, followed by (ii) a second volatile release starting at -75žC with a sharp decrease in heating rate at 300 min until it (iii) reaches a second plateau at 1.84 mbar. On the other hand, products formed in $[CH_4]_0$ = 1% conditions have a different release pattern. Notwithstanding the discrepancy in final pressure obtained (0.35 mbar, 5x less), the products take a much longer time to be desorbed, the release starting at about 90 min with a much smoother slope. Unlike at 10% methane, there is no plateau; the release of the volatiles is continuous and in a rather limited pressure range. These qualitative differences suggest, as a first approximation, different products in the two methane conditions. In particular, all the products released at temperatures below -100žC at 10% methane are absent in the case of 1% methane. This means that these specific compounds are not produced in significant amounts in the plasma discharge at 1% CH_4.

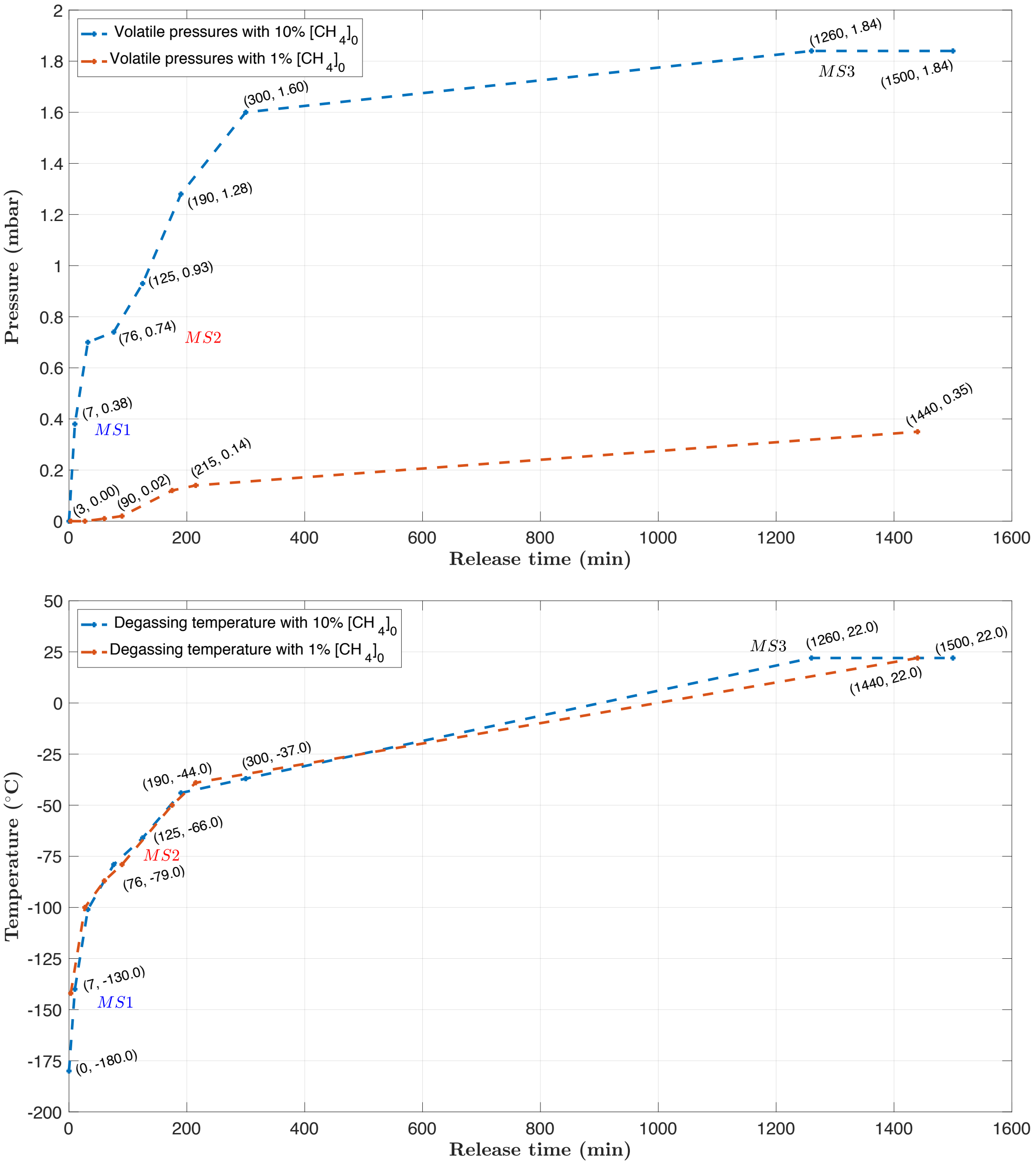

FIGURE 3.3: (Top) Pressure evolution of the gas products according to degassing time in a 90-10% (blue) and 99-1% N_2-CH_4 (red) gas mixture. Labeled at each data point are the times and vessel pressures, respectively. The MS1 (-130žC, 0.38 mbar), MS2 (-79žC, 0.74 mbar), MS3 (+22žC, 1.84 mbar) color-coded labels correspond to the three spectra of Fig. 4 taken at their corresponding temperatures and pressures, underlying significant detections at 10% methane. (Bottom) Temperature evolution during degassing of the volatiles with the same color code for both mixing ratios.

Products released at temperatures below -100°C in the case of $[CH_4]_0 = 10\%$

We are first interested in the molecules released below -100žC in the case of $[CH_4]_0$ = 10%, which are not produced (or at least not in detectable quantities) in $[CH_4]_0$ = 1%. As a first qualitative guess, we use the Antoine Law (Mahjoub et al.,

2014) Equ. 3.1 to calculate the vapor pressure of C_2H_6, which, at -180žC, is slightly above the triple point of -183.15žC (Fray and Schmitt, 2009). C_2H_6 is indeed one of four volatiles expected to be present in our final gas mixture (Gautier et al., 2011), along with C_2H_2, C_2H_4, and HCN. We use the A, B, C parameters from the NIST database (Carruth and Kobayashi, 1973). The low temperature used in the present study is at the edge of the validity range for C_2H_6. Nonetheless, we extend this laws validity domain and assume it to be applicable to these low-temperature conditions and thus must consider this calculation as a first approximation only. The vapor pressure is calculated at -180žC.

$$\log_{10}(P_s) = A - \left(\frac{B}{T+C}\right) \tag{3.1}$$

For C_2H_6, we find P_s = 5.7×10^2 mbar. This vapor pressure combined with the fact that we are slightly above the triple point of C_2H_6 near the liquid/vapor equilibrium, shows that this species will hardly condense. HCN, C_2H_2 and C_2H_4 all have their triple points (Fray and Schmitt, 2009) at temperatures higher than -180žC. They are listed in Table 3.1. Fray and Schmitt (2009) provided a review of vapor pressure relations obtained empirically and theoretically for a wide variety of astrophysical ices. They fitted polynomial expressions to extrapolate the sublimation pressures and used theoretical and empirical interpolation relations to obtain the coefficients of the polynomials. The polynomial expression from Fray and Schmitt (2009) is given Equ. 3.2. The polynomials (Table 3.1), noted A_i and T_i, are the corresponding temperatures, -180žC (93K) in our case. The sublimation pressures P_{sub} are presented in Table 3.1.

$$\ln(P_{sub}) = A_0 + \sum_{i=1}^{n} A_i/T_i \tag{3.2}$$

TABLE 3.1: Vapor pressures P_{sub} (mbar) calculated at 93K (-180žC) for HCN, C_2H_2 and C_2H_4. The T_p and A_i columns correspond to the triple points and coefficients of the polynomials of extrapolations, respectively, as given by Fray and Schmitt (2009).

	T_p(žC)	A_0	A_1	A_2	A_3	A_4	P_{sub} (-180žC) in mbar
HCN	-14.15	1.39×10^1	-3.62×10^3	-1.33×10^5	6.31×10^6	-1.13×10^8	1.69×10^{-12}
C_2H_2	-81.15	1.34×10^1	-2.54×10^3	0	0	0	9.48×10^{-4}
C_2H_4	-169.15	1.54×10^1	-2.21×10^3	-1.22×10^4	2.84×10^5	-2.20×10^6	1.3×10^3

The larger values (Table 3.1) for the two C_2 hydrocarbons in comparison with HCN agree with a first substantial release of the light C_2 hydrocarbons at temperatures below -100žC. HCN contributes to the gas composition mainly in the second stage, for temperatures larger than -80žC, because of its low vapor pressure at colder temperatures. The absence of C_2 hydrocarbons in the case of $[CH_4]_0$ = 1% is in agreement with the ex-situ analysis made in Gautier et al. (2011).

Detections by mass spectrometry

To go further in the analysis of the gas release, we monitored the gas phase composition by mass spectrometry at three threshold moments MS1, MS2, MS3 for 10% methane and only in the final gas mixture for 1%. In the case of 10% methane (Fig. 3.3 dashed blue line), the assigned MS1, MS2 and MS3 spectra are defined as the T, P conditions of -130žC and 0.38 mbar, -79žC and 0.74 mbar and +22žC and 1.84 mbar of products formed, respectively. MS1 is representative of the first release stage occurring at temperatures lower than -100žC, MS2 is on the pressure plateau beginning at -100žC, and MS3 corresponds to the final gas mixture obtained. For 1% methane conditions, we will only focus on the last point, where a substantial volatile pressure was measured.

A first iteration at $[CH_4]_0 = 10\%$ was done. Mass spectra of the volatiles are shown Figure 3.4 at different stages in their release after the plasma discharge, namely MS1, MS2 and MS3.

- MS1: 7min after stopping the cryogenic trap (blue line), C1, C2 and C3 block species have started to appear, with C_1 and C_2 (light volatiles of m/z < 30 amu) dominating the spectrum. Masses 15 and 28 stand out for the C_1 and C_2 blocks, respectively. Mass 28 cannot be attributed to N_2 as it was not trapped at -180žC during the experiment. It can be attributed to ethylene C_2H_4 or ethane C_2H_6 as both molecules are expected to be released at temperatures lower than -100žC and both have their major fragment at m/z 28 according to the NIST database. However, the previous ethane vapor pressure calculations and its triple point (Fray and Schmitt, 2009) show that it could not condense. In these plasma conditions, it is risky to attribute m/z 29 to methanimine ($CH_2{=}NH$) as the contribution of propane (C_3H_8) becomes non negligible (Carrasco et al., 2012). m/z 29 corresponds indeed to the main peak in the fragmentation pattern of C_3H_8. A few heavier volatiles in the C_3 and C_4 block are also beginning to be detected. At m/z 44 we could also suspect the contribution of CO_2. A blank mass spectrum of the mass spectrometer only has previously been measured (Carrasco et al., 2012), showing the same intensity of 2×10^{12} A at m/z 44 as the one seen in Figure 3.4 (blue plot), at low temperature. It corresponds to the weak air signature within the mass spectrometer at a vacuum limit of about 3×10^{-8} mbar. Consequently, the contribution of CO_2 observed in the mass spectra of Figure 3.4 at m/z 44 is minor inside the chamber among the released products and corresponds to the residual air in the mass spectrometer itself.

- MS2: The main differences compared to MS1 revolve around the C_3 and C_4 blocks with the appearance of heavier hydrocarbons (red line, m/z > 50). Within the C_3 block, an important contribution appears at m/z 39, consistent with the cyclopropene isomer C_3H_4. A significant increase is also observed at m/z 40 and 44 compatible with the fragmentation pattern of propane C_3H_8 in the NIST database. No species with masses higher than m/z 58 are detected yet.

- MS3: Remarkable changes occur at this final stage (black line), where many new species stand out. In the C_1 block, m/z 17 (NH_3) strongly increases to become the dominating C_1 compound.

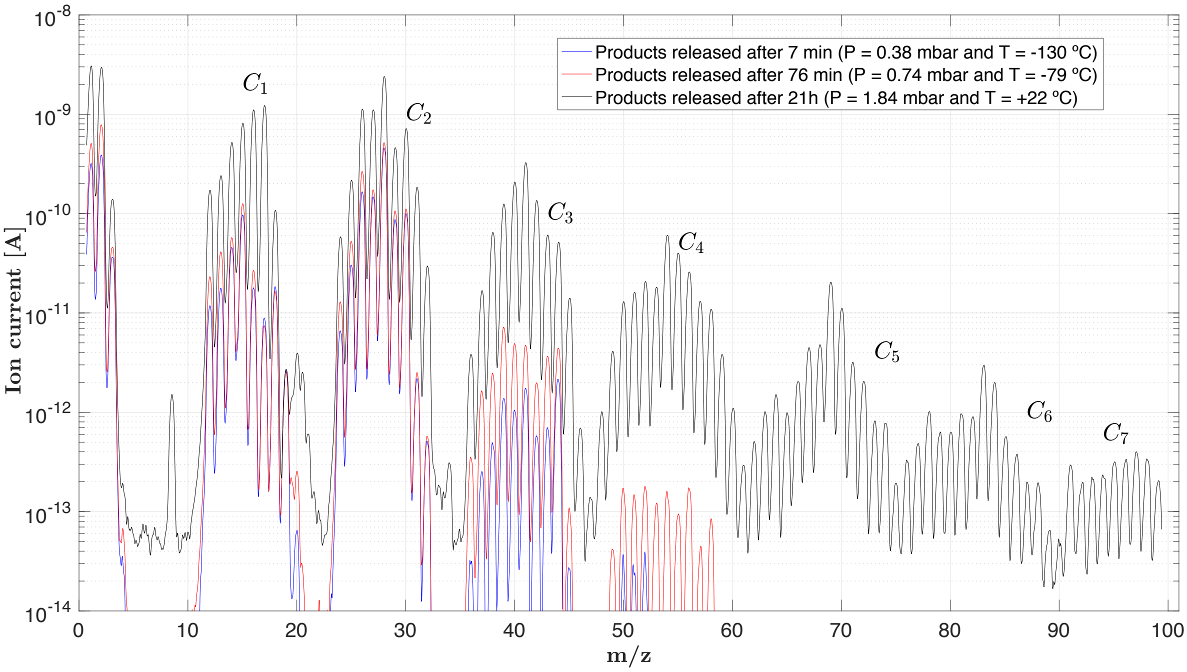

FIGURE 3.4: Detection and evolution of several C_n blocks for $[CH_4]_0$ = 10%. Plots marked in blue, red and black represent intermittent spectra taken 7 min, 76 min and 21h after commencing volatile release back to room temperature (MS1, MS2 and MS3, respectively). The indicated temperatures correspond to those taken at the start of a mass scan. Note that during a scan acquisition (∼ 200s long), the temperature may change over 0.3 žC to 23 žC depending on the heating rates. The color code used here is the same as MS1, MS2 and MS3 of Figure 3.3.

If we now compare the final stages obtained in the case of $[CH_4]_0$ = 1% and 10% in Figure 3.3, the total pressure of volatiles obtained (0.35 mbar, red line) is much less than in the case of $[CH_4]_0$ = 10% (blue). Figure 3.5 shows a comparison of the final states at $[CH_4]_0$ = 1% (brown) and $[CH_4]_0$ = 10% (blue), with the initial state (black), taken just before the volatile release at low-controlled temperature T = -180žC. As expected from the lower final pressure, the mass spectrum is much less intense in the case of $[CH_4]_0$ = 1% than 10%. No signature is detected beyond the C_5 block for 1% whereas large intensities are found until the C_7 block in the case of 10%. However, the major peaks are the same in both cases. The C_1 block is dominated by m/z 17, accountable for ammonia. This important production, discussed in section 4.2, is a new result compared to the work by Gautier et al. (2011) and Carrasco et al. (2012). Indeed, as detailed in Carrasco et al. (2012), ammonia was hardly detectable with the analytical methods used in the two latter studies. The C_2 block has high peak intensities at m/z 26, 27, 28, 30 for $[CH_4]_0$ = 10% but the one at 28 stands out in both methane conditions, compatible with C_2H_4 or C_2H_6. The C_3 block is dominated by m/z 41, accountable for acetonitrile CH_3CN; m/z 54 dominates C_4, which could correspond to butadiene C_4H_6 or $C_2N_2H_2$ (HCN dimer). For $[CH_4]_0$ = 10%, the C_5, C_6 and C_7 blocks are dominated by masses 69, 83 and 97, respectively. The odd masses predominantly detected suggest a strong contribution of N-bearing molecules in both conditions. The intensity evolution of m/z 17, 26, 27, 28 and 41 over time are shown in Figure 3.11 in the Supplementary Material.

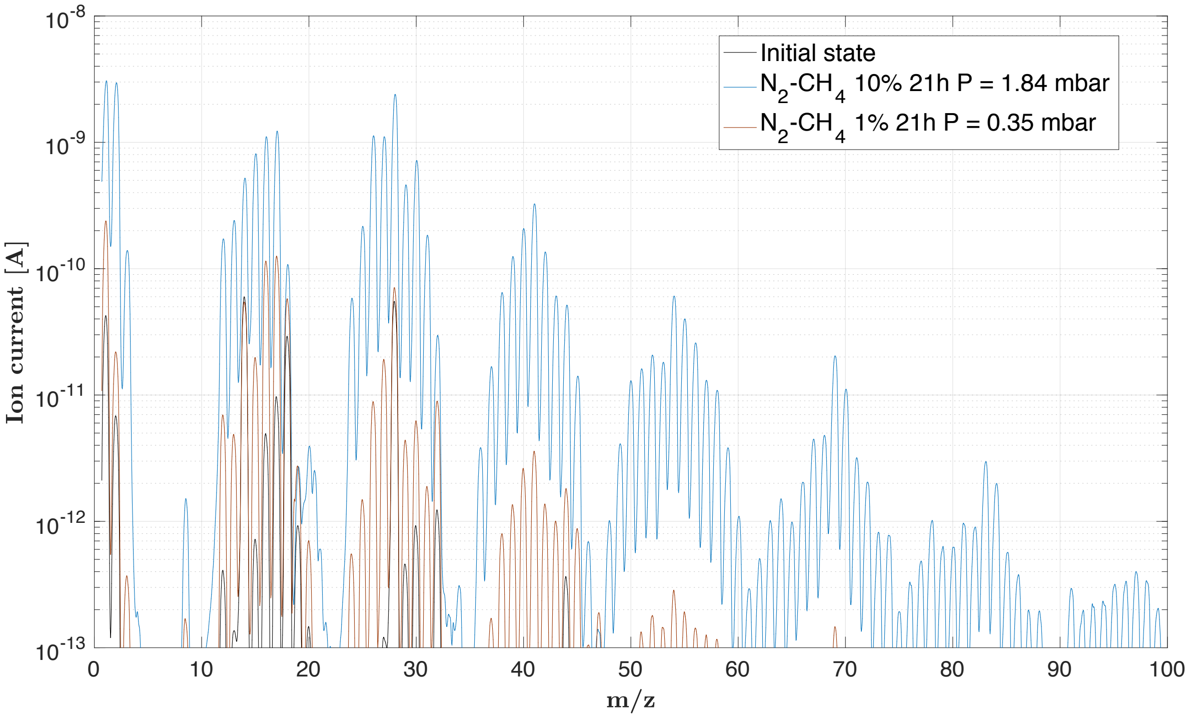

FIGURE 3.5: Three superimposed spectra at different $[CH_4]_0$ concentrations. In black, the initial mass spectrum taken before release of the volatiles, still at low-controlled temperature (and representative of the blank of our mass spectrometer). In blue and brown, the final state of volatiles at $[CH_4]_0$ = 10% after 21h and $[CH_4]_0$ = 1% after 21h of release, respectively.

3.3.2 Monitoring and quantification using Mid-Infrared spectroscopy

Alongside the neutral mass analysis, infrared spectra are simultaneously taken throughout the release of the volatiles inside the chamber to provide quantification of these volatiles. The measurement range is 650 cm^{-1} to 4000 cm^{-1} (2.5 μm to 15.4 μm) at a resolution of 1 cm^{-1} during the release of the gas phase products analyzed in situ. Figure 3.6 shows the spectra taken in both initial methane conditions. The top plot was taken for a $[CH_4]_0$ = 10%, the bottom at $[CH_4]_0$ = 1%. There is a clear discrepancy in the volatile products formed between the two conditions. $[CH_4]_0$ = 10% produces CH and CH_2 compounds visible in the stretching mode region 3,000-3,500 cm^{-1} that are absent in the $[CH_4]_0$ = 1% case. Likewise, there is a relatively far greater absorption of molecules bearing C=N and C=C bonds ($\sim$ 1,500 cm^{-1}) with $[CH_4]_0$ = 10%. Figure 3.6 (bottom) also has a large, broad absorption spread out over 2,000-2,500 cm^{-1} absent in the top figure. These signatures could correspond to a scattering feature of solid grains in suspension which could be the result of the released precursors reacting post-discharge. Furthermore, in Sciamma-OBrien et al. (2010), it had been shown that the gas to solid conversion yield was more important in the case of the 1% experiment than in the 10% experiment, in agreement with a higher amount of N-bearing gas phase products compared to hydrocarbons in the 1% experiment. The present results are consistent with this previous study.

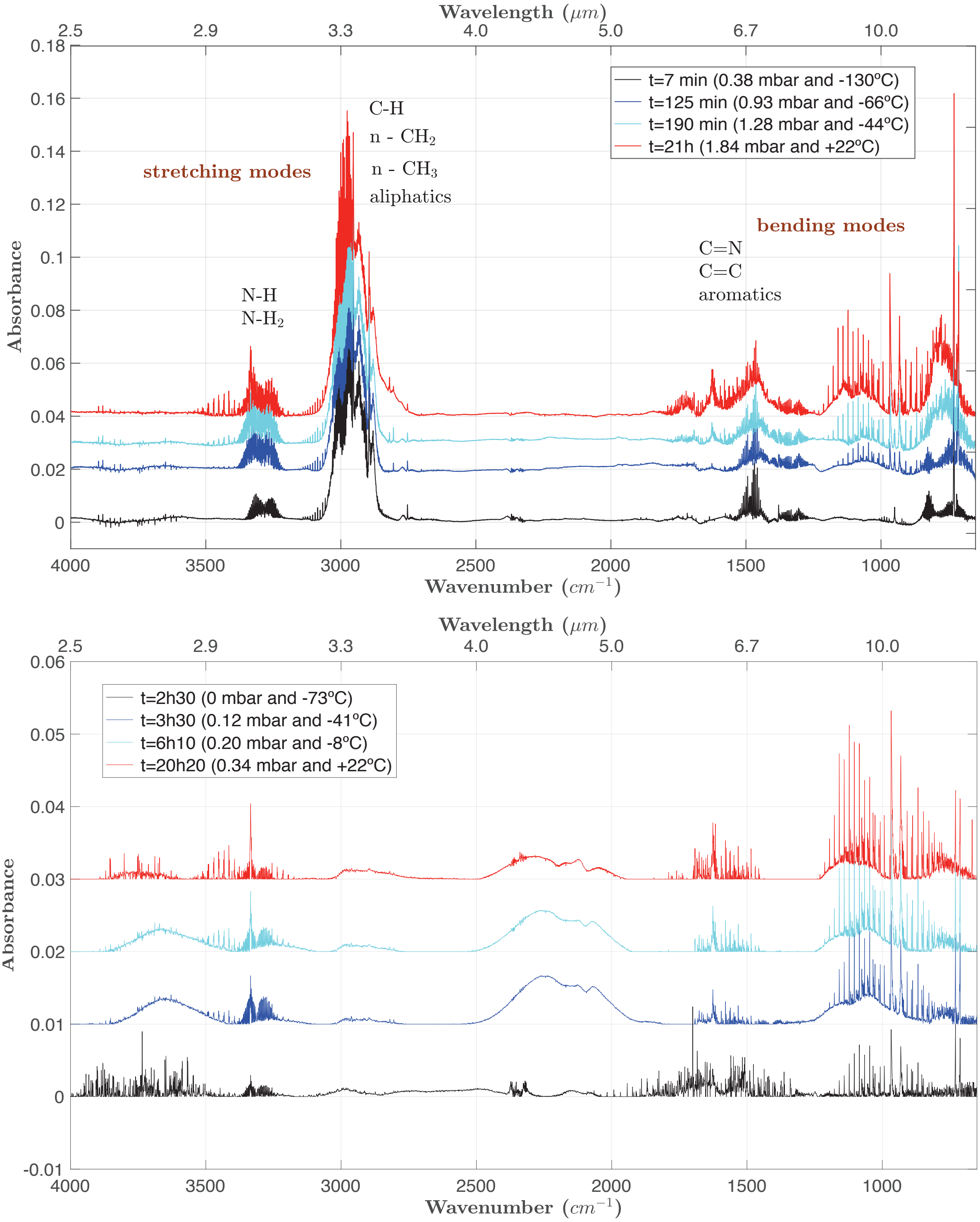

FIGURE 3.6: FT-IR spectra of the volatiles taken after the 90-10% (top) and 99-1% (bottom) N_2-CH_4 plasma conditions, plotted with an arbitrary absorbance against a 650-4000 cm^{-1} wavenumber range. The volatile density produced during the plasma discharge is being incrementally released and analyzed through IR spectroscopy. Top: Total gas pressures of 0.38 mbar (-130žC), 0.93 mbar (-66žC), 1.28 mbar (-44žC) and 1.84 mbar (+22žC) are shown in black, blue, cyan and red, respectively. Bottom: Total measured gas pressures of 0 mbar (-73žC), 0.12 mbar (-41žC), 0.20 mbar (-8žC) and 0.34 mbar (+22žC) with the same color code. One clear difference is in the absence of any substantial aliphatic compounds (2800-3100 cm^{-1}) at $[CH_4]_0$ = 1% (bottom) that stand out at $[CH_4]_0$ = 10% (top).

Among all the signatures observed, we identified and calculated the concentrations of four volatiles as they are released in the chamber: NH_3, C_2H_2, C_2H_4, and HCN. These species are listed in Table 3.2. Ammonia (NH_3), acetylene (C_2H_2), hydrogen cyanide (HCN), ethylene (C_2H_4), are all species present at ionospheric and/or stratospheric altitudes on Titan, considered to be key in the formation of Titans aerosols (Hanel et al., 1981; Kunde et al., 1981; Maguire et al., 1981; Wilson and Atreya, 2003; Wilson and Atreya, 2004) and formed in the upper atmosphere (Hörst, 2017).

TABLE 3.2: Four major volatile compounds detected and analyzed by infrared spectroscopy at $[CH_4]_0$ = 1% and $[CH_4]_0$ = 10%. The main infrared absorption bands which were used for density calculations are also given. References are 1: Vinatier et al. (2007), 2: Cui et al. (2009b), 3: Coustenis et al. (2007), 4: Nelson et al. (2009), 5: Paubert, Gautier, and Courtin (1984), 6: Teanby et al. (2007), 7: Moreno et al. (2015), 8: Molter et al. (2016). For more details on the bands and absorption cross-sections used for the molecular density calculations, the reader is referred to Table 3 and Figures 9 and 10 of the Supplementary Material.

Selected species	$C_xH_yN_z$	Main absorption bands (cm^{-1})	Detected in Titan's atmosphere
Ammonia	NH_3	962 (10.4 μm)	1, 4 (upper limit inferred)
Acetylene	C_2H_2	729.25 (13.7 μm)	1, 2, 6
Hydrogen cyanide	HCN	712.3 (14.0 μm)	1, 5, 6, 7, 8
Ethylene	C_2H_4	949.3 (10.5 μm)	1, 3

To track the production and evolution with time/temperature of these four compounds, we used in situ infrared quantification. By using Beer-Lamberts Law (Equ. 3.3), we can calculate the concentration of any given gas phase product.

$$I_t = I_0 \times e^{-l.\sigma.N} \tag{3.3}$$

I_t, I_0 and l are, respectively, the transmitted, incident intensities, optical path (cm) and σ the absorption cross-section ($cm^2.molecule^{-1}$) given by the Pacific Northwest National Lab (PNNL), University of Washington (Sharpe et al., 2004), GEISA (Armante et al., 2016) and ExoMol (Harris et al., 2006; Hill, Yurchenko, and Tennyson, 2013; Tennyson et al., 2016) databases. In addition, N is the molecular density (cm^{-3}). The absorption A is as follows:

$$A_{(\lambda)} = l \times \sigma_{(\lambda)} \times N \tag{3.4}$$

Using the integrated experimental absorption A with the integrated database absorption cross-section σ between the two wavelengths λ_1 and λ_2, Equ. 3.4 becomes:

$$\int_{\lambda_1}^{\lambda_2} A d\lambda = l \times N \times \int_{\lambda_1}^{\lambda_2} \sigma d\lambda \tag{3.5}$$

So, we obtain the molecular number density N ($molecules.cm^{-3}$):

$$N = \frac{1}{l} \times \frac{\int_{\lambda_1}^{\lambda_2} A d\lambda}{\int_{\lambda_1}^{\lambda_2} \sigma d\lambda} \tag{3.6}$$

Number densities are derived over a wavenumber range (see Table 3.3 of the Supplementary Material), covering the absorption band considered for each species. The main absorption band of each species was taken for all cases. The density results for both conditions are shown in Figure 3.7 and Figure 3.8. For the detailed number density calculation results and data points used with the specific integration bands, the reader is invited to peruse the Supplementary Material of the online version of this article. The 962 cm^{-1} (10.4 μm) NH_3 assigned band refers to the ν_2 N−H symmetric deformation. It is part of the NH_3 doublet at 930 and 960 cm^{-1}, caused by the motion of nitrogen through the plane of the three protons leading to an energy barrier. In the case of C_2H_2, we used acetylenes 729.25 cm^{-1} frequency of oscillation (13.7 μm). This band corresponds to the symmetric CH bending mode ν_5 of every other C and H atom to its respective neighboring atom. For HCN, we used the fundamental ν_2 bend frequency at 712 cm^{-1} (14.0 μm); C_2H_4 the ν_7 CH_2 wag deformation at 949 cm^{-1} (10.5 μm). C_2H_4 centered at 950 cm^{-1} is surrounded by the NH_3 doublet at 930 and 960 cm^{-1}. This absorption represents the fundamental absorption of ammonias ν_2 normal vibrational mode. The motion of nitrogen through the plane of the three protons causes this vibration with an energy barrier. For a summary on each band and frequency used, the reader is referred to Table 3.3 of the Supplementary Material.

Molecular number densities at N_2/CH_4 : 99/1% are listed in Table T-4. The measurements taken at t_{1-6} correspond approximately to 30 min, 60 min, 120 min, 180 min, 1200 min and 1440 min, respectively. Three datasets were acquired after three experiments in the same initial conditions. At this point, it is noteworthy to remember that t_0 represents the time when the plasma conditions and cryo-trap cooling are ended (Figure 3.3), and thus when the condensed volatiles can effectively desorb from the chamber (still under vacuum) walls into the gas phase. Overall, ammonia is the most dominant C_1 neutral ($\sim 1.1 \times 10^{15}$ cm^{-3}) produced at 1% CH_4, confirming its high intensity at m/z 17 detected in mass spectrometry (Figure 3.4). C_2H_2 and C_2H_4 also reached relatively high number density $\sim 3.2 \times 10^{12}$ cm^{-3} and $\sim 9.9 \times 10^{12}$ cm^{-3}, respectively. These number densities correspond to the final measurements.

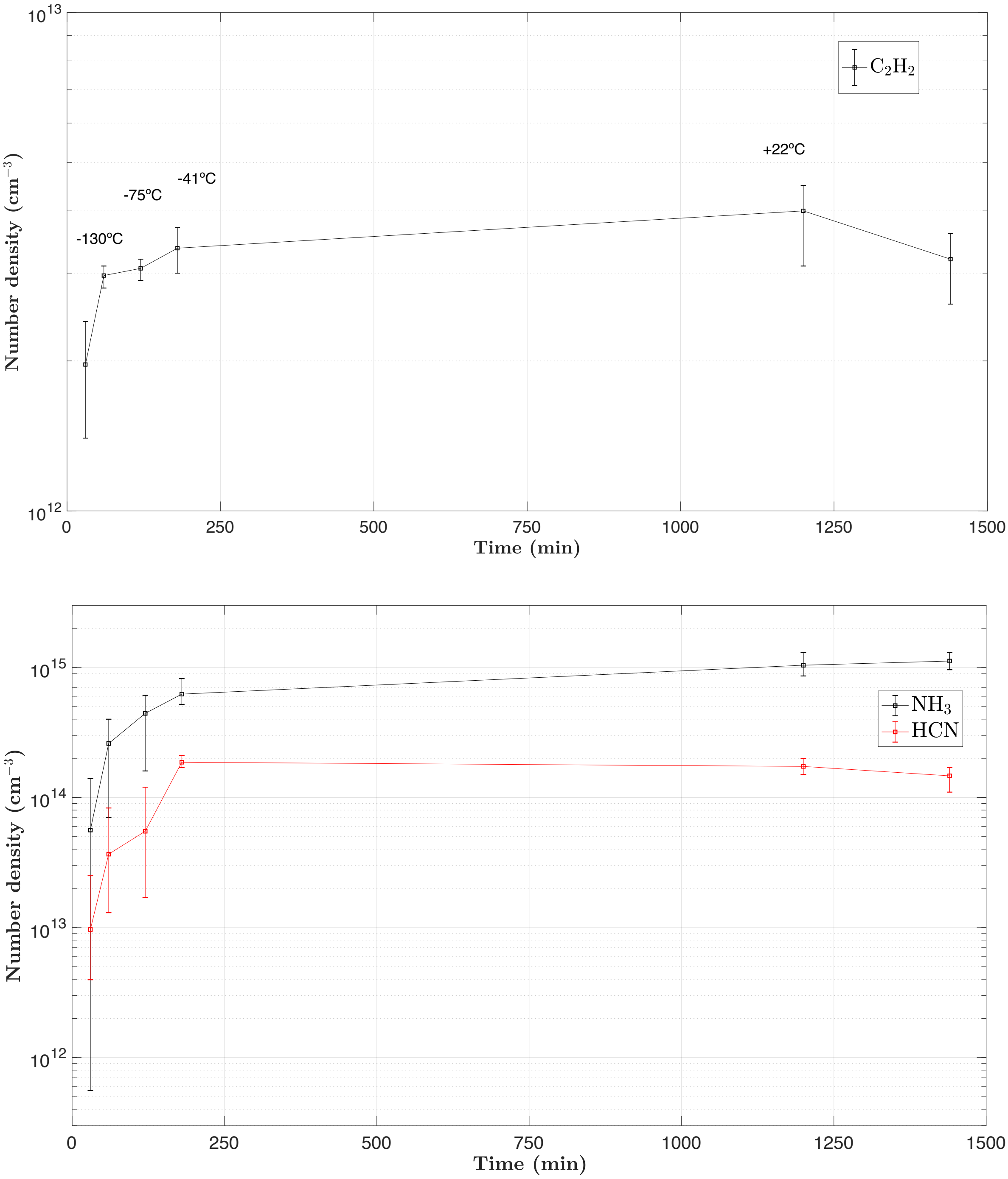

FIGURE 3.7: 1% methane conditions. Top: Molecular densities and average interpolated kinetic profile of C_2H_2. Bottom: NH_3 and HCN. Approximate temperatures are also labeled over each data point. The error bars represent the dispersion of the data points for all three experiments (Tables 3.4 and 3.5 of the online version of this article).

Figure 3.8 shows the same kinetic profiles from a 10% methane initial gas mixture, with the molecular densities listed in Table T-3.5. The C_2 species all reach concentrations at an order of magnitude higher than those at 1%, correlating with the higher methane concentration initially injected, which promotes the production of hydrocarbon species. C_2 species are thus strongly favorably produced with increasing methane concentrations. This is especially notable with the amount of HCN produced ($\sim 1.2 \times 10^{15} cm^{-3}$) in the 10% $[CH_4]_0$ condition.

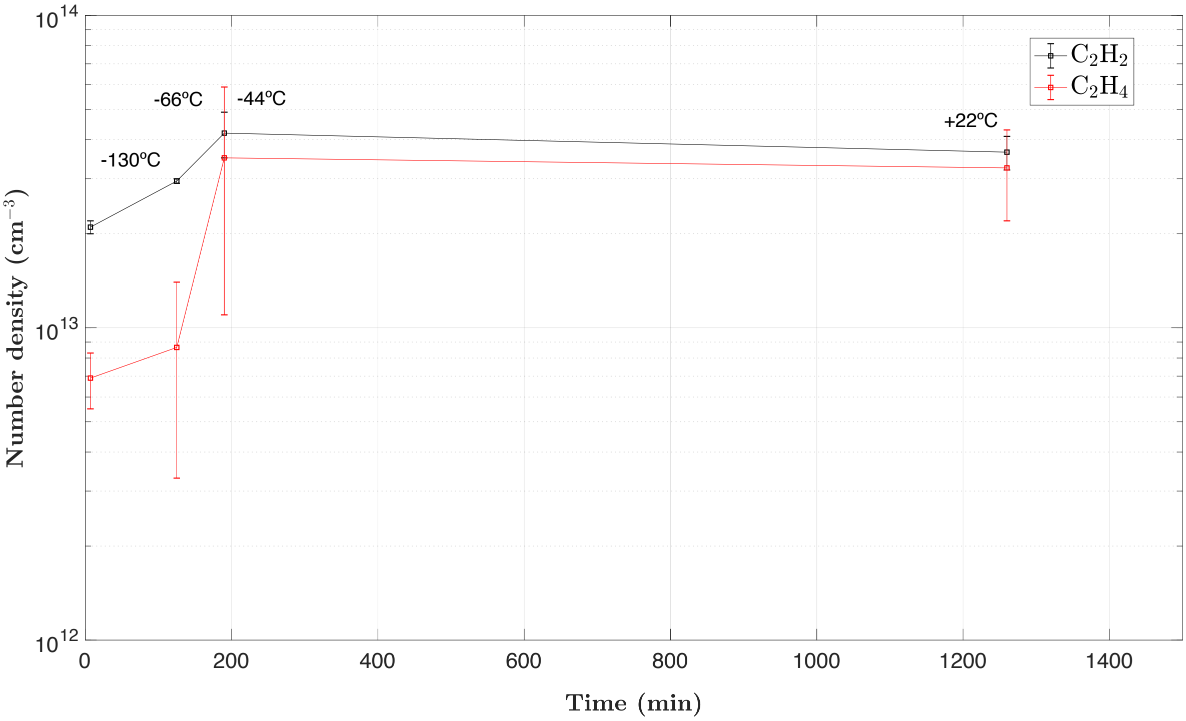

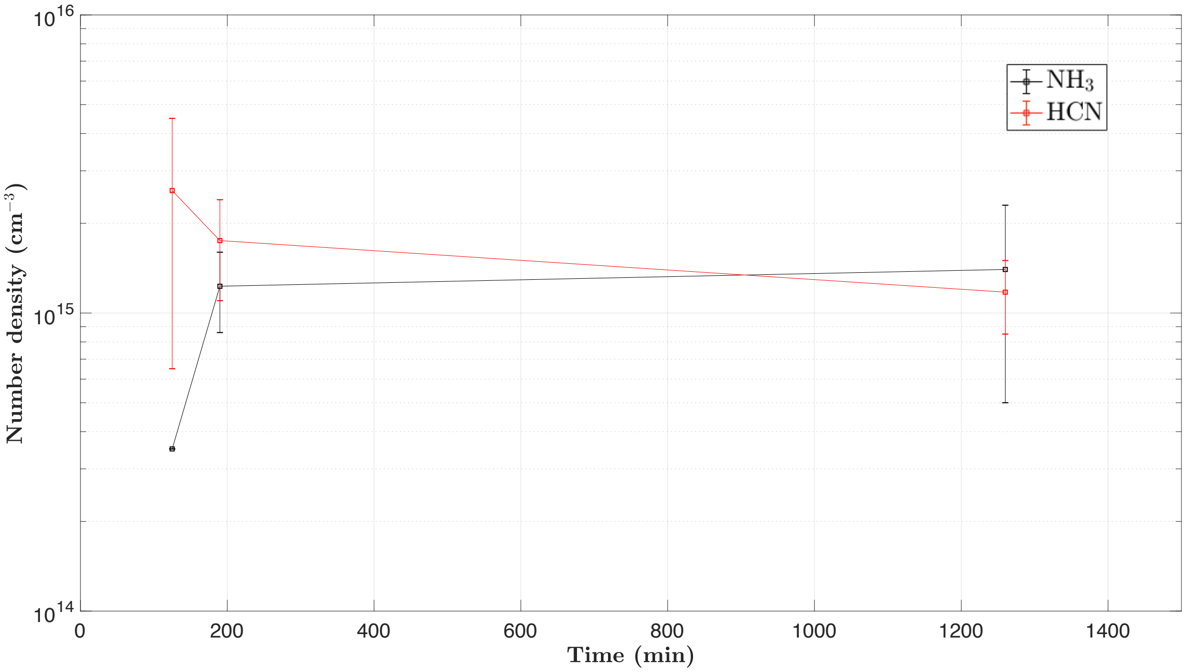

FIGURE 3.8: 10% methane conditions. Top: Molecular densities and average interpolate kinetic profiles of C_2H_2 and C_2H_4. Bottom: NH_3 and HCN. Approximate temperatures are also labeled over each data point. The error bars represent the dispersion of the data points for both experiments (Tables 3.4 and 3.5 of the online version of this article).

3.3.3 Methane consumption and hydrocarbon yield

With a 10% CH_4 mixing ratio, the condition with the most products, we consider the CH_4 consumption to provide yield estimates on the carbon conversion to hydrocarbon gas products. We note D as the total gas flow rate (N_2-CH_4) into the chamber in standard conditions. We first calculate the amount of CH_4 consumed in standard conditions ($mg.h^{-1}$), with $D = 55$ sccm. If n_{tot} is the total number of gas phase moles entering the reactor per second, the ideal gas law becomes:

$$\frac{d_{n_{tot}}}{d_t} = \frac{P_0}{R \times T_0} \times D \tag{3.7}$$

With P_0 the gas pressure in Pa, R the ideal gas constant, T the absolute temperature (300 K), $\frac{d_{n_{tot}}}{dt} = 2.22 \times 10^{19}$ $molecules.s^{-1}$. As seen previously, with a mixing ratio of $[CH_4]_0$ = 10%, we find a CH_4 consumption of 52%. So,

$$\frac{dn_{CH_{4cons}}}{dt} = D_{CH_4} \times CH_{4cons} \times \frac{d_{n_{tot}}}{d_t} \tag{3.8}$$

And the methane consumption rate is $\frac{dn_{CH_{4cons}}}{dt} = 1.15 \times 10^{18}$ $molecules.s^{-1}$. As the plasma runs for 2h, the total methane consumption is $\frac{n_{CH_4(2h)}}{dt} = 8.28 \times 10^{21}$ molecules. The total volume of the PAMPRE reactor is $\sim 28 \times 10^3$ cm^3. Consequently, there is a CH_4 total consumption of about $2.9 \times 10^{17} molecules.cm^{-3}$ over the 2h of the plasma discharge. With a calculated HCN total number of molecules of $\sim 1.2 \times 10^{15}$ cm^{-3}, HCN accounts for ~ 0.4 % of the carbon conversion from the consumed CH_4, while it is ~ 0.3 ‰ and 0.2 ‰ for C_2H_2 and C_2H_4, respectively.

3.4 Discussion

3.4.1 Volatile discrepancies at $[CH_4]_0 = 1\%$ and $[CH_4]_0 = 10\%$

There are notable differences in the volatile products formed in both methane concentrations used in this study (Figures 3.5 and 3.6, and Tables T-4 and T-5 of the online version of this article). Despite obtaining $\sim$ 1.84 mbar solely in volatile products with 10% methane and $\sim$ 0.35 mbar at 1% methane, both spectra in Figure 3.5 appear to qualitatively show the same nitrogen-bearing odd mass compounds, albeit at different intensities. One major discrepancy though, lies in the overwhelming amount of hydrocarbon species produced at 10% methane. The C_2 block is dominated by the m/z 28 amu signal (Figure 3.5), dominating the rest of the spectra, which according to the NIST database, corresponds to ethylene and ethanes main fragment (this mass cannot be linked to a release of N_2, as the cryotrap temperatures were not cold enough to trap any nitrogen during the experiment). However, the vapor pressure indicates that ethane is difficult to trap, and so m/z 28 can be mainly attributed to C_2H_4. Furthermore, the I_{30}/I_{28} ratio of the absolute intensities in the mass spectra at m/z 30 and m/z 28 amu corresponds to the ones given by NIST, $\sim$ 30-35%. On Titan, short-lived species such as C_2H_4 remain tantalizing to study, as they experience stratospheric dynamical processes with changing mixing ratios. By preventing the condensation of N_2, this study shows how m/z 28 may be attributed to C_2H_4 as one of the most abundant hydrocarbons at 10% CH_4.

3.4.2 Ammonia

Moreover, NH_3 stands out as being the most dominant N-bearing molecule in both $[CH_4]_0$ = 1% and $[CH_4]_0$ = 10% conditions, with final calculated concentrations of $\sim 1.1 \times 10^{15}$ and $\sim 1.4 \times 10^{15}$ $molecules.cm^{-3}$, respectively. Ammonia production was previously shown to be positively correlated with an increasing methane concentration (Carrasco et al., 2012). However, the latter study did not consider ammonia detection due to lack of a quantification approach as well as the m/z 17 H_2O fragment contamination. NH_3, as well as HCN, are nitrogen-bearing volatiles of utmost importance related to prebiotic chemistry in reducing atmospheric environments. So, studying NH_3 in Titans upper atmosphere is crucial to understanding the chemical pathways leading to the formation of aerosols and how it is incorporated in them. Cassini/INMS analyses of early Titan flybys (Vuitton, Yelle, and McEwan, 2007) first reported the presence of ammonia in the ionosphere, which was later more robustly confirmed by Cui et al. (2009b). Yelle et al. (2010), Carrasco et al. (2012), and Loison et al. (2015) discussed NH_3 chemical pathways. As such, the formation of ammonia in Titan's atmosphere is still unclear, though it is thought to most likely involve methanimine CH_2NH which itself acts as an important source for NH2 radicals in plasma conditions, to eventually forming NH_3. An ionic characterization of pathways and reactions pertaining to ammonia production is out of the scope of this paper. Yelle et al. (2010) proposed an explanation for the production of NH_3. Indeed, NH_3 is being photochemically formed in the upper atmosphere and fed down into the stratosphere. While photochemical models (Lara et al., 1996; Krasnopolsky, 2009) did not initially predict the formation of NH_3 in the upper atmosphere, its production can be explained through ion reactions (Yelle et al., 2010), by measuring the protonated ion NH_4^+. Based on the long chain reaction forming

NH_3 detailed by (Yelle et al., 2010) and its importance in our experimental results (major nitrogen-bearing molecule), the contribution of nitrogen-bearing functional groups (e.g. amines, nitriles or imine) or their contribution to be eventually incorporated into the organic aerosols seems pertinent. This appears to be the case for NH_3, being the main N-bearing compound. In more advanced environments whether on Titan (Neish et al., 2009) or in the interstellar medium (e.g. Largo et al., 2010), NH_3 remains an open and current topic to study prebiotic chemistry.

3.4.3 C_2H_4 pathways to tholin formation

The presence of ethylene in the ionosphere (Waite et al., 2007) and stratosphere (e.g. Coustenis et al., 2007) is well established. However, similar to the other volatiles chosen in this study, its influence and participation in tholin formation needs to be further investigated. The relative concentration of C_2H_4 in Titans atmospheric column is subject to distinct features. It was first noted by Coustenis et al. (2007) and Vinatier et al. (2007) how the retrieved stratospheric vertical abundances of C_2H_4 from Cassini/CIRS data showed both a unique decrease in the mixing ratios towards high northern latitudes as well as being the only species whose mixing ratio decreases with altitude at 15žS near the equator. Compared to other C_2 molecules (e.g. C_2H_2, C_2H_6, HCN), C_2H_4 is unique in that its mixing ratio decreases with altitude at equatorial and northern polar latitudes. One hypothesis given by Vinatier et al. (2007) was that C_2H_4 is subject to a photodissociative sink along with equatorward transport from the winter polar vortex in the lower stratosphere and troposphere (Crespin et al., 2005), essentially removing it away from the gaseous atmosphere. This sink could eventually be the multiple haze layer.

As discussed previously and shown in Figure 3.5 and Table 3.5 (Supplementary Material), C_2H_4 is an important C_2 compound in the 10% $[CH_4]_0$ mixture. Similar experiments (Gautier et al., 2014) argued that (in the absence of a cooling plasma system) tholins are formed with CH_2 patterns, coherent with C_2H_4 putatively acting as a strong gaseous precursor. This study comes in agreement, at least on a tholin formation scale that C_2H_4 participates in their formation. This experimental result also confirms that, if the stratospheric multiple haze layer is indeed the sink to this molecule (Vinatier et al., 2007), the latter can easily take chemical pathways leading to the formation of aerosols. Pathways involving C_2H_4 (alongside C_2H_2) loss have been suggested by Yelle et al. (2010). They proposed that C_2H_4 (and C_2H_2) reacts with NH radicals (Reaction 8) to produce heavier nitrile molecules such as CH_3CN (Reaction 9) or the cyanomethylene radical HC_2N.

$$N^+ + CH_4 \longrightarrow {CH_3}^+ + NH \tag{8}$$

$$NH + C_2H_4 \longrightarrow CH_3CN + H_2 \tag{9}$$

The formation of NH radicals, Reaction (8), occurs in ion chemistry conditions through proton exchange, while these same radicals can then react with ethylene, Reaction (9) in neutral conditions. Given the large abundance of produced NH_3, it is possible that NH radicals were formed and reacted with C_2H_4 during our 2h plasma, which incidentally is favorably produced with increasing CH_4 concentration (Reaction 8). Interestingly, C_2H_4 is implicated in NH_3 formation. According to Yelle et al. (2010),

$$\mathrm{NH_2 + H_2CN \longrightarrow NH_3 + HCN} \tag{\{10\}}$$

Prior to this, the formation of the amino radical NH_2 involves ion chemistry, with the following ion-neutral reaction:

$$\mathrm{N^+ + C_2H_4 \longrightarrow NH_2 + C_2H_2{}^+} \tag{\{11\}}$$

Thus, C_2H_4 in our plasma may participate in the production of heavier nitrile species or ammonia during the plasma discharge.

3.4.4 HCN production

Hydrogen cyanide in Titan's atmosphere is well documented and known to be the most abundant nitrile trace volatile (e.g. Kim et al., 2005; Vinatier et al., 2007), with high mixing ratios at stratospheric altitudes in the northern polar regions. HCN is also of prime importance in the search for prebiotic conditions in the solar system and beyond (Oró, 1961) as well as being one of the precursors to amino acids and peptides (Oró, 1961; Hörst et al., 2012; He and Smith, 2014; Rahm et al., 2016). In addition, the chemistry of HCN mainly relies on its relatively high polarity and quite strong CN triple bond, with a bond dissociation energy D(H-CN) of $\sim$ 5.2 eV calculated by photodissociation and photoionization models (Berkowitz, 1962; Davis and Okabe, 1968; Cicerone and Zellner, 1983). Thus, making it a relatively stable molecule. As shown Figures in 3.7 and 3.8, HCN is one of the most abundant products formed in both $[CH_4]_0$ = 1% and $[CH_4]_0$ = 10% conditions, with $\sim 1.5 \times 10^{14} cm^{-3}$ and $1.2 \times 10^{15} cm^{-3}$ on average, respectively. Carbon yield calculations stresses the carbon conversion to HCN ($\sim$ 0.4%), while other C_2 species are all favorably produced by an order of magnitude at 10% CH_4 than at 1% CH_4. HCN and HCN-based copolymers are also known to participate in the chemical growth patterns of tholin formation (Pernot et al., 2010; Gautier et al., 2014) along with the CH_2 monomer, which is in agreement with the idea that haze forming acts as an HCN sink in the stratosphere (McKay, 1996; Vinatier et al., 2007). This study seems to confirm the prevalent role of HCN in the formation of tholins.

3.5 Conclusions

The present study was aimed at expanding previous work focused on the volatile production and their participation in tholin production using a cold dusty plasma experiment (Gautier et al., 2011; Carrasco et al., 2012), but with one major twofold novelty (i) the ability to trap these volatiles in situ within our plasma reactor with a new experimental setup at low-controlled temperatures, and (ii) quantitatively analyze their formation using IR spectroscopy. It is important to be cautious in interpreting these quantitative results, as three (T, P and t) parameters change simultaneously during the sublimation phase entailing possible unsuspected ice-volatile chemistry. The approach we took was solely focused on the gas phase. Indeed, these volatiles, still poorly understood and which give Titan its unique nature of being one of the most chemically complex bodies in the Solar System, act as substantial gas phase precursors to the formation of Titans organic aerosols populating its haze layers. Hence, simulating ionosphere conditions is crucial in constraining the volatile population, its reactivity and potential chemical pathways.

Major discrepancies exist between the two initial methane concentrations we used, 1% and 10%, with many more hydrocarbons formed in the latter case (detection of C_7 species), but with similar amounts of N-bearing species, only at different concentrations. Our results confirm the important role of C_2 species in the tholin precursor volatile family (m/z 28 e.g.), as well as that of NH_3. One of them, ethylene C_2H_4, being a relatively major C_2 hydrocarbons, might even reveal an important "hub" role at least at 10% $[CH_4]_0$ through which specific chemical pathways involving C_2H_4 are favored (see Section 3.4.3). The importance of C_2H_4 might also be relevant at 1% $[CH_4]_0$ although this is difficult to assess in this study due to the cryotrapping efficiency which is not optimum at -180žC to quantify it, as suggested by the thermodynamical calculations and mass spectra during the discharge. Eventually, tholins themselves may be benefitting from the incorporation of C_2H_4, which itself stresses the value of considering a yet unaccomplished fully-coupled ion and neutral chemistry study. This is out of the scope of this paper, as the cryo-trap system prevents the formation of tholins. These experiments have also shown a strong incorporation of carbon into HCN, along with NH_3 being a competitive product to HCN, especially with a $[CH_4]_0$ = 1% (an order of magnitude more in final concentration).

Future compelling work to expand this study might be to consider other molecular families participating in the neutral reactivity, therefore increasing our knowledge of volatile chemistry precursor to tholin production. In addition, adding selected volatiles such as HCN, an important nitrile, in trace amounts into our gaseous mixture would improve the understanding of its influence on the chemical reactivity in plasma conditions in future work. Moreover, predicting ion densities and characterizing ion-neutral reactions in these conditions would be key to understanding their incorporation into the solid phase and validating chemical pathways which are still largely unknown in Titan ionosphere simulations. Perhaps most importantly, a fully-coupled ion-neutral characterization would fundamentally bring credence to understanding the complex organic realm encompassing Titans gas phase chemistry.

3.6 Supplementary Material

1% CH_4

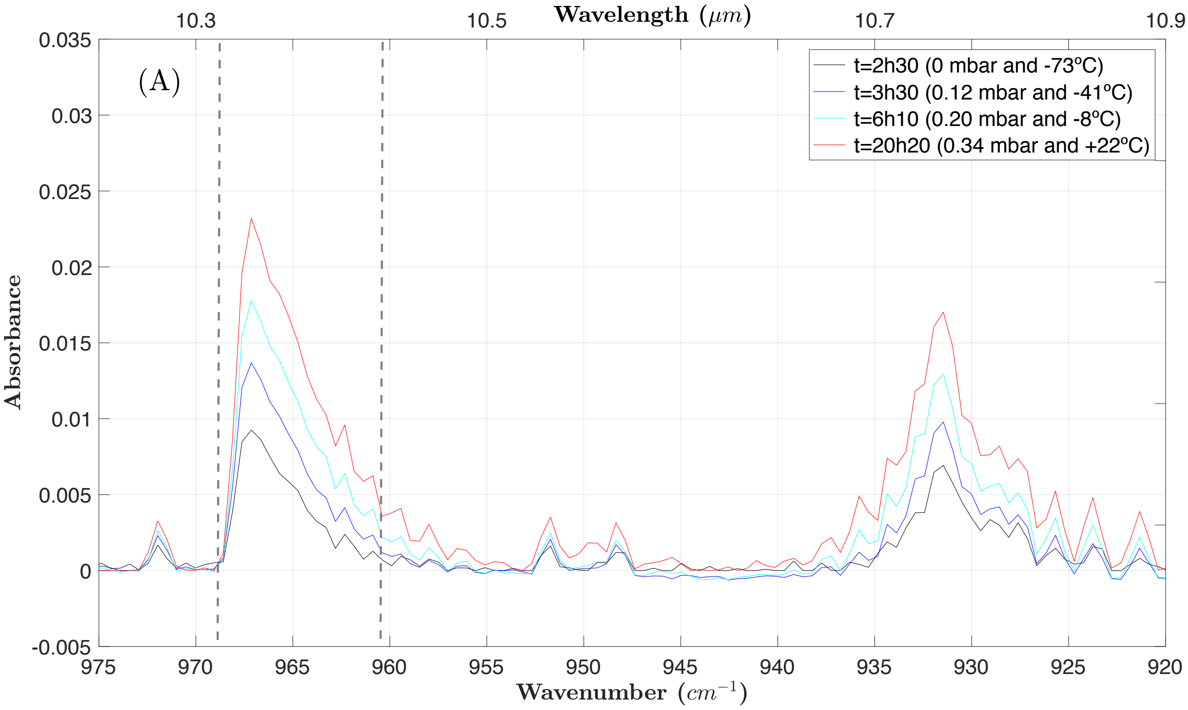

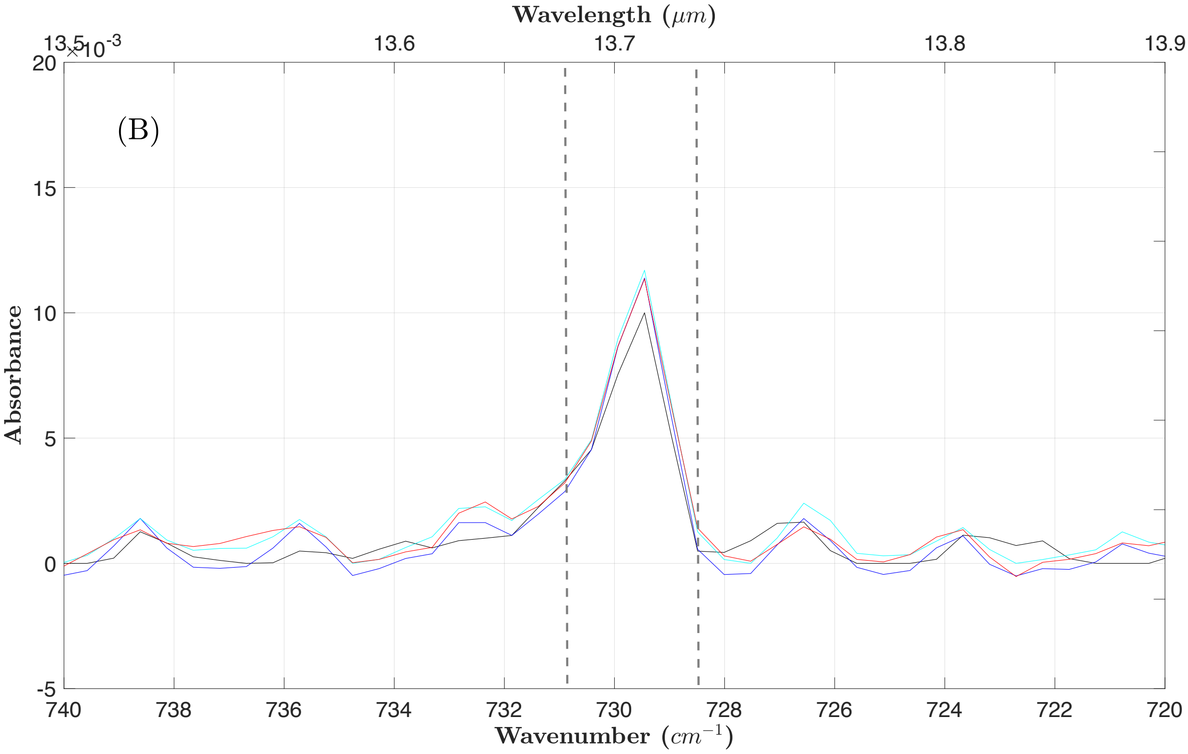

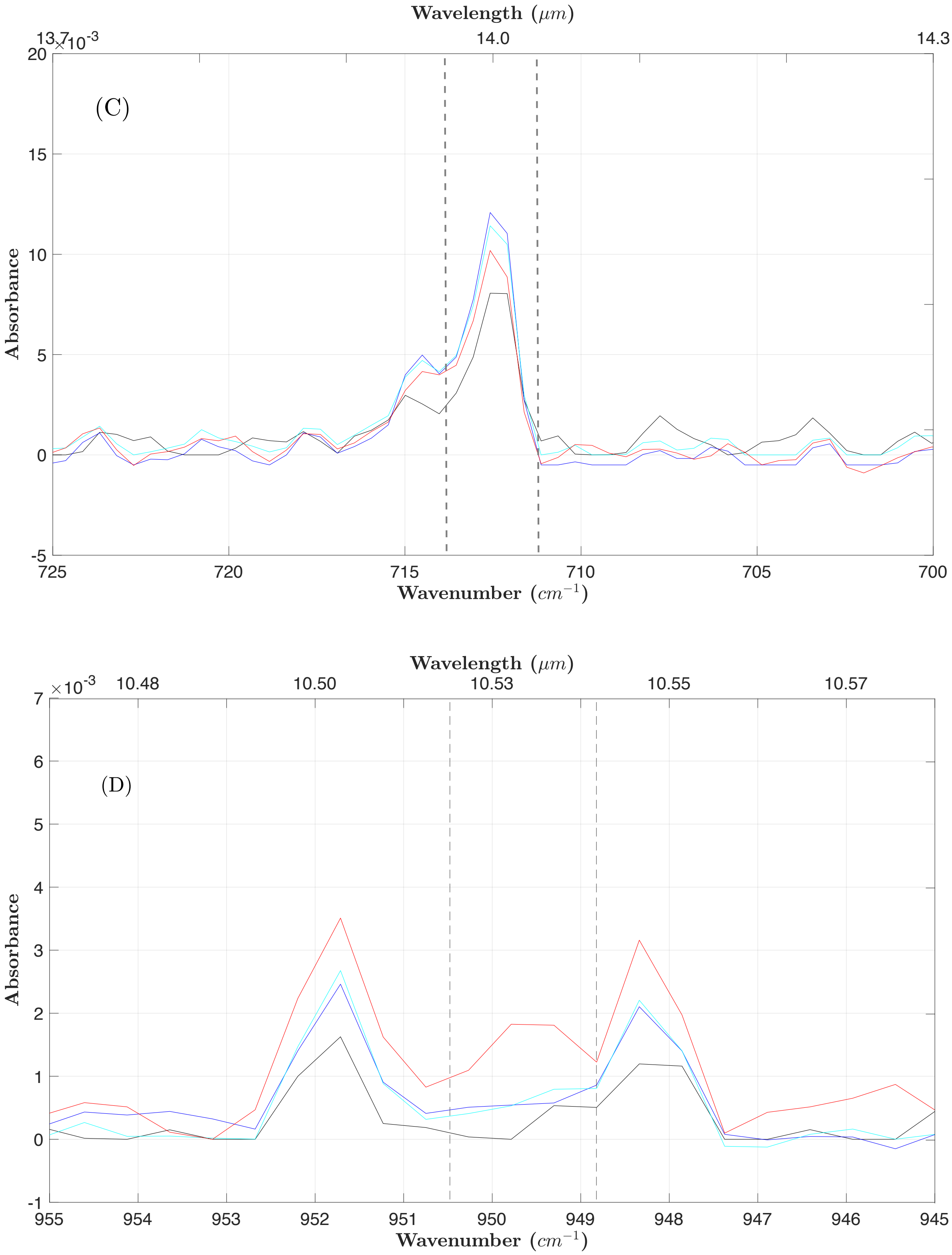

FIGURE 3.9: $[CH_4]_0$ = 1%. Main absorption bands of (A) NH_3 (930 cm^{-1} and 960 cm^{-1} doublet), (B) C_2H_2 (729.25 cm^{-1}), (C) HCN (713 cm-1), (D) C_2H_4 (949.55 cm^{-1}). The color code is the same as in Figure 3.6. The vertical dashed gray lines correspond to the integration band used for the density calculations on either side of the absorption peaks.

10% CH_4

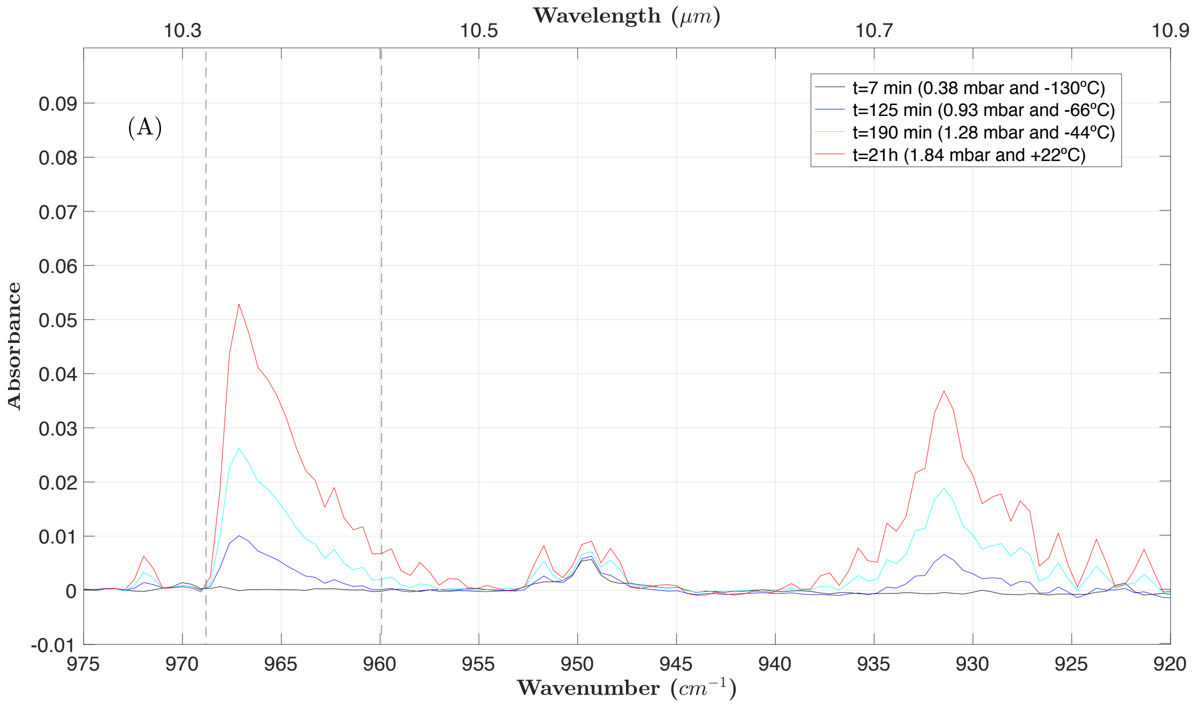
Wavelength (μm)
10.3
10.5
10.7
10.9
(A)
t=7 min (0.38 mbar and -130ºC)
t=125 min (0.93 mbar and -66ºC)
t=190 min (1.28 mbar and -44ºC)
t=21h (1.84 mbar and +22ºC)
Absorbance
0.09
0.08
0.07
0.06
0.05
0.04
0.03
0.02
0.01
0
-0.01
975
970
965
960
955
950
945
940
935
930
925
920
Wavenumber (cm⁻¹)

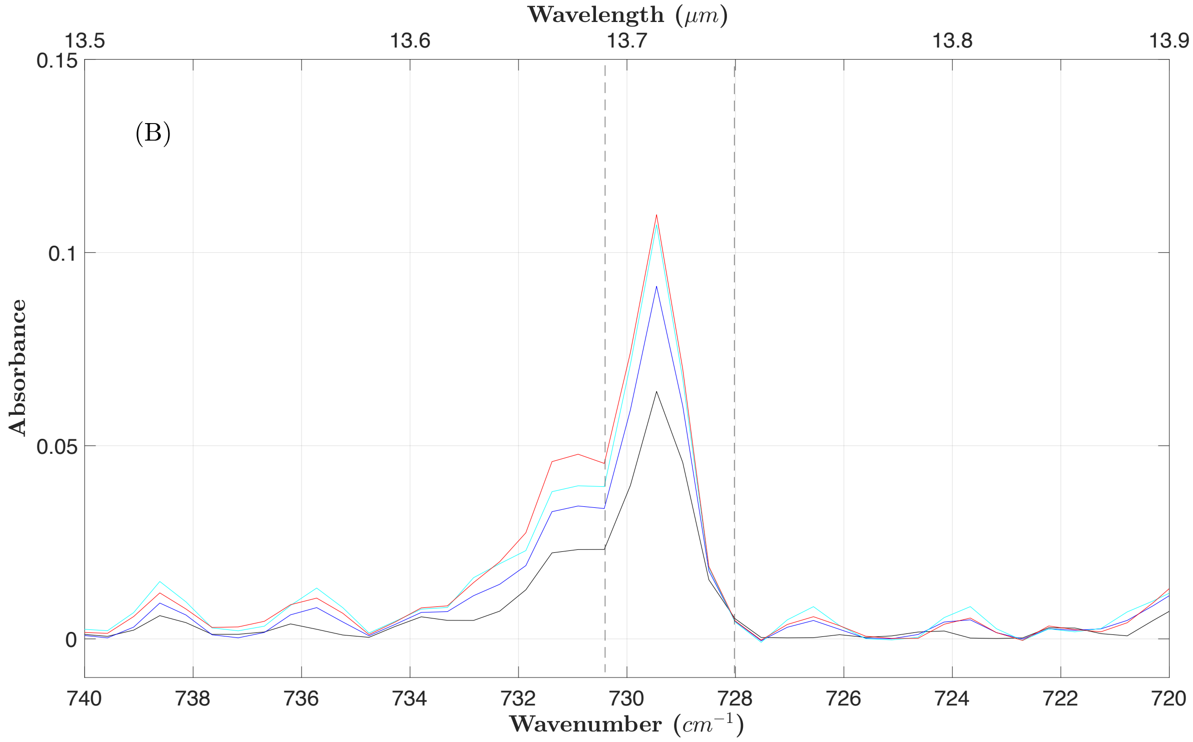
Wavelength (μm)
13.5
13.6
13.7
13.8
13.9
0.15
(B)
0.1
Absorbance
0.05
0
740
738
736
734
732
730
728
726
724
722
720
Wavenumber (cm⁻¹)

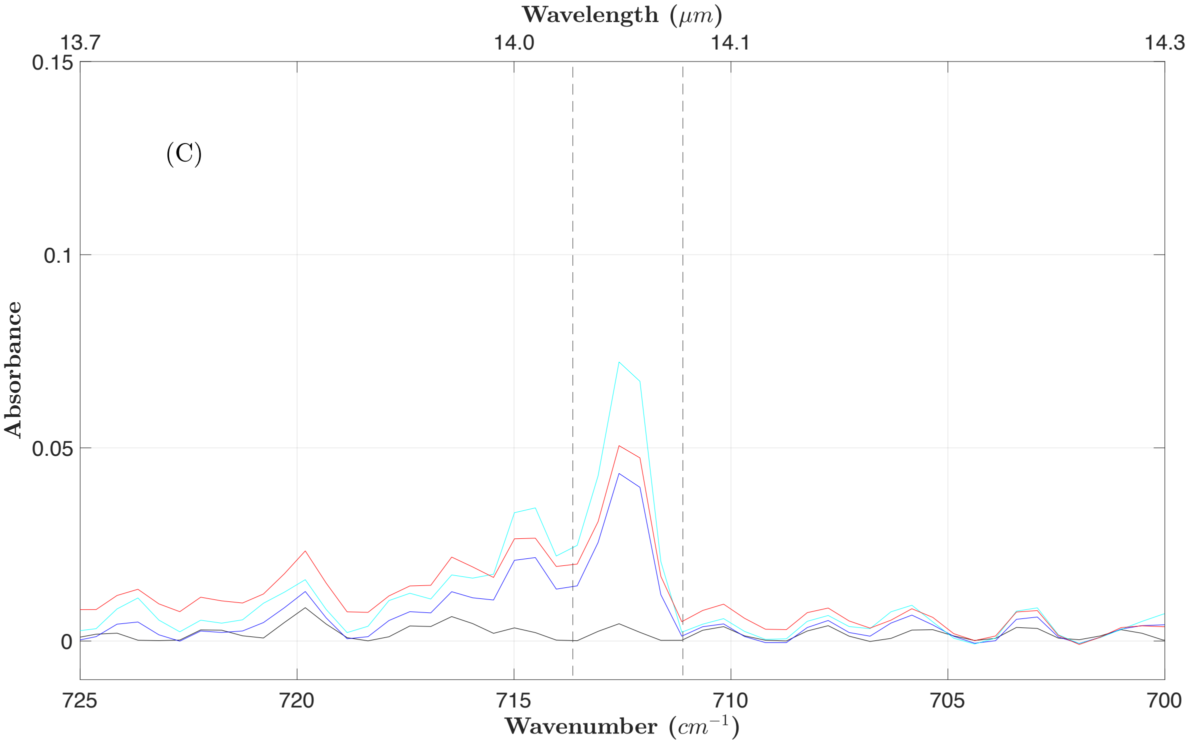

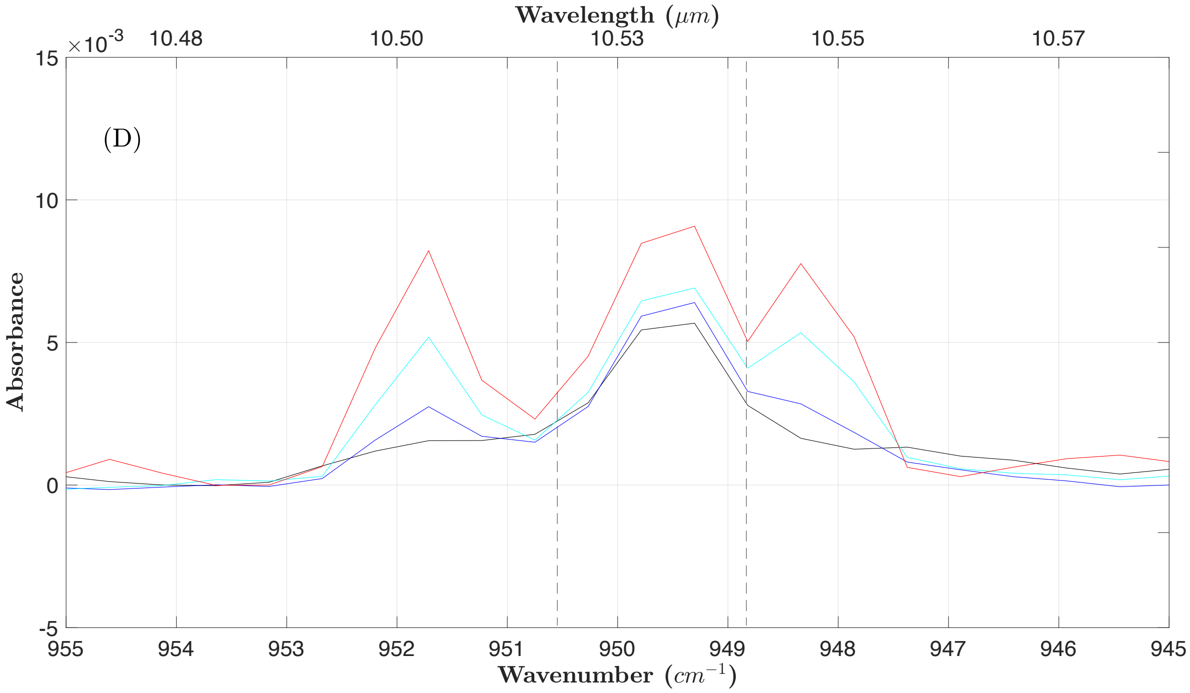

FIGURE 3.10: $[[CH_4]_0 = 10\%$. Main absorption bands of (A) NH_3 (930 cm^{-1} and 960 cm^{-1} doublet), (B) C_2H_2 (729.25 cm^{-1}), (C) HCN (713 cm^{-1}), (D) C_2H_4 (949.55 cm^{-1}). The color code is the same as in Figure 3.6. The vertical dashed gray lines correspond to the integration band used for the density calculations on either side of the absorption peaks.

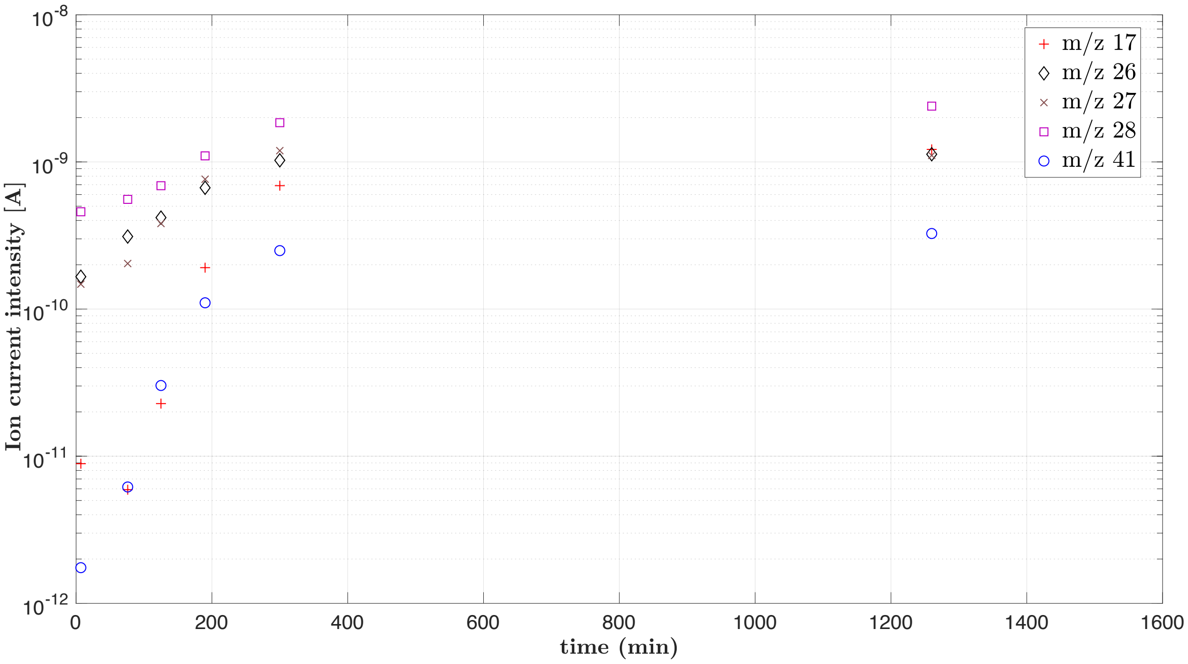

FIGURE 3.11: Evolution of the intensities (same time scale as Figure 3.3) of selected species, NH_3 (m/z 17), C_2H_2 (m/z 26), HCN (m/z 27), C_2H_4 (m/z 28) and CH_3CN (m/z 41) over time.

TABLE 3.3: IR peak locations, fundamental frequencies and integrated wavenumber ranges, absorption cross-sections ($cm^2.molecule^{-1}$) for each selected volatile, as analyzed in both methane conditions. For the calculation results (derived from Equation 3.6), see the following Tables 4-5. [1]Sharpe et al. (2004) and http://vpl.astro.washington.edu/spectra/allmoleculeslist.htm

Selected species	Fundamental frequency[1]	Main peak (cm^{-1})	FWHM (cm^{-1})	Integrated absorption cross-section σ ($cm^2.molecule^{-1}$)
Ammonia	ν_2	965	± 4.0	4.04×10^{-18}
Acetylene	ν_5	729.25	± 1.25	1.92×10^{-16}
Hydrogen Cyanide	ν_2	712.3	± 1.2	4.09×10^{-18}
Ethylene	ν_7	949.5	± 1.0	2.43×10^{-17}

TABLE 3.4: Calculated molecular densities from IR absorption at $[CH_4]_0$ = 1%, for three different data sets. T_{1-6} correspond to measurements done at approximately 30 min (-130žC), 60 min (-85žC), 120 min (-70žC), 180 min (-41žC), 1200 min (+22žC) and 1440 min (+22žC), respectively. Each column corresponds to one experiment. Number density calculations are performed with the integrated absorption cross-section of the ExoMol or Hitran databases at the resolution of our experimental spectra (see Table 3.3). Blank boxes indicate the absence of the species where no number density was derived.

Time/species	NH_3			C_2H_2			HCN			C_2H_4		
T1	5.6×10^{11}	2.8×10^{13}	1.4×10^{14}	2.1×10^{12}	2.4×10^{12}	1.4×10^{12}	4.0×10^{12}	2.5×10^{13}	-	-	-	-
mean	5.6×10^{13}			2.0×10^{12}			9.7×10^{12}			-		
T2	7.0×10^{13}	3.1×10^{14}	4.0×10^{14}	3.1×10^{12}	3.0×10^{12}	2.8×10^{12}	1.3×10^{13}	8.3×10^{13}	1.4×10^{13}	-	-	-
mean	2.6×10^{14}			3.0×10^{12}			3.7×10^{13}			-		
T3	1.6×10^{14}	5.6×10^{14}	6.1×10^{14}	3.1×10^{12}	2.9×10^{12}	3.2×10^{12}	1.7×10^{13}	1.2×10^{14}	2.8×10^{13}	-	-	-
mean	4.4×10^{14}			3.1×10^{12}			5.5×10^{13}			-		
T4	5.2×10^{14}	5.3×10^{14}	8.2×10^{14}	3.7×10^{12}	3.0×10^{12}	3.4×10^{12}	2.1×10^{14}	1.8×10^{14}	1.7×10^{14}	-	-	-
mean	6.2×10^{14}			3.4×10^{12}			1.9×10^{14}			-		
T5	9.6×10^{14}	8.6×10^{14}	1.3×10^{15}	4.4×10^{12}	3.1×10^{12}	4.5×10^{12}	2.0×10^{14}	1.5×10^{14}	1.7×10^{14}	-	-	-
mean	1.0×10^{15}			4.0×10^{12}			1.7×10^{14}			-		
T6	9.6×10^{14}	1.3×10^{15}	1.1×10^{15}	3.4×10^{12}	3.6×10^{12}	2.6×10^{12}	1.7×10^{14}	1.6×10^{14}	1.1×10^{14}	-	-	-
mean	1.1×10^{15}			3.2×10^{12}			1.5×10^{14}			-		

TABLE 3.5: Calculated molecular densities from IR absorption at $[CH_4]_0$ = 10%, for two different data sets. T_{1-4} correspond to measurements done at approximately 7 min (-130žC), 125 min (-66žC), 190 min (-44žC) and 21h (+22žC), respectively. Each column corresponds to one experiment. Number density calculations are performed with the integrated absorption cross-section of the ExoMol or Hitran databases at the resolution of our experimental spectra (see Table 3.3). Blank boxes indicate the absence of the species where no number density was derived.

Time/species	NH_3	C_2H_2	HCN	C_2H_4
T1	- -	2.0×10^{13} 2.2×10^{13}	- -	8.3×10^{12} 5.5×10^{12}
mean	-	2.1×10^{13}	-	6.9×10^{12}
T2	3.5×10^{14} -	2.9×10^{13} 3.0×10^{13}	6.5×10^{14} 4.5×10^{15}	1.4×10^{13} 3.3×10^{12}
mean	3.5×10^{14}	3.0×10^{13}	2.6×10^{15}	8.7×10^{12}
T3	8.6×10^{14} 1.6×10^{15}	3.5×10^{13} 4.9×10^{13}	1.1×10^{15} 2.4×10^{15}	1.1×10^{13} 5.9×10^{13}
mean	1.2×10^{15}	4.2×10^{13}	1.8×10^{15}	3.5×10^{13}
T4	2.3×10^{15} 5.0×10^{14}	4.1×10^{13} 3.2×10^{13}	8.5×10^{14} 1.5×10^{15}	2.2×10^{13} 4.3×10^{13}
mean	1.4×10^{15}	3.7×10^{13}	1.2×10^{15}	3.3×10^{13}

As seen in the Introduction and in Chapters 2 and 3, the complexity of Titan's upper atmosphere chemistry revolves around the coupling of neutral, positive and negative ion chemical processes. The positive ion results unveiled by Cassini have prompted the need for laboratory investigations simulating the high altitude methane conditions. Cassini has unveiled new positively charged species, ranging from 12 amu up to 300 amu. These results have provided insight to the puzzling question of how the organic haze is formed in the upper atmosphere and the species and chemical pathways involved? Laboratory experiments such as PAMPRE can be used as a strong analog to simulate upper atmospheric conditions. By analyzing the positive ion chemistry in our plasma discharge, we can then investigate the species present that are precursors to the tholins formed in the discharge. These results can then be compared to Cassini observations and help constrain the conditions that faithfully represent the observations. The determining parameter influencing this chemistry is the CH_4 content. By modifying the N_2-CH_4 mixing ratio in the laboratory, we are able to reach analogous conditions to those found in Titan's ionosphere. In the post-Cassini era, Earth-based observations, models and laboratory simulations remain the only ways of studying the ion chemistry in Titan's upper atmosphere before another mission reaches the Saturnian system. In this context, we have acquired an ion and neutral mass spectrometer, which was fitted to our plasma chamber. For the first time on our experimental setup, we performed mass measurements in different gas mixtures directly within the plasma. We also studied the impact of the energy distribution filtering specific to each methane condition. Finally, we compared our laboratory results with Cassini-INMS observations, and investigated general trends between ion groups.

Chapter 4

Positive Ion Chemistry in an N_2-CH_4 Plasma Discharge: Key Precursors to the Growth of Titan Tholins

The content of this Chapter is to be submitted for publication

Abstract

Titan is Saturns largest satellite. This object is unique in the solar system as it hosts a dense atmosphere (Kuiper, 1944) mainly made of molecular nitrogen N_2 and methane CH_4, with a surface pressure of 1.5 bar. The nitrogen-rich atmosphere and the presence of liquid areas on the surface make it one of the most interesting nearby objects to understand the evolution of the primitive Earth before the emergence of life and to look for habitable environments in the solar system. The Cassini-Huygens Mission probed Titan from 2005 to 2017. It has revealed an intense atmospheric photochemistry initiated by the photo-dissociation and ionization of N_2 and CH_4 (Waite et al., 2007). Photochemistry on Titan leads to the formation of solid organic aerosols responsible for a smog permanently surrounding the moon (Waite et al., 2007). In the upper atmosphere, Cassini detected signatures compatible with the presence of heavily charged molecules which are precursors for the solid core of the aerosols (Cravens et al., 2006; Crary et al., 2009; Wellbrock et al., 2013). These observations indicate that ion chemistry plays an important role in the aerosol organic growth. However, the processes coupling ion chemistry and aerosol production are mostly still unknown. In this study, we investigate the cation chemistry, responsible for an efficient organic growth that we observe in Titan's upper atmosphere, simulated using the PAMPRE plasma reactor (Szopa et al., 2006). These are our first cation results using the PAMPRE experiment. Positive ions are investigated by in situ ion mass spectrometry in a dusty cold plasma, alongside neutral products additionally studied through infrared absorption spectroscopy and mass spectrometry (Dubois et al., 2019).

4.1 Introduction

Titan is Saturns largest satellite. This object is unique in the solar system as it hosts a dense atmosphere (Kuiper, 1944) mainly made up of molecular nitrogen N_2 and methane CH_4, with a surface pressure of 1.5 bar. Early seminal studies (Khare and Sagan, 1973; Sagan, 1973; Hanel et al., 1981) showed how Titans reducing atmosphere is also composed of complex and heavy organic molecules and aerosols. Their laboratory analogous counterparts were coined *tholins*. This chemistry is initiated at high altitudes and participates in the formation of solid organic particles (Khare et al., 1981; Waite et al., 2007; Hörst, 2017). At these altitudes, the atmosphere is under the influence of energy deposition such as solar ultraviolet (UV) radiation, solar X-rays, Saturns magnetospheric energetic electrons and solar wind (Krasnopolsky, 2009; Sittler et al., 2009).

In Titan's upper atmosphere, Cassini's Ion and Neutral Mass Spectrometer (INMS) detected neutral and positive ion signatures (Waite et al., 2007). Subsequently, the Cassini Plasma Spectrometer electron spectrometer (CAPS-ELS) unveiled the existence of negative ion-molecules well over the detection range of INMS ($> 100\ amu$) consistent with the presence of heavy molecules (over 10,000 Da. in mass) which are presumably precursors for the solid core of the aerosols Coates et al., 2007; Desai et al., 2017. Furthermore, Lavvas et al. (2013) modeled the photochemistry and microphysics in the ionosphere, characterizing the interaction between the aerosols charged particles. They showed the dusty nature of the ionosphere, and found that the aerosol growth in the ionosphere, notably below 1000 km, occurs as negatively-charged particles collide with background positive ions. This in turn, leads to a rapid and important growth in mass (e.g. ∼500 Da at 1000 km). Ion-molecule reactions are thought to produce most of the positive ions present in Titan's ionosphere, and are thus controlled by the two initial neutral constituents, N_2 and CH_4. The direct ionization of N_2 and CH_4, and formation of the N^+ and N_2^+ primary ions set the basis for CH_3^+ and is predicted to participate in the production of the first light hydrocarbons, such as in Reaction 12. The ionization peaks at the ionospheric peak, about 1150 km. Ip, 1990 determined, using the Chapman layer theory, this electron density peak to be at an altitude of 1200 km, while Keller, Cravens, and Gan, 1992 found it at an altitude of 1175 km. Later, Fox and Yelle, 1997 predicted it to be at 1040 km with a solar zenith angle of 60°. They also predicted that H_2CN^+ would be the major ion, which included a model with over 60 species and 600 reactions. Keller, Anicich, and Cravens, 1998, with an improved model, estimated the major m/z 28 peak to consist of $HCNH^+$ at 75%. Some other major ions species include CH_5^+, $C_3H_3^+$ and $C_3H_5^+$. Based on Yung, Allen, and Pinto, 1984 and Toublanc, Parisot P., and McKay, 1995, Keller, Anicich, and Cravens, 1998 predicted higher masses than previous models, to be detected by Cassini, of up to C_6 species in the ionospheric peak region.

$$CH_3{}^+ + CH_4 \longrightarrow C_2H_5{}^+ + H_2 \tag*{\{12\}}$$

Since the Cassini era, extended models based on Keller, Anicich, and Cravens, 1998 have been used to predict ion densities and population, and construct a more cohesive view on neutral-ion interactions in Titan's ionosphere. Photochemical models (e.g. **Vuitton2008FormationTitan**; Keller, Cravens, and Gan, 1992; Keller, Anicich, and Cravens, 1998; Vuitton, Yelle, and McEwan, 2007; Carrasco et al., 2008) have provided insight on the chemical species involved in ion-molecule, proton transfer or ionization reactions to produce positive ions. In recent years, e.g. Ågren et al., 2009; Shebanits et al., 2013; Shebanits et al., 2017 have explored electron number densities with Solar Zenith Angle (SZA) dependencies and dayside/nightside ion charge densities with EUV flux correlations. The latter findings have shown how the positive ion and dust grain charge densities are, in addition, diurnally sensitive to EUV fluctuations, impacting ion density distributions.

Furthermore, the gas-to-solid conversion at these high altitudes coexists in a fully coupled ionic and neutral chemistry. However, the processes coupling ion and neutral chemistry and aerosol production are mostly unknown at the moment. Experimental simulations, as well as ground-based observations, should help in characterizing some of these cations.
Based on previous INMS observations and models, predictions of positive ion species have been made. Using laboratory simulations with different gas mixtures, it is possible to influence the chemistry and thus constrain species. In this way, laboratory results can for example, provide potential new species, rule out some, or probe higher masses with a higher resolution that were out of reach for the Cassini instruments, while improving chemical pathways. Detecting these ions (positive or negative) in Titan-like conditions remains challenging. Sciamma-O'Brien, Ricketts, and Salama (2014) used Time-of-Flight mass spectrometry to study neutrals and ions produced in a pulsed plasma jet expansion at low temperatures ($\sim$ 150 K). In such an apparatus, the ions are not fragmented by any kind of internal ionization. In this study, the authors focused on the first chemical stages before tholin production, by studying simple binary gas mixtures to more complex ones with light hydrocarbons and PAHs. Such real-time measurements are made possible by applying a negative polarization of the aperture, thus directly extracting said ions from the first chemical steps of the expanding plasma. With comparisons to CAPS-IBS data, they suggested for example that some of the ions of larger masses (>100 m/z) could be aromatic compounds.

In the present study, we use PAMPRE for the first time in a similar way, by measuring the ions directly inside a RF-CC plasma discharge (Figure 4.1). We used different N_2-CH_4 initial gas mixtures ranging from 1% to 10% CH_4, and investigate their energy distributions. Finally, we will compare our experimental results with INMS observations. The complexity of the aerosol material is already foreshadowed by the intricacies of the gas phase chemistry, acting as a precursor to the aerosol formation. Hence, the ion chemistry remains an open question for the characterization of the gas phase and chemical pathways leading to the formation of aerosols.

4.2 Experimental

We use the cold dusty plasma reactor PAMPRE (Szopa et al., 2006) and figure 4.1 to simulate Titan ionosphere conditions at different initial CH_4 conditions. A newly acquired ion mass spectrometer was fitted to the existing chamber, in order to detect the ions directly within the plasma *in situ*. Different experimental conditions were tested and are detailed hereafter. The plasma chamber and mass spectrometry techniques are presented in the following sections, respectively.

4.2.1 The PAMPRE cold plasma experiment

The PAMPRE dusty plasma reactor delivers electrons with a mean energy distribution comparable to that of the solar spectrum (Szopa et al., 2006; Cable et al., 2012). The plasma discharge is delivered through a radiofrequency (13.56 MHz) generator. N_2-CH_4 gas influx is monitored with mass flow controllers at 55 sccm in standard conditions, tuned from CH_4 mixing ratios from 1% to 10%. Nearly pure ($> 99.999\%$) bottles of N_2 and N_2-CH_4 were used. Plasma power is kept constant throughout the experiment at 30W, with a gas pressure of 0.9 mbar.

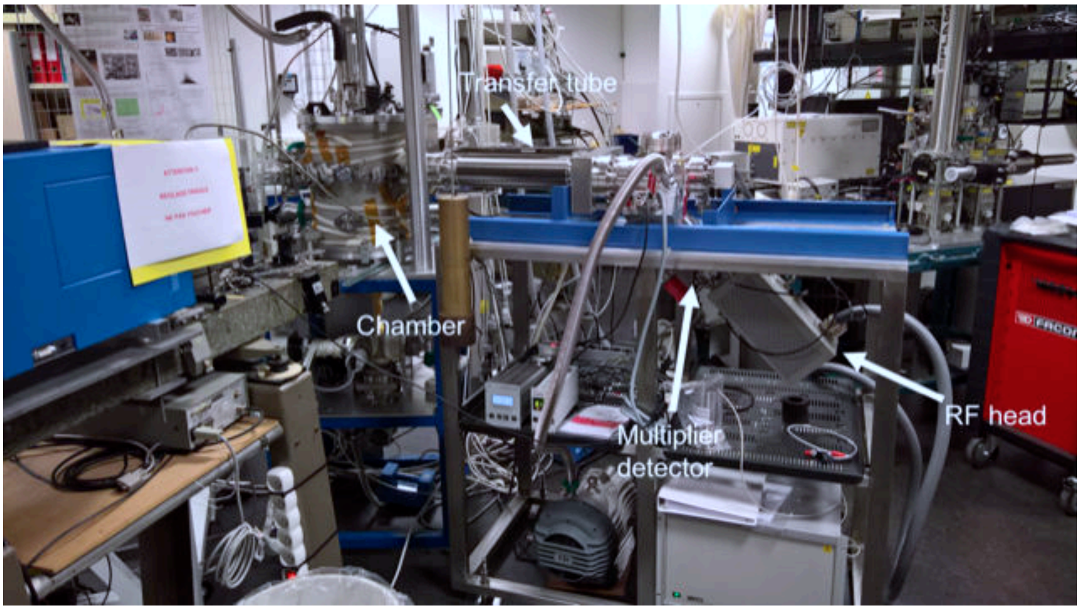

FIGURE 4.1: The PAMPRE cold plasma chamber, along with its suite of instruments. In particular, the ion and neutral mass spectrometer is visible to the right of the chamber. The chamber and mass spectrometer are separated by a VAT valve, enabling a residual gas pressure within the transfer tube of 10^{-9} mbar. The residual pressure in the PAMPRE chamber is 10^{-6} mbar.

The anode (reference of figure from Methodology chapter) can be configured in two different ways: with cage or cage-free. Previous studies using this reactor have analyzed the plasma parameters with a fitted cage (e.g. **Wattieaux2015TransientPlasma**). Without this cage, the plasma operates between the polarized electrode and a grounded plate at the bottom of the reactor, 10cm away from each other (Figure 4.2). The advantage of this method, as part of this study, is to probe the ions in an expanding plasma and not in a confined one. In the latter case and with a grounded cage electrode, the plasma, and especially the tholins, are focused through the cage's orifices and directly reach the spectrometer aperture, thus causing obstruction. This is something that we wanted to avoid, and operating cage-free prevents this aperture obstruction and enables us to acquire scans for longer periods of time.

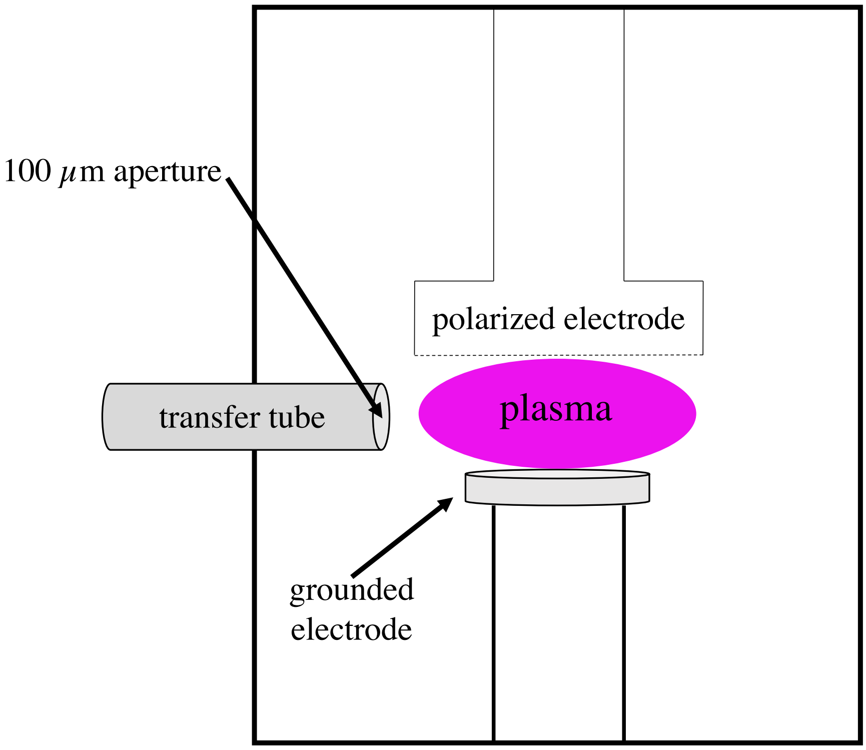

FIGURE 4.2: Schematic diagram of the two electrodes creating the plasma discharge, with the extractor head of the EQP extracting the ions from the plasma.

4.2.2 Coupled neutral and cation mass spectrometry

A new mass spectrometer has been fitted to the PAMPRE chamber. This spectrometer is a Hiden Analytical EQP 200, coupled with a Pfeiffer turbo pump. Its mass range goes up to 200 amu. The turbo pump enables us to reach secondary vacuums of 10^{-9} mbar inside the chamber, and 4×10^{-5} mbar during ion extraction. Different extraction holes can be fitted to the extractor, according to the pressure in the reactor. A gate valve was inserted between the chamber and the spectrometer to enable the 10^{-9} mbar vacuum inside the spectrometer. Thus, we make sure the CO_2 and H_2O contaminations are as low as possible. Furthermore, an accumulation of tholins within the instrument is possible over time. This is why keeping the extractor as clean as possible by keeping it isolated from the rest and either in an O_2 plasma or ultrasound bath, or both, is necessary before and after an experiment.

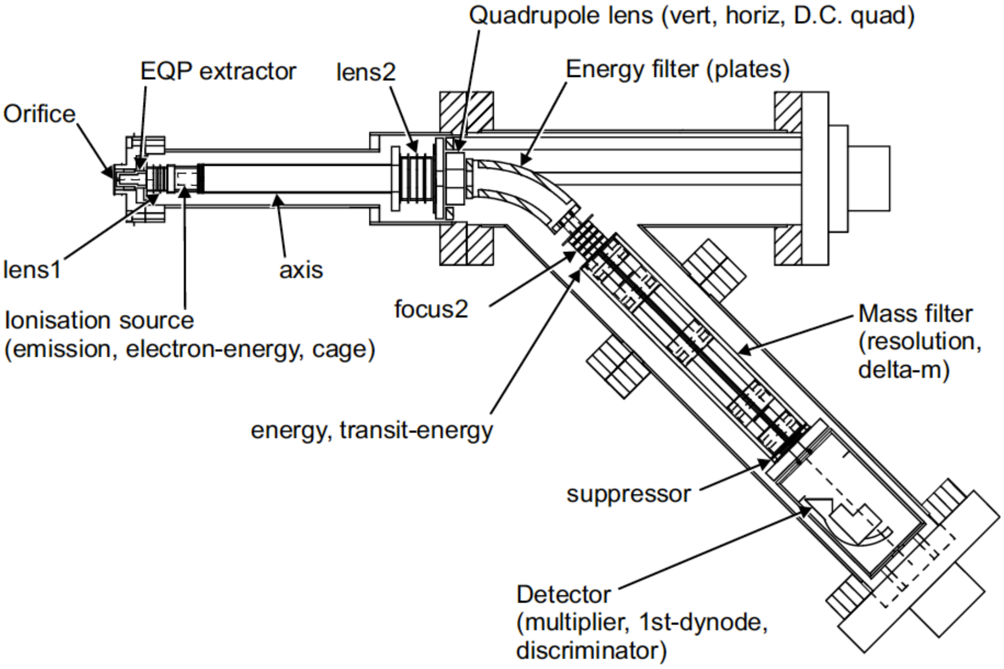

FIGURE 4.3: Diagram of the EQP by Hiden Analytics. The ions are extracted from the plasma by the transfer tube on the left-hand side. The extractor's floating potential enables the extraction of the positive ions. Then, the ions are guided by a series of lenses until they hit the multiple detector. We set the multiplier to 1800 V. The RF head analyzes the impacted particles and sends the counts to a computer.

A mass resolution $\Delta M = 0.1$ is used throughout the entire mass range for all experiments. The ion extractor comes in contact with the plasma, measures its composition, and then retracts (Figures 4.2 and 4.3). This proved to be efficient enough to have high counts detection ($\sim 10^6$c/s), without disrupting the plasma. The detection itself uses a count-per-second method, over an integration period called hereafter, *dwell time*. The dwell time is user-defined, and set to 100 ms. Once enough signal has been accumulated, the measurement starts. With a mass resolution of 0.1 at a dwelling time of 100 ms over a 100 amu range, a scan typically takes $0.1 \times 10 \times 100 = 100$ s/scan. Any signal $\leqslant$ 10 c/s corresponds to instrumental and electrical background noise. Limiting air and water contamination in the plasma and spectrometer chambers is essential in avoiding over-interpreting spectra (e.g. masses 18 and 32). A motorized Z-drive is mounted to the skimmer, giving a 300 mm stroke in order to approach the plasma closely ($< 2cm$) and measure the ion composition. This Z-drive system consists of a coil-shaped structure enclosing the transfer tube and is prone to water condensation in the interstice of each spiral. To minimize water contamination as much as possible, we bake the transfer tube enclosure before each experiment to 110°C until we reach a limited water signal (< 800 c/s). Once the extractor has been inserted into the plasma, a single ion measurement is completed, satisfying both mass range detection and ion count intensity. The intensity limit for this instrument is $\sim 10^7 c/s$. The multiplier potential is set at 1900 V. Within the transfer tube, in positive ion mode, two guiding lenses are set at -19 V and -102 V, respectively.

Table 4.1 lists all the intrinsic parameters, pertaining to the spectrometer's optics, used for our positive ion measurements. The different components can be seen in more detail in Figure 4.3. The detector part consists of the multiplier (Figure 4.3). It is connected with (i) the *1st dynode* which sets the voltage on the front of the detector and (ii) the *discriminator* setting a threshold on the pulse output of the multiplier. The multiplier potential is set to 1800 V. The Extraction group controls the gating system (for more details, the reader is referred to Chapter 2). This gating is only switched on and operational if the RF head is connected to a transistor-transistor logic (TTL) system. This is not the case here. The only relevant varying parameters here are the *lens1* and *extractor* potentials. The latter has a negative value for positive ion extraction. As we will see in Section 4.2.3, the *energy* variable part of the Sector component determines the energy filtering which will be fine-tuned for each gas mixture.

TABLE 4.1: Global Environment Editor example for a given positive ion mass spectrum acquisition using the MASoft Hiden Analytics software. The Group column corresponds to the different components of the Electrostatic Quadrupole Plasma system, as shown in Figure 4.3. The second column represents all of the tunable variables, and their respective values, either fixed after a tune, or changed by the user.

Group	Name	Value	Units
Detector	1st dynode	-3500	V
	discriminator	-10	%
	multiplier	1800	V
Extraction	extractor	-191	V
	gate delay	0.1	μS
	gate width	0.0	μS
	lens 1	-19	V
Flight-focus	flight-focus	-69	V
Quad	delta-m	0	%
	focus2	-176	V
	resolution	0	%
	suppressor	-200	V
	transit-energy	0.0	V
Sector	D.C. quad	22	%
	axis	-40.0	V
	energy	2.2	V
	horiz	-5	%
	lens2	-102	V
	plates	7.4	V
	vert	-20	%
Source	cage	0.0	V
	electron-energy	70.0	V
	emission	100.0	μA
Other	CRV-range	7	c/s
	CRV-resolution	6	bits
	gating	0	(1=on, 0=off)
	gating-invert	0	(0=normal, 1=invert)
	mass	28.0	amu
	mode-change	1000	ms

4.2.3 Ion Energy Profiles

Ion energy studies in plasma discharges have previously shown their variability. Field et al., 1991 first reported on the energy profile of certain ions (e.g. O_2^+) derived from theoretical calculations compared with experimental results, in a radio-frequency plasma discharge. Further studies examined the role of plasma rf sheaths and pressure-dependence on ion energy distributions (Gudmundsson, Kimura, and Lieberman, 1999; Kawamura, 1999; Wang and Olthoff, 1999).

In this setup, it is possible to measure and quantify the Energy Distribution (ED) at the energy filtering plate, for specific masses in different plasma conditions. The *energy* parameter from the Sector group (Table 4.1) corresponds to the energy filter (plates) of Figure 4.3 and controls the energy of the ions which are mass analyzed by the Quadrupole Mass Spectrometer (QMS) detector later. As stated in the previous section (4.2.2), different ions may have different kinetic energies during detection by INMS. This variation may be due to atmospheric composition, plasma flow composition, spacecraft velocity, (Waite et al., 2004b; Lavvas et al., 2013).

In our experiments, the main fluctuating parameter is the N_2-CH_4 mixing ratio. So, cation mass spectra were taken with a default energy value (14.05 V) set by the CPU, in all mixing ratios. These results are presented in the following section (4.3). At first, we had not expected the IEDs (Ion Energy Distributions) to vary with different mixing ratios. It turned out that the IED was very gas composition-dependent, with variations in ion energies from 0.6 V to 1 or 2 V, as detailed in the following sections. For reference, energy scans were also taken in pure N_2 and O_2 plasmas.

4.2.4 Protocol

As stated previously, the analysis of cations requires that (i) the spectrometer not be obstructed by incoming tholins to provide accurate intensity measurements and not interfere with the optics potentials in the transfer tube, and (ii) the mass analysis be optimized to the corresponding energy distribution of the highest mass (m/z 28); the latter being significant in most methane mixing ratios. A set of two to four experiments are performed for each mixing ratio chosen. Every other experiment, we "calibrate" our measurement by doing an O_2 plasma at given plasma parameters and at a certain distance from the plasma. This critical step assures us that the extractor was not obstructed by tholins, by setting a reference intensity value at m/z 32 ($O_2{}^+$). If the intensity of the latter mass has not decreased from one mixing ratio to another, this means tholins have not accumulated on the extractor. Thus, measurements from one experiment to the next are reliable. This is an important step not to overlook, given how easy and fast it is to produce tholins (Sciamma-OBrien et al., 2010).

4.2.5 Oxygen reference spectra

The purpose of taking oxygen spectra is twofold: an oxygen plasma cleans the chamber from any impurity in the reactor (water, dust particles) and serves as a reference point method from one methane condition to the other. We are then able to determine if the entrance orifice has been covered with tholins, especially in the conditions favorable for tholin production. If reference intensities are reached (Figure 4.5), the orifice is clean, and the measurement will not be perturbed by previously accumulated tholins. In the same way as previous mass spectra were taken, we first measure the IED in an O_2 discharge (Figure 4.4), on m/z 32, O_2^+. The Maxwellian energy distribution peaks at 0.6 V. The corresponding mass spectrum (Figure 4.5), mainly shows the presence of the O_2^+, NO^+ and to a lesser extent, O^+, at m/z 32, 30 and 16, respectively. The small presence (10^2 c/s) of nitronium NO_2^+ at m/z 46 may owe to a residual air contribution in the reactor. In this study, our reference value is $\sim 10^5$ c/s (Figure 4.5).

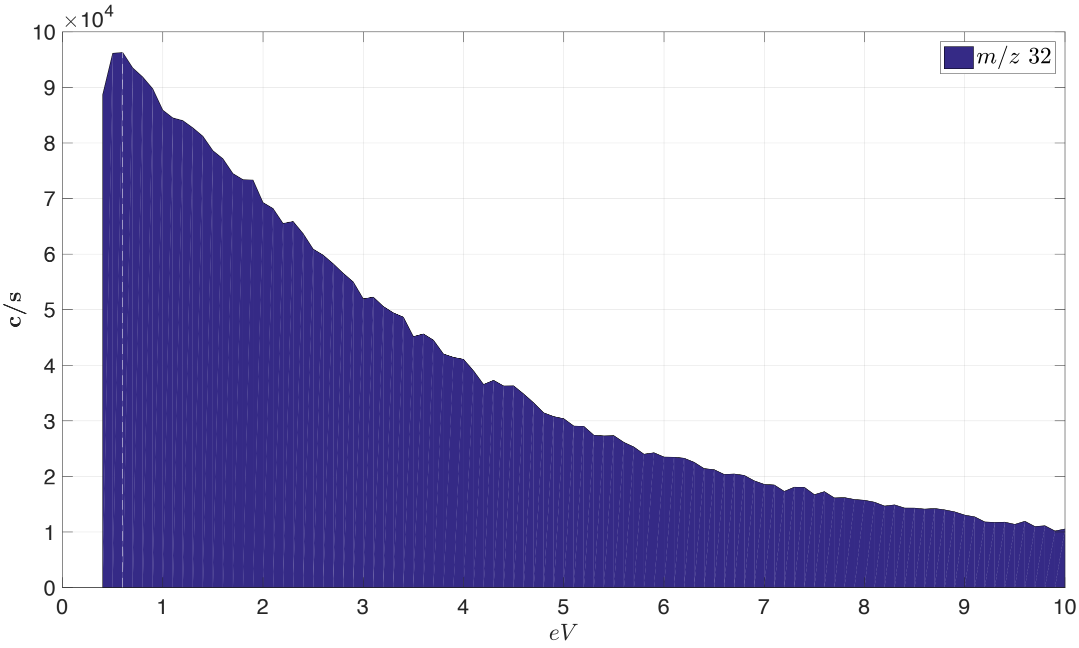

FIGURE 4.4: IED of m/z 32 in an O_2 plasma discharge. The vertical white dashed line indicates the energy peak for this ion, i.e. 0.6 V. This is the value that will be subsequently used hereafter.

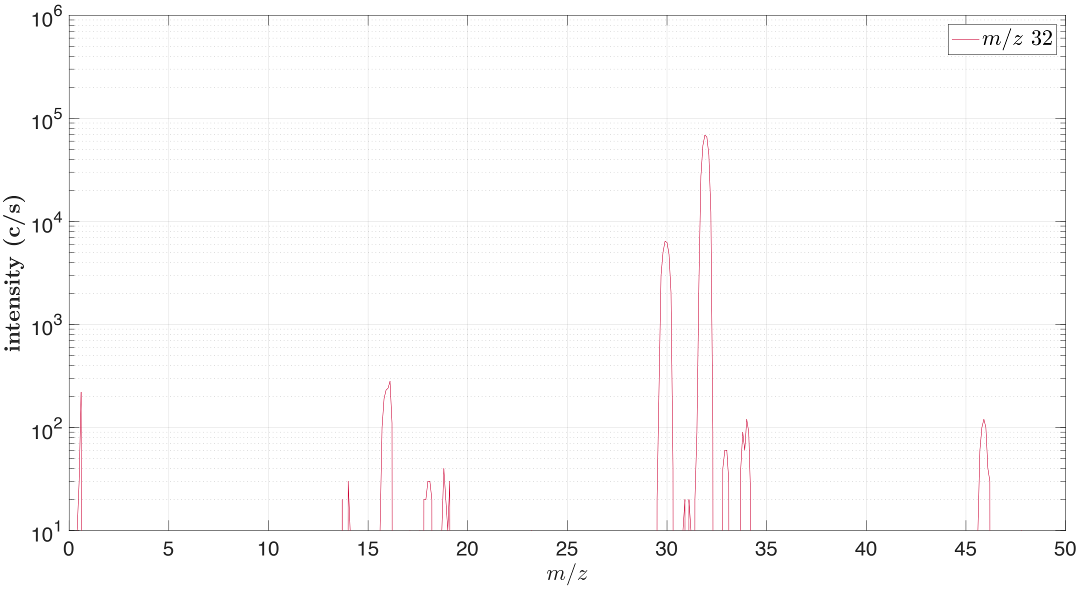

FIGURE 4.5: Mass spectra in an O_2 plasma discharge, with the positive ion energy filter set at 0.6 V.

4.3 Results

We present the positive ion mass spectra obtained in conditions ranging from $[CH_4]_0$ = 1% to $[CH_4]_0$ = 10% covering Titan methane conditions and staying consistent with previous studies (Sciamma-OBrien et al., 2010; Dubois et al., 2019). Firstly, three $[CH_4]_0$ conditions are presented, showing the diversity in ion population. Then, we show the disparity in ion energy distribution which is a crucial step to enabling measurements of energetic and heavy ions.

4.3.1 First mass measurements at $[CH_4]_0$ = 1%, $[CH_4]_0$ = 5% and $[CH_4]_0$ = 10% with the energy filter set to 14.05 V

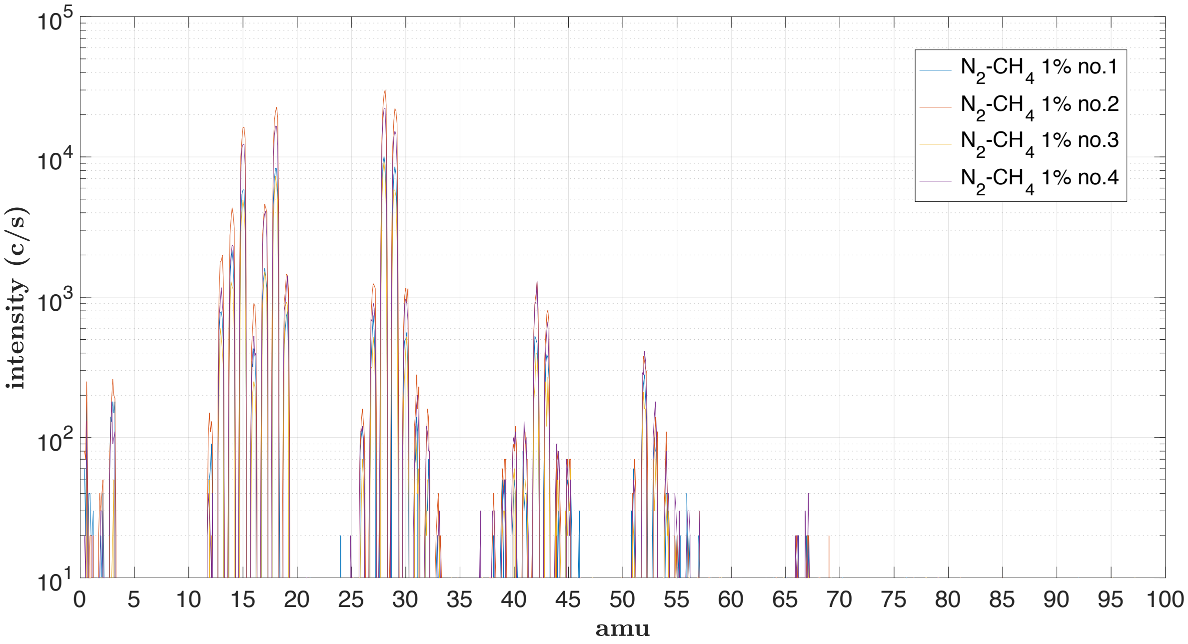

FIGURE 4.6: Mass spectra for $[N_2-CH_4]_0 = 1\%$ with m/z < 100. Four spectra are plotted, which overall, show similar ion distributions.

Figure 4.6 shows a series of four mass spectra taken in a $[N_2-CH_4]_0 = 1\%$ plasma mixing ratio. The C_2 block is dominant, with a mass peak at m/z 28. The C_1 block shows two main species dominating this block, m/z 15 and m/z 18. The intensity slope decreases abruptly, as the C_3 and C_4 block almost lose an order of magnitude. The main peaks of the C_3 and C_4 groups are m/z 42 and m/z 52, respectively. Above m/z 55, the scarce signal is lost in the noise.

For $[N_2-CH_4]_0 = 5\%$ (Figure 4.7), the detection is similar in intensity ($\sim 10^4 c/s$) and mass (m/z 55). However, we notice a peak inversion in the C_1 block: m/z 15 becomes the main product, whereas m/z 18 becomes the second most abundant ion. In the C_3 block, m/z 42 gains an order of magnitude.

A surprising observation was in the case of $[N_2-CH_4]_0 = 10\%$. Indeed, multiple measurements showed an almost entire depletion of ions, with maximum intensities of $10^3 c/s$.

The source of this confusion was more subtle, located within the instrument.

The ion extraction operates according to the way the potentials within the instrument are set prior to the measurement. The energy filter (Figure 4.3) controls the entire measurement line in that it selectively filters the ions. Thus, it is necessary to know what the ion energy distribution (IED) looks like for a given mixing ratio. A known IED can then be used to tune the QMS for a future measurement in order to detect the ions of interest. In the three cases of $[N_2{-}CH_4]_0 = 1\%$, $[N_2{-}CH_4]_0 = 5\%$ $[N_2{-}CH_4]_0 = 10\%$, the energy filter was set to 14.05 V by default, which, as we will see in Section 4.3.2, was not appropriate for our energy distributions.

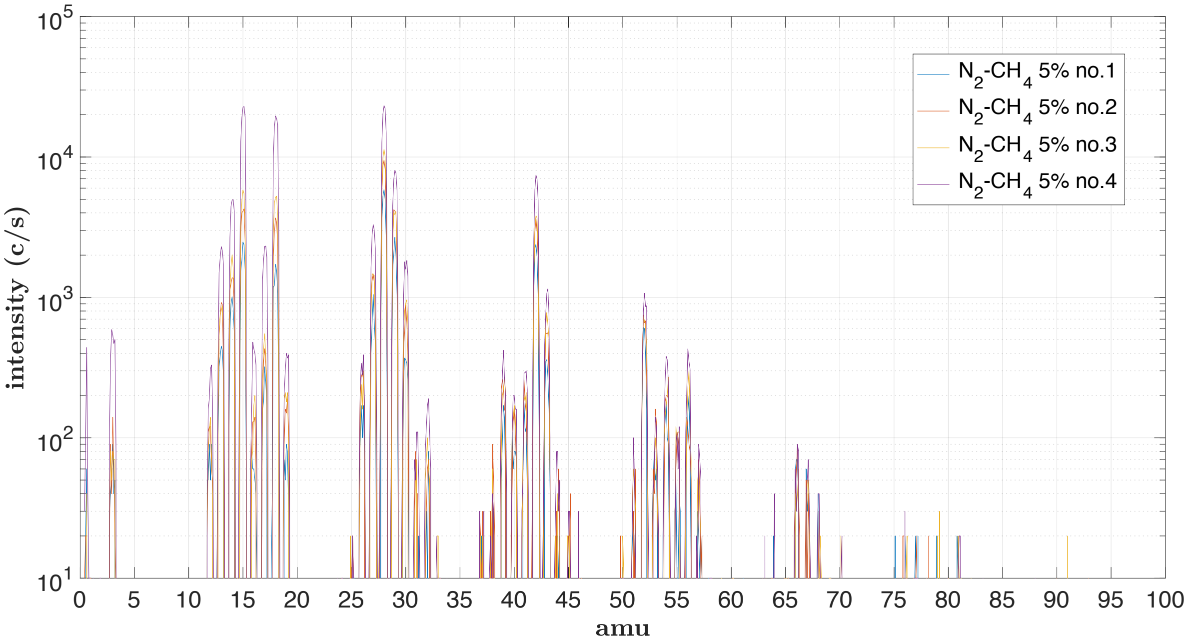

FIGURE 4.7: Mass spectra for $[N_2{-}CH_4]_0 = 5\%$ with m/z < 100.

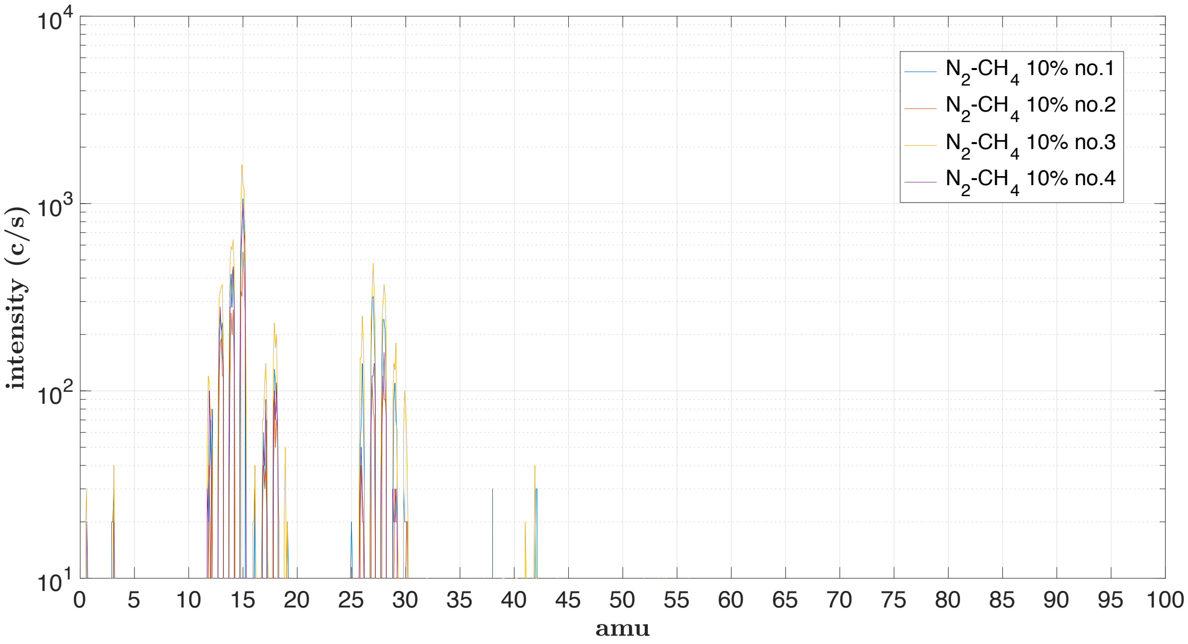

FIGURE 4.8: Mass spectra for $[N_2{-}CH_4]_0 = 10\%$ with m/z < 100.

The three above figures show spectra taken with the energy filter (Table 4.1) set to 14.05 V. We chose this factory set value, which, retrospectively, (i) is high for non-thermalized ions and (ii) is in the tail of the Maxwellian distribution (see following section). Furthermore, Wattieaux et al., 2015 showed how the electron density in our plasma remained relatively constant from 1% to 10% CH_4 (on the order of 10^{15} m^{-3}. Therefore, there should be a charge balance between the electrons and the positive ions, and both should remain in relatively same proportions throughout, whether at 1% or at 10% CH_4. An explanation for the absence of heavy ions at 10% CH_4 might be related to their energies. An ion energy distribution investigation is therefore crucial to better characterize the mass analysis of future spectra, regardless of gas mixture composition.

4.3.2 Energy Filter Distributions of selected species

The energy filter (Figure 4.3) scans the entirety of available potentials (< 100 V) for selected masses. This parameter represents the potential applied to the energy filter plate, between the *focus2* lens and the QMS. Consequently, one can obtain fairly reproducible energy distributions for different ions which are part of the same gas mixture and at the same pressure. Hence it is possible to get such a distribution for any given plasma discharge condition. To get a good estimate of these EDs and to make sure the energy distributions for specific ions are representative of the entire plasma, we chose six different ions: m/z 14, 16, 17, 18, 28 and 29, which are expected to be detected in our plasma. Figure 4.9 shows the measured EDs. They all show similar energy distributions, while the last two, m/z 28 and m/z 29 being major products, are likely the most representative given their high count intensities. Nonetheless, these EDs are consistent in their distribution for one given condition, as well as for ions of different masses. The distribution for m/z 14 is affected by low intensity counts, but all other five have Maxwellian distributions, centered at 2.2 V for 1% CH_4, 2.2 V for 5% CH_4 and 1.2 V for 10% CH_4 (Table 4.2). Figure 4.11 shows the IED for $[CH_4]_0$=1%, 5% and 10%. The EDs at 5% and 10% CH_4 are shown in the Appendix of this chapter. Figure 4.10 is a zoom at the maximum, which we found to be at 2.2 V at 1% CH_4. This value will be hereafter used in all $[N_2{-}CH_4]_0 = 1\%$ conditions. EDs can sometimes be bi-modal, as can be slightly seen for m/z 17. This bi-modal distribution could be an instrumental artifact (lens coating, re-acceleration of ions in the skimmer) or attributed to plasma sheath effects (**Kawamura1999**).

Figure 4.10 shows the superimposed EDs for m/z 28 in all conditions. The tail of the Maxwellian starts decreasing by orders of magnitude at $\approx$ 8 V, with peaks [1-3 V]. The decrease is especially significant for 10% CH_4. At 14 V, the energy initially used, the intensities are very low ($< 10^2\ c/s$), while they gain almost two orders of magnitude at 1.2 V. This shows how the earlier setting was inappropriate for these measurements. Thus, many of the ions, notably the heavier ones, were not being collected due to their inefficient energy filtering. In addition, as can be seen in Figure 4.10 and Table 4.2, the ion energy varies slightly, from 1.2 V to 2.2 V in our three gas mixtures, indicating different ion species in the plasma.

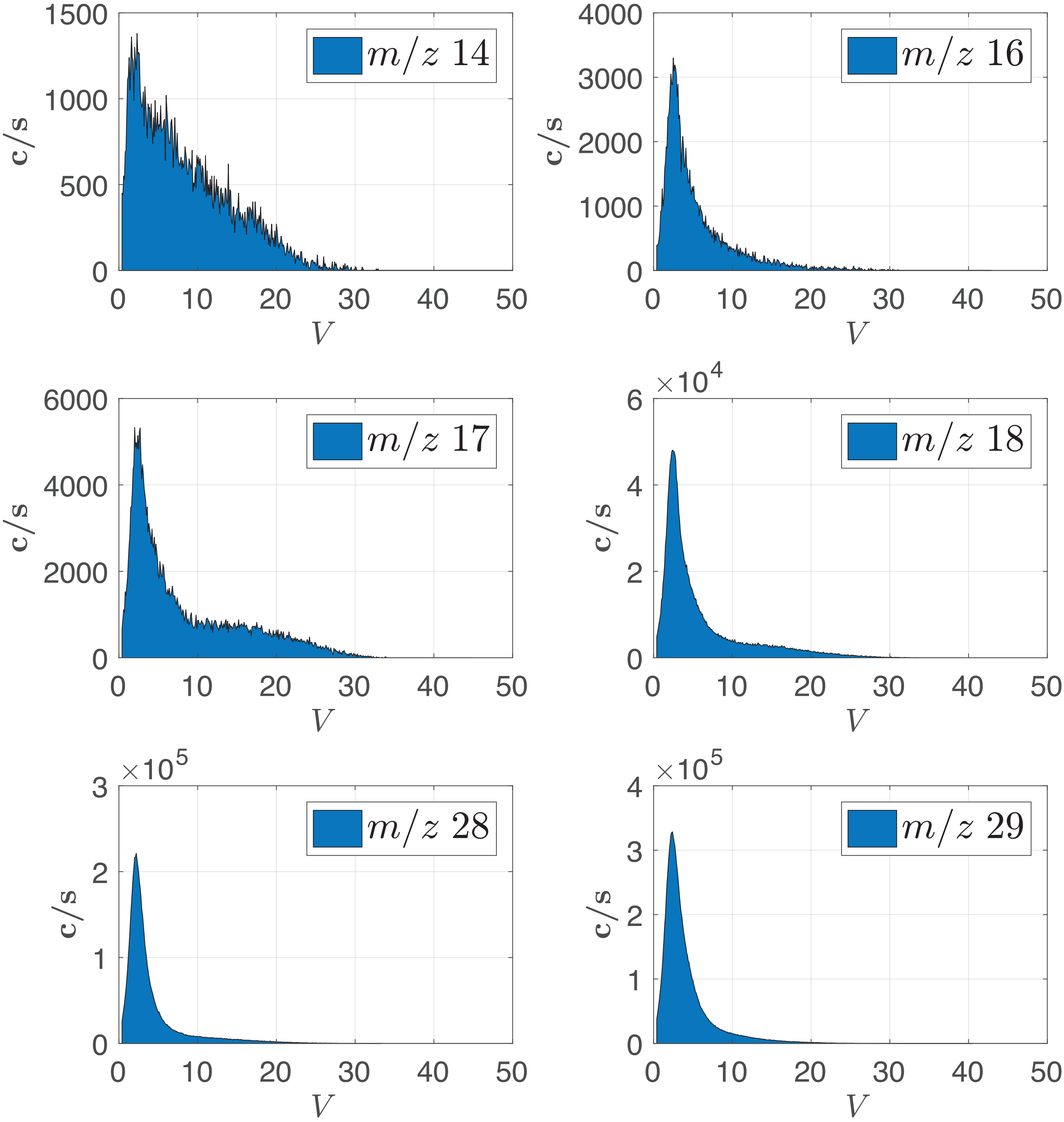

FIGURE 4.9: IEDs in an $[N_2{-}CH_4]_0 = 1\%$ mixing ratio for selected ions m/z 14, 16, 17, 18, 28 and 29.

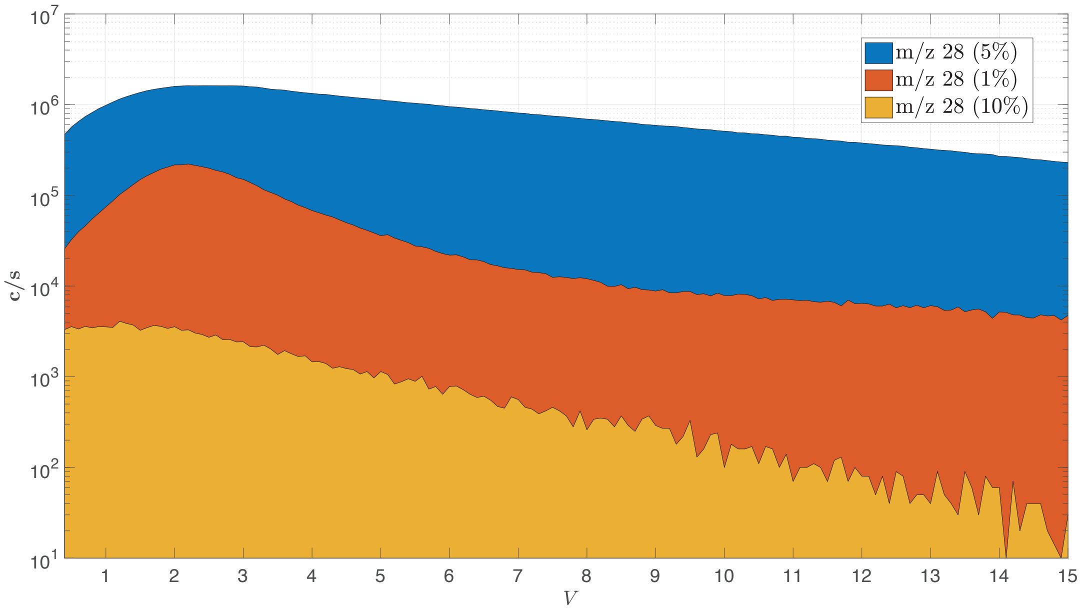

FIGURE 4.10: IED comparisons for the m/z 28 ion in the $[N_2{-}CH_4]_0 = 1\%$, $[N_2{-}CH_4]_0 = 5\%$ and $[N_2{-}CH_4]_0 = 10\%$ mixing ratios.

The discrepancy between Figure 4.11 and Figure 4.6 is noticeable. The overall intensities increased by an order of magnitude, and we can even see some peak inversions. For example, m/z 29 is now the most intense peak (> 10^5 c/s), with m/z 28 and m/z 18 in decreasing order. However, the relative proportions among the C_3 and C_4 ions have not been modified. This shows how the tuning of the energy filter prior to a scan is essential in order to detect as many ions and as efficiently as possible.

TABLE 4.2: Energy distribution maxima for $[CH_4]_0$=1%, 5% and 10%.

$[CH_4]_0$ (%)	energy (V)
1	2.2
5	2.2
10	1.2

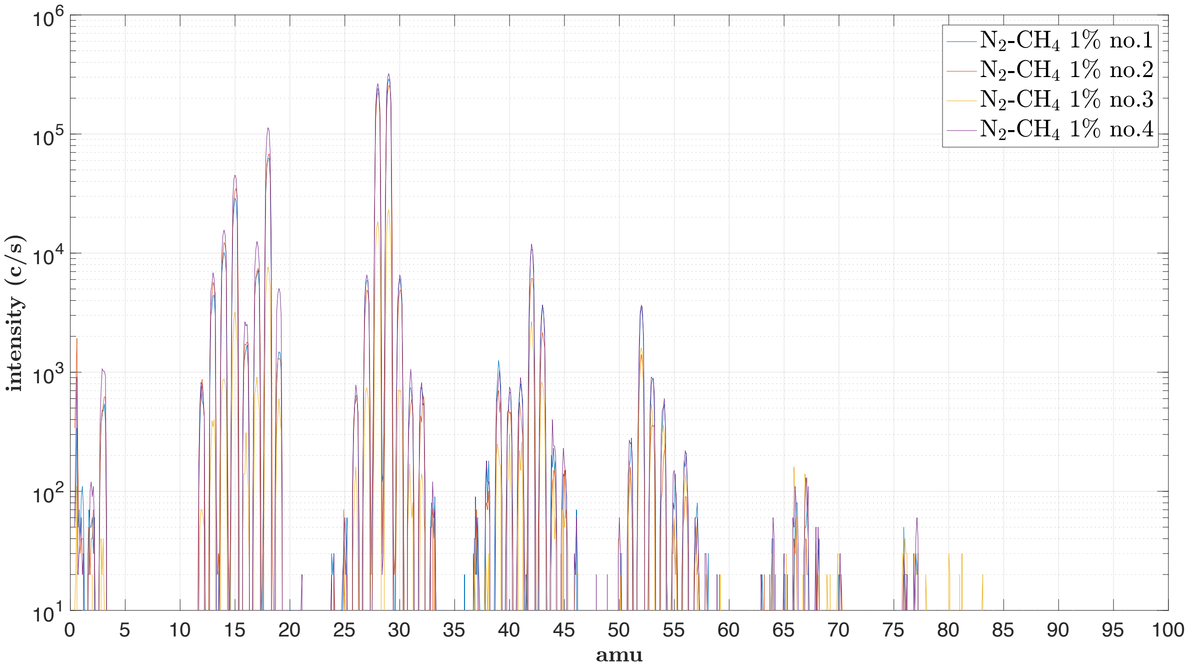

FIGURE 4.11: Mass spectra for a $[N_2-CH_4]_0 = 1\%$ mixing ratio, with the positive ion energy filter set at 2.2 eV, i.e. the maximum energy for m/z 28 (see Figure 4.10)

The same measurements were applied to $[N_2-CH_4]_0 = 10\%$. The differences between Figure 4.12 and Figure 4.8 are striking. The intensity of the highest peak (m/z 28) has increased by more than two orders of magnitude, and ions of masses m/z >30 that were previously absent are now detected. The energy optimization improved the detection of the ions. As Figure 4.10 shows, the initial 14.05 V factory value was near the end of the Maxwellian tail, and accounted for very low intensity counts. Therefore almost all of the ions were being filtered out and so unlikely to be detected by the SEM.

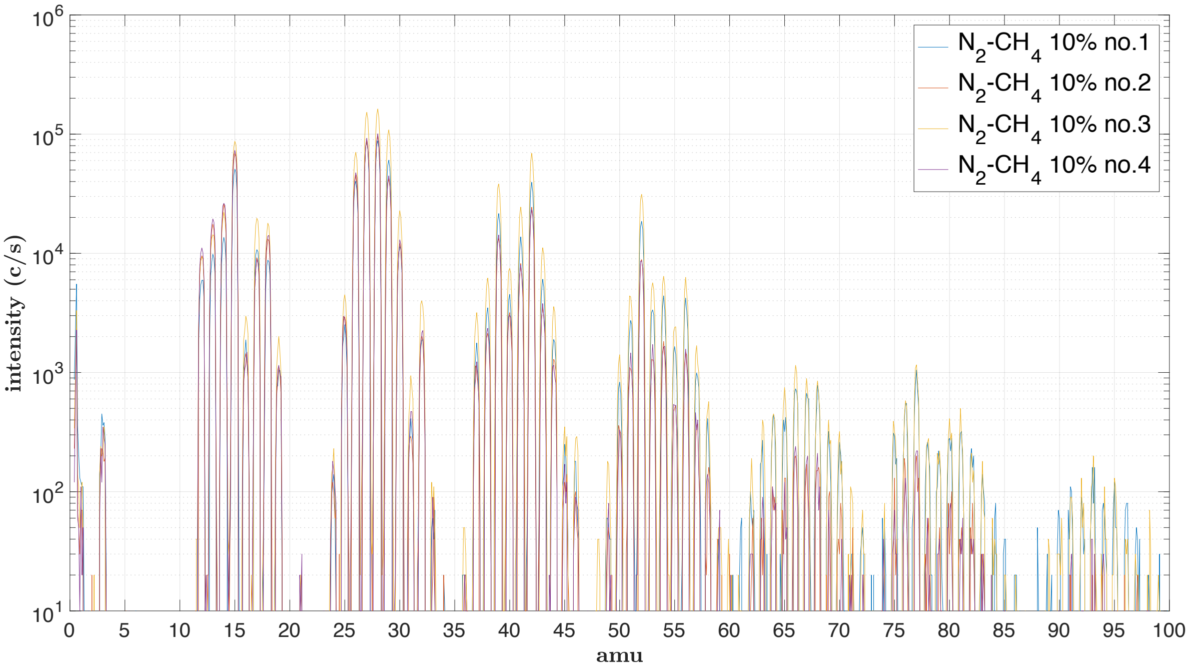

FIGURE 4.12: Mass spectra for a $[N_2{-}CH_4]_0 = 10\%$ mixing ratio, with the the positive ion energy filter set at 1.2 V, i.e. the maximum energy for m/z 28 (see Figure 4.10).

We acquired four spectra in each condition (Figures 4.11 and 4.12). We see a temporal signal variability, attributed to the potential instabilities between the extractor and the plasma. For example, the m/z 28 intensity at 10% (Figure 4.12) varies from 8.82×10^4 to 1.62×10^5 c/s, and from 8.67×10^3 to 3.12×10^4 c/s for m/z 52 (33,958 and 10,636 standard deviation, respectively). At 1% CH_4, the m/z 28 and m/z 52 intensities vary from 1.83×10^4 to 2.65×10^5 c/s, and 1.41×10^3 to 3.66×10^3 c/s, respectively (standard deviations of 186,000 and 1229). Other factors such as tholin coating on the extractor or intrinsic plasma variations may also play a role in these fluctuations. This is why we will henceforth normalize all spectra at m/z 28, and units will be expressed as arbitrary units (A.U.).

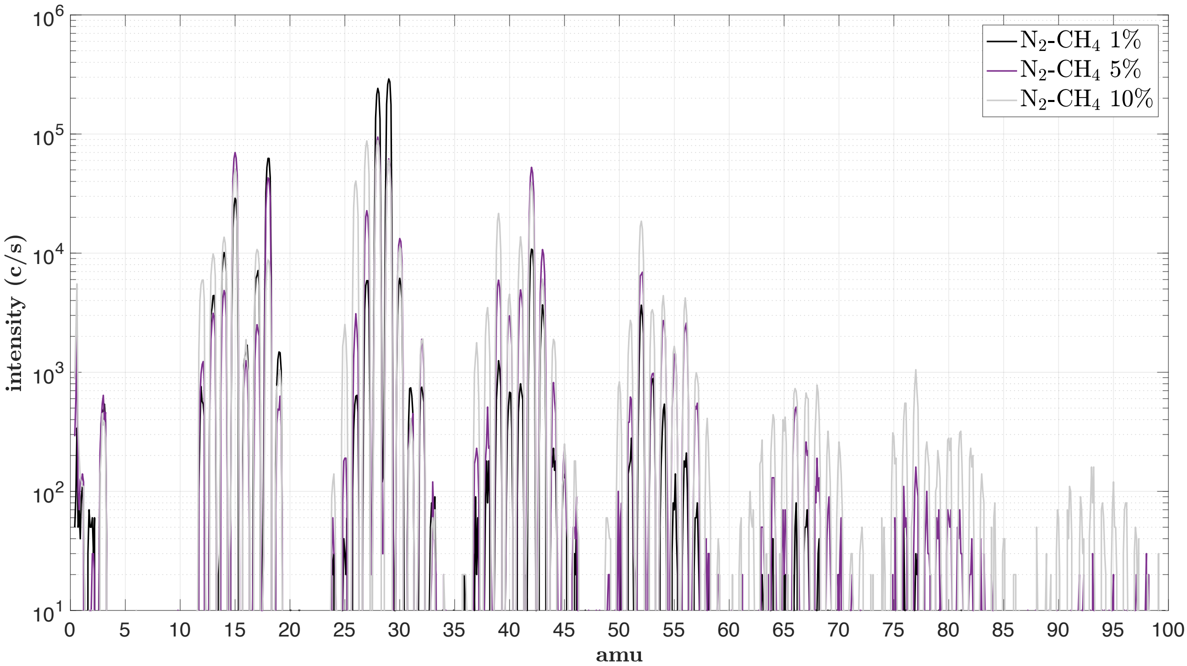

FIGURE 4.13: Mass spectra for $[N_2-CH_4]_0 = 1\%, 5\%$ and 10% mixing ratio, in black, purple and gray, respectively. The energy filter was settled at 2.2, 2.2 and 1.2 V for the experiments at 1%, 5% and 10%, respectively.

4.3.3 Ion variability

As shown previously, there is a large variability (e.g. C_7 blocks) in the spectra. Here, we tentatively assign positively charged species to the detected peaks. These assignations are listed in Table 4.3. We focus on the first four groups (< 55 amu) as it becomes speculative to attribute higher masses beyond this limit (influence of polymers, aromatics...). These group comparisons for three different initial methane mixing ratios are shown in the bar/box plots Figure 4.14 through 4.17. Plotted values correspond to mean normalized values taken from four data sets (e.g. 4.11 and 4.12). Lower and upper limits of the boxes represent the 1st and 3rd quartiles, respectively, of the minima and maxima experimental values (black whiskers), indicating the variability in intensity over four spectra. The spectra in green, black and red correspond to measurements done with 1%, 5% and 10% CH_4, respectively.

TABLE 4.3: Tentative attributions of several species from the C_1, C_2, C_3 and C_4 groups. These attributions are based on INMS observations and model-dependent calculated ion densities (Vuitton, Yelle, and McEwan, 2007). We give the different ions possible for each mass.

Group	m/z	Species
C_1	14	N^+/CH_2^+
	15	CH_3^+/NH^+
	16	CH_4^+/NH_2^+
	17	CH_5^+/NH_3^+
	18	NH_4^+
C_2	27	$C_2H_3^+/HCN^+$
	28	$HCNH^+/N_2^+/C_2H_4^+$
	29	$C_2H_5+/N_2H^+/CH_2NH^+$
	30	$CH_2NH_2^+/C_2H_6^+$
C_3	40	$HC_2NH^+/C_3H_4^+$
	41	$CH_3CN^+/C_3H_5^+$
	42	$CH_3CNH^+/N_3^+/C_3H_6^+$
	43	$C_3H_7^+/C_2H_3NH_2^+$
C_4	51	$HC_3N^+/C_4H_3^+$
	52	$HC_3NH^+/C_2N_2^+/C_4H_4^+$
	53	$C_4H_5^+/HC_2N_2^+/C_2H_3CN^+$ and m/z 52 isotopes
	54	$C_2H_3CNH^+/C_4H_6^+$

- C_1 - In Figure 4.14, the major ion detected at 5% and 10% CH_4 is m/z 15, which can be attributed to the NH^+ radical or the methyl CH_3^+ cation. Other CH_4 fragments, consistent with a CH_4 fragmentation pattern are also visible in all conditions at m/z 14 and 13, corresponding to CH_2^+ and CH^+. The N^+ fragment also contributes to m/z 14. CH_5^+ and NH_3^+ may contribute to m/z 17. There is a strong discrepancy between the 1% and 10% conditions, in particular regarding the m/z 15 and m/z 18 peak inversions. In a $[N_2{-}CH_4]_0 = 10\%$ mixing ratio, m/z 15 dominates the rest of the grouping, presumably due to the methane influence along with CH^+, $CH_2{}^+$ and $CH_3{}^+$. Carrasco et al. (2012) discussed the influence between the methyl ion with ammonia formation, and its favored production with increasing methane. Mutsukura, 2001, also using a CH_4/N_2 RF plasma albeit with much higher methane concentrations, found that the m/z 15 and m/z 18 ions were dominant in methane-rich conditions. This is confirmed by our results (Figure 4.14), showing the importance of CH_3^+ in methane-rich mixtures. However, in a nitrogen-rich plasma with a mixing ratio of $[N_2{-}CH_4]_0 = 1\%$, m/z 18 NH_4^+ becomes the most abundant ion. At 5% CH_4, m/z 18 is also important along with m/z 15.

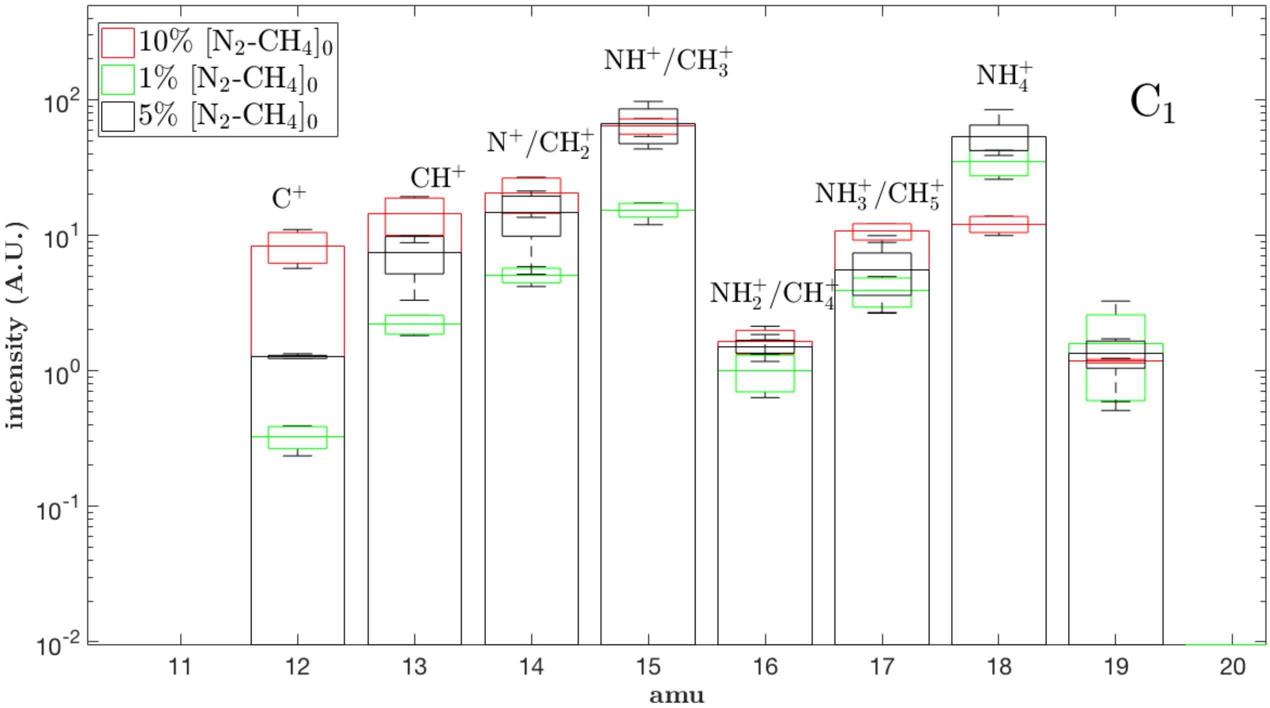

FIGURE 4.14: C_1 group in a $[N_2{-}CH_4]_0 = 1\%$ $[N_2{-}CH_4]_0 = 5\%$ and $[N_2{-}CH_4]_0 = 10\%$ mixing ratio.

- *C_2* - Figure 4.15 shows the C_2 species detected in the three conditions. This group is overall more intense than the *C_1* group. The most abundant ions are m/z 28 and 29 with intensities of $3 \times 10^1 - 10^2$ a.u. There is a strong increase in masses on the left tail of the red distribution (m/z 2427), as compared to the other two spectra. These species consistently increase well apart from the repeatability error bars with increasing methane. Presumably, these simple aliphatics such as $C_2H_2^+$ and $C_2H_3^+$ (m/z 26 and 27, respectively) increase by an order of magnitude from the black to red curve. m/z 29 is not as unambiguous, and N_2H^+ shares the same peak as $C_2H_5^+$. This peak is the most intense at 1% CH_4. As such, where m/z 28 dominates at 10%, the m/z 29 peak inversion occurs with decreasing CH_4. Therefore, N-bearing species such as N_2H^+/CH_2NH^+ are good candidates at this mass. Due to the limiting amount of CH_4 in the green spectrum, the m/z 29 ion in this condition is likely to be N_2H^+. However, with higher methane amounts, $C_2H_5{}^+$ formation prevails and becomes the dominant ion at m/z 29, as predicted by Vuitton, Yelle, and McEwan (2007). $C_2H_5{}^+$ formation partly depends on the presence of C_4H_2, indicating its presence in the plasma, as suspected by Dubois et al. (2019). $CH_2NH_2{}^+/C_2H_6{}^+$ at m/z 30 increases with higher methane concentrations.

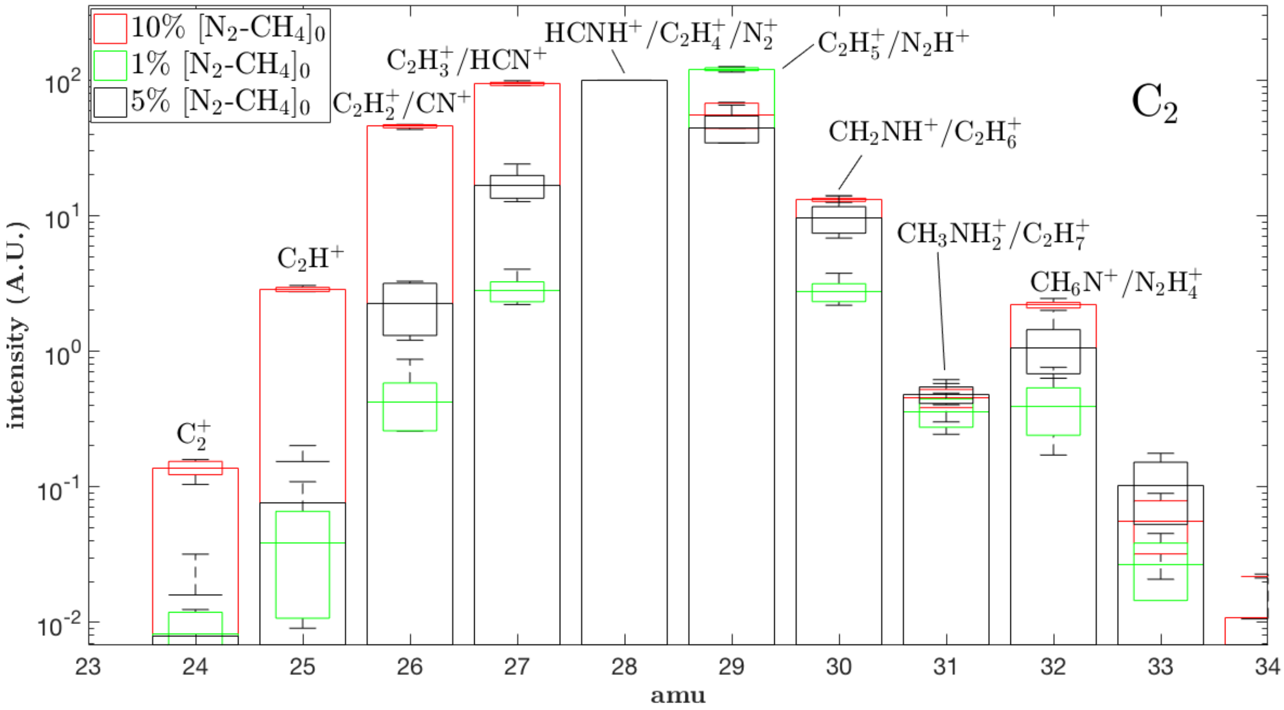

FIGURE 4.15: C_2 group in a $[N_2{-}CH_4]_0 = 1\%$ $[N_2{-}CH_4]_0 = 5\%$ and $[N_2{-}CH_4]_0 = 10\%$ mixing ratio.

- C_3 - These species are dominated by m/z 42 (Figure 4.16), whose overall intensity seems to be favored with increasing methane. The black and red curves reach intensities similar to the C_1 group (almost 10^2). Except in the 10% CH_4 condition, the second most abundant volatile is m/z 43, which can be attributed to the protonated form of propene, $C_3H_7^+$, or ethylenimine $C_2H_3NH_2{}^+$. With 10% CH_4, the intensity of m/z 39, attributed to $C_3H_3^+$ or HC_2N^+, increases by almost two orders of magnitude. The production of this ion seems to be favored with a richer methane mixing ratio. Similar to the sharp increase seen in Figure 4.15 (red bars) in signal on the left-half of the C_2 block, an important contribution of species between m/z 36 and m/z 39 accompanies higher methane concentrations. This is consistent with protons added to the simple C_3.

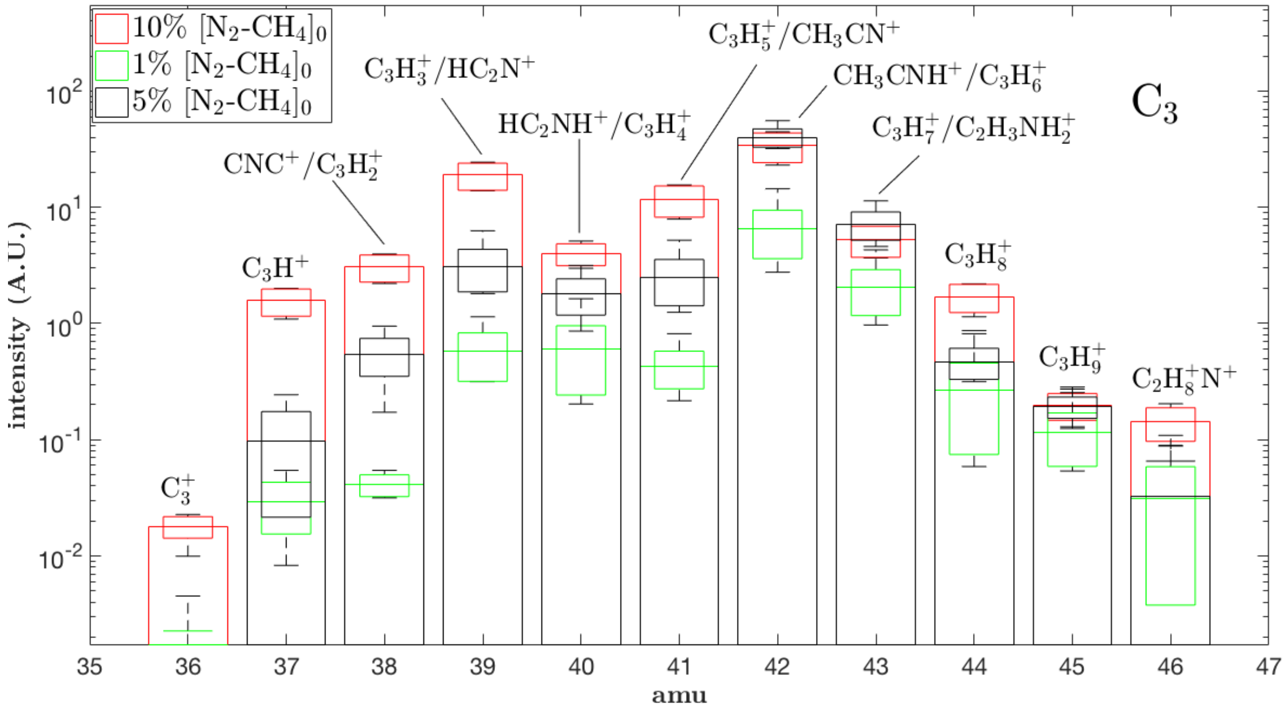

FIGURE 4.16: C$_3$ group in a $[N_2{-}CH_4]_0 = 1\%$ $[N_2{-}CH_4]_0 = 5\%$ and $[N_2{-}CH_4]_0 = 10\%$ mixing ratio.

- *C$_4$* - This block is dominated by the m/z 52 ion, which can correspond to HC_3NH^+, $C_4H_4{}^+$ or $C_2N_2{}^+$. We observe an overall increase in intensity of these species with increasing methane. However, the error bars overlap in most cases so species attribution remains difficult in this case. Ions with 1% CH_4 remain overall less intense than in the other two CH_4 conditions. To better characterize this observation among the different blocks, we represent these general trends as pie charts (Table 4.4) as a function of initial methane concentration.

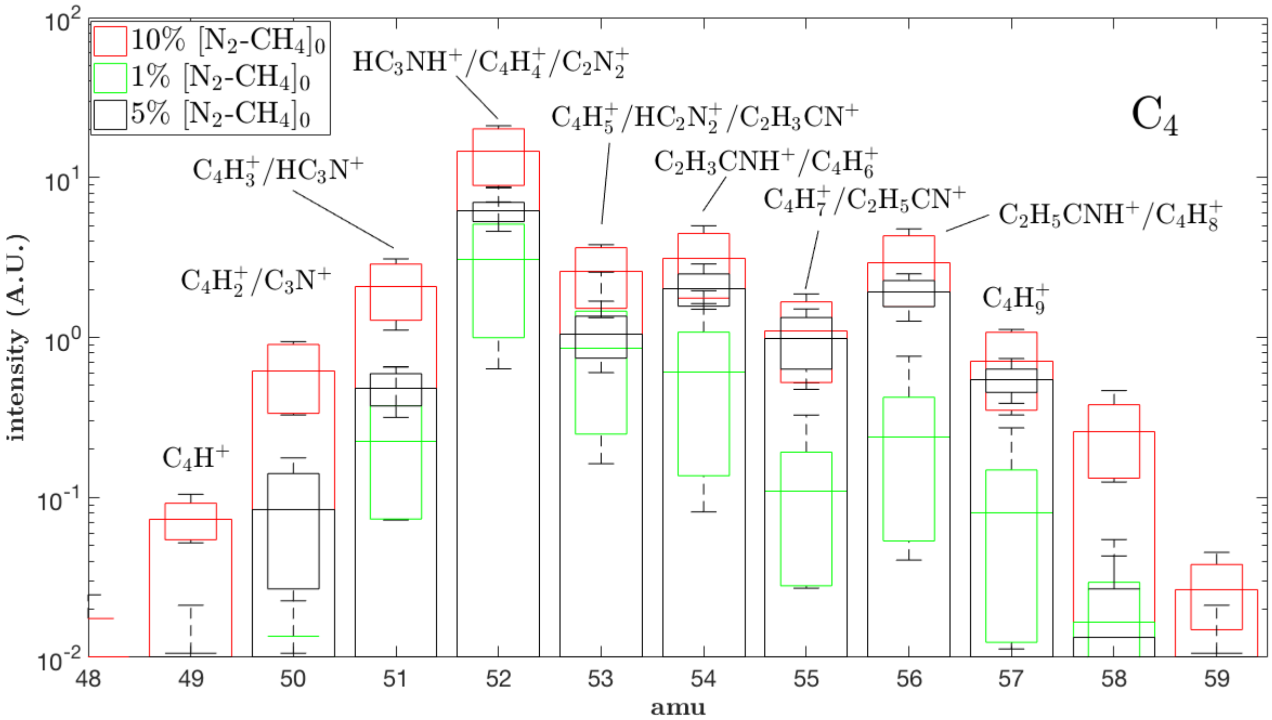

FIGURE 4.17: C_4 group in a $[N_2-CH_4]_0 = 1\%$ $[N_2-CH_4]_0 = 5\%$ and $[N_2-CH_4]_0 = 10\%$ mixing ratio.

In Table 4.4, we show systematic pie charts which are plotted for the C_{1-4} blocks, as a function of CH_4 mixing ratio. Each chart follows the same color code and is normalized over the sum of the mean values of all of the other masses (noted *misc.* in gray color). This representation helps us to draw the relative weights of each C_x block and better visualize their relative contributions.

The C_1 species are dominated by m/z 18, which represents $\sim$ 11% normalized over the entire spectrum, $\sim$ 13% at 5% CH_4 and decreases to $\sim$ 2% with 10% CH_4. As we can see in the last condition, m/z 15 accounts for the same contribution as m/z 18 does at 1% CH_4. In the intermediate methane condition, both m/z 15 and m/z 18 can be considered major ions. The C_2 compounds at 1% CH_4 are surprisingly significant, and represent almost 75% in intensity of the entire spectrum. This group is mainly represented by m/z 28 and m/z 29. This C_2 influence decreases slightly at 5% CH_4 while still contributing to $\sim$ 44% of all species detected. We observe that with increasing initial methane, the C_2 distribution gets wider and more populated, with eventually a more intense signature of m/z 26, m/z 29 and m/z 30, at 8%, 10% and 2%, respectively. This pattern is also seen in the C_3 pie charts, and to a lesser extent, the C_4 group. The C_3 compounds are dominated by m/z 42 in all three conditions. It is significant in particular at 5% CH_4 ($\sim$ 10% normalized), a favorable condition for efficient tholin formation. As seen in Table 4.3, m/z 42 can either be attributed to protonated acetonitrile CH_3CNH^+ or the cyclopropane positive ion $C_3H_6{}^+$.

TABLE 4.4: Pie charts representing the normalized mean intensities, for the C_x molecular groups, as a function of the methane initial concentration (%). Each chart is normalized by the total sum of all mean normalized intensities detected from 0-100 amu. Slices in gray correspond to these $1 - C_x$ values.

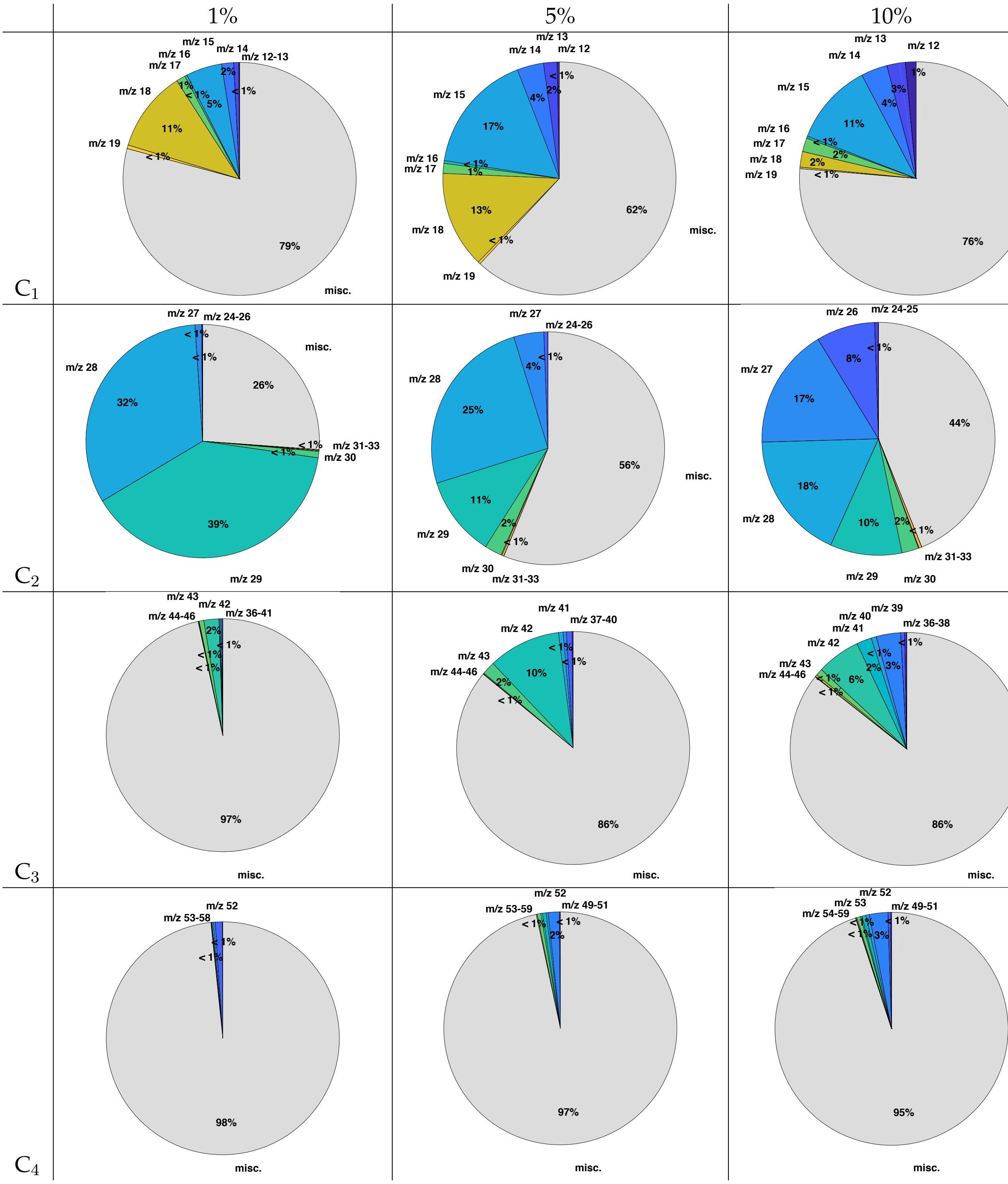

It is noteworthy to point out the 5% initial methane concentration charts (middle row, Table 4.4). At this concentration, tholins are efficiently produced in our chamber. The presence of the C_1 (m/z 15 and 18) and C_2 (m/z 28 and 29) ions (CH_3^+/NH_4^+ and $HCNH^+/C_2H_5^+$, respectively) is significant in this condition. This comes in agreement with the copolymeric HCN/C_2H_4 and poly-$(CH_2)_m(HCN)_n$-based structure found in the solid tholin material (Pernot et al., 2010; Gautier et al., 2014). As the tholins are negatively charged, they may react with these major ions to form and polymerize. These results could suggest that $HCNH^+$ and $C_2H_5^+$ are important contributors to the polymeric growth of tholins.

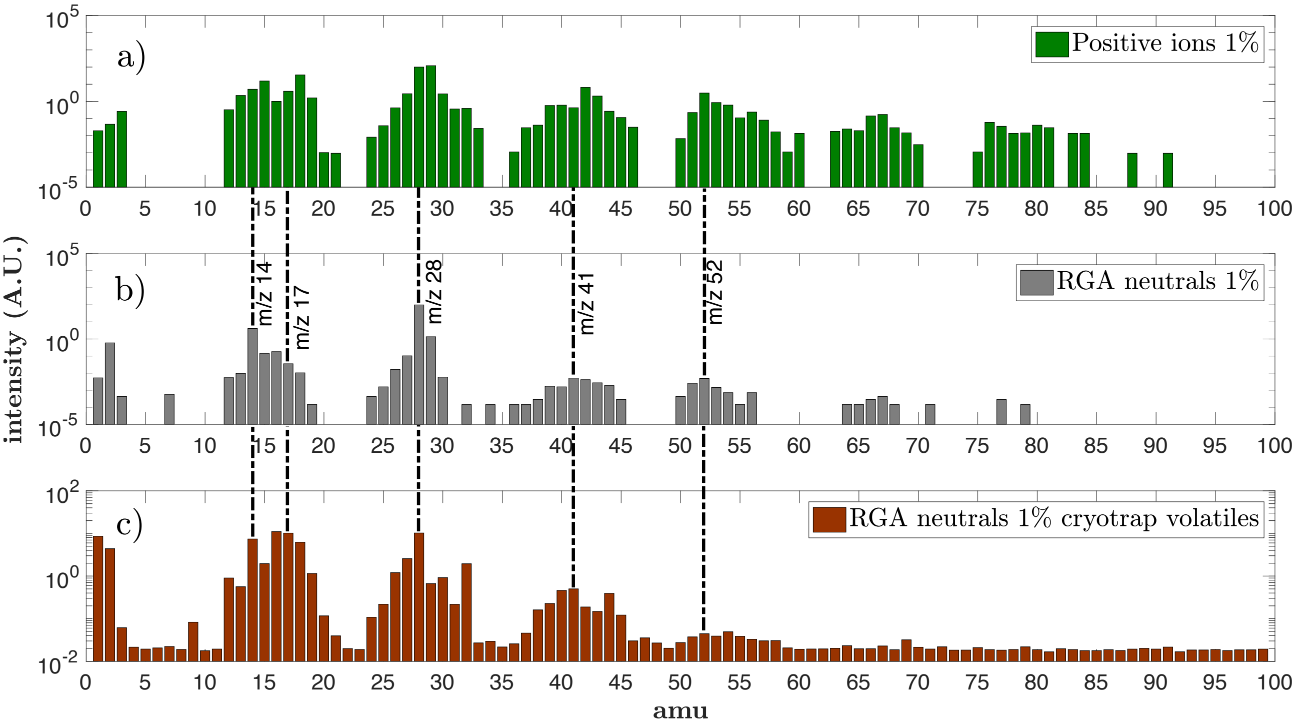

FIGURE 4.18: Comparison of three normalized mass spectra taken with 1% CH_4 and degraded at the same resolution of 1 amu. a) shows the entire normalized averaged spectrum in positive ion mode of Figures 4.144.17, b) was taken with the plasma discharge on in RGA neutral mode, with an electron energy of 70 V and filament emission of 5 μA in the same conditions. Lastly, c) is the neutral spectrum taken in our previous study, which analyzed the volatile products formed in N_2-CH_4 mixtures and released after being cryotrapped. For more details on these results, the reader is referred to Chapter 3, Figure 3.5., or Dubois et al., 2019

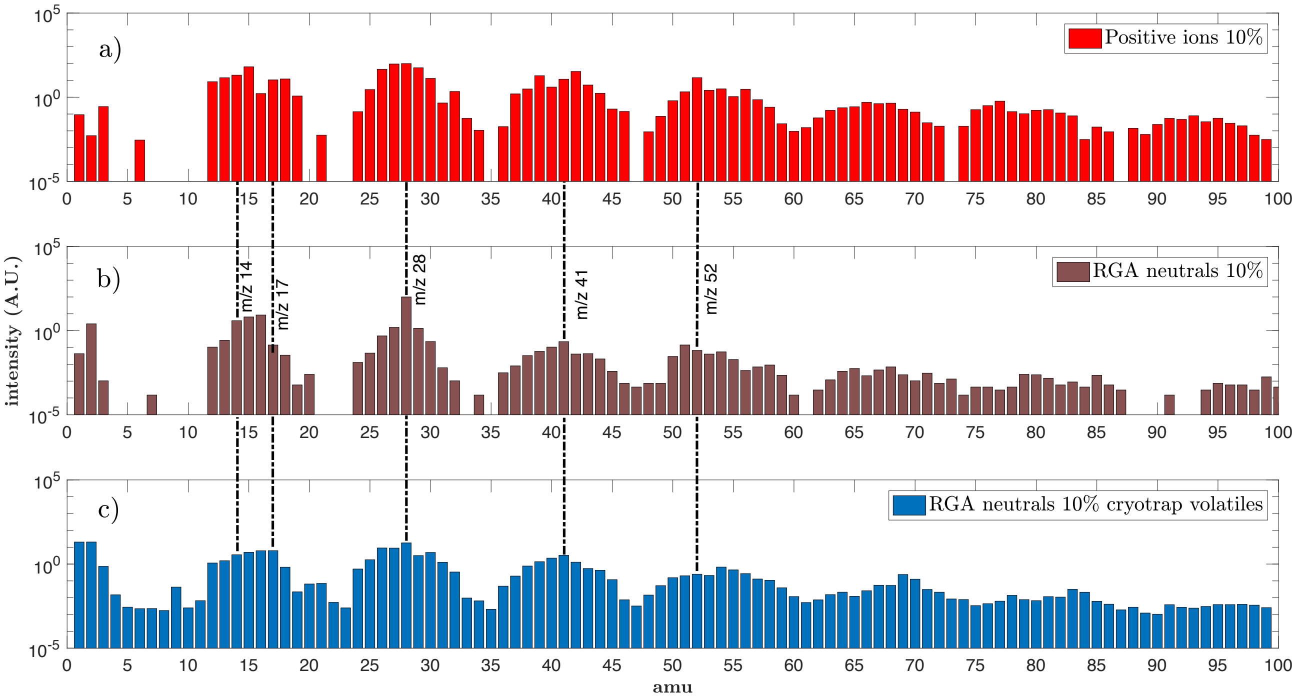

FIGURE 4.19: Same as Figure 4.18, with 10% [CH4]. Comparison of three normalized mass spectra taken with 10% CH_4 and degraded at the same resolution of 1 amu. a) shows the entire normalized averaged spectrum in positive ion mode of Figures 4.144.17, b) the spectrum was taken in RGA neutral mode with the plasma discharge on, with an electron energy of 70 V and filament emission of 5 μA under the same conditions. Lastly, c) is the neutral spectrum taken in our previous study, which analyzed the volatile products formed in N_2-CH_4 mixtures and released after being cryotrapped. For more details on these results, the reader is referred to Chapter 3, Figure 3.5., or Dubois et al., 2019

In order to see the interactions between the neutral and positive ion species, we show in Figures 4.18 and 4.19 comparisons between the mean normalized spectra in positive ion and residual gas analyzer (RGA) neutral modes at 1% and 10% CH_4, respectively. The neutral mode setting used a 70 V electron energy using a filament emission of 5 μA. As the cryogenic study only focused on 1% and 10% CH_4, this neutral/ion comparison was kept for these two conditions. We also qualitatively compare these spectra with measurements of neutral volatile products released after being cryotrapped (see Dubois et al., 2019 or Chapter 3). Note that the experiments were different in both cases: in the present study, ions were extracted from the plasma and detected *in situ*, while the cryotrap setup (described in Chapter 3) consisted in trapping the neutral products at a cold temperature, and acquiring mass spectra during their release. As explained in Chapter 3, the latter spectra serve here as a comparative basis only, where some species (e.g. C_2H_6) may not have been entirely trapped given the cryogenic temperatures. The color code for the two 1% and 10% CH_4 cryotrap spectra is the same as the one used in Figure 3.5 of Chapter 3.

The m/z 28 and 29 ions Figure 4.18 (a), dominate the spectrum as seen previously in Table 4.4. In the neutral spectrum (gray bar graph), m/z 28 corresponds to contributions from N_2 and C_2H_4. In the cryogenic study (brown bar graph), m/z 28 was attributed to C_2H_4, while the major m/z 17 peak was assigned to NH_3. In the middle plot, m/z 14, corresponding to the nitrogen atom or methylene CH_2, is the main C_1 fragment. In positive ion mode however, the C_1 group is much more populated, as are all of the other groups. In addition, m/z 15 and m/z 18 become the two major ions, coupled with a relatively richer spectrum on the right hand side of the group compared with the RGA spectrum. This 1 amu shift is consistent with reactions involving H^+ (see Discussion Section 4.4.1). This pattern is also seen in the C_2 and C_3 groups with m/z 28→29 and m/z 41→42 shifts. The C_4 shows no inversions in the m/z 52 peak. This molecule can be 1-buten-3-yne C_4H_4 or cyanogen C_2N_2, which were both identified in Gautier et al., 2011. Their cation counterparts $C_4H_4{}^+$ and $C_2N_2{}^+$, along with propiolonitrile HC_3NH^+ can explain the intense m/z 52 signature at $\sim 2.5 \times 10^0$ a.u. As seen at the beginning of this section and in Table 4.4, the 10% CH_4 is marked by broader blocks, notably for the first three. The m/z 12→16 methane fragments in the (b) plot of Figure 4.19 are visible along with the corresponding methylene and methyl cations (red plot). C_2 species are dominated by m/z 28 surrounded by m/z 26, 27 and 29. In our cryogenic study (blue plot, c), m/z 28 was attributed to C_2H_4. N_2 was absent from the chamber and so was ruled out. In the middle plot (b), N_2 was also present in the plasma and can also contribute to this peak. Furthermore, our cryogenic quantitative analysis (Dubois et al., 2019) showed a higher HCN production at 10% than at 1% CH_4, suggesting that the HCN reservoir may be an important C_2 contributor to HCN-based reactions leading to more various compounds. There is a m/z 41→42 shift in the C_3 group (red plot), similar to that at 1% CH_4, and again from m/z 51 in the neutral spectrum to m/z 52. However, unlike at 1% CH_4, the m/z 42 increase in intensity is accompanied by m/z 39, which represent 6% and 3% in relative intensity to the rest of the spectrum, respectively (Table 4.4). To go further in this inter-comparison and better understand the chemical processes, it would be crucial to model this neutral/cation interaction in the plasma.

4.3.4 T40 INMS comparisons and group patterns

INMS was built by a team of engineers and scientists from NASA's Goddard Space Flight Center, and the University of Michigan. One of its goals was to probe and analyze the neutral and ion chemistry of Titan's upper atmosphere, and thus characterize the gas composition (for a more detailed review regarding the scientific objectives of INMS, see 1 and Waite et al., 2004b). It was also possible to determine the gas number density thanks to the closed source mode (see hereafter). The mass range of INMS was from 1u to 99u, while the energy range was from 0 eV to 100 eV and a mass resolution of $\frac{m}{\Delta m} = 100$ at 10% of mass peak height. This instrument consisted of two mechanical subsystems, (i) the closed ion source mode and (ii) the open ion source mode. The open ion source mode was used to analyze reactive neutral species and positive ions. The latter were extracted through grounded ion deflectors, guided through four focusing lenses and then through a set of four quadrupole switching lenses (QL). These switching lenses provide a hyperbolic electrostatic field deflecting the ions by 90ž and subsequently directs them to a quadrupole mass analyzer. The QL essentially acted as an energy filter in open source mode, similar to our energy filter plates (Figure 4.3). Thus, it was possible to select specific masses (with their specific kinetic energies) and determine their ion energy distributions (range of 1-100 eV).

We compare our laboratory spectra with positive ion measurements taken by Cassini-INMS (Ion and Neutral Mass Spectrometer) during the T40 flyby (Figure 4.20). This encounter with Titan took place on January 5, 2008 at 13.0 h, just after Saturn local noon (sunward) with a closest approach at 1010 km above the surface. The passage occurred at 11.7 S latitude and 130.4 west longitude at closest approach. Cassini had a speed of 6.3 $km.s^{-1}$, with a 37.6° solar phase angle. This flyby was part of a series of high inclination sequences, near the end of the Prime Mission, as well as the fifth of a series of seven southern hemisphere approaches. During this flyby, four other instruments were also in operation, along with INMS: the Visual and Infrared Mapping Spectrometer (VIMS), the Ultraviolet Imaging Spectrograph (UVIS), the Imaging Science Subsystem (ISS) and the Composite Infrared Spectrometer (CIRS). The INMS operated in open source ion mode, enabling a detection of positive ions with energies < 100 eV. The integration period is ~ 34 ms, which corresponds to the sum of the set up/read out cycle and the sample integration period (Waite et al., 2004a). Therefore, it took INMS ~ 2.3 s to acquire an entire scan.

The fact that this flyby was entirely on the dayside of Titan and measured an important quantity of ions, makes it a valuable source for the investigation of positive ions, as well as comparing it with plasma discharge laboratory simulations like PAMPRE. Previous studies have specifically focused on this T40 flyby, which, incidentally, occurred during a solar minimum activity (Lavvas et al., 2011; Richard et al., 2015) with an $F_{10.7}$ index of 77.1. Westlake et al., 2011 found that the neutral average temperature during this flyby was 141 K. The plasma environment surrounding Titan during this encounter was unique. The measured electron distribution was categorized as bi-modal by Rymer et al., 2009, using CAPS Electron Spectrometer (ELS) and MIMI Low Energy Magnetospheric Measurements System (LEMMS) data. They proposed that this unusual distribution, also observed at T26, T31, T46 and T47, may have been the result of two sources: the more energetic ($\lessapprox$ 5 keV) electrons coming from the plasma sheet, while the less energetic electrons ($\lessapprox$ 0.2 keV) may be local pick-up electrons from the inner magnetosphere and interactions with Enceladus water group neutrals.

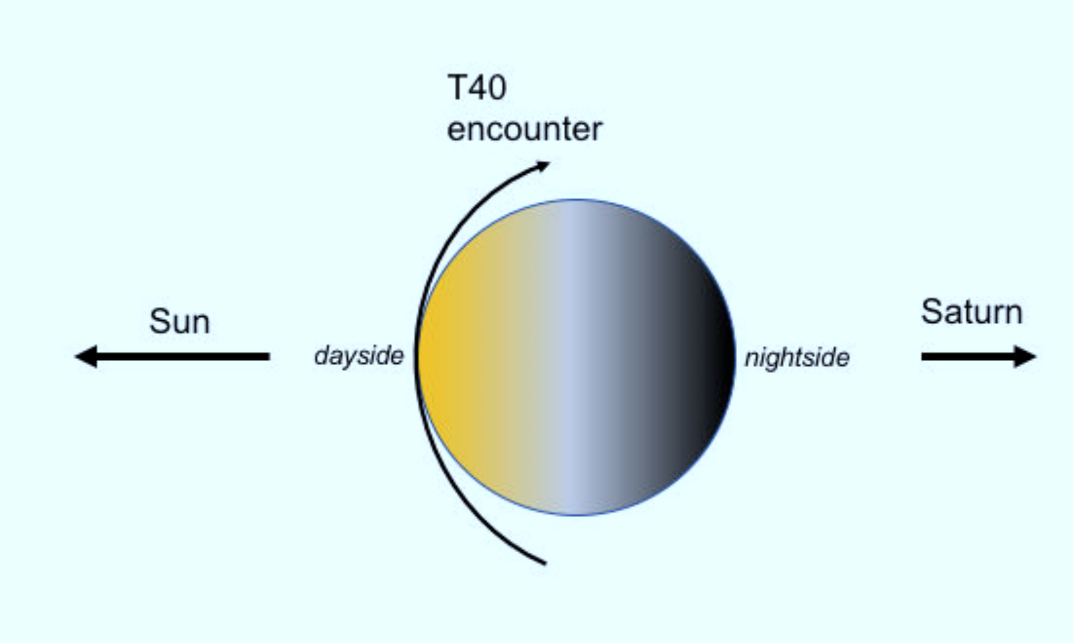

FIGURE 4.20: Schematic top view of the T40 dayside flyby configuration on January 5, 2008. Closest approach was at 1010 km, at 11.7 S latitude, 130.4 West longitude.

The spectrum Figure 4.21 is made of seven blocks, each separated by about 6-8 Da. The main C_1 compounds are m/z 15 and m/z 17, which have been attributed to CH_3^+ and CH_5^+ by Vuitton, Yelle, and McEwan, 2007. The presumed $HCNH^+$ and $C_2H_5^+$ are an order of magnitude higher in IP counts.

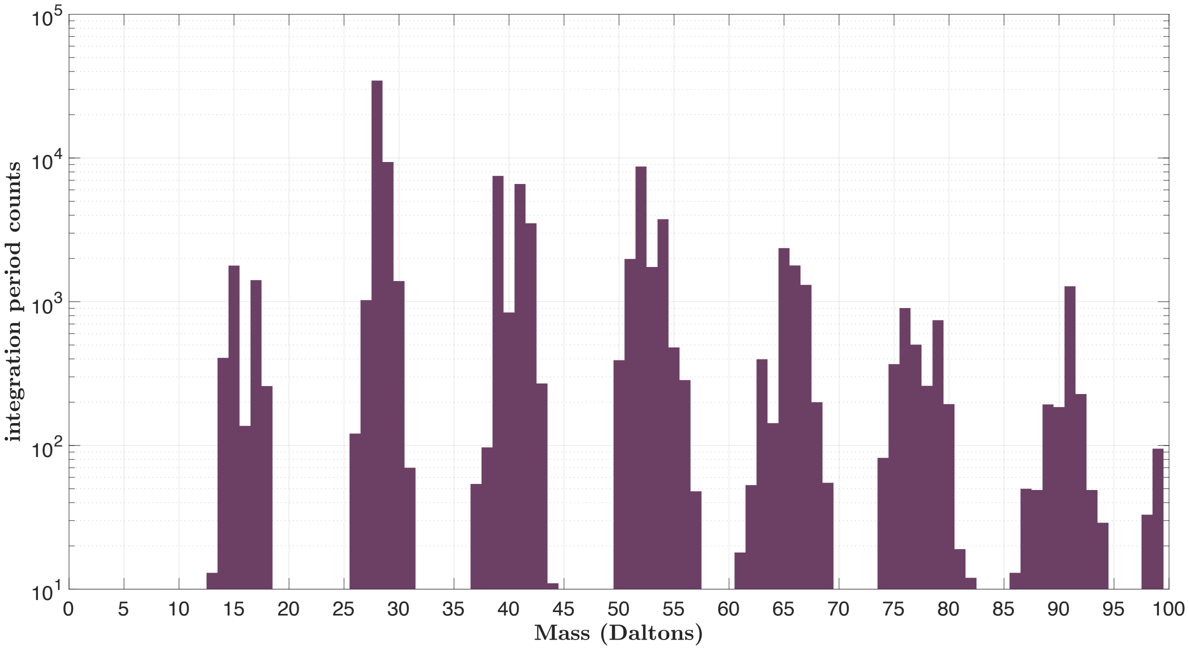

FIGURE 4.21: Mass spectrum taken by INMS during the outbound leg of the T40 flyby, at 1097 km. The mass plot is separated in 1 Da. bins and plotted against raw IP counts. The INMS operated in open source ion mode during this flyby in order to detect low energy ions (< 100 eV).

The same T40 spectrum is plotted in Figures 4.22—4.24, against our normalized experimental 1%, 5% and 10% CH_4 spectra from Figures 4.14—4.17. Our 1% spectrum reproduces fairly well the distributions of the grouping patterns of the lighter ions, up to the C_4 species (Figure 4.22). However, the subsequent intensities decrease by orders of magnitude with each new block, with no detection beyond m/z 84. Moreover, NH_4^+ is overrepresented in the experimental spectrum (11% of the entire spectrum, Table 4.4), although the efficient formation of ammonia and CH_4^+ may be facilitated by wall catalysis effects (Touvelle et al., 1987; Carrasco et al., 2012). The importance of C_2 compounds is faithfully reproduced by our experimental spectra, suggesting that they must play a key role in reactions with primary ions as precursors to tholin formation. As indicated in Table 4.4, C_2 species represent $\sim$ 44% to $\sim$ 74% of the spectrum, depending on the CH_4 condition. The equivalent charts for the T40 spectrum at 1097 km is shown in Table 4.5. The C_2 species account for $\sim$ 47% of this spectrum, led by m/z 28 at 35%, and m/z 29 at 10%. This distribution is similar to the one we find at 5% CH_4, i.e. 25% for m/z 28 and 11% for m/z 29 (Figure 4.23 and Table 4.4). The overall average C_2 contribution is $\sim$ 44% in the experimental case (Table 4.4), comparable with the $\sim$ 47% in the INMS spectrum (Table 4.5). Increasing the methane concentration favors the production of heavier ions, e.g. m/z 39, m/z 51, m/z 55 species larger than the C_5 group. In the C_3 group, $C_3H_3^+$/HC_2N^+ at m/z 39 is two orders of magnitude more intense at 10% CH_4 ($\sim 2 \times 10^1$ a.u. versus $\sim 4 \times 10^{-1}$ a.u. at 1% CH_4), although m/z 42 remains the major ion. The hydrogen cations, H^+, H_2^+ and H_3^+ are all visible in the experimental spectra and nearly absent from the INMS data. This hydrogen reservoir may play a role in further reactions (see Discussion).

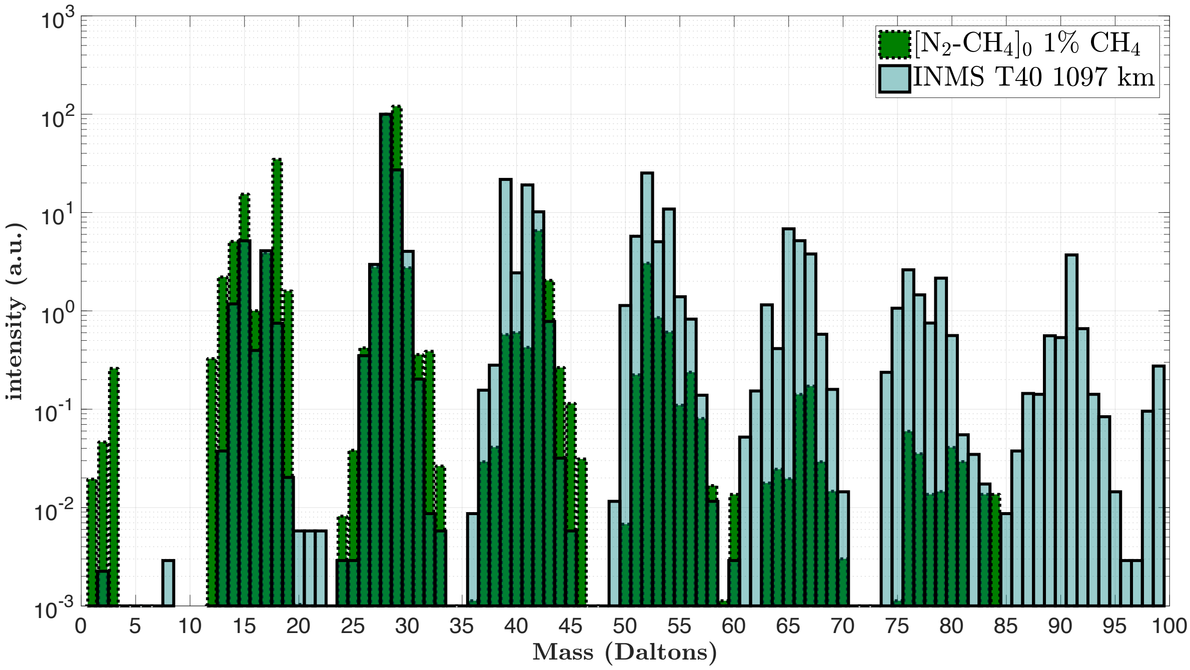

FIGURE 4.22: Mass spectrum taken during the outbound leg of the T40 flyby (in blue), at 1097 km, compared with our experimental averaged spectra taken in 1% CH_4. The mass plot is separated in 1 Da. bins.

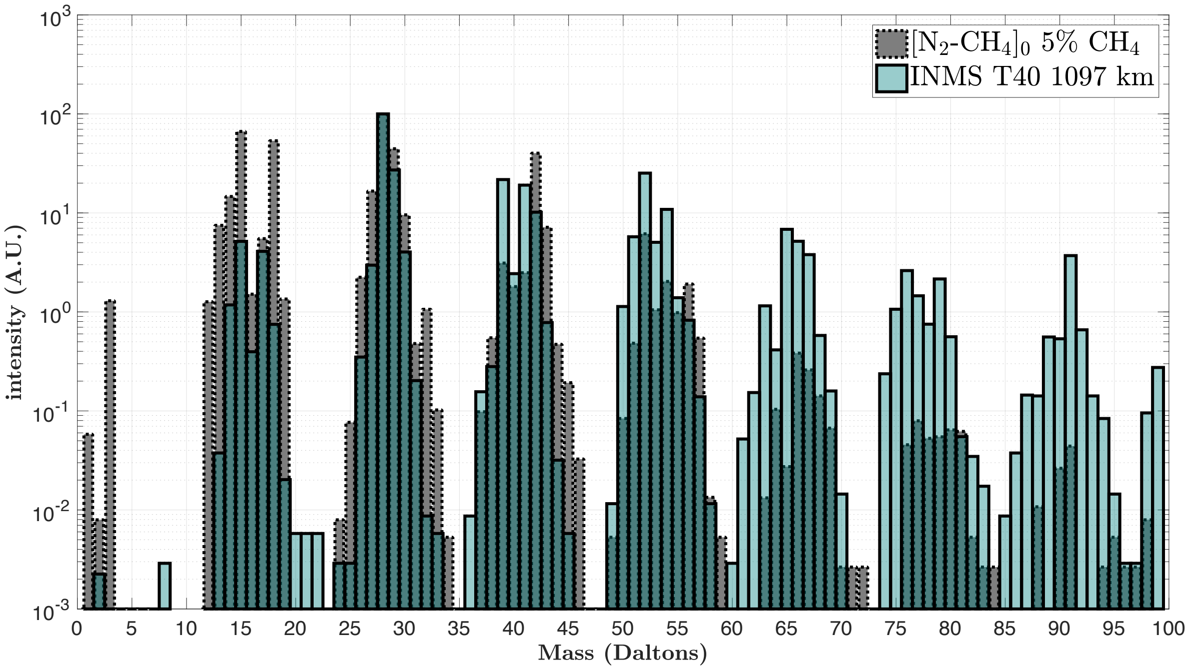

FIGURE 4.23: Mass spectrum taken during the outbound leg of the T40 flyby (in blue), at 1097 km, compared with our experimental averaged spectra taken in 5% CH_4. The mass plot is separated in 1 Da. bins.

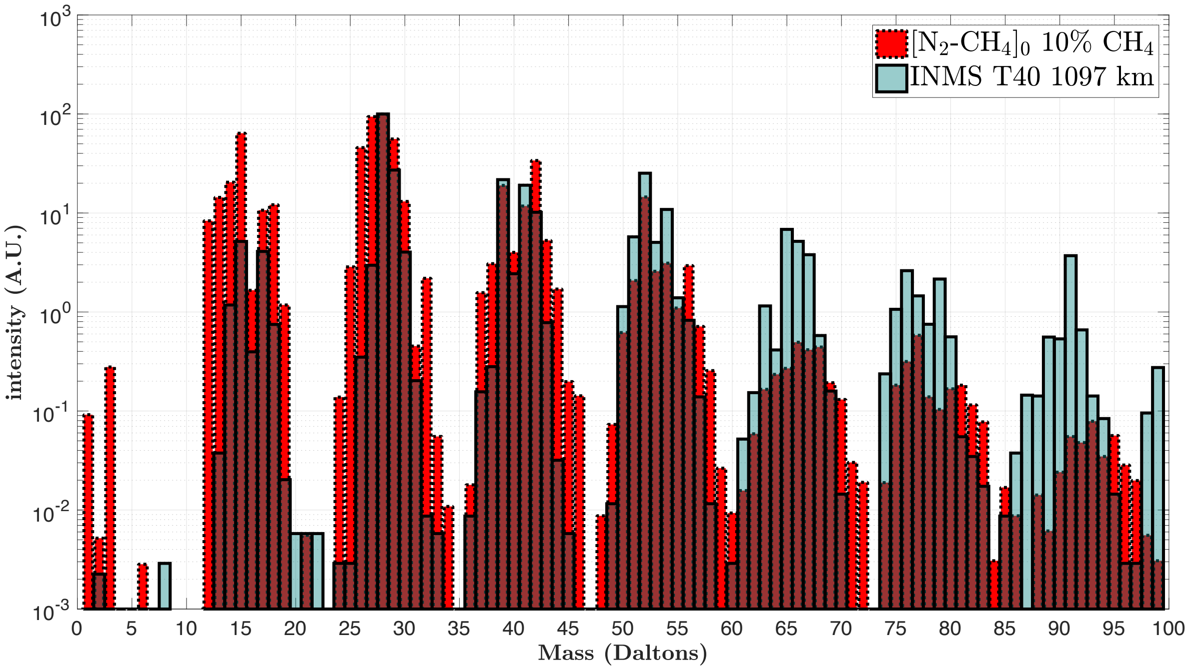

FIGURE 4.24: Mass spectrum taken during the outbound leg of the T40 flyby (in blue), at 1097 km, compared with our experimental averaged spectra taken in 10% CH_4. The mass plot is separated in 1 Da. bins.

The 10% methane-rich condition (Figure 4.24) displays the widest population of ions. We also see a rightward drift of the blocks, especially for higher masses. This is consistent with the rich presence of saturated hydrocarbons vs. nitrogenated species. The major ions coincide with INMS' for the C_1, C_2 and C_4 groups. As seen previously, the $\frac{I_{42}}{I_{39}}$ ratio in normalized intensities reaches ~ 2, when it was ~ 12 with 1% CH_4. Nonetheless, m/z 42 remains the most abundant C_3 ion in all three conditions we have studied, in particular with higher methane amounts. This behavior is especially noticeable for masses 12, 25, 26, 27, 37, 38, 39, 50, 55 and 56. The comparison with INMS also shows an asymmetry in the blocks, with respect to those of INMS. The former are wider, and tend to build up to the right hand side of each block. These extended *wings* are significant on either side of the C_1 and C_2 blocks.

TABLE 4.5: Pie charts of the first four $C_xH_yN_z$ groups of the T40 INMS spectrum taken at 1097 km, normalized by m/z 28.

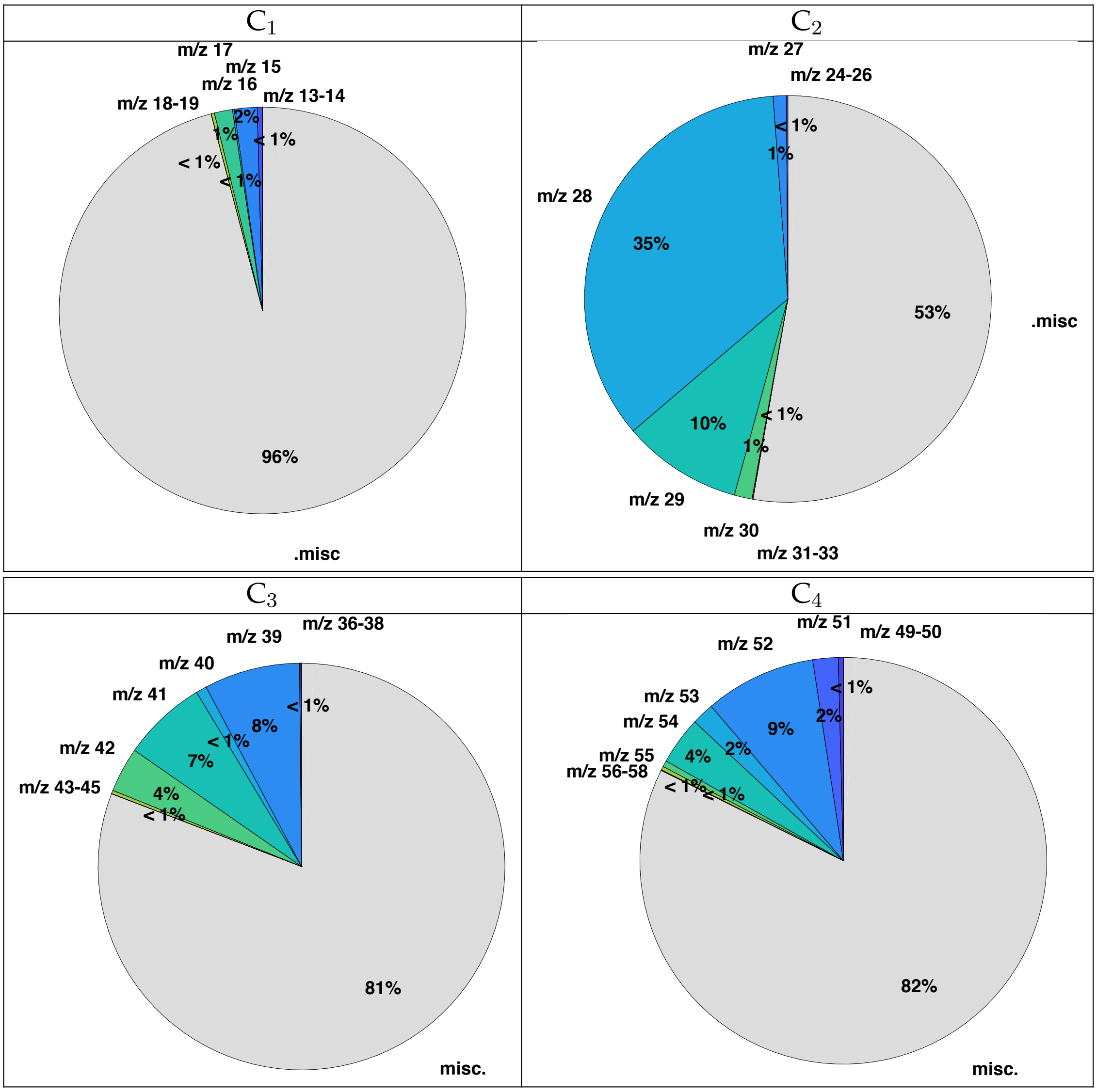

We note that C_4 and larger ions generally tend to be more intense in the INMS spectra than in our experimental ones. The latter show a faster decreasing slope in intensity. This could be due to an instrumental bias, whereby high-mass ions are extracted less efficiently in PAMPRE than the lighter ones.

Now that we have compared the PAMPRE spectra with an INMS spectrum taken at one altitude, we compare the former measurements with data obtained at 26 altitude in the 1000-1150 km range taken during both the inbound and outbound legs of this flyby. Generally, there is no altitudinal variation in peak ratio at each altitude, only the intensities vary.

Figures 4.25 to 4.28 show the normalized intensities contained within 1000-1150 km for each mass bin, along with the mean experimental points in our three methane mixing ratios. The INMS clusters indicate the maximum intensities measured throughout the inbound and outbound legs of the flyby within this altitude range. The C_1 m/z 15 and m/z 18 peak inversion at 10% and 1% CH_4 is clearly visible (Figure 4.25). The N_2/CH_4 (90/10) gas mixture faithfully reproduces the patterns seen in the INMS clusters of the C_1 group. The N_2/CH_4 (99/1) condition however (blue diamonds), matches well with the intensities of the m/z 14, 15, 16 and 17 ions. The dominant m/z 18 ion stands apart from the m/z 18 cluster by more than an order of magnitude, indicating a favorable production of NH_4^+ in a nitrogen-rich gas mixture.

The C_2 group (Figure 4.26) is dominated by $HCNH^+/C_2H_4{}^+$ in the 5% and 10% gas mixtures. These two mixtures reproduce well the main ion of this group. At 10% CH_4, the experimental $C_2H_3^+/HCN^+$ (m/z 27) accounts for $\sim$ 99% of the m/z 28 intensity. This intensity is larger than the INMS cluster by a factor of $\sim$ 7 to more than an order of magnitude. The 1% experimental points fall in the INMS range, except for $C_2H_5^+/N_2H^+/CH_2NH^+$ (m/z 29), which is the prevailing ion in this case, and $CH_2NH_2{}^+/C_2H_6{}^+$. The 5% CH_4 reproduces the C_2 pattern very well with a distribution centered at m/z 28, as also seen with Tables 4.4—4.5 and Figure B.8.

The larger ions of the C_3 group are, in all three gas mixtures, dominated by $CH_3CNH^+/C_3H_6{}^+$ at m/z 42 (Figure 4.27). However, the major ion measured by INMS in this group is m/z 39 (Table 4.5). Except the experimental data point at m/z 39 and 43, our measurements at 5% CH_4 fall within the range of the INMS intensities. The discrepancy observed at m/z 39 is compensated only by an increase in methane concentration. Finally, the C_4 group seems to be well represented by the 10% CH_4 mixture. However, given the wings seen earlier in Figure 4.23 the 5% CH_4 spectrum nicely overlaps the INMS spectrum.

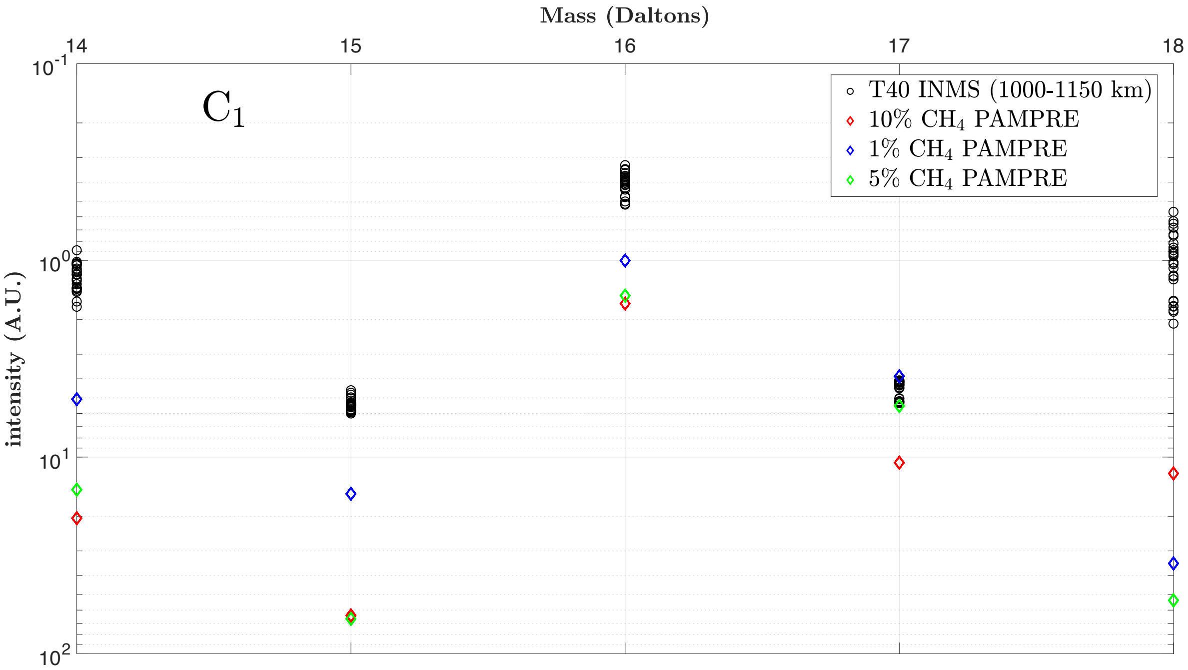

FIGURE 4.25: Relative evolution trends of the main C_1 species in our three experimental conditions, compared with 26 measurements during the inbound and outbound leg of T40, for an altitude range of 1000-1150 km. Mass data is all separated in 1 Da. bins and y axis values increase downward.

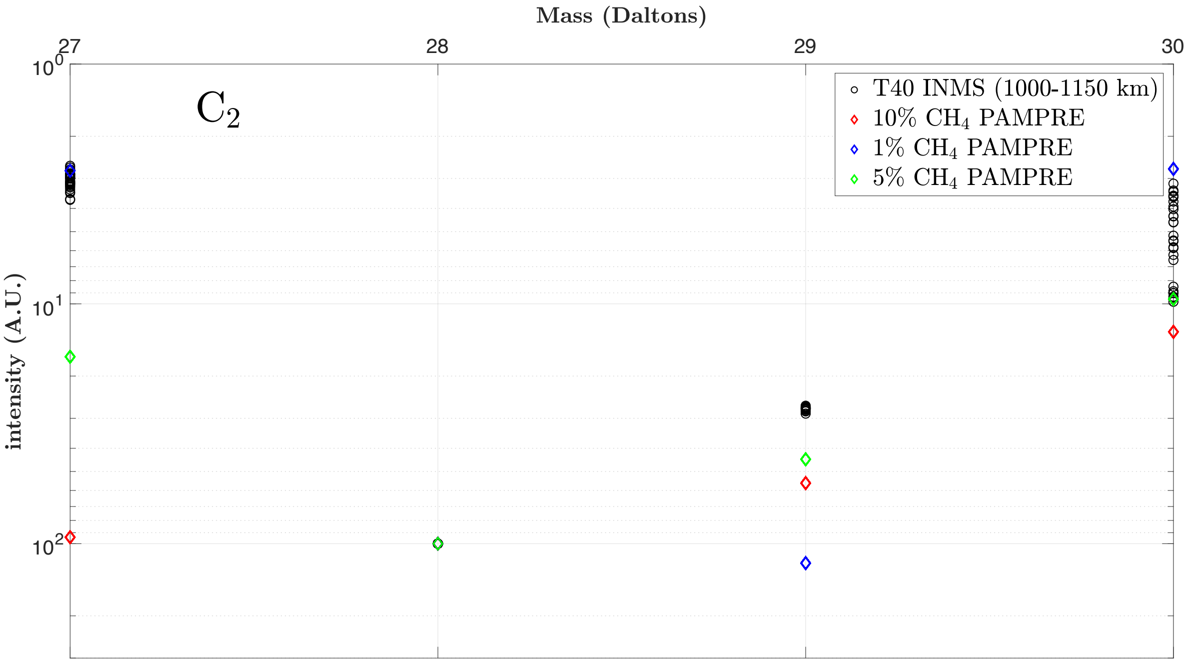

FIGURE 4.26: Relative evolution trends of the main C_2 species in our three experimental conditions, compared with 26 measurements during the inbound and outbound leg of T40, for an altitude range of 1000-1150 km. Mass data is all separated in 1 Da. bins and y axis values increase downward.

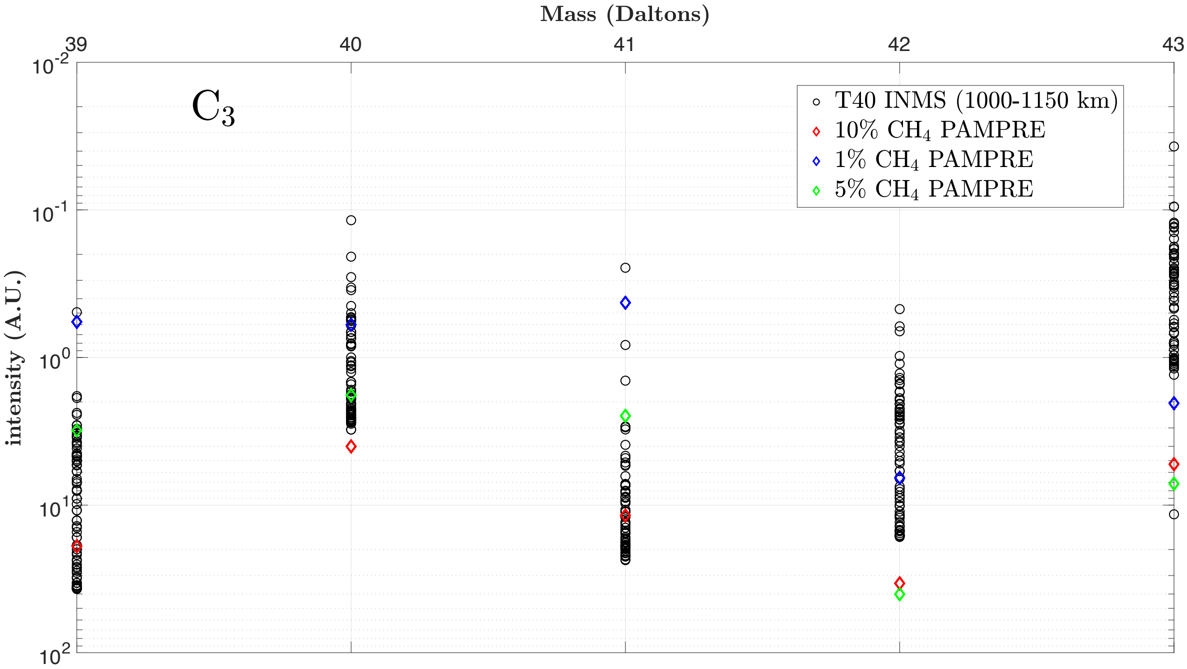

FIGURE 4.27: Relative evolution trends of the main C_3 species in our three experimental conditions, compared with 26 measurements during the inbound and outbound leg of T40, for an altitude range of 1000-1150 km. Mass data is all separated in 1 Da. bins and y axis values increase downward.

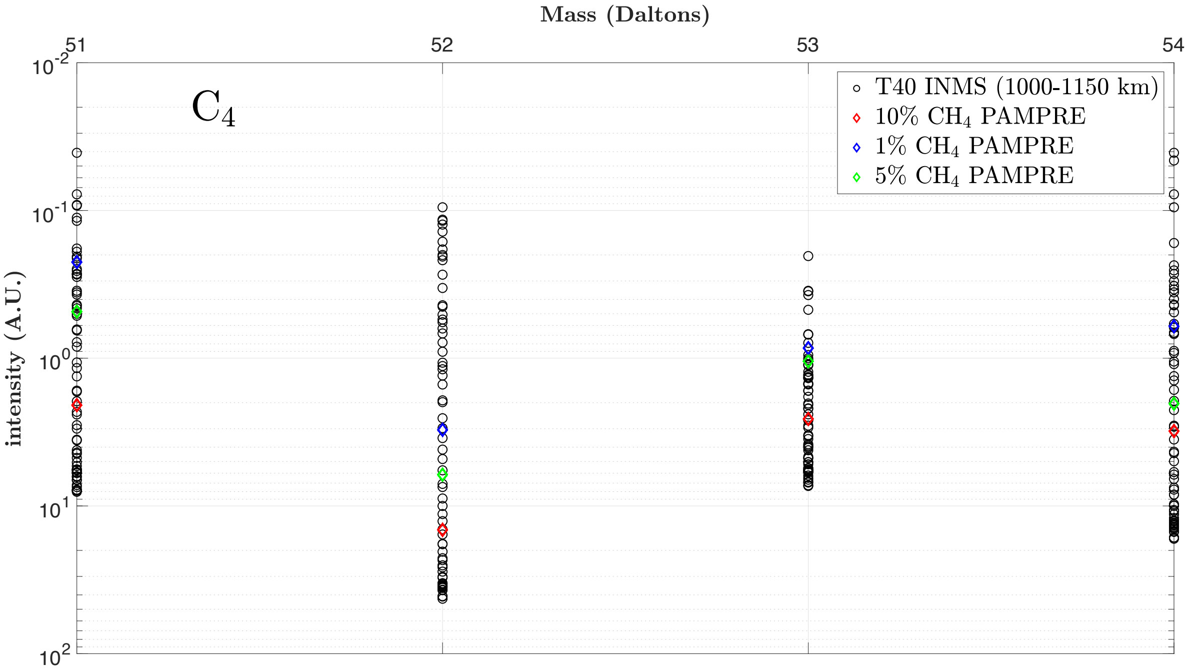

FIGURE 4.28: Relative evolution trends of the main C_4 species in our three experimental conditions, compared with 26 measurements during the inbound and outbound leg of T40, for an altitude range of 1000-1150 km. Mass data is all separated in 1 Da. bins and y axis values increase downward.

4.4 Discussion

4.4.1 Chemical pathways contributing to the major precursors

The abundant reservoir of neutral species in Titan's upper atmosphere is an important source for ion-molecule reactions. Based on the neutral chemistry modeled by Yung, Allen, and Pinto (1984), Yung (1987), and Toublanc, Parisot P., and McKay (1995), Keller, Cravens, and Gan (1992) and Keller, Anicich, and Cravens (1998) modeled ionization processes, whereby the major neutral compounds would form ${N_2}^+$ and N^+, and ${CH_4}^+$, ${CH_3}^+$, ${CH_2}^+$ and CH^+. These simple and primary light cations serve as a basis for further ion-neutral reactions, supplying the positively charged population with heavier species. Reaction 14 for example, where ${CH_3}^+$ reacts with methane, can form some of the very first hydrocarbons. With updated and extended photochemical models (Fox and Yelle, 1997; Keller, Anicich, and Cravens, 1998; Vuitton, Yelle, and Anicich, 2006; Vuitton, Yelle, and McEwan, 2007; Carrasco et al., 2008), many of the positive ions were shown to be products resulting from proton exchange reactions between neutrals and ions. In this section, we will discuss potential pathways to explain some of our main ions detected in our three methane mixing ratios. These pathways are detailed in order to constrain our understanding of cation gas phase reactivity in our plasma.

The ion variability observed in our PAMPRE reactor has shown to be highly methane-dependent. Few peak inversions exist (e.g. m/z 15 and 18). However, the decreasing slope after C_2 is much higher at 1% CH_4 than at 10%, and higher amounts of CH_4 lead to larger *wings* with respect to the INMS spectra. As the neutral and ion chemistry are tightly coupled, comparing these two sets of data can shed light on protonation-driven chemical pathways, if any. We will first focus on the very light ions of the C_1 group. As shown in Figure 4.18 (b and c), m/z 14 associated with N or CH_2 and m/z 17 (NH_3), the two major C_1 ions, become represented by m/z 15 and m/z 18 (top figure), respectively. The production of ${CH_3}^+$ comes from the direct ionization of methane or by charge transfer with ${N_2}^+$ with a branching ratio (*br*) of 0.89 (Reaction 13, Carrasco et al., 2008). ${CH_3}^+$ can react with other neutrals (Reaction 14), and thus become more intense with higher methane mixing ratios.

$$\mathrm{N_2}^+ + \mathrm{CH_4} \longrightarrow \mathrm{CH_3}^+ + \mathrm{H} + \mathrm{N_2} \tag*{\{13\}}$$

$$\mathrm{CH_3}^+ + \mathrm{CH_4} \longrightarrow \mathrm{C_2H_5}^+ + \mathrm{H_2} \tag*{\{14\}}$$

$$\mathrm{NH_3} + \mathrm{HCNH}^+ \longrightarrow \mathrm{NH_4}^+ + \mathrm{HCN} \tag*{\{15\}}$$

$$\mathrm{NH_3} + \mathrm{C_2H_5}^+ \longrightarrow \mathrm{NH_4}^+ + \mathrm{C_2H_4} \tag*{\{16\}}$$

In our chamber, ${CH_3}^+$ might form according to Reaction 13, the same way the ammonium ion ${NH_4}^+$ can form via Reactions 15 or 16 by proton attachment (Vuitton, Yelle, and McEwan, 2007; Carrasco et al., 2008). Initially, Keller, Anicich, and Cravens (1998) predicted m/z 18 to be dominated by H_2O^+. After the early T5 Titan flyby, Cravens et al. (2006) and Vuitton, Yelle, and Anicich (2006) first suggested

NH_4^+ to be a good candidate for the m/z 18 detection, which was confirmed by Vuitton, Yelle, and McEwan (2007) and Carrasco et al. (2008). Note that in our experiment, a small H_2O^+ contribution from residual air in the chamber cannot be ruled out, given the m/z 19 detection at $< 1\%$ (Figure 4.14 and Table 4.4). At 1% and 5% CH_4, NH_4^+ is a major precursor, representing 11% and 13% in intensity (Table 4.4), respectively. Reactions 15 and 16 require an ammonia reservoir. Pathways for NH_3 production in our chamber were detailed in Carrasco et al. (2012). The formation of ammonia (Reaction 17) relies on an NH radical reservoir, which can come from (i) radical chemistry through $N + H \longrightarrow NH$, or (ii) ion-neutral chemistry with Reaction 18, and its subsequent recombination, Reaction 19. Note however that in such a reaction volume, wall effects can act as a catalyzer to adsorbed N and H, and contribute to Reaction 17, as described in Touvelle et al. (1987) and Carrasco et al. (2012).

$$\mathrm{NH + H_2 \longrightarrow NH_3} \tag*{\{17\}}$$

$$\mathrm{N_2{}^+ + CH_4 \longrightarrow N_2H^+ + CH_3} \tag*{\{18\}}$$

$$\mathrm{N_2H^+ + e^- \longrightarrow NH + N} \tag*{\{19\}}$$

When increasing the methane concentration, ammonia production also increases, thanks to the available NH radicals. However, primary aliphatics also increase, and the ion population grows (e.g. Figure 4.14). So, at 10% CH_4, NH_4^+ no longer becomes significant, representing only 2% in intensity (Table B.1). The NH_4^+ contribution at 5% CH_4 is still important (13%), notwithstanding m/z 15 already dominating the C_1 group. At least at 1% and 5% CH_4, the ammonium ion NH_4^+ is a major gas phase precursor, and its formation couples ion and neutral chemistry. This ion seems to be a relevant primary precursor for the formation of tholins with a 5% CH_4 mixing ratio (Sciamma-OBrien et al., 2010). Further studies should explore intermediate conditions between 1% and 5% and examine the evolution of NH_4^+

As we saw in Section 4.3.3, the C_2 group prevails in all spectra. Comparing the neutral and ion mass spectra (Figures 4.18 and 4.19) gives us a clear evolution of the peaks. In the neutral spectrum at 1% CH_4, $m_{28/29}$ was ~ 2 orders of magnitude. In positive ion mode, m/z 29 exceeds m/z 28 at 39% (Table 4.4). Mass 28 can be attributed to $HCNH^+$, $C_2H_4^+$ or N_2^+. Carrasco et al. (2012) showed that an increase in m/z 28 for neutral species, was not necessarily due to N_2, but mainly C_2H_4. The formation of $C_2H_4^+$ depends on methane, and occurs through the rearrangement reaction (Carrasco et al., 2008):

$$\mathrm{CH_2{}^+ + CH_4 \longrightarrow C_2H_4{}^+ + H_2} \tag*{\{20\}}$$

However, according to Vuitton, Yelle, and McEwan (2007), $HCNH^+$ had a density over an order of magnitude greater than $C_2H_4^+$. Therefore, $HCNH^+$ is likely the prevailing ion at this mass.

$HCNH^+$ is mainly formed by proton attachment, by Reaction 21, but can also directly depend on a reaction with methane (Reaction 22),

$$C_2H_5{}^+ + HCN \longrightarrow HCNH^+ + C_2H_4 \tag*{\{21\}}$$

$$N^+ + CH_4 \longrightarrow HCNH^+ + H_2 \tag*{\{22\}}$$

Mass 29 can be $C_2H_5{}^+$ or N_2H^+. As noted previously, N_2H^+ might be dominant at 1% CH_4, whereas $C_2H_5{}^+$ is the main ion at higher initial methane concentrations. Yelle et al. (2010) propose a mechanism where N^+ reacts with hydrogen by proton transfer (Reaction 23), and the formed NH^+ reacts with neutral N_2 (Reaction 24).

$$N^+ + H_2 \longrightarrow NH^+ + H \tag*{\{23\}}$$

$$NH^+ + N_2 \longrightarrow N_2H^+ + N \tag*{\{24\}}$$

Two possible reactions can form $C_2H_5{}^+$, according to Vuitton, Yelle, and McEwan (2007) and Carrasco et al. (2008):

$$CH_3{}^+ + CH_4 \longrightarrow C_2H_5{}^+ + H_2 \tag*{\{25\}}$$

$$CH_5{}^+ + C_2H_4 \longrightarrow C_2H_5{}^+ + CH_4 \tag*{\{26\}}$$

Regarding the formation of H_2 relevant to Reaction 23, Lebonnois, Bakes, and McKay (2003), and later Krasnopolsky (2009) presented a scheme where H_2 is linked to the amount of methane following $H + CH_2 \longrightarrow H_2 + CH$. Methane controls the production of H_2 which, according to Reaction 23, can eventually control the N_2H^+ production. Here again however, the m/z 29 proportion decreases with increasing CH_4 (39% to 11% for example from 1% to 5% CH_4). Ongoing work in our lab focuses on N_2-H_2 mixtures, avoiding the carbon contribution from methane. We find that N_2H^+ is the dominant ion for H_2 mixing ratios $>5\%$ (A. Chatain, private communication). So given an abundant enough H_2 reservoir, N_2H^+ should not be neglected.

The C_3 group is mainly represented by m/z 42 (e.g. ∼10% at 5% CH_4, see Table 4.4), and can be attributed to CH_3CNH^+ in agreement with the neutral acetonitrile detected in abundance in Gautier et al., 2011. In our case, m/z 42 is largely the main ion detected. It can follow two protonation reactions:

$$HCNH^+ + CH_3CN \longrightarrow CH_3CNH^+ + HCN \tag*{\{27\}}$$

$$C_2H_5{}^+ + CH_3CN \longrightarrow CH_3CNH^+ + C_2H_4 \tag*{\{28\}}$$

Sciamma-O'Brien, Ricketts, and Salama (2014) examined the first products formed by $N_2-CH_4-C_2H_2$ mixtures, where C_3 species such as CH_3CN^+ were sensitive as to whether or not a source of nitrogen (N_2) was present. In its absence, m/z 39 was mostly represented by $C_3H_3^+$. Otherwise, CH_3CN^+ was favored at m/z 41.

Apart from m/z 42, the only other substantial C_3 contribution in our experiments occurs at 10% CH_4, with a m/z 39 ratio of ∼3%. This intense formation of $C_3H_3^+$ at m/z 39 agrees with the ion-neutral schemes proposed by Vuitton, Yelle, and McEwan (2007), Carrasco et al. (2008), Krasnopolsky (2009), and Sciamma-O'Brien, Ricketts, and Salama (2014):

$$\mathrm{CH_3}^+ + \mathrm{C_2H_2} \longrightarrow \mathrm{c,l\text{-}C_3H_3}^+ + \mathrm{H_2} \qquad \{29\}$$

$$\mathrm{C_2H_5}^+ + \mathrm{C_2H_2} \longrightarrow \mathrm{c,l\text{-}C_3H_3}^+ + \mathrm{CH_4} \qquad \{30\}$$

$$\mathrm{C_2H_4}^+ + \mathrm{C_2H_2} \longrightarrow \mathrm{c,l\text{-}C_3H_3}^+ + \mathrm{CH_3} \qquad \{31\}$$

Sciamma-O'Brien, Ricketts, and Salama (2014) find their highest m/z 41 intensity when adding C_2H_2 to their mixture, and explain its presence with the two following reactions, linked to C_2H_2 incorporation:

$$\mathrm{C_2H_2}^+ + \mathrm{CH_4} \longrightarrow \mathrm{C_2H_5}^+ + \mathrm{H} \qquad \{32\}$$

$$\mathrm{C_2H_3}^+ + \mathrm{CH_4} \longrightarrow \mathrm{C_3H_5}^+ + \mathrm{H_2} \qquad \{33\}$$

By incorporating neutral acetylene, which Dubois et al. (2019) found to be on the order of $\sim 10^{13}$ cm^{-3} produced during a 2h discharge at 10% CH_4, $C_3H_3^+$ at m/z 39 is particularly abundant in mixtures of high methane amount. Unlike what Sciamma-O'Brien, Ricketts, and Salama (2014) found regarding m/z 41 being their most abundant ion, m/z 42 is the main ion in all of our spectra. We find it to be most abundant at 5% CH_4.

Finally, the most abundant C_4 ion is m/z 52, which increases with increasing methane concentration. Sciamma-O'Brien, Ricketts, and Salama (2014) noticed an increase of this ion only when injecting C_6H_6 to their 10% N_2-CH_4 mixture, and attributed it to the $C_4H_4^+$ benzene fragment. In our case, we detect it in all three methane conditions. Benzene may be a hydrocarbon aromatic product in our plasma, although its detection has been inconclusive (Gautier et al., 2011; Carrasco et al., 2012). Therefore, a $C_4H_4^+$ attribution is ambiguous here. The cyanogen $C_2N_2^+$ and propiolonitrile HC_3NH^+ cations are the two other potential candidates. Gautier et al. (2011) noted the presence of neutral cyanogen using gas chromatography coupled with mass spectrometry, especially with at 1% CH_4. Carrasco et al. (2012) firmly confirmed its presence. C_2N_2 can form from two recombining CN radicals, or from the reaction between HCN and a CN radical (Yung, 1987; Seki et al., 1996), and can be an important ion in particular, at 1% CH_4. Protonated propiolonitrile HC_3NH^+ forms via two proton transfer reactions (Reactions 34 and 35), and are consistent with higher methane amounts, and a shift in peaks from m/z 51 to m/z 52 (Figure 4.19). This absence of peak shift in the 1% CH_4 neutral and ion spectra (Figure 4.18) and m/z 52 being the most intense to begin with, confirms the attribution of $C_2N_2^+$ for m/z 52 in the positive ion spectrum at 1% CH_4.

$$HCNH^+ + HC_3N \longrightarrow HC_3NH^+ + HCN \tag{34}$$

$$C_2H_5{}^+ + HC_3N \longrightarrow HC_3NH^+ + C_2H_4 \tag{35}$$

4.4.2 Contribution of aliphatic, amine and nitrile positive ion precursors for tholin growth

The gas phase precursors present in the plasma form an extensive population of cations, whose ion-molecule reactions appear to mainly rely on protonation processes. These ions consist of nitriles ($HCNH^+$, $C_2N_2{}^+$), amine ($NH_4{}^+$), aliphatics (e.g. $CH_5{}^+, C_2H_3{}^+, C_2H_5{}^+, C_3H_3{}^+$) and some imines (e.g. $CH_2NH_2{}^+$). Constraining the major ion tholin precursors is critical in understanding pathways to their formation in the laboratory, as analogs of Titan's aerosols.

Infrared absorption of film solid phase material produced in the PAMPRE reactor was done by Gautier et al. (2012). They found that changing the methane mixing ratio from 1% to 10% significantly impacted the absorption coefficient of tholins, particularly that of primary and secondary amine, aliphatic methyl and −CN/−NC regions. At low CH_4 concentration, the amine signature is most intense while the aliphatic bands are hardly present. The saturated and unsaturated nitriles are absorbant, and the saturated ones mostly remain up to 5% CH_4. This amine influence at 1% and 5% CH_4, mostly represented by $NH_4{}^+$ in the current gas phase study, is consistent with the solid phase infrared analysis by Gautier et al. (2012). Future experiments probing intermediate methane conditions would be interesting in order to evaluate the sensitivity of main ions like $CH_3{}^+$, $NH_4{}^+$, $HCNH^+$, N_2H^+ to a broader range of methane mixing ratios. Aliphatic cations are especially important at 10% CH_4, where we detect the most ions with wider block distributions. This is in agreement with neutral gas phase studies (Gautier et al., 2011; Carrasco et al., 2012; Dubois et al., 2019) that found an increased production of volatiles with high methane concentrations. Cation pathways that might occur in these conditions rely on the efficient production of e.g. $CH_3{}^+, C_2H_2{}^+, C_2H_4{}^+, C_2H_5{}^+$ (see Section 4.4.1). On the contrary, a small methane concentration was shown by Carrasco et al. (2012) to produce almost exclusively nitrogen-bearing volatile compounds. Our results show 1% CH_4 spectra largely dominated by the two m/z 28 and m/z 29 C_2 species, attributed to $N_2{}^+/HCNH^+$ and N_2H^+, respectively. As a result, ion-molecule reaction schemes for the production of tholins involving species such as $NH_4{}^+$, N_2H^+ and $HCNH^+$ might be favored.

Sciamma-OBrien et al. (2010) found an optimum tholin production for a 3-5% initial methane concentration. At 5% CH_4, the C_2 represents ∼44% of all species, and are mainly supported by $HCNH^+$ and $C_2H_5{}^+$. Our results agree with previous studies by Pernot et al. (2010) and Gautier et al. (2014) which indicated copolymeric HCN/C_2H_4 and poly-$(CH_2)_m(HCN)_n$ structure found in the tholin material. These patterns also seem to be found as cation precursors.

The contribution of m/z 42 attributed to CH_3CNH^+ is more intense than some of the C_1 and C_2 species. As seen in the previous section, its production is favored by increasing methane, specifically by $HCNH^+$ and $C_2H_5{}^+$. Protonated acetonitrile could be a key positive ion precursor in the peak tholin production region of 5% CH_4. A model where aliphatic chain precursors, along with some amine and nitrile cations are significant at 5% CH_4, is consistent with the solid phase analysis by Gautier et al. (2012).

4.4.3 Comparisons with the INMS T40 measurements

The INMS measurements are characterized by a repetition of block patterns separated by 6-8 Da., and 1-6 Da. in the PAMPRE spectra. The INMS data shows a significant contribution of the C_2 group, ~47% at 1097 km. Vuitton, Yelle, and McEwan (2007) determined that at the ionospheric peak during T5, the primary ions formed by ionization are quickly converted into higher mass hydrocarbons, such as $C_2H_5{}^+$ and c-$C_3H_3{}^+$ for example. The few nitrogen-bearing compounds are led by $HCNH^+$, CH_3CNH^+ and HC_3NH^+, with densities of 4.6×10^2, 7.3×10^1 and 1.4×10^2 cm^{-3}, respectively. We find matchings with these peaks obtained during T40, in our 5% and 10% CH_4 spectra, with one discrepancy at m/z 39/41. The C_3 ions detected during T40 are dominated by m/z 39 and m/z 41, which neither stand out in our spectra, except for m/z 39 in the 10% CH_4 condition, which we attributed to $C_3H_3{}^+$. Comparing these findings with neutral spectra is essential for interpretation. Acetonitrile was unambiguously attributed to m/z 41 by Gautier et al. (2011) and Carrasco et al. (2012) in their neutral gas phase studies, and correlated with methane concentration. Protonation of acetonitrile seems therefore likely to explain its significant presence, notably at 5% CH_4 (Table B.1), following Reaction 27.

Westlake et al. (2012) used a 1-D photochemical model which was able to reproduce the ion-molecule chemistry between the primary ion products, using retrieved INMS data from the same T40 flyby. They deducted that among the two major nitrogen-bearing species in the C_3 group, i.e. HC_2NH^+ and CH_3CNH^+, the latter had a higher density by a factor of ~4 at the ionospheric peak. Overall, the 5% experimental spectrum appears to match well the INMS spectra of the first four groups, as the intensity decreases for higher masses. The 10% CH_4 spectra also reproduce some of the higher mass features, although the group distributions present large wings, which is most likely due to unsaturated hydrocarbons. According to Westlake et al. (2012), the three *major* ions, $CH_5{}^+$, $C_2H_5{}^+$ and $HCNH^+$ are connected through the following reactions:

$$CH_5{}^+ + C_2H_4 \longrightarrow C_2H_5{}^+ + CH_4 \tag{36}$$

$$CH_5{}^+ + HCN \longrightarrow HCNH^+ + CH_4 \tag{37}$$

$$C_2H_5{}^+ + HCN \longrightarrow HCNH^+ + C_2H_4 \tag{38}$$

Table 4.6 shows a comparison of these three major ions between our experimental normalized intensities from Table B.1 (Σ column) and their signal from the T40 flyby near the ionospheric peak ($\Sigma_{T40,1150km}$ row) taken from Westlake et al. (2012). On average the 1% and 5% CH_4 row values for these three ions match with the intensities of T40, except for $C_2H_5{}^+$ which is much higher at 1% CH_4. Note however that, at 1% CH_4 in particular, N_2H^+ may also be an important ion at m/z 29 in our experimental spectra, as explained in Section 4.4.1.

TABLE 4.6: Relative contributions of the major ions CH_5^+, $C_2H_5^+$ and $HCNH^+$ in all three initial methane concentrations, taken from Table B.1. The last row corresponds to the values from Table 4.5, compared with the ones from Westlake et al. (2012), denoted W2012. The m/z 29 contribution attributed to N_2H^+ at 39% is only given in a nitrogen-rich mixture. Other values correspond to the $C_2H_5^+$ attributions.

$[CH_4]_0$	CH_5^+	N_2H^+	$C_2H_5^+$	$HCNH^+$	Σ
	m/z 17	m/z 29		m/z 28	
1%	1%	39%	-	33%	74%
5%	1%	-	11%	25%	37%
10%	2%	-	10%	18%	30%
Σ_{W2012}	2%	-	14%	50%	66%
$\Sigma_{T40,1097km}$	1%	-	10%	35%	46%

Future work studying methane concentrations between 1% and 5% could improve this comparison and narrow in the methane mixing ratio that could best reproduce the contributions of these major ions with those observed with INMS. These comparisons have also shown the prevalent role of $HCNH^+$ and $C_2H_5^+$ as major cation precursors for tholin production.

4.4.4 Detecting cations in the era of ground-based observations

In the post Cassini era, more Earth-based observations of Titan are required to pursue the legacy of the Cassini-Huygens mission. Complementary laboratory experiments are also needed in order to improve our understanding of Titan's organic gas phase and solid phase chemistry. Current and recent utilization of the ALMA telescope has given us major results based on detections of neutral species such as N-bearing, oxygen, isotopic and sulfurated species (Cordiner et al., 2014b; Molter et al., 2016; Serigano et al., 2016; Palmer et al., 2017; Thelen et al., 2017; Teanby et al., 2018). Future space-based observations with the James Webb Telescope (JWST) and other optical telescopes are also promising, although they will probe from the haze layers all the way down to the surface (Nixon et al., 2016). In particular, observing positive ions in Titan's upper atmosphere would be unique, especially since Titan passed aphelion in April of 2018 and has entered an 8-year southern winter, which could potentially impact the volatile distribution in the upper atmosphere. Potential frequent detections could further (i) characterize, (ii) constrain mixing ratios in the ionosphere, or (iii) detect new molecules based on computational quantum modeling. The latter are necessary to provide rotational frequency lines, needed for predicting ion frequencies and hopefully detect them.

The aminomethyl ($CH_2NH_2^+$) cation is a potential candidate for future observations. Indeed, this species participates in the hydrogenation of HCN, which is known to eventually form aminoacetonitrile (NH_2CH_2CN), itself a precursor for glycine, which uses the Strecker synthesis in its final stage (Bernstein, Bauschlicher, and Sandford, 2004; Danger et al., 2011; Theule et al., 2011; Noble et al., 2013). Extraterrestrial objects such as comets and meteorites can potentially be hosts to such molecules (i.e. CH_2NH_2, HCN, $CH_2NH_2^+$...) relevant to prebiotic conditions and amino acids. Its recent theoretical analyses by Fortenberry et al. (2017) makes it a hopeful candidate. Still, detecting positive ions is no easy task, as these ions are short-lived and in trace amounts. Vuitton, Yelle, and McEwan (2007) estimated a 10^{-5} mole fraction of neutral CH_2NH near the ionospheric peak and a $CH_2NH_2{}^+$ density of 4.8×10^1 cm^{-3}. These detections would be constrained to the upper part of the atmosphere as well. The imine intermediate neutral radical counterpart methylene imine $CH_2{=}NH$ (also called methanimine), to which CH_2NH_2 and $CH_2NH_2{}^+$ are closely linked, has been detected in the Sagittarius B2 dark interstellar gas cloud (Godfrey et al., 1973; Oliveira et al., 2001) and whose chemistry is intertwined with ammonia and aminomethyl at high altitudes ($> 1,000$ km), through electron recombination and proton exchange (Yelle et al., 2010).

Another candidate is $HCNH^+$ which models have predicted to be the most abundant positive ion (Fox and Yelle, 1997; Keller, Anicich, and Cravens, 1998; Vuitton, Yelle, and McEwan, 2007; Carrasco et al., 2008). Westlake et al. (2012) described the $HCNH^+$ density as being the result of ion-molecule reactions, dependent on H_2, C_2H_2 and C_2H_4, from retrieved INMS measurements during T40. The close coupling between these neutral and ion molecules is indicative of processes that require further observations, in order to map out some of the many ions present in the upper atmosphere. HCN is the most abundant nitrile trace species present on Titan, thus acting as the incipient to a very complex and long chain of molecular reactions. Indeed, the hydrogenation of HCN, in particular at low temperatures relevant to Titan's (~ 94 K), serves as a source to more complex nitriles and imines such as CH_3N, CH_2NH, CH_2NH_2 and eventually CH_3NH_2 (Theule et al., 2011). Mapping such species with the advent of radiotelescopes needs theoretical support such as with the rise of quantum spectroscopy modeling (e.g. Fortenberry, 2017) to keep exploring new chemical venues, whether on Titan or beyond. In 2017, I submitted two proposals as PI, intended for radio-observations. The first one (Project 2017.1.01665.S) was for Cycle 5 of the Atacama Large Millimeter/submillimeter Array (ALMA). The second one (Project 2017B-S060) was submitted to the SubMillimeter Array, located at Kilauea, Hawaii.

4.5 Conclusions

We have conducted the first positive ion analysis in our PAMPRE plasma chamber using an ion mass spectrometer, aimed at analyzing the gas phase cation precursors to the formation of Titan tholins. This setup enables us to approach the extracting tube in direct contact with the plasma and analyze the positive ions *in situ*. We used three initial methane concentrations, 1%, 5% and 10%, which showed a wide variability in peak distribution and size among the different conditions.

Furthermore, spectra at 1% CH_4 are mostly dominated by nitrogen-bearing ions, such as $NH_4{}^+$, $HCNH^+$ and N_2H^+. We also found that the spectra in this condition are largely dominated by two C_2 species, m/z 28 and m/z 29, representing $\sim$ 72% of the entire spectrum. The ammonium ion $NH_4{}^+$ is the third major ion with an N_2:CH_4 (99:1) mixing ratio. Positive ions in a methane-rich mixture of 10% CH_4 are more diverse and abundant in hydrocarbon cations. Primary methane ions (CH^+, $CH_2{}^+$, $CH_3{}^+$) dominate the C_1 group. This aliphatic contribution in the gas phase agrees with aliphatic absorption present in the solid phase of 10% CH_4 tholins. The intermediate 5% methane concentration that we chose falls in the optimum of tholin production in our plasma discharge. Here, the ion precursors are composed of protonated nitrile and aliphatic species. $HCNH^+$ and $C_2H_5{}^+$ are major ions. Their dominating presence is in agreement with the HCN/C_2H_4 copolymerization patterns found in tholins. The largest contribution of the large CH_3CNH^+ ion is seen in this condition.

A majority of attributed ions seems to form via proton transfer reactions, consistent with methane injection. The primary ions of the C_1 group are most abundant with a 5% CH_4 mixing ratio, suggesting that at least in this condition, these species are a key precursor reservoir, available to react with larger ions. Our preliminary comparisons with INMS measurements done near the ionospheric peak during the T40 flyby show promising overlaps, particularly with the 1% and 5% CH_4 spectra. Future work should thus explore intermediate concentrations to constrain the importance of the primary ions as key precursors involved in the reaction schemes leading to the formation of Titan tholins.

4.6 Supplemental

IED of positive ions in a 10% CH_4 mixing ratio

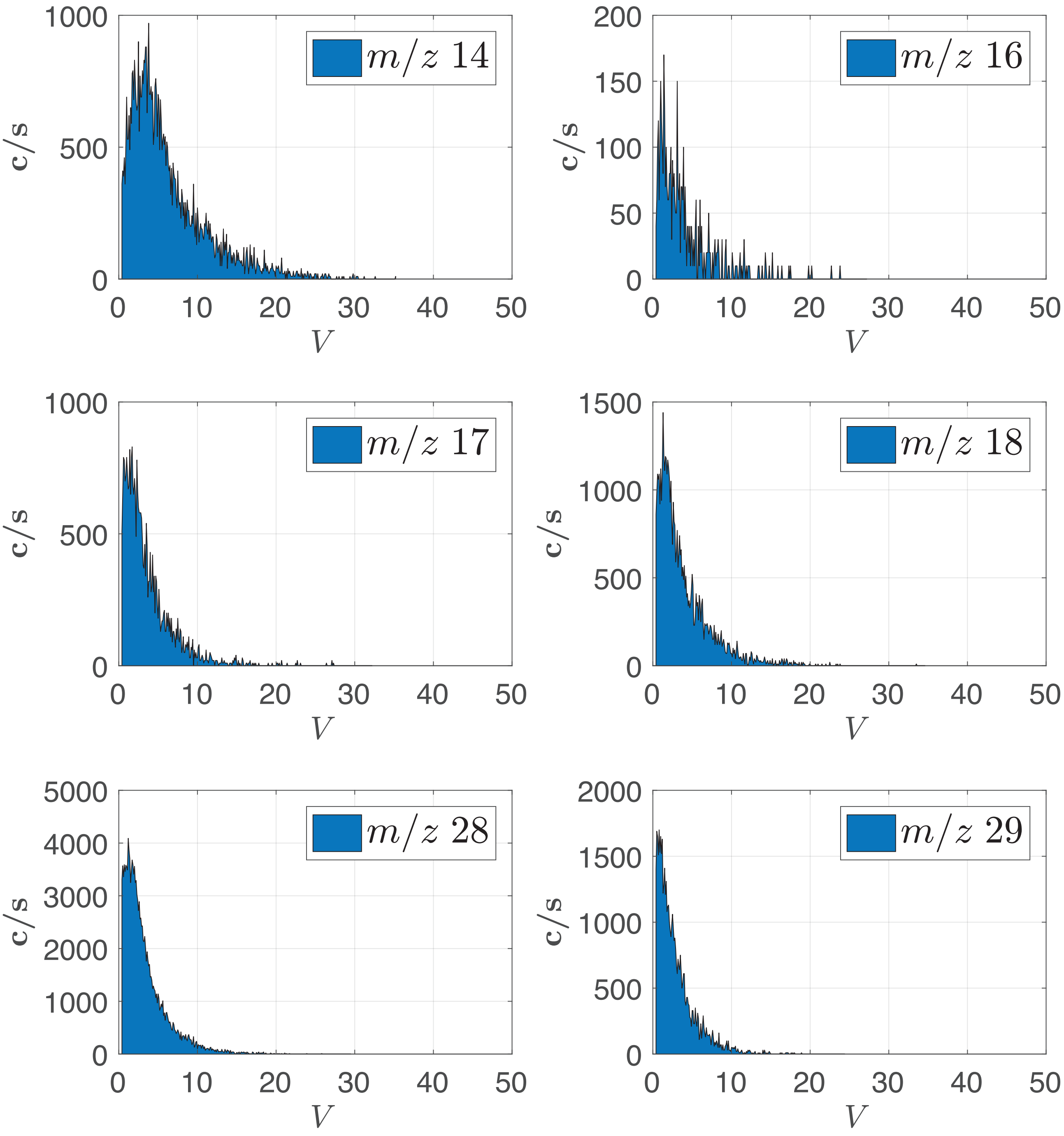

FIGURE 4.29: IEDs with a $[N_2{-}CH_4]_0 = 10\%$ mixing ratio for m/z 14, 16, 17, 18, 28 and 29 ions.

m/z 28 IED in a 5% CH_4 mixing ratio

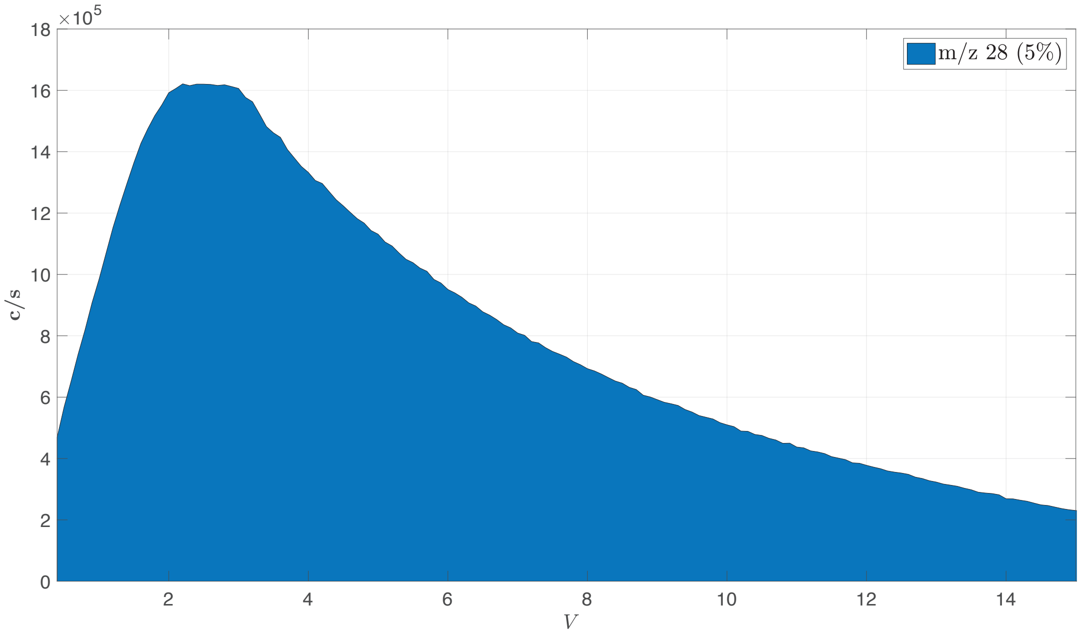

FIGURE 4.30: IED with a $[N_2{-}CH_4]_0 = 5\%$ mixing ratio for m/z 28. The maximum is at 2.2 V. As the two previous conditions have shown similar IEDs for all ions, and tholins are rapidly produced at 5% CH_4, we only obtained an IED for m/z 28.

Any given molecule in Titan's atmosphere undergoes various environments: from its inception with the very first newly formed ion and neutral precursors in the upper atmosphere, to larger, condensed macromolecules condensing with each other near the tropopause. Nearly all of these volatiles formed in Titan's upper atmosphere are destined to condense in the lower stratosphere. The previous chapters were aimed at studying processes relating to the precursor gas phase reactivity, which occur in the upper atmosphere. The following chapter was part of a project where I studied the fate of these molecules, i.e. once the precursors have condensed and likely formed more complex ice mixtures below the tropopause. The results hereafter are still part of an ongoing investigation.

Part II

The Condensed Lower Atmosphere

Chapter 5

Photochemical Activity of HCN-C_4H_2 Ices in Titan's Lower Atmosphere

Abstract

Revealed by the Cassini and Voyager Missions, a plethora of volatile species are formed in Titans upper atmosphere from the initial N_2:CH_4 (98:2%) composition. Most of the volatiles condense in the colder lower atmosphere where they can form icy clouds (e.g. C_4N_2, HCN, C_2H_6) which have been detected above the poles. HCN is the most abundant nitrile in Titans atmosphere and suspected to condensate in Titans lower stratosphere (typically <100 km). Micron-sized HCN ice particles were also observed above the south pole at high altitudes (300 km). This cloud is thought to have been formed in the post-equinox winter polar vortex. In the north polar regions, HCN is also a likely prominent contributor to the *haystack* spectral signature seen at 221 cm^{-1}. These stratospheric ices may contribute as condensation nuclei for ices deeper down in the troposphere. Furthermore, C_4H_2, a simple alkyne formed by the chemistry and relatively abundant in the stratosphere, condenses near 75 km, lower than HCN. C_4H_2 can also absorb the lesser energetic photos at these low altitudes, forming the radical C_4H which then reacts with CH_4, causing the consumption of methane. Consequently, the loss mechanism for C_4H_2 is photochemistry. As soon as C_4H_2 condenses, small molecular and complex accretion with HCN may occur. The reactive state that these ices may undergo with long-UV radiation after they form is still largely unknown. We explore these conditions by stuying HCN-C_4H_2 ice mixtures in the laboratory, by using the Titan Organic Aerosol Spectroscopy and chemisTry (TOAST) setup at JPLs Ice Spectroscopy Laboratory (ISL). These ices are then irradiated at long-UV wavelengths pertaining to these low-altitude regions at low-controlled temperatures. The residue is analyzed using mid-IR spectroscopy. Our results show a solid-state HCN consumption due to irradiation and to C_4H_2 photochemistry, indicating HCN ice particle ageing in the troposphere may be facilitated by more complex condensed nuclei.

5.1 Introduction

Titan's substantive atmosphere is composed of a plethora of gas phase molecules. Hanel et al. (1981) provided the first positive detection of HCN, and at the same time Kunde et al. (1981) detected C_4H_2 in the stratosphere. Since then, hydrogen cyanide in Titans atmosphere is well documented and is known to be the most abundant nitrile trace volatile (Kim et al., 2005; Vinatier et al., 2007), with varied mixing ratios at stratospheric altitudes at different latitude regions ranging from a few 10^{-8} to almost 10^{-6} (Vinatier et al., 2009) using CIRS measurements in the early flybys. Vuitton, Yelle, and McEwan (2007) found HCN mole fractions of $\sim 10^{-4}$ derived from INMS measurements at 1,100 km. Although, the reactive behavior of HCN in the gas and solid phases are limited, its impact on Titans atmospheric photochemical activity appears to be significant with the presence of stratospheric HCN ices (Samuelson et al., 2007; Lavvas et al., 2011; De Kok et al., 2014; West et al., 2016 and Figure 5.1), underlying the importance of studying its chemical behavior in laboratory experiments.

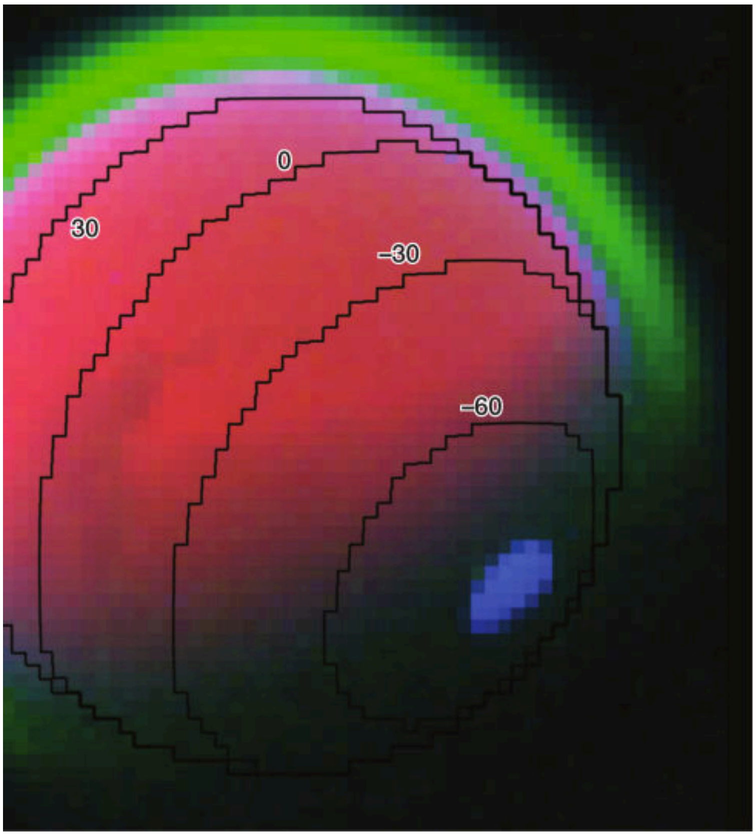

FIGURE 5.1: Titan's southern hemisphere as seen with VIMS (De Kok et al., 2014), with the detection of an HCN cloud in the winter polar vortex (blue) at 300 km. Red and green correspond to the illuminated surface and non-LTE emission, respectively. The presence of HCN ice particles at these high altitudes was unexpected and explained by an efficient post-equinox cooling.

Most of Titan's atmospheric reactivity occurs at high altitudes, coupling neutral and ion chemistry, under energetic UV photon radiation. Albeit, very little radiation reaches the surface, most of it being cut-off in the ionosphere, mesosphere and upper stratosphere. Thus, it has been assumed that the entirety of atmospheric reactivity takes place in these higher regions, while only ice condensation and precipitation occurs at the lower altitudes. Recent studies (Gudipati et al., 2013; Couturier-Tamburelli et al., 2014; Couturier-Tamburelli, Piétri, and Gudipati, 2015; Anderson et al., 2016; Rahm et al., 2016; Couturier-Tamburelli et al., 2018 suggest otherwise. We take this idea further, by studying the chemistry of a key volatile present at Titan, HCN, with high prebiotic interest (Oró, 1961; Danger et al., 2011; Theule et al., 2011; Hörst et al., 2012; He and Smith, 2014; Rahm et al., 2016). Models related to stratospheric solid-state chemistry are limited, and a current *in situ* investigation is not possible. This is why, at present, laboratory measurements remain critical in understanding Titan's atmosphere.

The initial formation of HCN and C_4H_2 occurs in the upper atmosphere. The ground state of atomic nitrogen N(^{4}S) reacts with CH_3 to form the methylene-amidogen radical H_2CN (Reaction 39) which can form HCN with atomic hydrogen (Reaction 40).

$$\mathrm{N(^4S) + CH_3 \longrightarrow H_2CN + H} \tag{39}$$

$$\mathrm{H_2CN + H \longrightarrow HCN + H_2} \tag{40}$$

The production of C_4H_2 relies on the presence of acetylene (Reaction 41. It is mainly lost through photolysis Reaction 42. Its relative abundance in the ionosphere (1077 km) detected with INMS was on the order of 10^{-5} (Cui et al., 2009a). In the mesospheric layer, stellar occultations seen with UVIS determined a 7.6×10^{-7} relative abundance at ~600 km (Koskinen et al., 2011). This abundance drops to 10^{-9} in the stratosphere (Coustenis et al., 2010).

$$\mathrm{C_2H + C_2H_2 \longrightarrow C_4H_2 + H} \tag{41}$$

$$\mathrm{C_4H_2 + h\nu \longrightarrow C_4H + H} \tag{42}$$

In the lower stratosphere, near 100 km, the majority of hydrocarbon and N-bearing compounds reach their saturation levels and condense. HCN and C_4H_2 are one of the first compounds to condense (Barth, 2017) $>$ 80 km with temperatures ~70 K. This creates condensation nuclei which can be recipients for other compounds to coagulate onto their surface. This coagulation can also occur on larger aerosols and macromolecular compounds. These condensates descend the atmospheric column and eventually precipitate down to the surface. This condensation+precipitation phase was generally considered to be relatively inert, given the low energy UV photons reaching these layers. High-energy-UV-induced photolysis occurring in the upper atmosphere is more efficient than the FUV wavelengths reaching the lower stratosphere. However, photons at $\lambda > 300$ nm can still penetrate at depths below 100 km (Lavvas, Coustenis, and Vardavas, 2008). HCN is non-absorbant at $\lambda > 225$ nm, while C_4H_2 has one of the largest absorbance ranges in the UV among the major unsaturated hydrocarbons. Due to the significant photosensitivity of C_4H_2 at these wavelengths, it makes for a potential good candidate to initiate UV-induced reactivity.

Here, this reactivity, or lack thereof of HCN, is tested. We used the Acquabella cryogenic chamber to simulate the temperature and radiation environment which these icy aerosols in Titan's lower stratosphere undergo. HCN and C_4H_2 were synthesized in the laboratory and deposited on a sapphire window and tholin films. They were irradiated at far-UV wavelengths bearing to these low-altitude regions, under low-controlled temperature conditions. The residue was analyzed with long-IR absorption.

5.2 Experimental Setup

Simulating Titan's lower atmosphere temperatures requires working at controlled low temperatures (< 150 K). A cold chamber is necessary. The chamber used in this study is briefly described hereafter, and in Chapter 2 in more detail.

5.2.1 The Acquabella chamber

The Acquabella chamber (Figure 5.2) is located at the Ice Spectroscopy Laboratory (ISL) of NASA's Jet Propulsion Laboratory (JPL) in Pasadena, CA, USA. The experiment consists of the main cryo-chamber which is made of stainless steel. It contains three ZnSe windows (Figure 5.2) used for infrared and laser transmissions. Using a Pfeiffer turbo molecular pump, typical pressure at room temperature is 10^{-7} mbar and can go down to 10^{-9} below 100 K. Pressure is measured with a Pirani penning gauge. The cryostat is maintained by an Advanced Research System closed-circuit helium system.

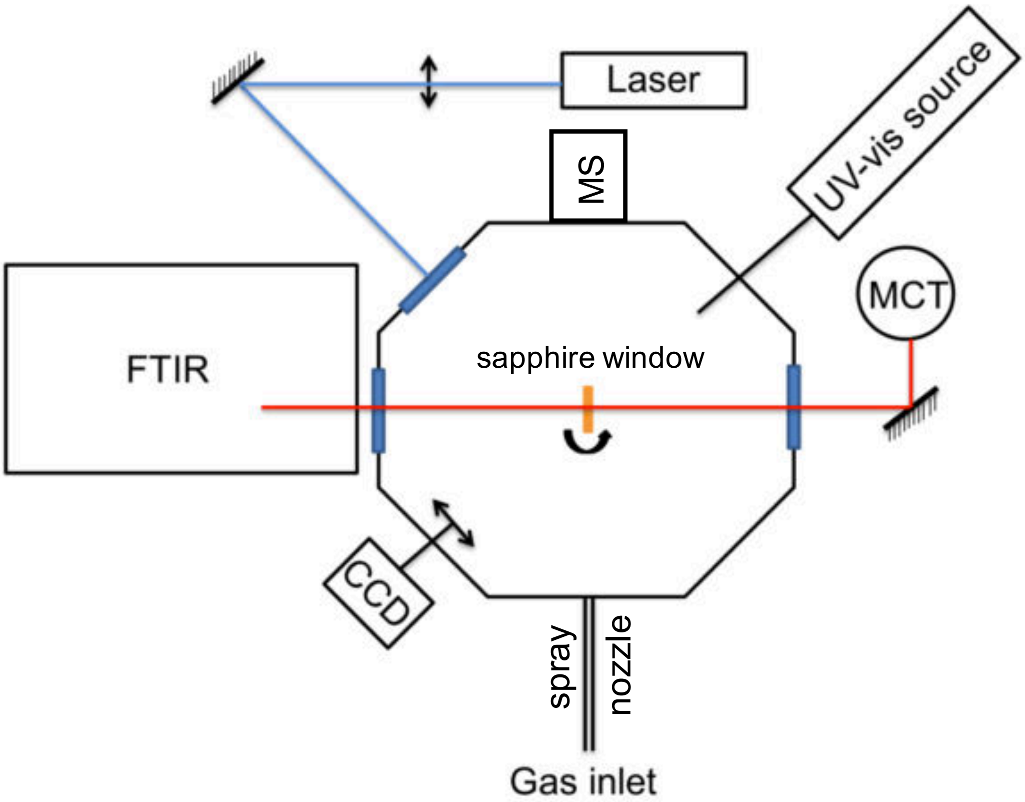

FIGURE 5.2: Acquabella chamber top-view diagram, adapted from Fleury, 2015. The sample holder containing the sapphire window is at the center. It can be rotated over 360°. The MCT corresponds to the Mercury Cadmium Telluride infrared detector.

Mass spectrometry

The volatile content inside the chamber is analyzed thanks to a Residual Gas Analyzer RGA200 from Stanford Research Systems (SRS) fitted to the cold chamber. We use a 0.1 amu resolution, with an electron emission energy of 70 eV and a filament current of 1 mAmps. The filament consists of two thoriated-iridium ThO_2/Ir filaments for electron emission. This RGA system has a 5×10^{-14} torr detection limit, and six orders of magnitude dynamic range for a single scan. Scans are taken during gas deposition in order to monitor and track the presence and partial pressures of the gases considered, HCN and C_4H_2.

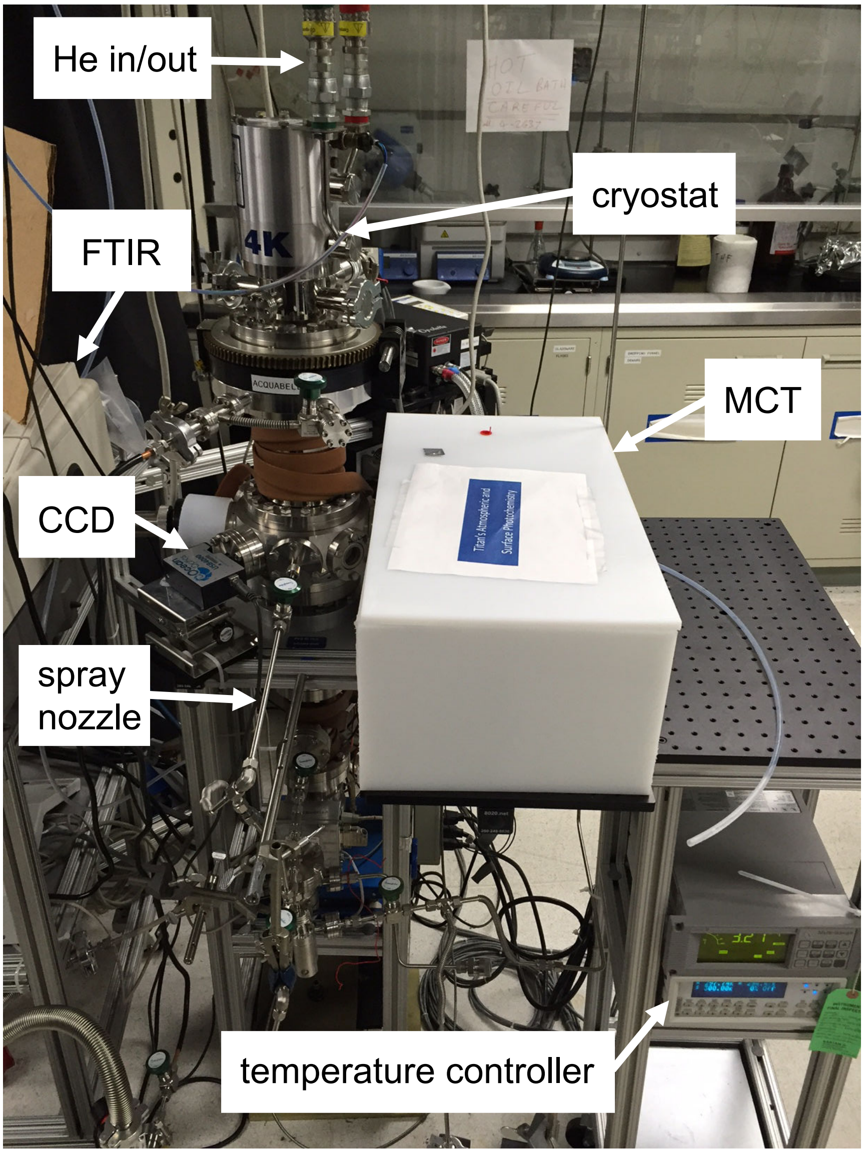

FIGURE 5.3: Cryogenic setup. On the left-hand side, the chamber surrounded by the FTIR, the spray nozzle, the UV-VIS CCD detector and cooling system.

Sample holder

Figure 5.4 shows a close-up of the cryostat, with the sample holder containing the sapphire substrate. The latter is 2 mm thick and 25 mm in diameter. During our work, I irradiated four different types of samples (i) HCN ice deposited on 10% CH_4 tholins, (ii) HCN ice deposited on 1% CH_4 tholins, (iii) pure HCN ice on sapphire window and (iv) HCN-C_4H_2 ice on sapphire window. Figure 5.5 shows schematic diagrams of the film samples. We assume as a first order that the incoming irradiation hits the film with an angle $\theta = \pi/2$. This assumption will be necessary when estimating the film thickness in section 5.3.

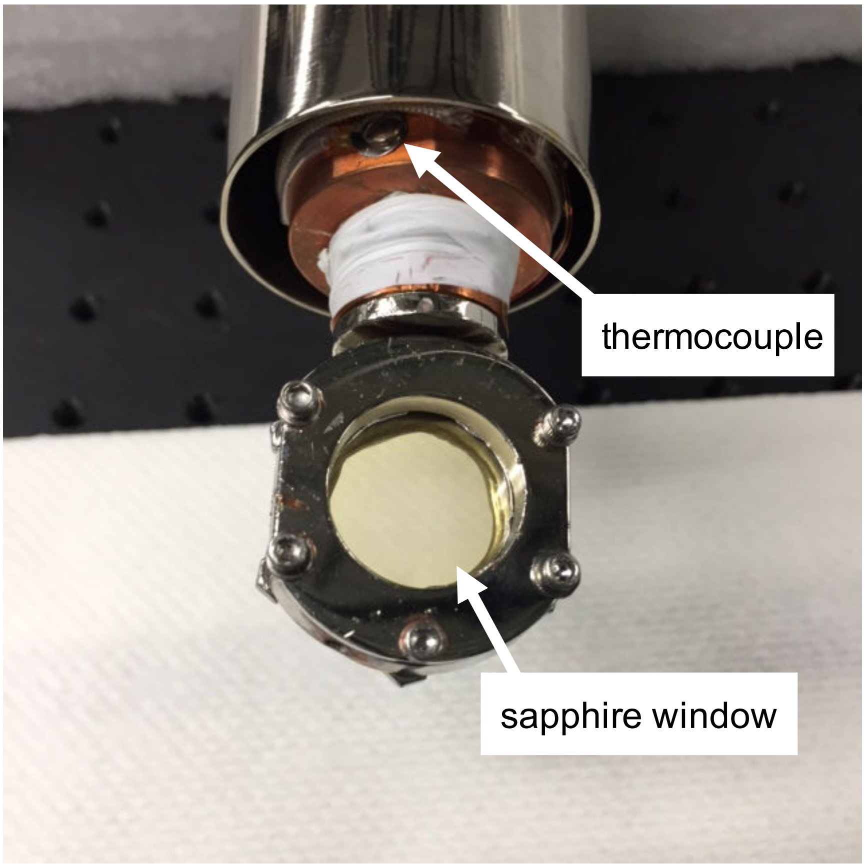

FIGURE 5.4: The sample holder holds a sapphire window substrate, with a N_2-CH_4 10% yellowish-coated tholin deposition, produced in the PAMPRE reactor. The sapphire windows are cleaned with isopropanol and in an ultrasonic bath in between experiments to remove any room-temperature residue.

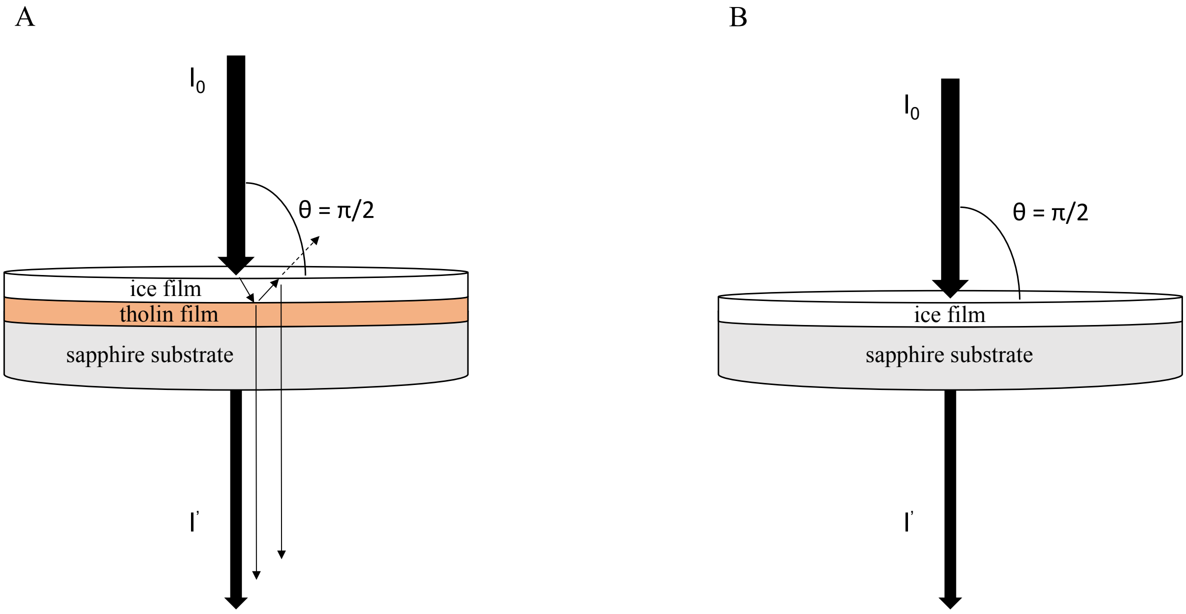

FIGURE 5.5: Schematics of the substrate/sample holder setup in UV-VIS transmission configuration. A: an example of an ice deposition sprayed onto a tholin thin film itself on a sapphire window. Internal reflections are also drawn. B: ice mixture sprayed directly onto the sapphire window, without any tholins.

FTIR spectroscopy

The Fourier Transform InfraRed instrument is a Thermo Scientific Nicolet 6700, and measurements were done in transmission mode. The infrared beam goes through the sample at a 90° angle (Figure 5.2) and reaches the mercury cadmium telluride (MCT/B) detector out of the second ZnSe window. In order to avoid any thermal perturbations to the signal, the detector is cooled down with liquid nitrogen. The sapphire window absorption cut-off starts at 1600 cm^{-1}. 300 scans were collected in the 1000-8000 cm^{-1} range. The chosen resolution was 1 cm^{-1}.

UV-VIS absorption

In complement to the previous techniques, I also used UV-VIS spectroscopy in the 250-1000 nm range, to observe any potential changes in the wavelengths at which we irradiate. I used an Ocean Optics USB4000 spectrometer, with a deuterium-hydrogen lamp as a beam source. The lamp is connected to the chamber through a first optical fiber, at 90° from the sample. At the other end, a lens refocuses the beam before it reaches a second optical fiber. There, a Charge-coupled Device (CCD) detector measures the transmitted signal I' (Figure 5.5). Measurements were typically averaged over 300 scans with an integration time of 150 ms.

5.2.2 HCN and C_4H_2 syntheses

HCN is chemically highly toxic. It is an odorless and invisible volatile, and a blueish to white liquid under 26.7° C (Hartung, 1994; Budavari, O'Neil, and Smith, 1996). We must carefully synthesize it in the laboratory first. C_4H_2 is also synthesized in the laboratory. Their respective syntheses are described hereafter.

HCN synthesis

The synthesis of the HCN monomer requires great care and precaution. I synthesized HCN at the TOAST Laboratory at JPL under a fume hood in controlled pressure conditions. The technique we used has already been described in Gerakines, Moore, and Hudson, 2004; Romanini et al., 2007; Danger et al., 2011; Theule et al., 2011; Mamajanov and Herzfeld, 2014; Couturier-Tamburelli et al., 2018. Masterson and Khanna, 1990 used a nearly identical reaction with a different base reactant, sodium cyanide NaCN. Bonnet et al., 2013 also used a similar acid/base reaction, although they focused on HCN polymer synthesis. In our case, the synthesis uses a straightforward thermal reaction, whereby stearic acid $CH_3(CH_2)_{16}COOH$ is in excess and mixed with potassium cyanide KCN. The reaction forms potassium stearate $C_{18}H_{35}KO_2$ which remains in solid phase and HCN in vapor phase (Reaction 43). Both reactants are approximately in equimolar proportions 1.2 mmol for KCN and 1.4 mmol for the stearic acid. We used ~78.1 mg of KCN and 398.3 mg of stearic acid. Once both solids (still non-reactive at this stage) have been added into the flask, the latter is sealed onto the vacuum manifold (Figure 5.6), and the line is pumped for 24h. The flask is then heated to about 350 K, in order to vaporize the solid reactants, thus forming potassium stearate and HCN, following Reaction 43. As the reaction occurs, a pressure gauge fitted at the top of the manifold (Figure 5.6) monitors the HCN release. The heating was generally applied for 2-3 mn, until an HCN pressure of ~ 2 mbar in the manifold was reached. In contact with room-temperature water, the flask cools down, the reactants re-solidify, and the reaction stops. 2 mbar of HCN kept in the vacuum manifold is enough for 5-6 depositions (see Section 5.2.3).

$$\mathrm{KCN} + \mathrm{CH_3(CH_2)_{16}COOH} \xrightarrow{80\,^\circ\mathrm{C}} \mathrm{C_{18}H_{35}KO_2} + \mathrm{HCN} \qquad \{43\}$$

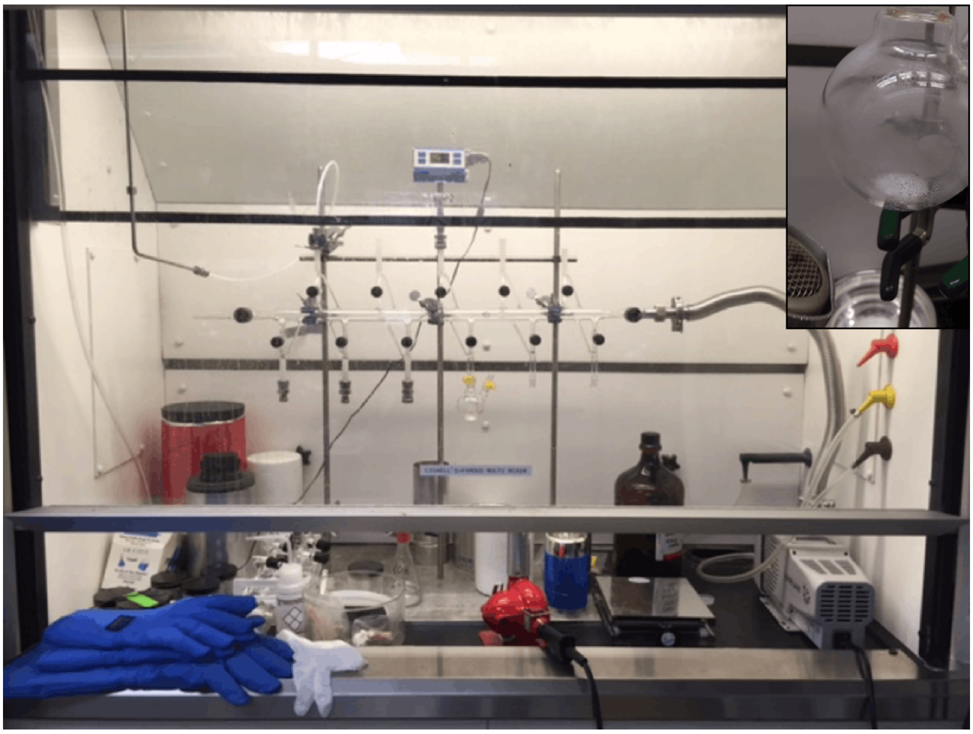

FIGURE 5.6: The ramp under a fume hood that we used, connected to a primary pump, on the right. The HCN is synthesized in the Schlenk flask (see inset), transferred to the manifold until the pressure is stable, and finally reaches the cryogenic chamber. The flask seen in the upper-right corner contains the stearic acid in excess, and the KCN as a white powder.

C_4H_2 synthesis

The synthesis of diacetylene that we use is actually the first part of a 3-step synthesis of HC_5N. Here however, we are only interested in the first step. According to the protocol described by Brandsma, 2004, C_4H_2 is formed from the exothermal reaction between 1,4-Dichloro-2-butyne $C_4H_4Cl_2$ and KOH in a H_2O-DMSO (dimethyl sulfoxide) mixture (Reaction 44). $C_4H_4Cl_2$ starts reacting with the soluble KOH at 70°. DMSO serves to increase the solubility of 1,4-Dichloro-2-butyne in the aqueous phase. An intermediate step first forms the unstable compound chlorobutatriene C_4H_3Cl. The latter may precipitate to form a residue polymer if the dichlorobutyne is added too quickly into the mixture. N_2 is also added into the aqueous solution in the apparatus, serving two functions: reducing the diyne's explosive decomposition by diluting it in N_2, and helping its transport from the aqueous solution to the cold trap. The cold trap consists of a Liebig condenser. This condenser was stored in a cooler at -40°C and could typically be used for several experiments before a new synthesis would be needed.

$$\mathrm{Cl{-}CH_2C{\equiv}C{-}CH_2{-}Cl} \xrightarrow[\mathrm{H_2O+DMSO}]{2\,\mathrm{KOH},\ 70\,^\circ\mathrm{C}} [\mathrm{Cl{-}CH{=}C{=}C{=}CH_2}] \xrightarrow{95\,^\circ\mathrm{C}} \mathrm{H{-}C{\equiv}C{-}C{\equiv}C{-}H} \qquad \{44\}$$

5.2.3 Gas deposition

Once our volatiles of interest are synthesized, they are transferred to the main line, before being vapor-deposited onto the window, through the spray nozzle seen in Figures 5.3 and 5.7. Depositions are usually carried out for ∼10 min, which typically correspond to films of a few hundreds of nm (Section 5.3.1).

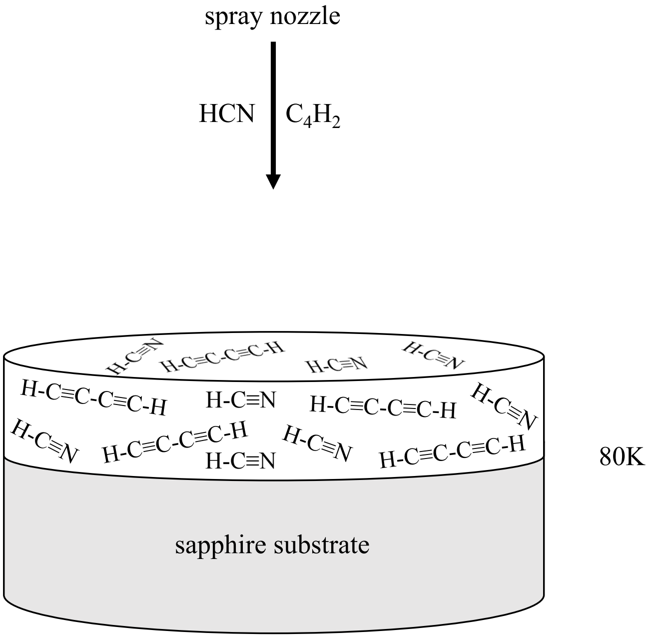

FIGURE 5.7: Schematic diagram of an HCN-C_4H_2 deposition performed at 80K.

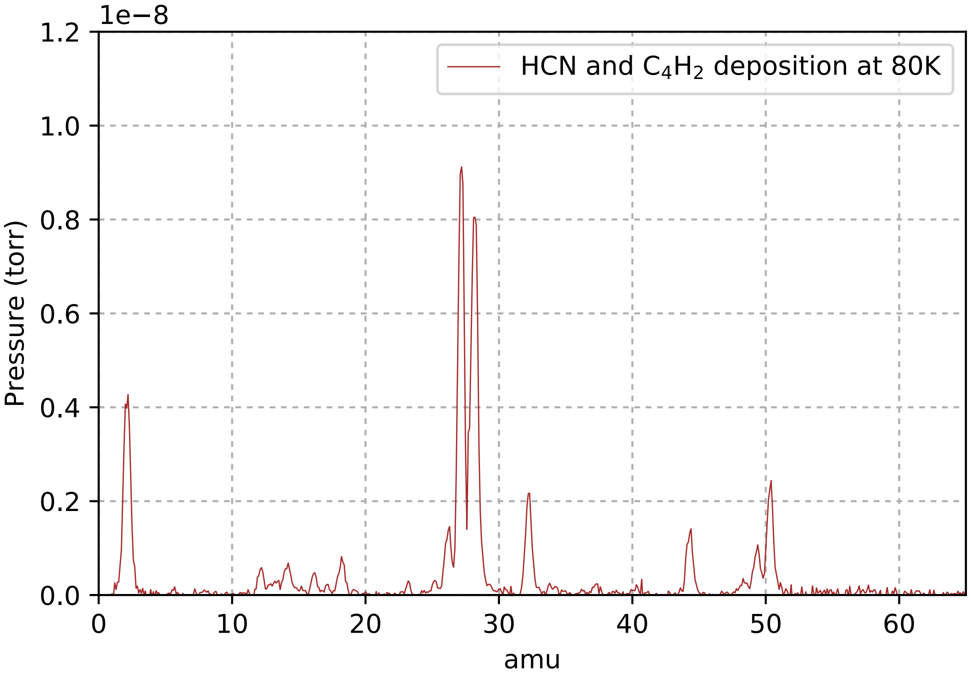

FIGURE 5.8: A mass spectrum taken at 80K during an HCN-C_4H_2 deposition. HCN is visible at m/z 27, with its CN fragment at m/z 26. C_4H_2 at m/z 50 and its m/z 49 and m/z 48 fragments are also visible.

Table 5.1 lists the gas phase spectroscopic properties of HCN and C_4H_2, with their respective ground sates, first excited singlet S_0-S_1 and triplet S_0-T_1 states, as found in the literature. The HCN singlet and triplet thresholds indicate no absorption at irradiations with $\lambda > 225$ nm. For C_4H_2, its potential reaction with HCN would therefore occur in the triplet state T_1 under 355 nm irradiations.

TABLE 5.1: Gas-phase UV-Vis spectroscopic properties of HCN and C_4H_2, with their S_0 ground states, first excited singlet S_0-S_1 and triplet S_0-T_1 thresholds, compiled from Couturier-Tamburelli, Piétri, and Gudipati (2015) and [a]Minaev et al. (2004), [b]Gudipati (1994), [c]Stiles, Nauta, and Miller (2003) and Couturier-Tamburelli et al. (2018), [d]Robinson, Winter, and Zwier (2002), [e]Fischer and Ross (2003), [f]Vila, Borowski, and Jordan (2000)

	Ground state (S_0 dipole moment)	S_0-S_1	S_0-T_1
HCN	2.7^b, 3.02^c λ_D	$\sim155^a$ nm	$\sim225^a$ nm
C_4H_2	0	286^e, 301^e, 298 nm^b	$\sim481^d$, 387^f, 385^b nm

5.2.4 Laser Irradiation

To irradiate our ice samples in the 310-420 nm range, I used a tunable Opotek OPO laser of the Opolette 355 series. It relies on optical parametric oscillator (OPO) technology to achieve UV-Vis-IR wavelengths (410-2400), which can be manually tuned in the UV. The 355 nm pump wavelength is generated by a 5 ns pulse. For wavelengths <300 nm, a Continuum Nd-Yag laser with a quadrupling frequency crystal can be used. The unit is cooled with a closed-loop air-water circuit. A suited optical bench is needed to defocus the beam ($\sim$ 3mm) to avoid multi-photon processes, which is then reflected by a 45° angle, and finally reaches the sample in the chamber. The 10-cm focal length quartz lens in the beam path close to the laser exit helps to expand the laser and reduces any multi-photon absorption processes. At the sample location, the beam is $\sim$ 25mm in diameter. The incoming photon flux at the entrance of the chamber can be calculated using the Planck relation (Equation 5.1), where $\hbar$ is Planck's constant, c the speed of light and λ the considered wavelength.

$$E_{ph} = \frac{\hbar \times c}{\lambda} \tag{5.1}$$

Using Equation 5.1, the corresponding photon flux becomes,

$$Flux = \frac{Power}{E_{ph} \times A} \tag{5.2}$$

where the measured $Power$ is $\sim 0.15\ W$ and A being the approximate effective area ($\sim$ 25 mm) measured after the defocused beam. At this wavelength, we obtain a photon flux of $\sim 5.5 \times 10^{16}\ photons.cm^{-2}.s^{-1}$, on the same order as that calculated by Gudipati et al. (2013).

5.3 Results

In this section I will present our results involving ice photochemistry of N-bearing and hydrocarbon species, under long-UV irradiation. I will first present ice thickness and UV-VIS considerations, and then the dominant ice photochemical changes seen in IR. A series of 16 experiments were performed (see Table 5.2), under various temperature, irradiation and gas phase mixing ratio conditions. A first run included various HCN ice depositions on tholin films (1% and 10% CH_4), exploring wavelengths from 310 nm to 420 nm. A second run revolved around HCN$-C_4H_2$ ice mixtures under 355 nm irradiations.

TABLE 5.2: Compilation of all the experiments that were done with respective temperature, irradiation and mixing ratio conditions.

	Ice mixture	Gas phase ratio	λ (nm)	Accumulated irradiation	T° (K)
1	HCN-tholins (10% CH_4)	100	355	2h	70
2	HCN-tholins (10% CH_4)	100	355	1h	90
3	HCN-tholins (10% CH_4)	100	355	50 min	70
4	HCN-tholins (10% CH_4)	100	355	4h30	70
5	HCN-tholins (10% CH_4)	100	320/310	4h	70
6	HCN-tholins (10% CH_4)	100	310	2h	70
7	HCN-tholins (10% CH_4)	100	310	7h	70
8	HCN-tholins (1% CH_4)	100	330/320/310	3h	70
9	HCN-tholins (1% CH_4)	100	420	4h	70
10	Pure HCN ice	100%	320/310/300	6h	70
11	HCN:C_4H_2	90:10	355	30 min	70
12	HCN:C_4H_2	90:10	355	6h30	70
13	HCN:C_4H_2	80:20	355	20h	70-75
14	HCN:C_4H_2	~60:40	355	1h30 (aborted)	
15	HCN:C_4H_2	~45:55	355	17h	70-100K
16	HCN:C_4H_2	~45:55	355	12h	80K

5.3.1 Fringes and ice thickness

Interference fringes in UV-VIS transmittance spectra can be a valuable way to estimate ice film thicknesses, provided that the film thickness is on the same order as the irradiation wavelength. Fringes occur when constructive and destructive interferences meet between the ice film and the substrate (Figure 5.5). We consider an incident phase angle of $\pi/2$,

$$\arcsin\left(\frac{2d}{\lambda}\right) = \frac{\pi}{2} \tag{5.3}$$

The amount of diffracted light will depend on the thickness of the sample, and the wavelength, according to Equation 5.4.

$$2d = \frac{n}{2} \times \lambda \tag{5.4}$$

with the positive integer $n = 1, 2, 3 ...$.

The total transmitted intensity noted I (Equation 5.5) is proportional to the oscillation period and d corresponding to the ice thickness.

$$I \propto \sin^2\left(\frac{2d}{\lambda} \times \frac{\pi}{2}\right) \tag{5.5}$$

The parameter d gives us the ice thickness that we are looking for.

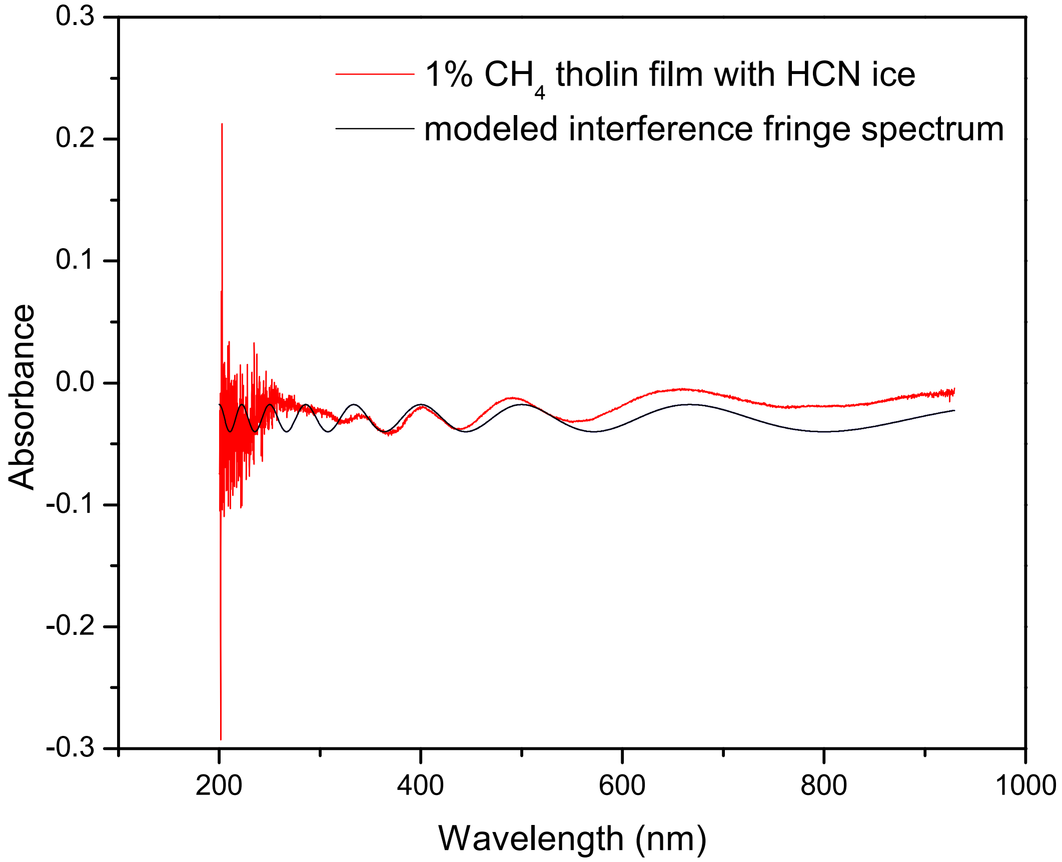

FIGURE 5.9: UV-VIS interference fringes, for pure HCN ice sample deposited atop a 1% CH_4 tholin film, with a thickness $d \approx 500$ nm.

Figure 5.9 shows an example of a UV-VIS absorption spectrum of pure HCN ice coated on a 1% CH_4 tholin film and the modeled thickness with a value of ~ 500 nm, consistent with the ices obtained by Couturier-Tamburelli, Piétri, and Gudipati (2015). Interference fringes starting in the UV are seen propagating into the visible wavelengths.

5.3.2 Pure HCN ice and HCN/tholin irradiations

UV-VIS absorption

I first carried out ice depositions of pure HCN on our sapphire windows. As expected (Figure 5.10), HCN does not absorb in wavelengths ranging from the visible to the near ultraviolet (200 nm). As seen in Table 5.1, HCN is transparent at wavelengths $> \sim 225$ (Minaev et al., 2004), and may thus react under photolysis below 225 nm. In the vacuum UV, HCN becomes highly sensitive (e.g. Price, 1934; Price and Walsh, 1945; Herzberb and Innes, 1957), although these energies are out of the scope of this study.

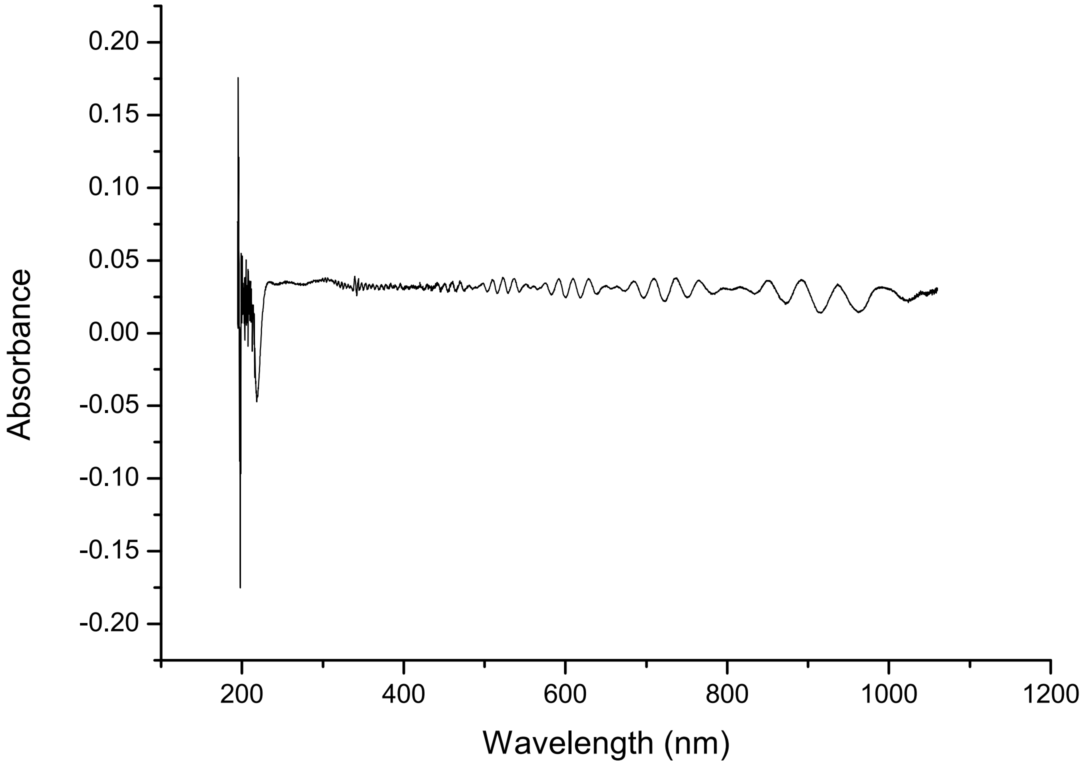

FIGURE 5.10: UV spectrum of HCN ice at 70K. Absence of absorption features. Note the interference patterns caused by the sapphire window.

Infrared absorption

The corresponding IR spectrum taken at 70K is shown in Figure 5.11. HCN possesses $3N - 5 = 4$ vibrational frequencies listed Table 5.3. In the spectrum Figure 5.11, only the first two modes ν_1 and ν_2 are visible. They peak at 3126 cm^{-1} and 2099 cm^{-1}, respectively. The presence of CO_2 is also visible at ~2300 cm^{-1}. This CO_2 is residual air in the FTIR beam path outside the chamber.

TABLE 5.3: List of the 4 vibrational modes of gas phase HCN. 3a and 3b are degenerated modes. All are Raman and IR active.

	Vibrational modes	Approximate position (cm^{-1})	Carrier
HCN	1	3126 (Figure 5.11)	C−H stretch
	2	2099 (Figure 5.11)	C≡N stretch
	3a	713	C−H bend
	3b	713	C−H bend

Pure HCN ice serves as a reference for all other spectra. At these temperatures, HCN is still transitioning from an amorphous to a crystalline state. This transition is gradual from 10 K to ~120 K (Noble et al., 2013). Crystallization also induces a shift in bands to higher frequencies. HCN starts to sublime above 100-110 K in our chamber (P = 10^{-9} mbar). Working at T $<$ 90 K assures us that the ice does not go through sublimation or annealing processes.

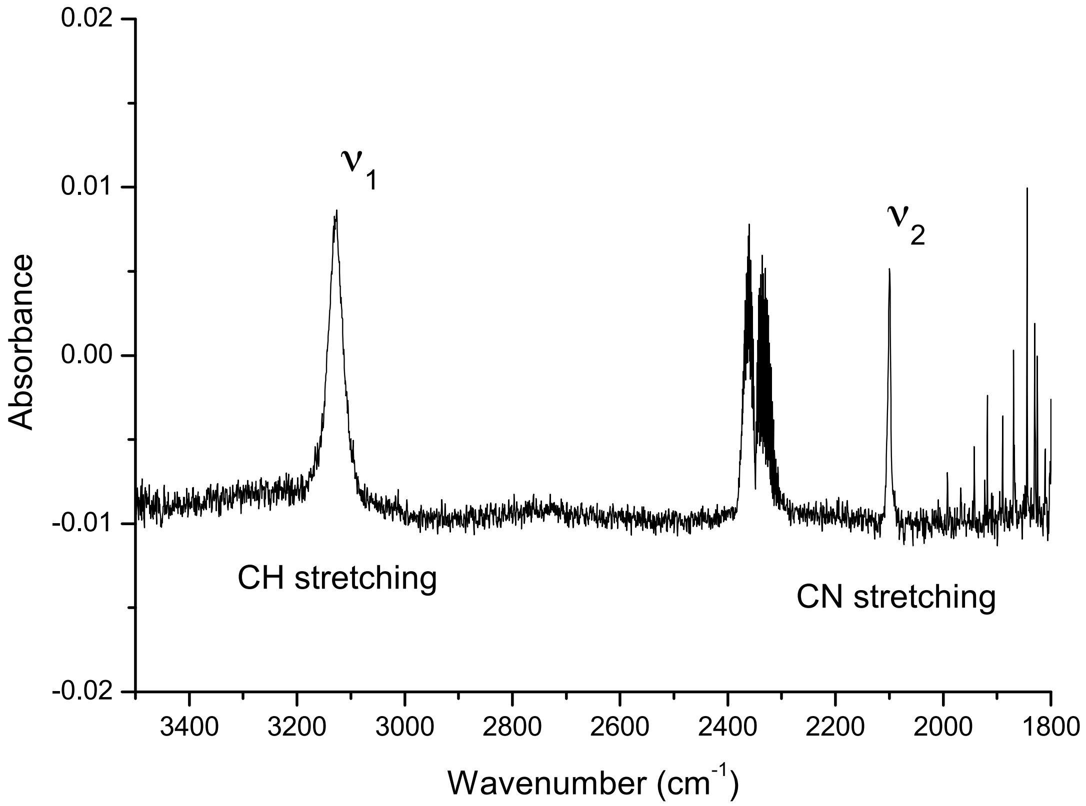

FIGURE 5.11: IR spectrum of pure HCN ice taken at 70K. The ν_1 and ν_2 fundamentals are clearly distinguishable at 3126 cm^{-1} and 2099 cm^{-1}, respectively.

Our first aim was to get a reference of pure HCN ice, at or near 70-80 K, deposited on a sapphire window. I then accumulated irradiation perpendicularly to the substrate, for 6h at three wavelengths; 320, 310, and 300 nm. The resulting absorbance of the sample is shown Figure 5.12. Spectra taken after each irradiation are normalized by the initial t=0 ice absorbance spectrum. Thus, potential products would increase positively while consumed reactants would decrease negatively. No significant perturbations in the CN or CH bands are seen. Condensating water starts to appear in the purple plot, near 3200, 3400 cm^{-1}, creating a dip in the H$-$C band of HCN.

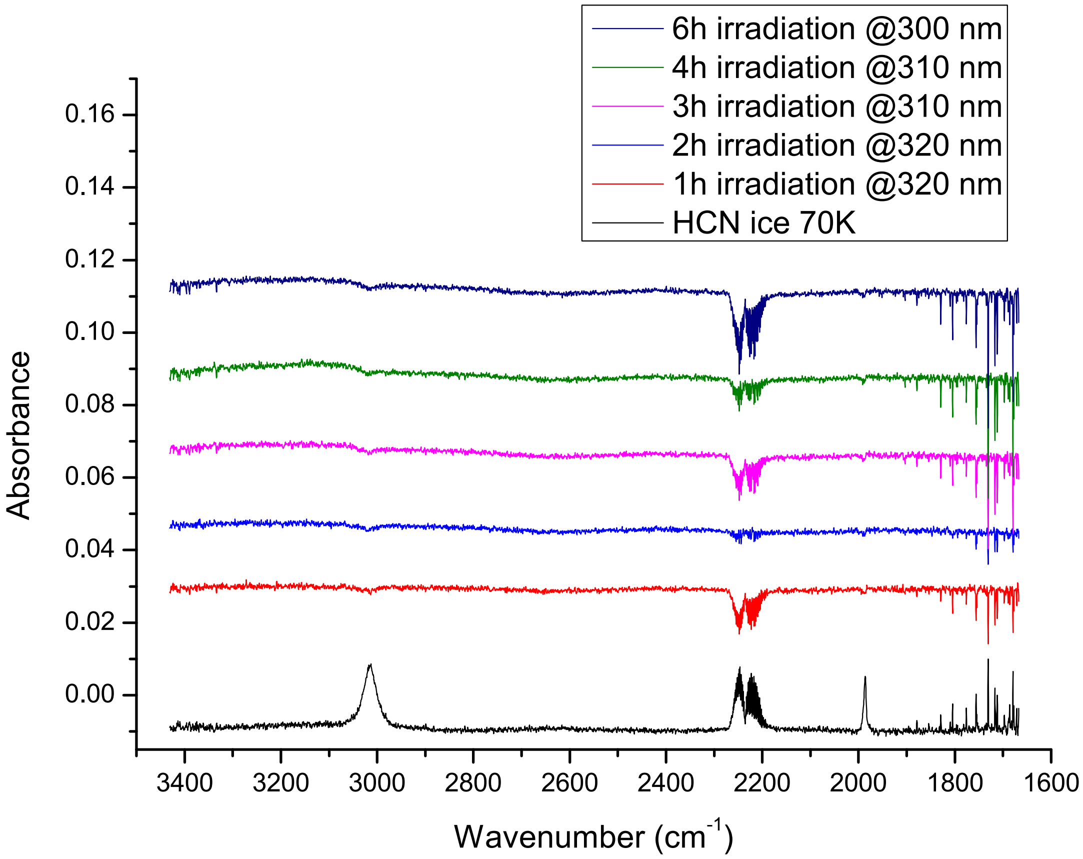

FIGURE 5.12: HCN ice evolution after an accumulation of a 6h irradiation at 320 nm. No significant HCN consumption is seen.

Previous work (Fleury, 2015, PhD thesis) analyzed C_2H_2 and CH_3CN ices coated on tholins, and their reactivity under near-UV/visible excitation. They found that C_2H_2, an unsaturated hydrocarbon, was easily reactive with tholins under irradiation; CH_3CN was not, though slightly at higher energies. They suggested that unsaturated C≡C bonds were more likely to react through covalent bonds with the tholin material, compared to unsaturated C≡N nitrile bonds. Tholins that form in a gas mixture with 10% of initial CH_4 concentration will preferentially produce aliphatic chains and saturated hydrocarbons, while a 1% CH_4 mixture will favor nitrogen-bearing compounds and associated functional groups (nitriles, amines...), and is less likely to be saturated. For this reason, we decided to deposit HCN ices onto 1% and 10% CH_4 tholins. Figure 5.13 shows an IR spectrum of an HCN coating on the tholin sample. The spectrum shows characteristic bands, namely the significant band of primary amines at ~3000 cm^{-1}, saturated and unsaturated nitriles at ~2000 cm^{-1}, and the absence of saturated aliphatic hydrocarbons at ~2800 cm^{-1}. The small HCN ν_1 and ν_2 absorption bands are also visible.

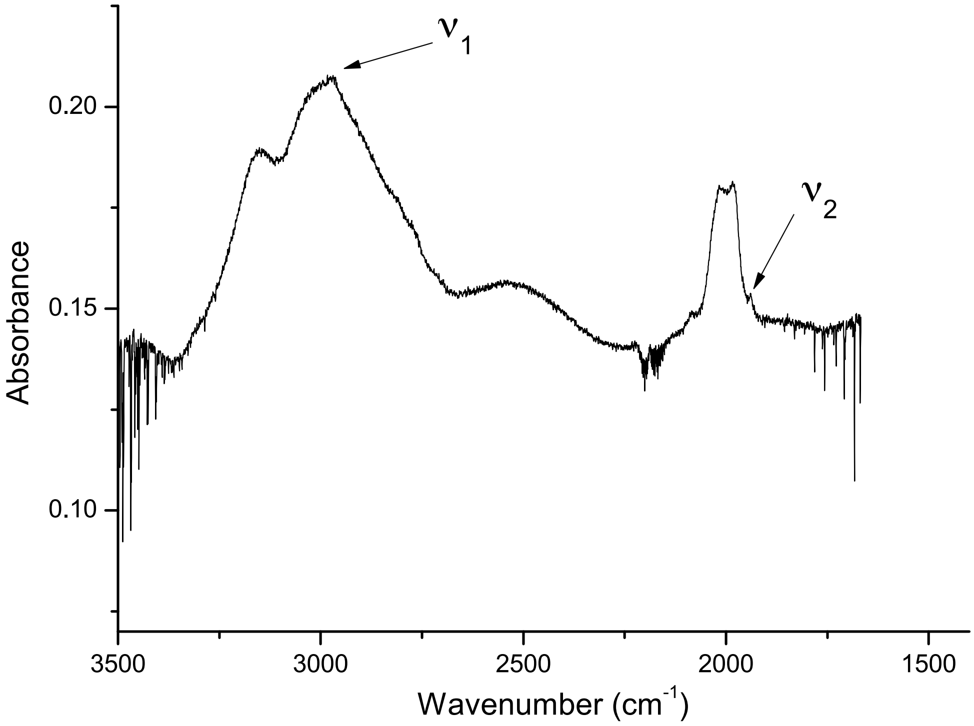

FIGURE 5.13: IR spectrum of pure HCN ice deposited on a 1% CH_4 tholin film at 70K.

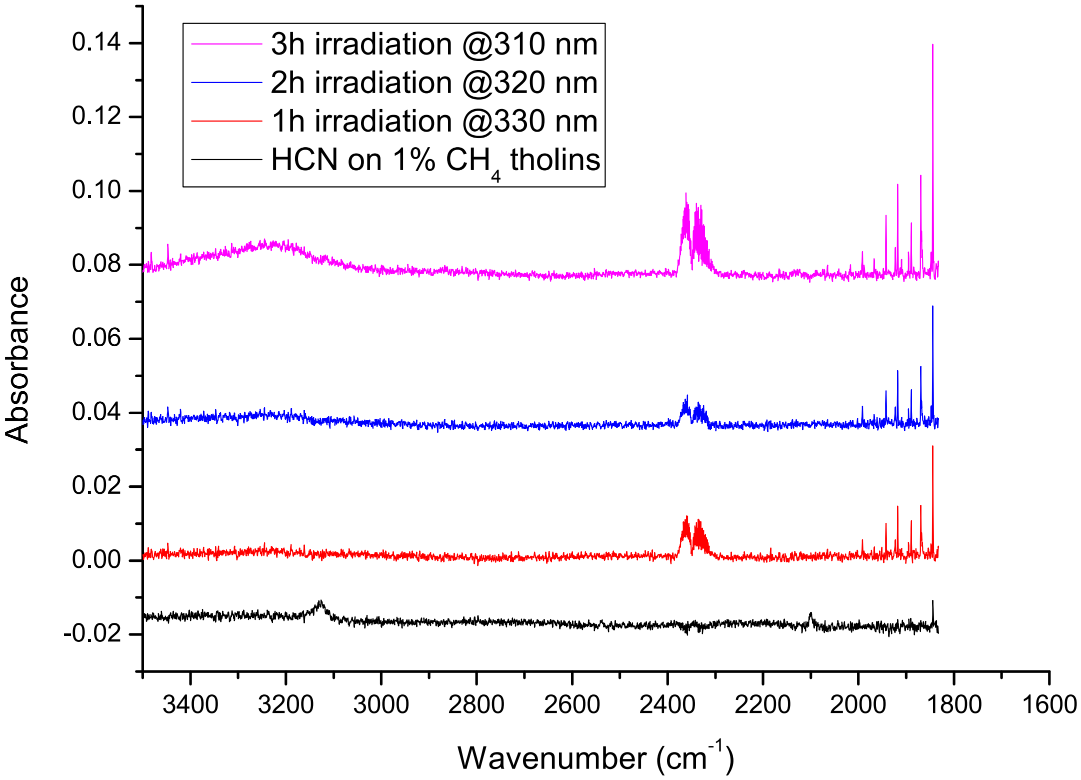

FIGURE 5.14: HCN coated on a 1% CH_4 tholin sample. The successive irradiation does not seem to affect the ice film.

Figure 5.14 shows spectra taken after three successive 1h-irradiations at 330, 320 and 310 nm, respectively. We note no clear consumption in either of the HCN bands with increasing irradiation. The same deposition done on our 10% CH_4 tholin film (Figure 5.15) shows no changes in the C−H stretch band, and a minor dip in the C≡N band, on the order of 10^{-3} a.u. in intensity. This decrease is observed after the first irradiation (red curve) and becomes stagnant following the successive irradiations. This dip might either be due to rearrangement or bonding with the tholin material, or vaporization of the first outer layers. Combined gas analysis was coupled during each irradiation in order to detect potential volatile products (e.g. Figure 5.16). However, we never were able to detect volatile products or desorbed volatiles (e.g. C_2H_2, C_2H_4, C_2H_6, N_2) during irradiations. The observed signal (Figure 5.16) actually corresponds to the detection limit of the mass spectrometer. This non-detection can be explained by the mass spectrometer not being sensitive enough to detect these potential volatiles in trace amounts, or that the irradiation-induced photochemistry, if any at this stage, occurs in the ice.

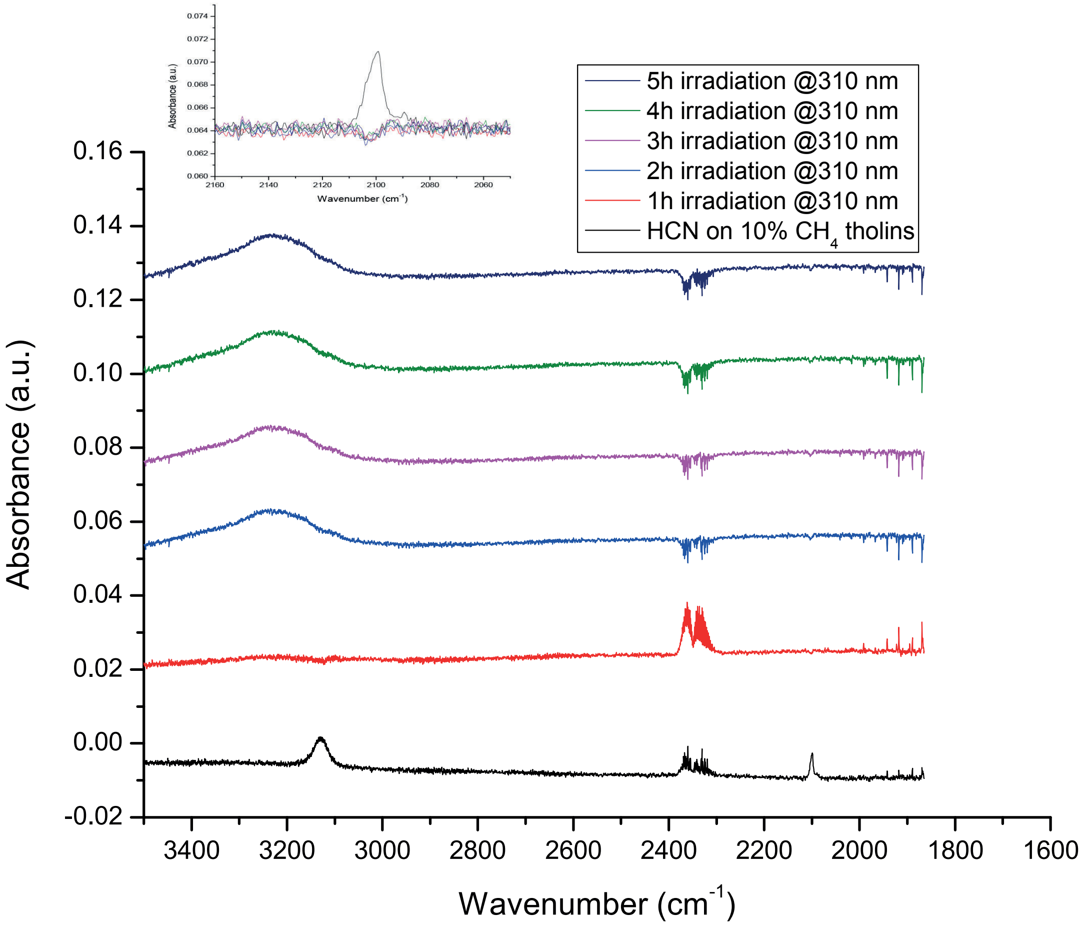

FIGURE 5.15: HCN coated on a 10% CH_4 tholin sample. The successive irradiation does not seem to affect the ice film.

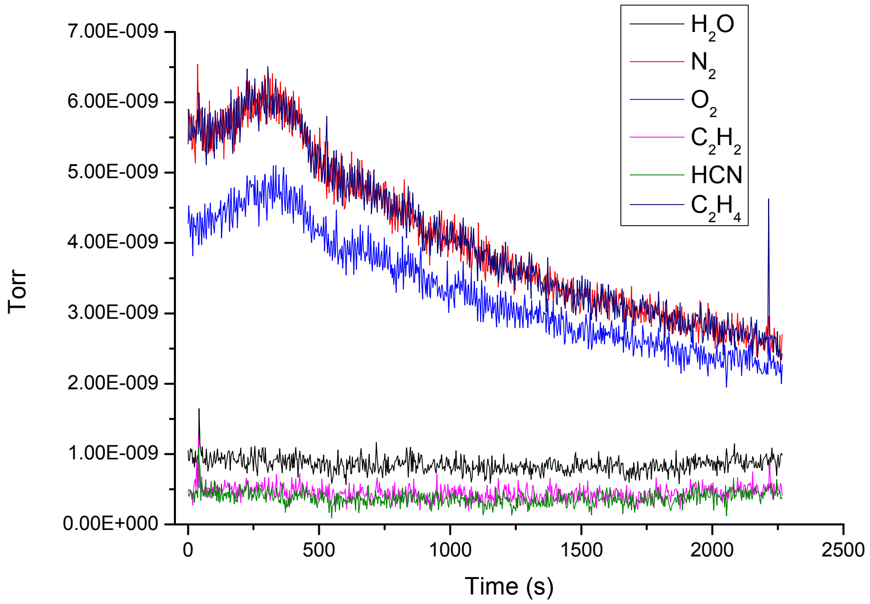

FIGURE 5.16: Residual gas analysis measurements of a few select species, during irradiation of our sample. The reason for the absence of any volatile products detected in our chamber during irradiation can be instrumental or that the putative chemistry occurs in the solid phase.

In conclusion, initiating photochemistry with pure HCN ice irradiated at near-UV/visible wavelengths and coated on tholin material has been challenging. Although HCN coated on 10% CH_4 films appears to be partially consumed under a 310 nm irradiation, its detection needs to be more robust. In this context, we decided to simplify our setup and the ice sample analysis. The HCN ice by itself being relatively inert, its putative photochemical activity might be favored by the coaddition of an unsaturated hydrocarbon, such as C_4H_2. In this way, C_4H_2 may contribute in initiating a specific type of photochemistry with HCN. Furthermore, as stated in the Introduction (Section 5.1), C_4H_2 is one of the ten most abundant photochemically-produced volatiles in Titan's atmosphere.

5.3.3 HCN/C_4H_2 ice mixture irradiations

UV-VIS absorption

C_4H_2 is photosensitive in ultraviolet wavelengths (Fihtengolts, 1969), as can be seen in the UV-vis absorption spectrum Figure 5.17. Here it starts absorbing at the sapphire window's transmission threshold, i.e. ~180 nm, until ~250 nm. The spectrum is the average of 50 scans, taken with an integration time of 10 ms.

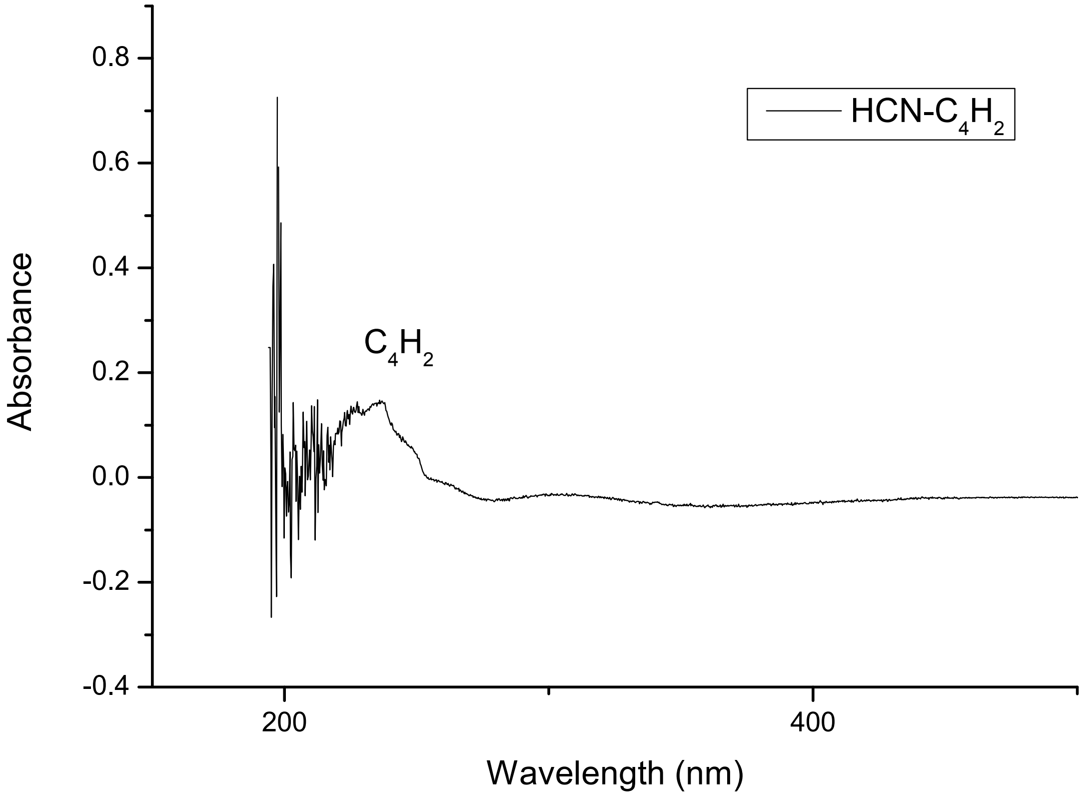

FIGURE 5.17: An HCN−C_4H_2 UV absorption spectrum, showing the important photosensitivity of C_4H_2 in the UV.

Infrared absorption

In the infrared wavelengths, the spectrum is much more rich. We see the ν_4 mode of C_4H_2 at 3272 cm^{-1}, corresponding to the C−H stretch. We can notice the distinctive distribution of this band, indicative of crystalline C_4H_2 (Zhou, Kaiser, and Tokunaga, 2009). The ν_4 shape in amorphous C_4H_2 would feature a larger half-width. The ν_5 asymmetric C≡C stretch is also present at 2010 cm^{-1}, and consistent with values found in the literature (Khanna, Ospina, and Zhao, 1988; Zhou, Kaiser, and Tokunaga, 2009). Both these frequencies, ν_4 and ν_5, listed in Table 5.4, are part of a total of four infrared active fundamentals of C_4H_2, along with ν_8 and ν_9 (out-of-plane bends). We also note the presence of hydrogen cyanide's ν_1 and ν_2 C−H and C≡N fundamentals, at 3126 cm^{-1} and 2105 cm^{-1}, respectively. A third band $2\nu_3$ located at ∼1620 cm^{-1} is attributed to the first NCH bend overtone (Gerakines, Moore, and Hudson, 2004; Theule et al., 2011; Couturier-Tamburelli et al., 2018).

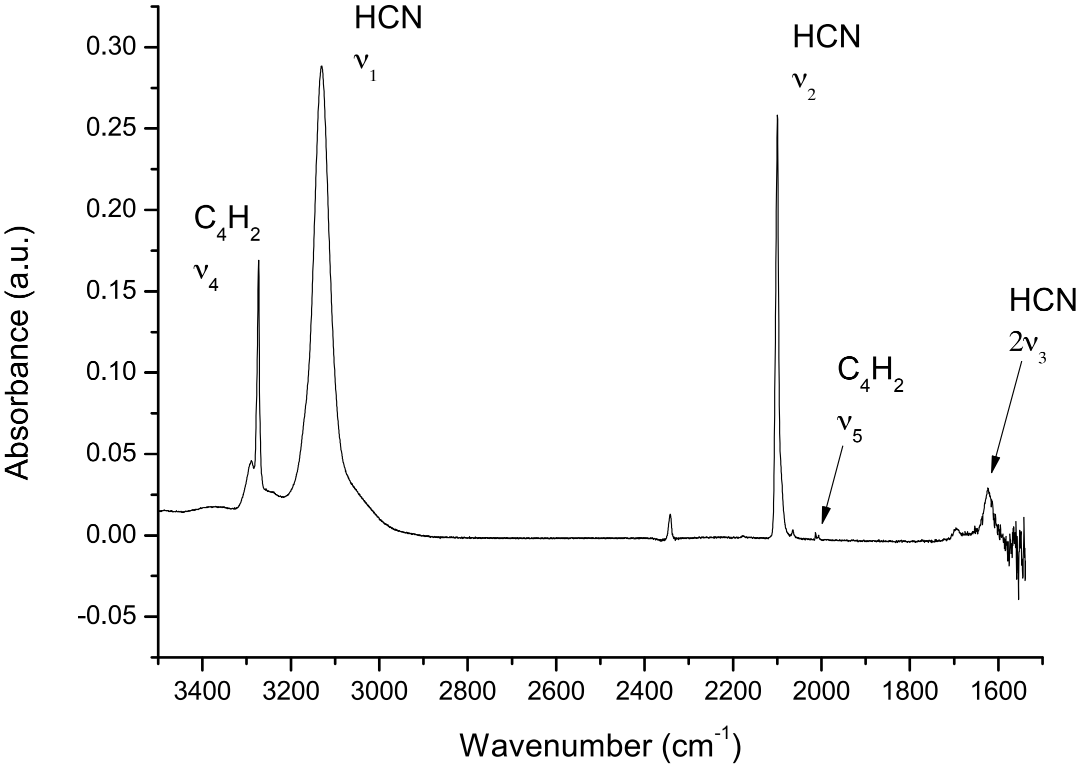

FIGURE 5.18: IR spectrum of an HCN–C_4H_2 mixture taken at 80K. The first two HCN modes dominate the spectrum, while the $2\nu_3$ overtone also peaks out. C_4H_2 is visible through its ν_4 C–H stretch, and less importantly the ν_5 C≡C stretch.

TABLE 5.4: The ν_4 and ν_5 vibrational modes of C_4H_2 seen Figure B.10.

	Vibrational modes	Position (cm^{-1})	Carrier
C_4H_2	4	3272	C–H stretch
	5	2010	C≡C stretch

For this experiment, the last to date, performed in 2017, I irradiated the HCN–C_4H_2 sample for an accumulated total time of 12h at 355 nm (in about a 1:1 gas phase ratio). After the first hour, the ν_4 band of C_4H_2 located at 3272 cm^{-1} starts to decrease, eventually leading to an ∼4% drop in arbitrary units. A smaller dip is also noticeable at ∼3120 cm^{-1}, which is eventually subdued by the large water band, shifting the baseline upwards. This water is especially present after long hours of irradiation, when residual water vapor in the chamber comes in contact with the cold sample. Moreover, a prominent dip is most notable at the C≡N location, 2105 cm^{-1}. These negative absorbances are indicative of HCN consumption, and are accompanied by simultaneous protrusions, extending at slightly higher frequencies for the C–H band, and slightly lower for the C≡N one. Such an increase in intensity could suggest the production of a new compound, from the relative consumption of HCN. Zoom-ins on the HCN ν_2 and C_4H_2 ν_4 fundamentals are shown in Figures 5.20 and 5.21.

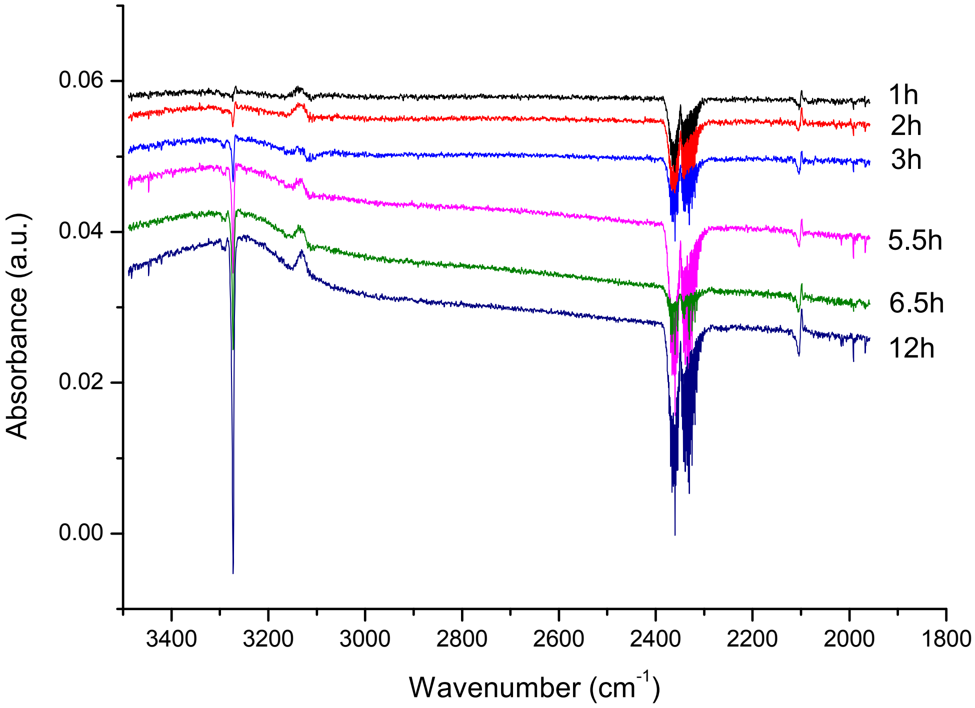

FIGURE 5.19: 12h of accumulated irradiation. The C_4H_2 consumption at 3272 cm^{-1} is clearly visible. HCN is marked by a consumption of both the CN and CH bands.

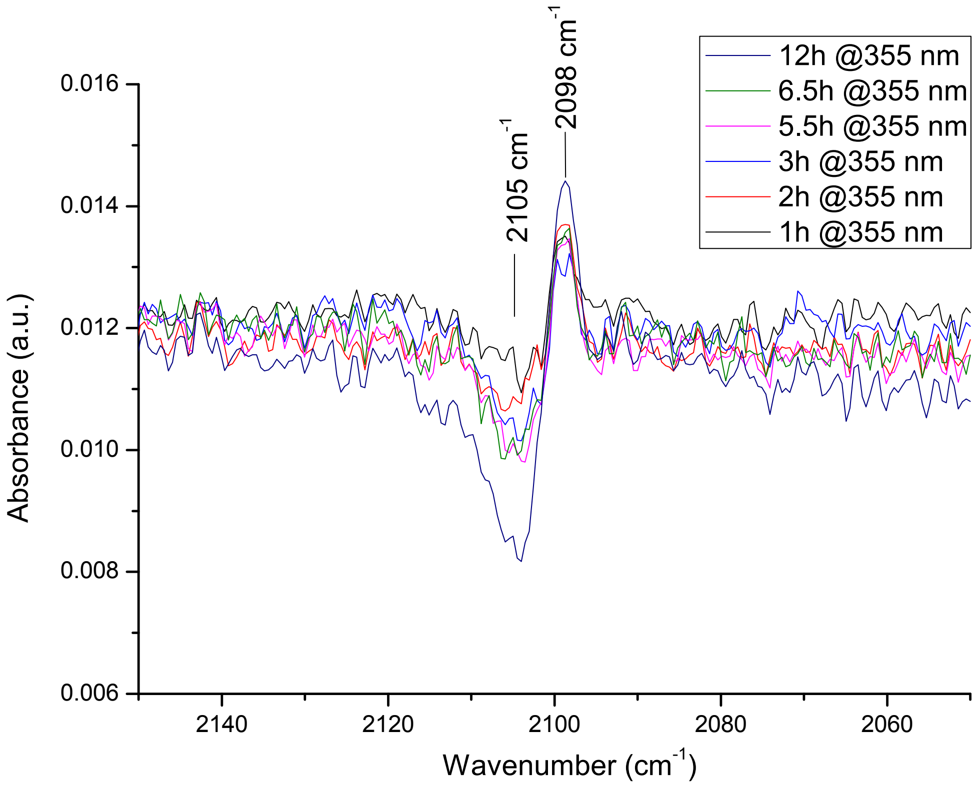

FIGURE 5.20: The ν_2 fundamental of HCN, showing its consumption centered at 2105 cm^{-1}, after a 12h accumulated irradiation at 355 nm. This consumption is accompanied by an increasing active compound at a slightly lower frequency of 2098 cm^{-1}.

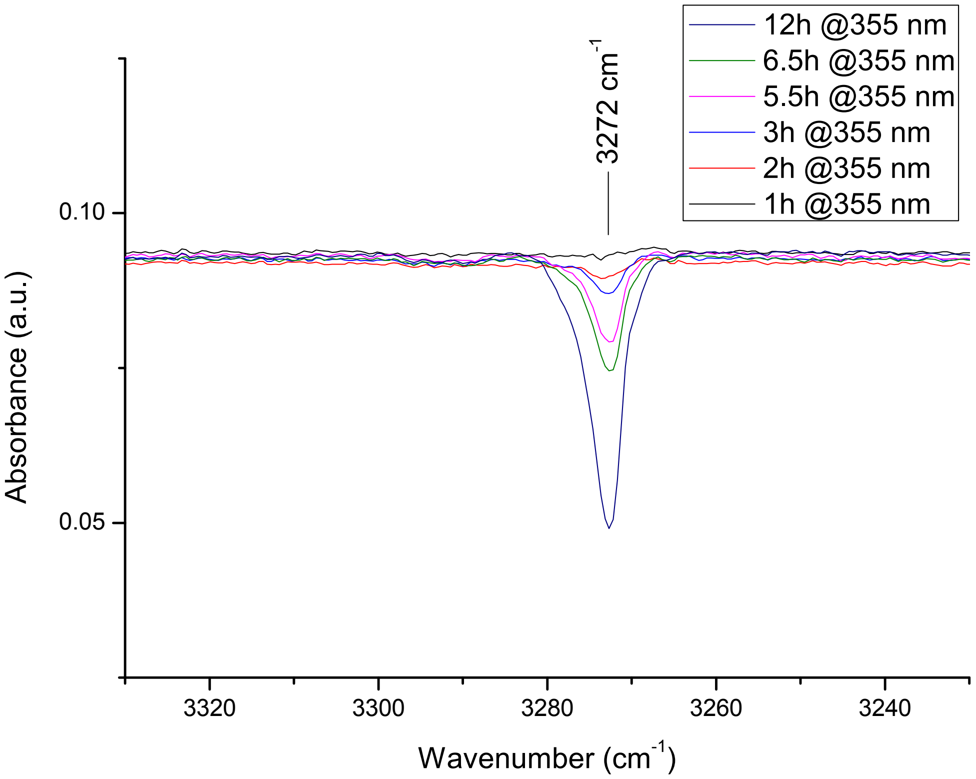

FIGURE 5.21: The ν_2 fundamental of C_4H_2, showing its consumption centered at 3272 cm^{-1}, after a 12h accumulated irradiation at 355 nm.

These results show a consumption of HCN which preliminarily suggest that HCN photochemistry is enabled with the presence of another hydrocarbon compound, namely C_4H_2. As seen Figure 5.21, C_4H_2 easily and directly reacts under photolysis. We can quantitatively estimate this consumption by calculating the area under a given consumed absorption band measured after each irradiation, relative to the reference 80K sapphire window spectrum. The relative surfaces, proportional to the respective consumptions, are presented in Figure 5.22 for HCN and C_4H_2. The most important decrease at this stage is observed for C_4H_2, which reaches a ∼22.5% loss in relative area after 12h of irradiation. This decrease is less intense for HCN, nonetheless still visible, with ∼3% and ∼1.5% relative area decrease for the ν_1 and ν_2 bands.

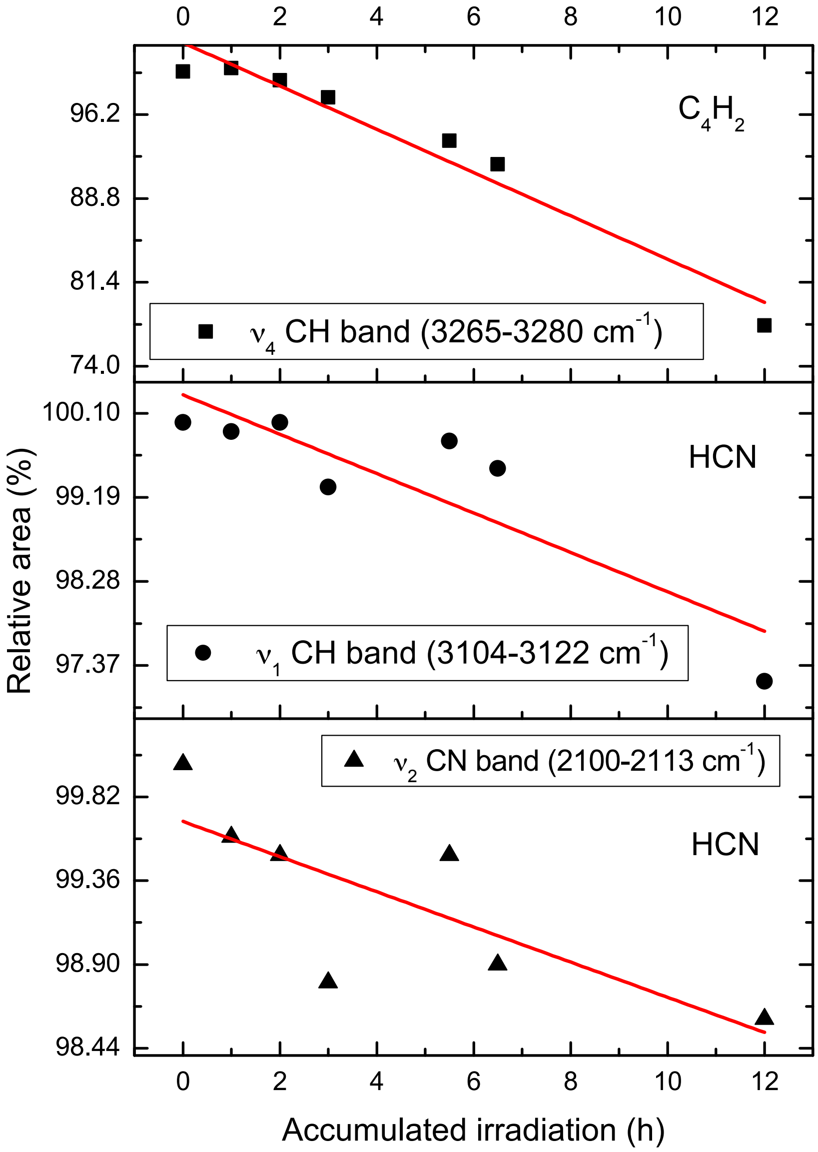

FIGURE 5.22: Relative area losses due to photochemical consumption for C_4H_2 (top) and HCN (middle and bottom), of their respective bands. Each data point corresponds to the area calculated under each band after the 7 irradiations.

5.4 Discussion and perspectives

5.4.1 Implications for HCN reactivity near the tropopause

HCN is the most abundant nitrile in Titan's atmosphere. Its main production pathways are Reactions 45 and 46, and is mainly lost through condensation in the lower atmosphere.

$$\mathrm{N(^4S) + CH_3 \longrightarrow H_2CN + H} \qquad \{45\}$$

$$\mathrm{H_2CN + H \longrightarrow HCN + H_2} \qquad \{46\}$$

HCN is also a major positive ion in the protonated form $HCNH^+$ and, as presented in the previous chapter, a key precursor to tholin formation. It is even predicted to play a role in negative ion chemistry through ion-pair and dissociative electron attachment photochemical reactions for the production of CN^-, the most abundant negative ion. Thus, HCN is ubiquitously involved in many different reactions. Theule et al. (2011) also showed the prebiotic implications of $-C{\equiv}N$ hydrogenation reactions as precursory to the formation of CH_3NH_2 in cold interstellar conditions. HCN is a key compound to better characterize in cold interplanetary and interstellar nitrogen-rich environments, where UV radiation may trigger important reactions.

Barth (2017) determined an HCN altitude of condensation <100 km, where all species reach saturation. At ~400 km in the stratosphere, the temperature decreases with a sharp slope, and reaches its lowest value ~80 K near the tropopause. At these altitudes, only the near-UV and near-visible photons can penetrate the atmosphere this low. The HCN ice particles can reach radii of 1-5 μm between 40 and 80 km. The processes leading to their growth are still uncertain, though they likely undergo coagulation, surface growth rounding and accretion onto larger aerosol particles. In the condensed phase, solid-state photochemical processes may also contribute to chemical changes and ageing occurring in these ices, and thus particle growth. Compounds solely present in the gas phase undergo photochemical changes according to their spectroscopic properties. So, while the gas phase compounds go through their own specific photochemical activity, their interaction with condensed ices can further their evolution by (i) incorporating with other compounds, and (ii) initiating solid-state activity to create more complex condensed nuclei, as our results show between HCN and C_4H_2. HCN and C_4H_2 being two major photochemically-induced constituents of Titan's atmosphere, can even further condense with other highly unsaturated species (e.g. C_2H_2, C_2H_4). Given the photochemical response by an HCN/C_4H_2 mixture under near-UV light, such a scenario could foster a more advanced complexity of photochemical reactions at altitudes between ~75-100 km. The lower stratosphere and upper troposphere could therefore be incubators for unsuspected solid-state photochemical reactivity, as the icy aerosols rain down to the surface.

5.4.2 Theoretical considerations

HCN smoothly transitions from amorphous to crystalline state between 20K and 120K (**Couturier-Tamburelli2018UVVisIce**). Zhou, Kaiser, and Tokunaga (2009) gave the first amorphous-to-crystalline transition temperature of 70K for C_4H_2. Thus, both compounds in our samples are mostly in crystalline state. Irradiating these samples induces depletion of C_4H_2 and HCN after 12h of irradiation. The ν_4 band of the former reaches a ~22.5% depletion, and ~3% and ~1.5% of the ν_1 and ν_2 bands of the latter. As seen previously, this simultaneous consumption suggests a solid-state reactivity between the two compounds, while the emergence of a new band within the two aforementioned HCN bands indicates a new product being formed. These signatures are consistent with the locations of C−H and C≡N stretching frequencies. We propose a reaction scheme (Figure 5.23) modeling the HCN photoreactivity under 355 nm light.

A first step in the reaction scheme in Figure 5.23 consists of the photolysis of C_4H_2, according to Reaction 47, followed by the addition of C_4H on HCN in Reaction 48 (Hébrard, 2006). The photolysis and photochemistry of C_4H_2 in the gas phase has been described by Glicker and Okabe (1987).

$$C_4H_2 + h\nu \longrightarrow C_4H + H \tag{47}$$

$$C_4H + HCN \longrightarrow HC_5N + H \tag{48}$$

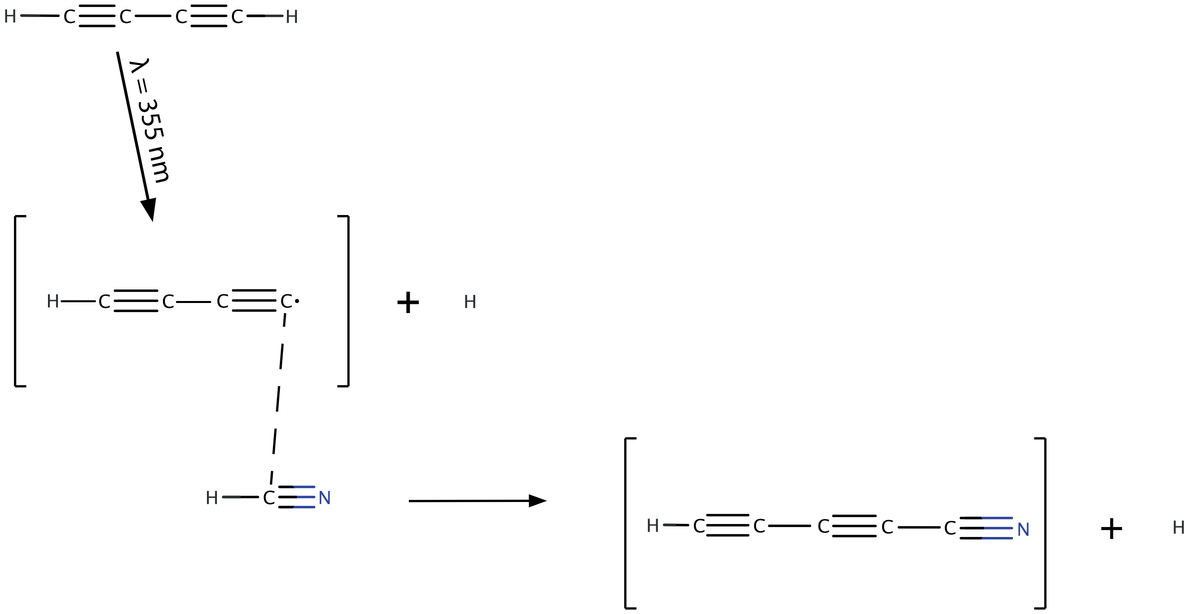

FIGURE 5.23: Proposed reaction scheme model for the HCN photochemistry observed in the presence of C_4H_2, under 355 nm irradiation. C_4H_2 undergoes photolysis which produces C_4H. C_4H is then added to HCN whose −CH bond has been photolyzed. The resulting product is the stable cyanobutadiyne (H-CC-CC-CN). HC_5N contains two C≡C bonds and one nitrile functional group.

With this proposed reaction scheme, we obtain the HC_5N product with two C≡C bonds, and one nitrile function. This compound is highly unsaturated, and could potentially be a viable candidate for the appearance of the unidentified bands at 2098 cm^{-1} and $\sim$3130 cm^{-1}. This however remains to be tested and confirmed theoretically. A current investigation using density functional theory (DFT) is underway to answer this question, and reveal whether such a compound could be possible at these temperatures.

5.5 Conclusions

This chapter presents preliminary results on the solid-state photochemistry of HCN and HCN/C_4H_2 ices, simulated in conditions representing the radiating and cold environment at Titan's lower atmosphere. HCN, the most abundant nitrile in the atmosphere, condenses with other volatiles near the tropopause, which may undergo further photochemical changes during their descent. Generally, the low-energy photons reaching these altitudes have not been suspected to photochemically affect these ices and icy aerosols, even less so for such strongly bonded molecules. However, earlier work by Fleury (2015) using the Acquabella chamber first showed C_2H_2 reactivity coated on tholin material. Their nitrile of interest CH_3CN was shown to be relatively inert in comparison and indifferent to near-UV irradiation.

In the present experiments, HCN in contact with tholins irradiated at near-UV wavelengths was not conducive to any substantial photochemical activity. Thus, we decided to facilitate any putative HCN reactivity, by coadding the unsaturated hydrocarbon C_4H_2, without the presence of tholins. With these preliminary results, we show for the first time HCN photochemical activity. For now, the state and extent of this reactivity remains an open question. Nevertheless, under near-UV/visible irradiation, HCN undergoes solid-state photochemical changes. These changes are favored and initiated by the presence of C_4H_2. On the basis of this work, future experiments will be carried out to expand on HCN/C_4H_2 mixtures, with irradiation times longer than the ones used here in order to constrain the HCN consumption under the influence of C_4H_2. In addition, investigating other UV wavelengths relevant to Titan's lower atmosphere will be crucial in determining the optimum conditions for HCN photochemistry. Supporting these results with theoretical predictions is essential to better understand the changes occurring in the solid phase. I am currently collaborating with a team at the Rahmlab form Chalmers University of Technology in Gothenburg using a quantum chemical approach, in order to help characterize the molecular changes occurring at these low temperatures.

Regarding Titan, understanding unsuspected photochemical processes potentially occurring in the lower atmosphere is crucial in characterizing the ageing of the aerosols. Revealing photochemically-induced spectroscopic changes in ices can be helpful to interpret Cassini data or provide new theoretical pathways relevant to Titan's cold lower atmosphere and other nitrogen and hydrocarbon-rich worlds.

General Conclusions and Perspectives

Titan's complex atmosphere chemistry relies on a plethora of organic compounds: from simple hydrocarbons to large nitrogen-bearing compounds. These species are the result of advanced reactions following the photodissociation of N_2 and CH_4 in the upper atmosphere. In the ionosphere, Cassini revealed abundant positive and negative ion compounds which are coupled with the neutral chemistry. These gas phase precursors eventually participate in the formation of larger solid particles, making up the haze shrouding Titan's surface. Understanding the chemical processes forming these hazy particles requires us to first characterize the gas phase chemistry and the ion-neutral coupling in the upper atmosphere.

To undertake this task, I have used laboratory experiments as analogs to certain conditions of Titan's atmosphere. In particular, I worked with a dusty plasma reactor named PAMPRE to simulate the plasma conditions of Titan's upper atmosphere using N_2-CH_4 mixtures. With this apparatus, I was able to investigate the ion-neutral coupling and gas phase precursors to the formation of tholins within the plasma.

Using mass spectrometry, infrared spectroscopy and a cryogenic setup, I studied the major neutrals present in the PAMPRE plasma discharge using different methane concentrations. This work presented in Chapter 3 provided insight on key compounds acting as major precursors to tholin formation with the help of a student intern whom I supervised. Our internal cryogenic system enabled us to trap the gas phase products in the chamber during a 1h plasma discharge and perform a quantification analysis on them with *in situ* infrared measurements. These products were then released in the reactor while mass measurements and infrared spectra were collected during their release. Major neutrals such as NH_3, HCN, C_2H_2 and C_2H_4 appear to be key tholin precursors in our experimental conditions. For instance, the total number density of HCN and C_2H_2 produced during 2h increases from $\sim 10^{14}$ to $\sim 10^{15}$ and $\sim 10^{12}$ to $\sim 10^{13}$ cm^{-3}, respectively, from a 1% to 10% methane mixing ratio. Vapor pressure calculations also showed that ethane C_2H_6 hardly condenses at -180žC in this experimental setup, and is difficult to trap at these temperatures.

The coupled positive ion chemistry in the plasma was also examined by ion mass spectrometry with the help of another summer intern I supervised. This was the first time such measurements were performed in our reactor. I carried out a series of experiments in different methane concentrations, thus examining the relative contribution of hydrocarbon species. The results presented in this thesis (Chapter 4) indicate the prominent contribution of ions such as CH_5^+, $HCNH^+$ and $C_2H_5^+$. We also notice strong variability in our spectra depending on the initial gas composition, underlying the importance of constraining the positive ion chemistry for the interpretation of the solid phase aerosol composition. In addition, high methane amounts i.e. with a 10% mixing ratio results in a wider distributions of cations, notably with a more diverse population of C_2 compounds. For comparison, I compared our experimental spectra with spectra taken on the dayside of Titan by the INMS instrument during the T40 flyby. A 10% methane mixing ratio leads to a wider distribution than observed by INMS, while the 1% and 5% CH_4 conditions match well with the INMS spectra. In all cases, however, the C_2 compounds dominate the spectra. With low CH_4 amounts (i.e. using 1% mixing ratio), N_2H^+ is likely to account for the main peak see at m/z 29. However, adding methane results in $C_2H_5^+$ being the dominant ion at this mass. It is accompanied by $HCNH^+$ at m/z 28. Both account for most of the C_2 compounds detected using a 5% methane mixing ratio. NH_4^+ also stand out as the most abundant C_1 compound at 1% and 5% CH_4, but largely decreases at the profit of CH_3^+ in a 10% CH_4 mixing ratio. We also find similarities with solid phase analyses regarding the amine signature at 1% and 5% CH_4 as well as the HCN/C_2H_4 polymerization patterns that bear to the $HCNH^+$ and $C_2H_5^+$ ions.

The gas phase products formed in Titan's upper atmosphere involving ion-neutral reactions diffuse downward to the stratosphere. Eventually, these hydrocarbon and N-bearing species reach the lower atmosphere where volatiles can condense and form icy particles. This condensation typically occurs below 120 km. At these altitudes, condensed nuclei may form by the aggregation of several icy particles. HCN is the dominant N-containing compound in Titan's atmosphere and its condensation takes place $\sim$80-100 km. After condensing to form cloud nuclei in the lower atmosphere, it may undergo accretion with other compounds and therefore participate in a complex growth of icy particles. Clouds composed of micrometer-sized particles were observed in Titan's lower atmosphere and suggest that such clouds may be common and influence by seasonal patterns. During the cloud formation process, other ices may form larger aggregates. We chose C_4H_2 to accompany HCN as an analog of this condensation mechanism. C_4H_2 is indeed an abundant hydrocarbon in Titan's atmosphere and condenses at a slightly lower atltitude than HCN ($\sim$75-80 km).

The ageing of these icy particles (i.e. how they evolve during their descent to the lower atmosphere) in lower atmospheric conditions was studied by irradiating simple and complex ices under near-UV/VIS wavelengths (Chapter 5). To simulate these ageing processes, I used a cryogenic chamber where ices were irradiated by a laser. I focused on icy samples involving HCN ices. The putative photochemistry of these ices was put to test by performing long irradiations on those samples. Our results show a solid-state HCN consumption due to irradiation at λ = 355 nm and to C_4H_2 photochemistry. After 12h irradiation, a consumption of $\sim 1.5 - 3\%$ is observed for the ν_1 and ν_2 bands of HCN. In addition, HCN alone or combined with C_4H_2 but in small amounts leads to no or hardly detectable consumption of HCN. Furthermore, the reaction between these two icy species is accompanied by a new formed product, located in the nitrile absorption region. We propose HC_5N as a potential candidate for the formed product resulting from HCN-C_4H_2 solid-state chemistry. These results indicate HCN ice particle ageing in the troposphere may be facilitated by more complex condensed nuclei.

Complementary future work related to the gas phase reactivity in the PAMPRE plasma should be carried out. Currently, I am studying the negative ion chemistry, which Cassini measurements showed to be significant in the upper atmosphere of Titan. Our current setup permits us to probe these anions directly in the plasma. Our knowledge at present regarding the precursor negative ion compounds is largely unknown, and this laboratory investigation should hopefully shed light on their coupling with neutrals. In addition, it may be relevant to investigate the cations (and anions) at intermediate methane concentrations to obtain a continuum of spectra from 1% to 10% CH_4. Using gas mixtures with the presence of other trace species (nitrogenated, oxygenated) may also be useful in determining their effect, if any, on the ion population. Complementary analyses of the irradiation effect on HCN-C_4H_2 ices are also being performed. It would also be useful in future work to investigate more complex ice mixtures along with HCN, by co-adding other N-bearing and/or unsaturated hydrocarbon species. Parallel theoretical work should also be taken into account to confirm the appearance of new products in our laboratory spectra. Finally, given the end of the Cassini mission, laboratory testing and photochemical modeling working together would help the momentum towards using available and soon-to-be ground and space-based telescopes (ALMA, SOFIA, JWST, TMT) for Titan observations and new detections until a new spacecraft is sent.

Bibliography

Achterberg, R. K. et al. (2011). "Temporal variations of Titan's middle-atmospheric temperatures from 2004 to 2009 observed by Cassini/CIRS". In: *Icarus* 211.1, pp. 686–698. ISSN: 00191035. DOI: `10.1016/j.icarus.2010.08.009`. URL: `http://dx.doi.org/10.1016/j.icarus.2010.08.009`.

Ågren, K. et al. (2009). "On the ionospheric structure of Titan". In: *Planetary and Space Science* 57, pp. 1821–1827. DOI: `10.1016/j.pss.2009.04.012`.

Alcaraz, C. et al. (2004). "15N+ + CD4 and O+ + 13CO2 State-Selected Ion-Molecule Reactions Relevant to the Chemistry of Planetary Ionospheres". In: *J. Phys. Chem. A* 108, p. 9998. ISSN: 10895639. DOI: `10.1021/jp0477755`.

Alcouffe, G. et al. (2010). "Capacitively coupled plasma used to simulate Titan's atmospheric chemistry". In: *Plasma Sources Science and Technology* 19.1, p. 15008. ISSN: 0963-0252. DOI: `10.1088/0963-0252/19/1/015008`. URL: `http://stacks.iop.org/0963-0252/19/i=1/a=015008`.

Alves, L. L. et al. (2012). "Capacitively coupled radio-frequency discharges in nitrogen at low pressures". In: *Plasma Sources Science and Technology* 21.4, p. 045008. ISSN: 0963-0252. DOI: `10.1088/0963-0252/21/4/045008`.

Anderson, C. M. and R. E. Samuelson (2011). "Titan's aerosol and stratospheric ice opacities between 18 and 500 um: Vertical and spectral characteristics from Cassini CIRS". In: *Icarus* 212.2, pp. 762–778. ISSN: 00191035. DOI: `10.1016/j.icarus.2011.01.024`. URL: `http://dx.doi.org/10.1016/j.icarus.2011.01.024`.

Anderson, C. M. et al. (2014). "Subsidence-induced methane clouds in Titan's winter polar stratosphere and upper troposphere". In: *Icarus* 243, pp. 129–138. ISSN: 10902643. DOI: `10.1016/j.icarus.2014.09.007`. URL: `http://dx.doi.org/10.1016/j.icarus.2014.09.007`.

Anderson, C. M. et al. (2016). "Solid-state chemistry as a formation mechanism for Titan's stratospheric C4N2 ice clouds". In: *Geophysical Research Letters*, n/a–n/a. ISSN: 00948276. DOI: `10.1002/2016GL067795`. URL: `http://doi.wiley.com/10.1002/2016GL067795`.

Armante, R et al. (2016). "The 2015 edition of the GEISA spectroscopic database". In: *Journal of Molecular Spectroscopy*.

Atreya, S. K. (1986). "Atmospheres and Ionospheres of the Outer Planets and their satellites". In: 15.

Atreya, SK, TM Donahue, and WR Kuhn (1978). *Evolution of a nitrogen atmosphere on Titan*. URL: `http://www-personal.umich.edu/~atreya/Articles/1978_Evolution_Nitrogen.pdf`.

Bagenal, Fran (2005). "Saturns mixed magnetosphere". In: *Nature* 433.February 1955, pp. 695–696.

Barnett, K. N. and V. F. Chevrier (2016). "Solubility and Reactivity of Tholins in Liquid Hydrocarbons on Titan". In: *LPSC2016* 1814, pp. 1–2.

Barth, Erika L. (2017). "Modeling survey of ices in Titan's stratosphere". In: *Planetary and Space Science* 137.January, pp. 20–31. ISSN: 00320633. DOI: `10.1016/j.pss.2017.01.003`. URL: `http://dx.doi.org/10.1016/j.pss.2017.01.003`.

Béghin, Christian (2015). “Self-consistent modeling of induced magnetic field in Titan’s atmosphere accounting for the generation of Schumann resonance”. In: *Icarus* 247, pp. 126–136. ISSN: 10902643. DOI: `10.1016/j.icarus.2014.10.005`.

Běhounková, M. et al. (2017). “Plume Activity and Tidal Deformation on Enceladus Influenced by Faults and Variable Ice Shell Thickness”. In: *Astrobiology* 17.9, ast.2016.1629. ISSN: 1531-1074. DOI: `10.1089/ast.2016.1629`. URL: `http://online.liebertpub.com/doi/10.1089/ast.2016.1629`.

Berkowitz, J (1962). “Heat of formation of the CN radical”. In: *The Journal of Chemical Physics* 1555.1962, pp. 2533–2539. ISSN: 00219606. DOI: `10.1063/1.1732330`. URL: `http://link.aip.org/link/?JCPSA6/36/2533/1`.

Bernstein, M. P., C. W. Bauschlicher, and S. A. Sandford (2004). “The infrared spectrum of matrix isolated aminoacetonitrile, a precursor to the amino acid glycine”. In: *Advances in Space Research* 33.1, pp. 40–43. ISSN: 02731177. DOI: `10.1016/j.asr.2003.07.002`.

Berteloite, C. et al. (2008). “Low temperature (39-298 K) kinetics study of the reactions of the C4H radical with various hydrocarbons observed in Titan’s atmosphere”. In: *Icarus* 194.2, pp. 746–757. ISSN: 00191035. DOI: `10.1016/j.icarus.2007.10.012`.

Bertucci, C. et al. (2015). “Titan’s interaction with the supersonic solar wind”. In: *Geophysical Research Letters* 42.2, pp. 193–200. ISSN: 19448007. DOI: `10.1002/2014GL062106`.

Bezard, B. and G. Paubert (1993). *Detection of acetonitrile on Titan*.

Biennier, Ludovic et al. (2014). “Low temperature reaction kinetics of CN-+HC3N and implications for the growth of anions in Titan’s atmosphere”. In: *Icarus* 227, pp. 123–131. ISSN: 00191035. DOI: `10.1016/j.icarus.2013.09.004`. URL: `http://dx.doi.org/10.1016/j.icarus.2013.09.004`.

Bonnet, J-Y. et al. (2013). “International Journal of Mass Spectrometry Compositional and structural investigation of HCN polymer through high resolution mass spectrometry”. In: 355, pp. 193–203. DOI: `10.1016/j.ijms.2013.06.015`.

Bourgalais, J. et al. (2016). “Elusive anion growth in Titan’s atmosphere: Low temperature kinetics of the C3N-+ HC3N reaction”. In: *Icarus* 271, pp. 194–201. ISSN: 10902643. DOI: `10.1016/j.icarus.2016.02.003`.

Brandsma, L. (2004). “Synthesis of Acetylenes, Allenes and Cumulenes. Methods and Techniques”. In: *Academic Press*.

Broadfoot, A. L. et al. (1981). “Extreme Ultraviolet Observations from Voyager 1 Encounter with Saturn”. In: 212.April.

Brown, M., A. H. Bouchez, and C. A. Griffith (2002). “Direct detection of variable tropospheric clouds near Titan’s south pole.” In: *Nature* 420.6917, pp. 795–797. ISSN: 0028-0836. DOI: `10.1038/nature01302`.

Brown, R. H., J. P. Lebreton, and J. H. Waite (2009). *Titan from Cassini-Huygens*. Springer. Springer, p. 412.

Brown, R. H. et al. (2004). “The Cassini visual and infrared mapping spectrometer (VIMS) investigation”. In: *Space Science Reviews* 115.1-4, pp. 111–168. ISSN: 00386308. DOI: `10.1007/s11214-004-1453-x`.

Budavari, S., M. J. O’Neil, and A. Smith (1996). *The Merck Index*. 12th ed. Co., Merck &.

Cable, Morgan L. et al. (2012). “Titan tholins: Simulating Titan organic chemistry in the Cassini-Huygens era”. In: *Chemical Reviews* 112.3, pp. 1882–1909. ISSN: 00092665. DOI: `10.1021/cr200221x`.

Carrasco, N. et al. (2007). "Influence of neutral transport on ion chemistry uncertainties in Titan ionosphere". In: *Icarus* 192.2, pp. 519–526. ISSN: 00191035. DOI: `10.1016/j.icarus.2007.08.016`. URL: `http://www.sciencedirect.com/science/article/pii/S0019103507003533`.

Carrasco, N. et al. (2008). "Sensitivity of a Titan ionospheric model to the ion-molecule reaction parameters". In: *Planetary and Space Science* 56.12, pp. 1644–1657. ISSN: 00320633. DOI: `10.1016/j.pss.2008.04.007`. URL: `http://www.sciencedirect.com/science/article/pii/S0032063308001025`.

Carrasco, N. et al. (2009). "Chemical characterization of titan's tholins: Solubility, morphology and molecular structure revisited". In: *Journal of Physical Chemistry A* 113.42, pp. 11195–11203. ISSN: 10895639. DOI: `10.1021/jp904735q`.

Carrasco, N. et al. (2012). "Volatile products controlling Titan's tholins production". In: *Icarus* 219.1, pp. 230–240. ISSN: 00191035. DOI: `10.1016/j.icarus.2012.02.034`. URL: `http://dx.doi.org/10.1016/j.icarus.2012.02.034`.

Carrasco, N. et al. (2013). "VUV photochemistry simulation of planetary upper atmosphere using synchrotron radiation". In: *Journal of Synchrotron Radiation* 20.4, pp. 587–589. ISSN: 09090495. DOI: `10.1107/S0909049513013538`.

Carrasco, N. et al. (2016). "Laboratory analogues simulating titan's atmospheric aerosols: Compared chemical compositions of grains and thin films". In: *Planetary and Space Science*. ISSN: 00320633. DOI: `10.1016/j.pss.2016.05.006`. URL: `http://linkinghub.elsevier.com/retrieve/pii/S0032063316300459`.

Carrasco, N. et al. (2018). "The evolution of Titans high-altitude aerosols under ultraviolet irradiation". In: *Nature Astronomy*, p. 1. ISSN: 2397-3366. DOI: `10.1038/s41550-018-0439-7`. URL: `http:https://doi.org/10.1038/s41550-018-0439-7`.

Carruth, G. and R Kobayashi (1973). "Vapor Pressure of Normal Paraffins Ethane Through n-Decane from Their Triple Points to About 10Mm Hg". In: *Journal of Chemical and Engineering* 18.2, pp. 115–126. ISSN: 0021-9568. DOI: `10.1021/je60057a009`. URL: `http://pubs.acs.org/doi/abs/10.1021/je60057a009`.

Chadha, M. S. et al. (1971). "Organic Synthesis in a Simulated Jovian Atmosphere". In: *Icarus* 15, pp. 39–44.

Chang, Jen Shih, Phil A. Lawless, and Toshiaki Yamamoto (1991). "Corona Discharge Processes". In: *IEEE Transactions on Plasma Science* 19.6, pp. 1152–1166. ISSN: 19399375. DOI: `10.1109/27.125038`.

Chang, S. et al. (1979). "Organic Chemistry on Titan". In: *Reviews of Geophysics and Space Physics* 17.8, pp. 1923–1933.

Cicerone, R J and R. Zellner (1983). "The atmospheric chemistry of hydrogen cyanide (HCN)". In: *Journal of Geophysical Research* 88.C15, p. 10689. ISSN: 0148-0227. DOI: `10.1029/JC088iC15p10689`. URL: `http://doi.wiley.com/10.1029/JC088iC15p10689`.

Coates, A J et al. (2007). "Ionospheric electrons in Titans tail : Plasma structure during the Cassini T9 encounter". In: *Geophysical Research Letters* 34, pp. 1–6. DOI: `10.1029/2007GL030919`.

Coates, A. J. et al. (2009). "Heavy negative ions in Titan's ionosphere: Altitude and latitude dependence". In: *Planetary and Space Science* 57.14-15, pp. 1866–1871. ISSN: 00320633. DOI: `10.1016/j.pss.2009.05.009`. URL: `http://dx.doi.org/10.1016/j.pss.2009.05.009`.

Coll, P. et al. (1995). "Organic chemistry in Titan's atmosphere: New data from laboratory simulations at low temperature". In: *Advances in Space Research* 16.2, pp. 93–103. ISSN: 02731177. DOI: `10.1016/0273-1177(95)00197-M`.

Coll, P. et al. (1999). "Experimental laboratory simulation of Titans atmosphere: aerosols and gas phase". In: *Planetary and Space Science* 47.10-11, pp. 1331–1340. ISSN: 00320633. DOI: `10.1016/S0032-0633(99)00054-9`.

Cordiner, M. A. et al. (2014a). "ALMA measurements of the HNC and HC_3N distributions in Titan's atmosphere". In: 2012, pp. 2–7. ISSN: 2041-8213. DOI: `10.1088/2041-8205/795/2/L30`. URL: `http://arxiv.org/abs/1408.6461%0Ahttp://dx.doi.org/10.1088/2041-8205/795/2/L30`.

Cordiner, M. A. et al. (2014b). "Ethyl cyanide on Titan: Spectroscopic detection and mapping using ALMA". In: pp. 3–8. ISSN: 2041-8213. DOI: `10.1088/2041-8205/800/1/L14`. URL: `http://arxiv.org/abs/1410.5325%0Ahttp://dx.doi.org/10.1088/2041-8205/800/1/L14`.

Cottini, V. et al. (2012). "Water vapor in Titan's stratosphere from Cassini CIRS far-infrared spectra". In: *Icarus* 220.2, pp. 855–862. ISSN: 00191035. DOI: `10.1016/j.icarus.2012.06.014`. URL: `http://dx.doi.org/10.1016/j.icarus.2012.06.014`.

Courtin, R. et al. (2011). "First results of Herschel -SPIRE observations of Titan". In: *Astronomy & Astrophysics* 536, p. L2. ISSN: 0004-6361. DOI: `10.1051/0004-6361/201118304`. URL: `http://www.aanda.org/articles/aa/full_html/2011/12/aa18304-11/aa18304-11.html`.

Coustenis, A. (2003). "Surfaces and atmospheres of the outer planets, their satellites and ring systems". In: *Planetary and Space Science* 51.14-15, p. v. ISSN: 00320633. DOI: `10.1016/S0032-0633(03)00209-5`. URL: `http://linkinghub.elsevier.com/retrieve/pii/S0032063303002095`.

Coustenis, A. et al. (2007). "The composition of Titan's stratosphere from Cassini/CIRS mid-infrared spectra". In: *Icarus* 189.1, pp. 35–62. ISSN: 00191035. DOI: `10.1016/j.icarus.2006.12.022`.

Coustenis, A. et al. (2010). "Titan trace gaseous composition from CIRS at the end of the Cassini-Huygens prime mission". In: *Icarus* 207.1, pp. 461–476. ISSN: 00191035. DOI: `10.1016/j.icarus.2009.11.027`. URL: `http://dx.doi.org/10.1016/j.icarus.2009.11.027`.

Coustenis, Athena et al. (2016). "Titan's temporal evolution in stratospheric trace gases near the poles". In: *Icarus* 270, pp. 409–420. ISSN: 10902643. DOI: `10.1016/j.icarus.2015.08.027`. URL: `http://dx.doi.org/10.1016/j.icarus.2015.08.027`.

Couturier-Tamburelli, I., N. Piétri, and M. Gudipati (2015). "Simulation of Titans atmospheric photochemistry Formation of non-volatile residue from polar nitrile ices". In: *Astronomy and Astrophysics* 111. ISSN: 14320746. DOI: `10.1051/0004-6361/201425518`.

Couturier-Tamburelli, I. et al. (2014). "Spectroscopic studies of non-volatile residue formed by photochemistry of solid C4N2: A model of condensed aerosol formation on Titan". In: *Icarus* 234, pp. 81–90. ISSN: 10902643. DOI: `10.1016/j.icarus.2014.02.016`. URL: `http://dx.doi.org/10.1016/j.icarus.2014.02.016`.

Couturier-Tamburelli, I. et al. (2018). "UVVis Light-induced Aging of Titans Haze and Ice". In: *The Astrophysical Journal* 852.2, p. 117. ISSN: 1538-4357. DOI: `10.3847/1538-4357/aa9e8d`. URL: `http://stacks.iop.org/0004-637X/852/i=2/a=117?key=crossref.abe561613a5ab2e74417801d20fd9c92`.

Crary, F. J. et al. (2009). "Heavy ions, temperatures and winds in Titan's ionosphere: Combined Cassini CAPS and INMS observations". In: *Planetary and Space Science* 57.14-15, pp. 1847–1856. ISSN: 00320633. DOI: `10.1016/j.pss.2009.09.006`. URL: `http://dx.doi.org/10.1016/j.pss.2009.09.006`.

Cravens, T. E. et al. (2006). "Composition of Titan's ionosphere". In: *Geophysical Research Letters* 33.7, pp. 8–11. ISSN: 00948276. DOI: `10.1029/2005GL025575`.

Cravens, T. E. et al. (2009). "Model-data comparisons for Titans nightside ionosphere". In: *Icarus* 199.1, pp. 174–188. ISSN: 0019-1035. DOI: `10.1016/j.icarus.2008.09.005`. URL: `http://dx.doi.org/10.1016/j.icarus.2008.09.005`.

Crespin, A. et al. (2005). "Seasonal variations of Titans stratospheric composition in the LMD/SA Global ClimateModel". In: *Bull. Am. Astron. Soc.* 37, 718.

Cui, J. et al. (2009a). "Analysis of Titan's neutral upper atmosphere from Cassini Ion Neutral Mass Spectrometer measurements". In: *Icarus* 200.2, pp. 581–615. ISSN: 00191035. DOI: `10.1016/j.icarus.2008.12.005`. URL: `http://dx.doi.org/10.1016/j.icarus.2008.12.005`.

Cui, J. et al. (2009b). "Diurnal variations of Titans ionosphere". In: *Journal of Geophysical Research* 114, pp. 1–20. DOI: `10.1029/2009JA014228`.

Curtis, Daniel B. et al. (2008). "Laboratory studies of methane and ethane adsorption and nucleation onto organic particles: Application to Titan's clouds". In: *Icarus* 195.2, pp. 792–801. ISSN: 00191035. DOI: `10.1016/j.icarus.2008.02.003`.

Danger, G et al. (2011). "Experimental investigation of aminoacetonitrile formation through the Strecker synthesis in astrophysical-like conditions: reactivity of methanimine (CH2NH), ammonia (NH3), and hydrogen cyanide (HCN)". In: *Astronomy & Astrophysics* 535, A47. ISSN: 0004-6361. DOI: `10.1051/0004-6361/201117602`.

Danielson, R. E., John J. Caldwell, and D. R. Larach (1973). "An inversion in the atmosphere of Titan". In: *Icarus* 20.4, pp. 437–443. ISSN: 10902643. DOI: `10.1016/0019-1035(73)90016-X`.

Davis, Douglas D. and H. Okabe (1968). "Determination of Bond Dissociation Energies in Hydrogen Cyanide. Cyanogen and Cyanogen Halides by the Photodissociation Method". In: *The Journal of Chemical Physics* 49.12, p. 5526. ISSN: 00219606. DOI: `10.1063/1.1670082`. URL: `http://scitation.aip.org/content/aip/journal/jcp/49/12/10.1063/1.1670082`.

De Kok, Remco J et al. (2014). "HCN ice in Titan's high-altitude southern polar cloud". In: *Nature* 514.7520, pp. 65–7. ISSN: 1476-4687. DOI: `10.1038/nature13789`. URL: `http://adsabs.harvard.edu/abs/2014Natur.514...65D`.

Desai, R. T. et al. (2017). "Carbon chain anions and the growth of complex organic molecules in Titan's ionosphere". In: *The Astrophysical Journal Letters* 844.2, pp. 1–8. ISSN: 2041-8213. DOI: `10.3847/2041-8213/aa7851`. URL: `http://arxiv.org/abs/1706.01610`.

Dobrijevic, M. et al. (2016). "1D-coupled photochemical model of neutrals, cations and anions in the atmosphere of Titan". In: *Icarus* 268, pp. 313–339. ISSN: 10902643. DOI: `10.1016/j.icarus.2015.12.045`. URL: `http://dx.doi.org/10.1016/j.icarus.2015.12.045`.

Dodonova, N. Y. (1966). "Activation of nitrogen by vacuum ultraviolet radiation". In: *Russian Journal of Physical Chemistry*.

Doose, Lyn R. et al. (2016). "Vertical structure and optical properties of Titan's aerosols from radiance measurements made inside and outside the atmosphere". In: *Icarus* 270, pp. 355–375. ISSN: 10902643. DOI: `10.1016/j.icarus.2015.09.039`. URL: `http://dx.doi.org/10.1016/j.icarus.2015.09.039`.

Dubois, D. et al. (2019). "In Situ Investigation of Neutrals Involved in the Formation of Titan Tholins". In: *Icarus* 317.July 2018, pp. 182–196. ISSN: 00191035. DOI: `10.1016/j.icarus.2018.07.006`. URL: `https://doi.org/10.1016/j.icarus.2018.07.006`.

Elachi, C et al. (2004). “Radar: the Cassini Titan radar mapper”. In: *Space Sci. Rev.* 115.1, pp. 71–110.

English, M. A. et al. (1996). “Ablation and chemistry of meteoric materials in the atmosphere of Titan”. In: *Advances in Space Research* 17.12, pp. 157–160. ISSN: 02731177. DOI: 10.1016/0273-1177(95)00774-9.

Esposito, Larry W et al. (2004). “The Cassini Ultraviolet Imaging Spectrograph Investigation”. In: pp. 299–361.

Ferris, James et al. (2005). “The role of photochemistry in Titan’s atmospheric chemistry”. In: *Advances in Space Research* 36.2, pp. 251–257. ISSN: 02731177. DOI: 10.1016/j.asr.2005.03.056.

Field, D. et al. (1991). “Ion energy distributions in radio-frequency discharges”. In: *Journal of Applied Physics* 70.1, pp. 82–92. ISSN: 00218979. DOI: 10.1063/1.350247.

Fihtengolts, V. S. (1969). “Atlas of UV absorption spectra of substances used in synthetic rubber manufacture”. In: ed. by NIST Chemistry WebBook.

Fischer, Gad and I. G. Ross (2003). “Electronic spectrum of dicyanoacetylene. 1. Calculations of the geometries and vibrations of ground and excited states of diacetylene, cyanoacetylene, cyanogen, triacetylene, cyanodiacetylene, and dicyanoacetylene”. In: *Journal of Physical Chemistry A* 107.49, pp. 10631–10636. ISSN: 10895639. DOI: 10.1021/jp034966j.

Flasar, F M et al. (2005). “Titan’s Atmospheric Temperatures, Winds, and Composition”. In: *Science* 308.5724, pp. 975–978. ISSN: 0036-8075. DOI: 10.1126/science.1111150. URL: http://www.sciencemag.org/cgi/content/abstract/308/5724/975.

Fleury, B. et al. (2014). “Influence of CO on Titan atmospheric reactivity”. In: *Icarus* 238, pp. 221–229. ISSN: 10902643. DOI: 10.1016/j.icarus.2014.05.027.

Fleury, Benjamin (2015). “The upper atmopshere of the early Earth , a source of prebiotic organic compounds”. In:

Fleury, Benjamin et al. (2015). “Water Formation in the Upper Atmosphere of the Early Earth”. In: *The Astrophysical Journal* 807.2, p. L29. ISSN: 2041-8213. DOI: 10.1088/2041-8205/807/2/L29. URL: http://stacks.iop.org/2041-8205/807/i=2/a=L29?key=crossref.28b314bf53635235f7d2ca5fda4505c1.

Fortenberry, Ryan et al. (2017). “Quantum Chemical Spectral Characterization of CH 2 NH 2 + for Remote Sensing of Titans Atmosphe”. In: *Icarus*.

Fortenberry, Ryan C. (2017). “Quantum astrochemical spectroscopy”. In: *International Journal of Quantum Chemistry* 117.2, pp. 81–91. ISSN: 1097461X. DOI: 10.1002/qua.25180.

Fox, Jane L. and Roger V. Yelle (1997). “Hydrocarbon ions in the ionosphere of Titan”. In: *Geophysical Research Letters* 24.17, pp. 2179–2182. ISSN: 1944-8007. DOI: 10.1029/97GL02051.

Frankland, Victoria L. et al. (2016). “Uptake of acetylene on cosmic dust and production of benzene in Titan’s atmosphere”. In: *Icarus* 278, pp. 88–99. ISSN: 10902643. DOI: 10.1016/j.icarus.2016.06.007. URL: http://dx.doi.org/10.1016/j.icarus.2016.06.007.

Fray, N. and B. Schmitt (2009). “Sublimation of ices of astrophysical interest: A bibliographic review”. In: *Planetary and Space Science* 57.14-15, pp. 2053–2080. ISSN: 00320633. DOI: 10.1016/j.pss.2009.09.011. URL: http://dx.doi.org/10.1016/j.pss.2009.09.011.

Fulchignoni, M. et al. (2005). “In situ measurements of the physical characteristics of Titan’s environment”. In: *Nature* 438.7069, pp. 785–791. ISSN: 0028-0836. DOI:

10.1038/nature04314. URL: http://www.nature.com/doifinder/10.1038/nature04314.

Garnier, P. et al. (2007). "The exosphere of Titan and its interaction with the kronian magnetosphere: MIMI observations and modeling". In: *Planetary and Space Science* 55.1-2, pp. 165–173. ISSN: 00320633. DOI: 10.1016/j.pss.2006.07.006.

Gautier, Thomas et al. (2011). "Nitrile gas chemistry in Titan's atmosphere". In: *Icarus* 213.2, pp. 625–635. ISSN: 00191035. DOI: 10.1016/j.icarus.2011.04.005.

Gautier, Thomas et al. (2012). "Mid- and far-infrared absorption spectroscopy of Titan's aerosols analogues". In: *Icarus* 221.1, pp. 320–327. ISSN: 00191035. DOI: 10.1016/j.icarus.2012.07.025. URL: http://dx.doi.org/10.1016/j.icarus.2012.07.025.

Gautier, Thomas et al. (2013). "Experimental simulation of Titans aerosols formation". In:

Gautier, Thomas et al. (2014). "Nitrogen incorporation in titan's tholins inferred by high resolution orbitrap mass spectrometry and gas chromatography-mass spectrometry". In: *Earth and Planetary Science Letters* 404, pp. 33–42. ISSN: 0012821X. DOI: 10.1016/j.epsl.2014.07.011. URL: http://dx.doi.org/10.1016/j.epsl.2014.07.011.

Gavilan, L. et al. (2017). "Organic Aerosols in the Presence of CO<inf>2</inf> in the Early Earth and Exoplanets: UV-Vis Refractive Indices of Oxidized Tholins". In: *Astrophysical Journal Letters* 848.1, p. L5. ISSN: 20418213. DOI: 10.3847/2041-8213/aa8cc4. URL: http://dx.doi.org/10.3847/2041-8213/aa8cc4.

Gerakines, P. A., M. H. Moore, and R. L. Hudson (2004). "Ultraviolet photolysis and proton irradiation of astrophysical ice analogs containing hydrogen cyanide". In: *Icarus* 170.1, pp. 202–213. ISSN: 00191035. DOI: 10.1016/j.icarus.2004.02.005.

Giver, P. (1976). "Methane Contamination of H2 Features in the Spectrum of Titan". In:

Glicker, S. and H. Okabe (1987). "Photochemistry of Diacetylene". In: *Journal of Physical Chemistry* 9, pp. 437–440.

Godfrey, P. D. et al. (1973). "Discovery of Interstellar Methanimine (Formaldimine)". In: *Astrophysical Letters* 13, p. 119. ISSN: 0004-6388. URL: http://adsabs.harvard.edu/abs/1973ApL....13..119G.

Gudipati, Murthy S. (1994). "Exciton, exchange, and through-bond interactions in multichromophoric molecules: An analysis of the electronic excited states". In: *Journal of Physical Chemistry* 98.39, pp. 9750–9763. ISSN: 00223654. DOI: 10.1021/j100090a007.

Gudipati, Murthy S et al. (2013). "Photochemical activity of Titan's low-altitude condensed haze." In: *Nature communications* 4.April, p. 1648. ISSN: 2041-1723. DOI: 10.1038/ncomms2649. URL: http://www.ncbi.nlm.nih.gov/pubmed/23552063.

Gudmundsson, J T, T. Kimura, and M. Lieberman (1999). "Experimental studies of O 2 /Ar plasma in a planar inductive discharge". In: *Plasma Sources Science and Technology* 8.1, pp. 22–30. ISSN: 0963-0252. DOI: 10.1088/0963-0252/8/1/003. URL: http://stacks.iop.org/0963-0252/8/i=1/a=003?key=crossref.47514f9adf2b7c80d343b6ddf2104a36.

Gupta, S., E. Ochiai, and C. Ponnamperuma (1981). "Organic synthesis in the atmosphere of Titan". In: *Nature* 293.

Hadamcik, E. et al. (2009). "Laboratory light-scattering measurements with Titan's aerosols analogues produced by a dusty plasma". In: *Planetary and Space Science*

57.13, pp. 1631–1641. ISSN: 00320633. DOI: 10.1016/j.pss.2009.06.013. URL: http://dx.doi.org/10.1016/j.pss.2009.06.013.

Hadamcik, E. et al. (2013). "Optical properties of analogs of Titan's aerosols produced by dusty plasma". In: *Earth, Planets and Space* 65.10, pp. 1175–1184. ISSN: 13438832. DOI: 10.5047/eps.2013.05.019. URL: http://labs.adsabs.harvard.edu/adsabs/abs/2013EP%26S...65.1175H/.

Hanel, R. et al. (1981). "Infrared Observations of the Saturnian System from Voyager 1". In: *Science* 212.4491, pp. 192–200. ISSN: 0036-8075. DOI: 10.1126/science.212.4491.192. URL: http://www.sciencemag.org/cgi/doi/10.1126/science.212.4491.192.

Harris, G. J. et al. (2006). "Improved HCN/HNC linelist, model atmospheres and synthetic spectra for WZ Cas". In: *Monthly Notices of the Royal Astronomical Society* 367.1, pp. 400–406. ISSN: 00358711. DOI: 10.1111/j.1365-2966.2005.09960.x.

Hartung, R. (1994). *Cyanides and nitriles*. 4th ed. vo. John Wiley & Sons, 31193172.

He, Chao and Mark A. Smith (2014). "Identification of nitrogenous organic species in Titan aerosols analogs: Implication for prebiotic chemistry on Titan and early Earth". In: *Icarus* 238, pp. 86–92. ISSN: 10902643. DOI: 10.1016/j.icarus.2014.05.012. URL: http://dx.doi.org/10.1016/j.icarus.2014.05.012.

Hébrard, Eric (2006). "Incertitudes photochimiques dans les modèles de latmosphère de Titan : Revue et conséquences". In: *Thèse*.

Herzberb, G. and K. K. Innes (1957). "ULTRAVIOLET ABSORPTION SPECTRA OF HCN AND DCN 1. The Alpha-X and Beta-X Systems". In: *Canadian Journal of Physics*.

Hidayat, T et al. (1997). "Millimeter and Submillimeter Heterodyne Observations of Titan : Retrieval of the Vertical Profile of HCN and the 12 C / 13 C Ratio". In: 182, pp. 170–182.

Hill, Christian, Sergei N. Yurchenko, and Jonathan Tennyson (2013). "Temperature-dependent molecular absorption cross sections for exoplanets and other atmospheres". In: *Icarus* 226.2, pp. 1673–1677. ISSN: 00191035. DOI: 10.1016/j.icarus.2012.07.028. URL: http://dx.doi.org/10.1016/j.icarus.2012.07.028.

Hörst, S. M. and M. A. Tolbert (2013). "In situ measurements of the size and density of titan aerosol analogs". In: *Astrophysical Journal Letters* 770.1, pp. 1–21. ISSN: 20418205. DOI: 10.1088/2041-8205/770/1/L10.

Hörst, Sarah M. (2017). "Titan's Atmosphere and Climate". In: *Journal of Geophysical Research: Planets*, pp. 432–482. ISSN: 21699097. DOI: 10.1002/2016JE005240. URL: http://arxiv.org/abs/1702.08611.

Hörst, Sarah M. et al. (2018). "Laboratory investigations of Titan haze formation: In situ measurement of gas and particle composition". In: *Icarus* 301, pp. 136–151. ISSN: 10902643. DOI: 10.1016/j.icarus.2017.09.039.

Hörst, S.M. et al. (2012). "Formation of Amino Acids and Nucleotide Bases in a Titan Atmosphere Simulation Experiment". In: *Astrobiology* 12.9, pp. 809–817. ISSN: 1531-1074. DOI: 10.1089/ast.2011.0623. URL: http://online.liebertpub.com/doi/abs/10.1089/ast.2011.0623.

Horvath, G. et al. (2009). "Negative ions formed in N 2 /CH 4 /Ar discharge A simulation of Titan's atmosphere chemistry". In: *The European Physical Journal Applied Physics* 49.1, p. 13105. ISSN: 1286-0042. DOI: 10.1051/epjap/2009192. URL: http://www.epjap.org/10.1051/epjap/2009192.

Howling, A. A. et al. (1994). "Time-resolved measurements of highly polymerized negative ions in radio frequency silane plasma deposition experiments". In: *Journal of Applied Physics* 75.3, pp. 1340–1353. ISSN: 00218979. DOI: `10.1063/1.356413`.

Hunten, Donald M. (1973). "The escape of light gases from planetary atmospheres". In: *Journal of Atmospheric Sciences* 30.8, 14811494. ISSN: 0022-4928. DOI: `10.1175/1520-0469(1973)030<1481:TEOLGF>2.0.CO;2`. URL: `http://adsabs.harvard.edu/abs/1973JAtS...30.1481H`.

Huygens, Christiaan (1659). *Systema Saturnium, sive de causis mirandorum Saturni phaenomenon, et comite ejus planeta novo*. Ed. by The Hague: Adrian Vlacq.

Hyodo, Ryuki and Keiji Ohtsuki (2015). "Saturn's F ring and shepherd satellites a natural outcome of satellite system formation". In: *Nature Geoscience* 8.9, pp. 686–689. ISSN: 17520908. DOI: `10.1038/ngeo2508`.

Imanaka, Hiroshi and Mark A. Smith (2009). "EUV photochemical production of unsaturated hydrocarbons: Implications to EUV photochemistry in Titan and Jovian planets". In: *Journal of Physical Chemistry A* 113.42, pp. 11187–11194. ISSN: 10895639. DOI: `10.1021/jp9041952`.

Imanaka, Hiroshi et al. (2004). "Laboratory experiments of Titan tholin formed in cold plasma at various pressures: Implications for nitrogen-containing polycyclic aromatic compounds in Titan haze". In: *Icarus* 168.2, pp. 344–366. ISSN: 00191035. DOI: `10.1016/j.icarus.2003.12.014`.

Ip, W. H. (1990). "Titan's upper ionosphere". In: *The Astrophysical journal*, pp. 354–363.

Israel, G. L. et al. (2005). "Complex organic matter in Titan's atmospheric aerosols from in situ pyrolysis and analysis." In: *Nature* 438.7069, pp. 796–799. ISSN: 0028-0836. DOI: `10.1038/nature04349`.

Jeans, J. (1925). "The Dynamical Theory of Gases". In: 4th Editio.

Jennings, Donald E. et al. (2012). "Seasonal disappearance of far-infrared haze in Titan's stratosphere". In: *Astrophysical Journal Letters* 754.1, pp. 1–4. ISSN: 20418205. DOI: `10.1088/2041-8205/754/1/L3`.

Joalland, Baptiste et al. (2016). "Low-Temperature Reactivity of C2n+1N- Anions with Polar Molecules". In: *Journal of Physical Chemistry Letters* 7.15, pp. 2957–2961. ISSN: 19487185. DOI: `10.1021/acs.jpclett.6b01191`.

Johnson, R E, O J Tucker, and A N Volkov (2016). "Evolution of an early Titan atmosphere". In: *Icarus* 271, pp. 202–206. DOI: `10.1016/j.icarus.2016.01.014`.

Karkoschka, Erich et al. (2007). "DISR imaging and the geometry of the descent of the Huygens probe within Titan's atmosphere". In: *Planetary and Space Science* 55.13, pp. 1896–1935. ISSN: 00320633. DOI: `10.1016/j.pss.2007.04.019`.

Kawamura, E (1999). "Ion energy distributions in rf sheaths; review, analysis and simulation". In: *Plasma Sources Science and Technology* 8, R45–R64.

Keller, C. N., V. G. Anicich, and T. E. Cravens (1998). "Model of Titan's ionosphere with detailed hydrocarbon ion chemistry". In: *Planet. Space Sci.* 46, pp. 1157–1174. ISSN: 00320633. DOI: `Doi:10.1016/s0032-0633(98)00053-1`.

Keller, C N, T E Cravens, and L Gan (1992). "A model of the ionosphere of Titan". In: *Journal of Geophysical Research, [Space Physics]* 97.A8, pp. 12117–12135.

Khanna, R. K., Mario J. Ospina, and Guizhi Zhao (1988). "Infrared band extinctions and complex refractive indices of crystalline C2H2and C4H2". In: *Icarus* 73.3, pp. 527–535. ISSN: 10902643. DOI: `10.1016/0019-1035(88)90062-0`.

Khare, B. and C. Sagan (1973). "Red clouds in reducing atmospheres". In: *Icarus* 20.3, pp. 311–321. ISSN: 00191035. DOI: `10.1016/0019-1035(73)90008-`

0. URL: http://www.sciencedirect.com/science/article/pii/0019103573900080.

Khare, B. N. and C. Sagan (1971). "Synthesis of Cystine in Simulated Primitive Conditions". In: *Nature* 232.

Khare, B. N. et al. (1981). "Organic solids produced by electrical discharge in reducing atmospheres: Tholin molecular analysis". In: *Icarus* 48.2, pp. 290–297. ISSN: 10902643. DOI: 10.1016/0019-1035(81)90110-X.

Khare, B. N. et al. (1984). "Optical constants of organic tholins produced in a simulated Titanian atmosphere: From soft x-ray to microwave frequencies". In: *Icarus* 60.1, pp. 127–137. ISSN: 10902643. DOI: 10.1016/0019-1035(84)90142-8.

Kim, Sang J. et al. (2005). "Clouds, haze, and CH4, CH3D, HCN, and C2 H2 in the atmosphere of Titan probed via 3 ţm spectroscopy". In: *Icarus* 173.2, pp. 522–532. ISSN: 00191035. DOI: 10.1016/j.icarus.2004.09.006.

Koskinen, T. T. et al. (2011). "The mesosphere and lower thermosphere of Titan revealed by Cassini/UVIS stellar occultations". In: *Icarus* 216.2, pp. 507–534. ISSN: 00191035. DOI: 10.1016/j.icarus.2011.09.022. URL: http://dx.doi.org/10.1016/j.icarus.2011.09.022.

Krasnopolsky, Vladimir A. (2009). "A photochemical model of Titan's atmosphere and ionosphere". In: *Icarus* 201.1, pp. 226–256. ISSN: 00191035. DOI: 10.1016/j.icarus.2008.12.038. URL: http://www.sciencedirect.com/science/article/pii/S0019103509000062.

Kuiper, G P (1944). "Titan: a Satellite with an Atmosphere". In: *Astrophys. J.* 100, pp. 378–383. ISSN: 0004-637X. DOI: 10.1086/144679.

Kunde, V. G. et al. (1981). "C4H2, HC3N and C2N2 in Titan's atmosphere". In: *Nature* 292.5825, pp. 686–688. ISSN: 0028-0836. DOI: 10.1038/292686a0. URL: http://www.nature.com/doifinder/10.1038/292686a0.

Kunde, Virgil G. et al. (1996). "Cassini infrared Fourier spectroscopic investigation". In: *Proceedings of SPIE* October, pp. 162–177. DOI: 10.1117/12.253416. URL: http://proceedings.spiedigitallibrary.org/proceeding.aspx?articleid=1020839.

Lammer, H. et al. (2001). "Lightning activity on Titan: Can Cassini detect it?" In: *Planetary and Space Science* 49.6, pp. 561–574. ISSN: 00320633. DOI: 10.1016/S0032-0633(00)00171-9.

Lara, L. M. et al. (1996). "Vertical distribution of Titan's atmospheric neutral constituents". In: *Journal of Geophysical Research* 101.E10, p. 23261. ISSN: 0148-0227. DOI: 10.1029/96JE02036. URL: http://adsabs.harvard.edu/abs/1996JGR...10123261L.

Largo, L. et al. (2010). "The reaction between NH + and CH 3 COOH : a possible process for the formation of glycine precursors in the interstellar medium". In: *Astronomy & Astrophysics* 516, A79. ISSN: 0004-6361. DOI: 10.1051/0004-6361/201014057.

Lavvas, P., C. A. Griffith, and R. V. Yelle (2011). "Condensation in Titan's atmosphere at the Huygens landing site". In: *Icarus* 215.2, pp. 732–750. ISSN: 00191035. DOI: 10.1016/j.icarus.2011.06.040. URL: http://dx.doi.org/10.1016/j.icarus.2011.06.040.

Lavvas, P. et al. (2011). "Energy deposition and primary chemical products in Titan's upper atmosphere". In: *Icarus* 213.1, pp. 233–251. ISSN: 00191035. DOI: 10.1016/j.icarus.2011.03.001. URL: http://dx.doi.org/10.1016/j.icarus.2011.03.001.

Lavvas, P. et al. (2013). “Aerosol growth in Titan’s ionosphere”. In: *Proceedings of the National Academy of Sciences* 110.8, pp. 2729–2734. ISSN: 0027-8424. URL: `http://www.pnas.org/cgi/doi/10.1073/pnas.1217059110`.

Lavvas, P. P., A. Coustenis, and I. M. Vardavas (2008). “Coupling photochemistry with haze formation in Titan’s atmosphere, Part II: Results and validation with Cassini/Huygens data”. In: *Planetary and Space Science* 56.1, pp. 67–99. ISSN: 00320633. DOI: `10.1016/j.pss.2007.05.027`.

Lebonnois, Sébastien, E. L.O. Bakes, and Christopher P. McKay (2003). “Atomic and molecular hydrogen budget in Titan’s atmosphere”. In: *Icarus* 161.2, pp. 474–485. ISSN: 00191035. DOI: `10.1016/S0019-1035(02)00039-8`.

Lebreton, J. P. and D. L. Matson (1992). “An overview of the Cassini mission”. In: *Il Nuovo Cimento C* 15.6, pp. 1137–1147. ISSN: 03905551. DOI: `10.1007/BF02506708`.

Lebreton, Jean-pierre et al. (2005). “An overview of the descent and landing of the Huygens probe on Titan”. In: 438.December. DOI: `10.1038/nature04347`.

Lethuillier, A et al. (2018). “Electrical Properties of Tholins and Derived Constraints on the Huygens Landing Site Composition at the Surface of Titan”. In: *Journal of Geophysical Research: Planets* 2016, pp. 1–16.

Loison, J. C. et al. (2015). “The neutral photochemistry of nitriles, amines and imines in the atmosphere of Titan”. In: *Icarus* 247, pp. 218–247. ISSN: 10902643. DOI: `10.1016/j.icarus.2014.09.039`. URL: `http://dx.doi.org/10.1016/j.icarus.2014.09.039`.

Lorenz, Ralph D. et al. (2008). “Titan’s inventory of organic surface materials”. In: *Geophysical Research Letters* 35.2, pp. 4–9. ISSN: 00948276. DOI: `10.1029/2007GL032118`.

Louwman, Peter (2004). “Christiaan Huygens and his telescopes”. In: *Proceedings of the International Conference "Titan - from discovery to encounter"*.

Loveday, J. S. et al. (2001). “Stable methane hydrate above 2[thinsp]GPa and the source of Titan’s atmospheric methane”. In: 410.6829, pp. 661–663. ISSN: 0028-0836. DOI: `10.1038/35070513`. URL: `http://dx.doi.org/10.1038/35070513`.

Lunine, Jonathan I. (2017). “Ocean worlds exploration”. In: *Acta Astronautica* 131.November 2016, pp. 123–130. ISSN: 00945765. DOI: `10.1016/j.actaastro.2016.11.017`. URL: `http://dx.doi.org/10.1016/j.actaastro.2016.11.017`.

Luspay-Kuti, A. et al. (2015). “Experimental constraints on the composition and dynamics of Titan’s polar lakes”. In: *Earth and Planetary Science Letters* 410, pp. 75–83. ISSN: 0012821X. DOI: `10.1016/j.epsl.2014.11.023`. URL: `http://dx.doi.org/10.1016/j.epsl.2014.11.023`.

Lutz, B. L., T. Owen, and R. D. Cess (1976). “Laboratory band strengths of methane and their application to the atmospheres of Jupiter, Saturn, Uranus, Neptune, and Titan”. In: *The Astrophysical Journal* 203, p. 541. ISSN: 0004-637X. DOI: `10.1086/154110`. URL: `http://adsabs.harvard.edu/abs/1976ApJ...203..541L`.

Magee, Brian A. et al. (2009). “INMS-derived composition of Titan’s upper atmosphere: Analysis methods and model comparison”. In: *Planetary and Space Science* 57.14-15, pp. 1895–1916. ISSN: 00320633. DOI: `10.1016/j.pss.2009.06.016`. URL: `http://dx.doi.org/10.1016/j.pss.2009.06.016`.

Maguire, W. C. et al. (1981). “C3H8 and C3H4 in Titan’s atmosphere”. In: *Nature* 292.5825, pp. 683–686. ISSN: 0028-0836. DOI: `10.1038/292683a0`. URL: `http://www.nature.com/doifinder/10.1038/292683a0`.

Mahjoub, A. et al. (2012). “Influence of methane concentration on the optical indices of titan’s aerosols analogues”. In: *Icarus* 221.2, pp. 670–677. ISSN: 00191035. DOI:

10.1016/j.icarus.2012.08.015. URL: http://dx.doi.org/10.1016/j.icarus.2012.08.015.

Mahjoub, A. et al. (2016). “Development of a new Experimental Platform to Constrain the Chemical Composition of Titan’s Lakes”. In: *Lunar and Planetary Science Conference XLVII* 2787, pp. 46–47. ISSN: 19453027. DOI: 10.1038/ngeo2474..

Mahjoub, Ahmed et al. (2014). “Effect of the synthesis temperature on the optical indices of organic materials produced by N2-CH4 RF plasma”. In: *Plasma Processes and Polymers* 11.5, pp. 409–417. ISSN: 16128869. DOI: 10.1002/ppap.201300150.

Mamajanov, Irena and Judith Herzfeld (2014). “HCN polymers characterized by solid state NMR : Chains and sheets formed in the neat liquid HCN polymers characterized by solid state NMR : Chains and sheets”. In: 134503.2009. DOI: 10.1063/1.3092908.

Masterson, C. M. and R. K. Khanna (1990). “Absorption intensities and complex refractive indices of crystalline HCN, HC3N, and C4N2 in the infrared region”. In: *Icarus* 83.1, pp. 83–92. ISSN: 10902643. DOI: 10.1016/0019-1035(90)90007-V.

Maurice, S. et al. (1996). “Comprehensive analysis of electron observations at Saturn: Voyager 1 and 2”. In: *Journal of Geophysical Research* 101.

McDonald, G D et al. (1994). “Chemical Investigation of Titan and Triton Tholins”. In: *Icarus* 108, pp. 137–145.

McKay, Christopher P. (1996). “Elemental composition, solubility, and optical properties of Titan’s organic haze”. In: *Planetary and Space Science* 44.8, pp. 741–747. ISSN: 00320633. DOI: 10.1016/0032-0633(96)00009-8.

Miller, Stanley L. (1953). “A Production of Amino Acids under Possible Primitive Earth Conditions”. In: 117.3046, pp. 528–529.

Minaev, Boris et al. (2004). “Singlet-triplet transitions in three-atomic molecules studied by time-dependent MCSCF and density functional theory”. In: *Molecular Physics* 102.13, pp. 1391–1406. ISSN: 00268976. DOI: 10.1080/00268970410001668435.

Miranda, Barbara Cunha de et al. (2015). “Reactions of State-Selected Atomic Oxygen Ions O(+)((4)S, (2)D, (2)P) with Methane.” In: *The journal of physical chemistry. A* 119.23, pp. 6082–98. ISSN: 1520-5215. DOI: 10.1021/jp512846v. URL: http://dx.doi.org/10.1021/jp512846v.

Mizutani, Hiroshi et al. (1975). “Study of the photochemical reaction of HCN nd its polymer prodcts relating to primary chemical evolution”. In: *Origins of Life* 6.1975, pp. 513–525.

Molter, Edward M. et al. (2016). “ALMA Observations of HCN and its Isotopologues on Titan”. In: pp. 1–14. URL: http://arxiv.org/abs/1606.00348.

Molton, P. M. and Cyril Ponnamperuma (1974). “Organic synthesis in a simulated Jovian atmosphere. III. Synthesis of Aminonitriles”. In: *Icarus* 21.2, pp. 166–174. ISSN: 10902643. DOI: 10.1016/0019-1035(74)90133-X.

Moreno, R. et al. (2015). “ALMA observations of Titan : Vertical and spatial distribution of nitriles”. In: *EPSC 2015* 10, p. 2015.

Mukundan, Vrinda and Anil Bhardwaj (2018). “A Model for Negative Ion Chemistry in Titans Ionosphere”. In: *The Astrophysical Journal* 856.2, p. 168. ISSN: 1538-4357. DOI: 10.3847/1538-4357/aab1f5. URL: http://stacks.iop.org/0004-637X/856/i=2/a=168?key=crossref.b14d1b74b2ca76356a92ed40f24250fa.

Muller-Wodarg et al. (2014). “Titan: Interior, Surface, Atmosphere, and Space Environment”. In: pp. 1–287.

Mutsukura, Nobuki (2001). “Deposition of Diamondlike Carbon Film and Mass Spectrometry Measurement in CH 4 / N 2 RF Plasma”. In: 21.2, pp. 265–277.

Nagy, Andrew F and Thomas E Cravens (1998). "Titan's ionosphere: A review". In: pp. 38–44.

Navarro-González, Rafael and Sandra I. Ramírez (1997). "Corona discharge of Titan's troposphere". In: *Advances in Space Research* 19.7, pp. 1121–1133. ISSN: 02731177. DOI: 10.1016/S0273-1177(97)00361-X.

Neish, C. D. et al. (2009). "Low temperature hydrolysis of laboratory tholins in ammonia-water solutions: Implications for prebiotic chemistry on Titan". In: *Icarus* 201.1, pp. 412–421. ISSN: 00191035. DOI: 10.1016/j.icarus.2009.01.003. URL: http://dx.doi.org/10.1016/j.icarus.2009.01.003.

Nelson, R. M. et al. (2009). "Saturn's Titan: Surface change, ammonia, and implications for atmospheric and tectonic activity". In: *Icarus* 199.2, pp. 429–441. ISSN: 00191035. DOI: 10.1016/j.icarus.2008.08.013. URL: http://dx.doi.org/10.1016/j.icarus.2008.08.013.

Nixon, Conor A. et al. (2013). "Upper limits for PH3 and H2S in Titan's atmosphere from Cassini CIRS". In: *Icarus* 224.1, pp. 253–256. ISSN: 00191035. DOI: 10.1016/j.icarus.2013.02.024. URL: http://dx.doi.org/10.1016/j.icarus.2013.02.024.

Nixon, Conor A. et al. (2016). "Titan Science with the James Webb Space Telescope". In: *Astronomical Society of the Pacific* 128.959, pp. 1–28. ISSN: 0004-6280. DOI: 10.1088/1538-3873/128/959/018009. URL: http://dx.doi.org/10.1088/1538-3873/128/959/018009.

Nna-Mvondo, Delphine, Carrie; Anderson, and Robert E. Samuelson (2018). "CIRS-Observed Titans Stratospheric Ice Clouds Studied in the Laboratory". In: *American Astronomical Society, AAS Meeting #232, id.#313.03*.

Noble, J. A. et al. (2013). "The thermal reactivity of HCN and NH3 in interstellar ice analogues". In: *Monthly Notices of the Royal Astronomical Society* 428.4, pp. 3262–3273. ISSN: 00358711. DOI: 10.1093/mnras/sts272.

Oliveira, Glênisson D E et al. (2001). "Definitive Heat of Formation of Methylenimine, CH2=NH, and of Methylenimmonium Ion, CH2NH2+, by Means of W2 Theory". In: *Technology* 22.13, pp. 1297–1305.

Oró, J. (1961). "Comets and the Formation of Biochemical Compounds on the Primitive Earth". In: *Nature* 189, pp. 775–776.

Owen, T. C. (1982). "The composition and origin of Titan's atmosphere". In: *Planetary and Space Science* 30.8, pp. 833–838. URL: http://www.sciencedirect.com/science/article/pii/0032063382901155.

Palmer, Maureen Y et al. (2017). "ALMA detection and astrobiological potential of vinyl cyanide on Titan". In: July, pp. 1–7.

Paubert, G., D. Gautier, and R. Courtin (1984). "The millimeter spectrum of Titan: Detectability of HCN, HC3N, and CH3CN and the CO abundance". In: *Icarus* 60.3, pp. 599–612. ISSN: 10902643. DOI: 10.1016/0019-1035(84)90167-2.

Peng, Z et al. (2013). "Titan's atmosphere simulation experiment using continuum UV-VUV synchrotron radiation". In: *Journal of Geophysical Research: Planets* 118.4, pp. 778–788. ISSN: 2169-9100. DOI: 10.1002/jgre.20064. URL: http://dx.doi.org/10.1002/jgre.20064.

Pernot, Pascal et al. (2010). "TholinomicsChemical Analysis of Nitrogen-Rich Polymers". In: *Analytical Chemistry* 82.4, pp. 1371–1380. ISSN: 0003-2700. DOI: 10.1021/ac902458q. URL: http://pubs.acs.org/doi/abs/10.1021/ac902458q.

Pilling, S. et al. (2009). "DNA nucleobase synthesis at Titan atmosphere analog by soft X-rays". In: *Journal of Physical Chemistry A* 113.42, pp. 11161–11166. ISSN: 10895639. DOI: 10.1021/jp902824v.

Pintassilgo, C D et al. (1999). “Methane decomposition and active nitrogen in a N2-CH4 glow discharge at low pressures”. In: *Plasma Sources Science Technology* 1, pp. 463–478. ISSN: 0019-1035. DOI: `http://dx.doi.org/10.1016/0019-1035(91)90068-5`.

Porco, C.C. Carolyn C et al. (2004). “Cassini Imaging Science: Instrument Characteristics And Anticipated Scientific Investigations At Saturn”. In: *Space Science Reviews* 115.1-4, p. 363. ISSN: 00386308. DOI: `10.1007/s11214-004-1456-7`. URL: `http://adsabs.harvard.edu/cgi-bin/nph-data_query?bibcode=2004SSRv..115..363P&link_type=ABSTRACT%0Apapers3://publication/doi/10.1007/s11214-004-1456-7`.

Price, W. C. (1934). “The absorption spectra of formaldehyde and hydrogen cyanide in the far ultraviolet”. In: *Physical Reviews* 46.529, p. 4.

Price, W. C. and A. D. Walsh (1945). “THE Absorption Spectra of Triple Bond Molecules in the Vacuum Ultraviolet”. In: *Trans. Faraday Society* 41.381.

Pryor, Wayne R. et al. (2011). “The auroral footprint of Enceladus on Saturn”. In: *Nature* 472.7343, pp. 331–333. ISSN: 00280836. DOI: `10.1038/nature09928`.

Rahm, Martin et al. (2016). “Polymorphism and electronic structure of polyimine and its potential significance for prebiotic chemistry on Titan”. In: pp. 1–6. DOI: `10.1073/pnas.1606634113`.

Ramírez, Sandra I. et al. (2005). “Organic chemistry induced by corona discharges in Titan’s troposphere: Laboratory simulations”. In: *Advances in Space Research* 36.2, pp. 274–280. ISSN: 02731177. DOI: `10.1016/j.asr.2005.09.010`.

Rengel, M. et al. (2014). “Herschel/PACS spectroscopy of trace gases of the stratosphere of Titan”. In: *Astronomy & Astrophysics* 561, A4. ISSN: 0004-6361. DOI: `10.1051/0004-6361/201321945`. URL: `http://www.aanda.org/10.1051/0004-6361/201321945`.

Richard, M S et al. (2015). “An empirical approach to modeling ion production rates in Titan’s ionosphere I: Ion production rates on the dayside and globally”. In: pp. 1–17. DOI: `10.1002/2014JA020343.An`.

Robertson, I P et al. (2009). “Structure of Titans ionosphere : Model comparisons with Cassini data”. In: 57.April 2005, pp. 1834–1846. DOI: `10.1016/j.pss.2009.07.011`.

Robinson, Allison G., Paul R. Winter, and Timothy S. Zwier (2002). “The singlet-triplet spectroscopy of 1,3-butadiene using cavity ring-down spectroscopy”. In: *Journal of Chemical Physics* 116.18, pp. 7918–7925. ISSN: 00219606. DOI: `10.1063/1.1467903`.

Romanini, Daniele et al. (2007). “Cavity ringdown overtone spectroscopy of HCN , H13CN and HC15N Cavity ring-down overtone spectroscopy of HCN , H 13 CN and HC 15 N”. In: 633.1995. DOI: `10.1063/1.469462`.

Romanzin, C. et al. (2018). “Gas phase ion-molecule chemistry: controlled reactions of methyl cations with O-bearing compounds and hydrocarbons”. In: *XXIst Symposium on Atomic, Cluster and Surface Physics 2018 (SASP 2018)*.

Rymer, A. M. et al. (2009). “Discrete classification and electron energy spectra of Titan’s varied magnetospheric environment”. In: *Geophysical Research Letters* 36.15, pp. 1–6. ISSN: 00948276. DOI: `10.1029/2009GL039427`.

Sagan, C. (1973). “The greenhouse of Titan”. In: *Icarus* 18.4, pp. 649–656. ISSN: 10902643. DOI: `10.1016/0019-1035(73)90068-7`.

— (1974). “The origin of life in a cosmic context”. In: *Origins of Life* 5.3-4, pp. 497–505. ISSN: 03021688. DOI: `10.1007/BF01207649`.

Sagan, C. and B. N. Khare (1971a). “Experimental Jovian Photochemistry: Initial Results”. In: *The Astrophysical Journal* 15.c, pp. 563–569.

— (1971b). “Long-wavelength ultraviolet photoproduction of amino acids on the primitive earth”. In: *Science* 173.3995, pp. 417–420. ISSN: 00368075. DOI: 10.1126/science.173.3995.417.

— (1979). “Tholins: organic chemistry of interstellar grains and gas”. In: *Nature* 277.5692, pp. 102–107. ISSN: 0028-0836. DOI: 10.1038/277102a0. URL: http://adsabs.harvard.edu/abs/1979Natur.277..102S.

Sagan, C. and S. Miller (1960). “Molecular Synthesis in Simulated Reducing Planetary Atmospheres”. In: *AAS*, p. 6800.

Sagan, Carl and W. Reid Thompson (1984). “Production and condensation of organic gases in the atmosphere of Titan”. In: *Icarus* 59.2, pp. 133–161. ISSN: 00191035. DOI: 10.1016/0019-1035(84)90018-6. URL: http://www.sciencedirect.com/science/article/pii/0019103584900186.

Samuelson, Robert E. et al. (2007). “Cassini CIRS update on stratospheric ices at Titan’s winter pole”. In: *Icarus* 189.1, pp. 63–71. ISSN: 00191035. DOI: 10.1016/j.icarus.2007.02.005.

Sanchez, R. A., J. P. Ferris, and L. E. Orgel (1966). “Cyanoacetylene in Prebiotic Synthesis”. In: *Science* 154.3750, pp. 785–786. ISSN: 00368075. DOI: 10.1126/science.154.3750.785.

Scattergood, T., P. Lesser, and T. Owen (1975). “Production of organic molecules in the outer solar system by proton irradiation - Laboratory simulations”. In: 471, pp. 465–471.

Scattergood, Thomas W. et al. (1989). “Production of organic compounds in plasmas: A comparison among electric sparks, laser-induced plasmas, and UV light”. In: *Icarus* 81.2, pp. 413–428. ISSN: 10902643. DOI: 10.1016/0019-1035(89)90061-4.

Schröder, S. E. and H. U. Keller (2008). “The reflectance spectrum of Titan’s surface at the Huygens landing site determined by the descent imager/spectral radiometer”. In: *Planetary and Space Science* 56.5, pp. 753–769. ISSN: 00320633. DOI: 10.1016/j.pss.2007.10.011.

Sciamma-O’Brien, E. et al. (2012). “Optical constants from 370nm to 900nm of Titan tholins produced in a low pressure RF plasma discharge”. In: *Icarus* 218.1, pp. 353–363. ISSN: 00191035. DOI: 10.1016/j.icarus.2011.12.014. URL: http://dx.doi.org/10.1016/j.icarus.2011.12.014.

Sciamma-O’Brien, Ella, Claire L. Ricketts, and Farid Salama (2014). “The Titan haze simulation experiment on cOsmic: Probing titan’s atmospheric chemistry at low temperature”. In: *Icarus* 243, pp. 325–336. ISSN: 10902643. DOI: 10.1016/j.icarus.2014.08.004. URL: http://dx.doi.org/10.1016/j.icarus.2014.08.004.

Sciamma-O’Brien, Ella et al. (2015). “The THS experiment: Simulating Titan’s atmospheric chemistry at low temperature (200 K)”. In: *Proceedings of the International Astronomical Union* 11.A29A, pp. 327–328. ISSN: 1743-9213. DOI: 10.1017/S1743921316003197. URL: https://www.cambridge.org/core/product/identifier/S1743921316003197/type/journal_article.

Sciamma-OBrien, E. et al. (2010). “Titans atmosphere: An optimal gas mixture for aerosol production?” In: *Icarus* 209.2, pp. 704–714. ISSN: 00191035. DOI: 10.1016/j.icarus.2010.04.009. URL: http://www.sciencedirect.com/science/article/pii/S0019103510001570.

Seki, K. et al. (1996). “Reaction rates of the CN radical with diacetylene and dicyanoacetylene”. In: *Chemical Physics Letters* 4.August, pp. 0–5.

Serigano, Joseph et al. (2016). “Isotopic Ratios of Carbon and Oxygen in Titan’s CO using ALMA”. In: *The Astrophysical Journal Letters* 821.1, pp. 1–6. ISSN: 2041-8213.

DOI: 10.3847/2041-8205/821/1/L8. URL: http://arxiv.org/abs/1602.07707%0Ahttp://dx.doi.org/10.3847/2041-8205/821/1/L8.

Sharpe, S.N. et al. (2004). "Gas Phase Database for Quantitative Infrared Spectroscopy". In: *Applied Spectroscopy* 58.12, pp. 1452–1461. ISSN: 0003-7028. DOI: 10.1366/0003702042641281.

Shebanits, O. et al. (2013). "Negative ion densities in the ionosphere of Titan-Cassini RPWS/LP results". In: *Planetary and Space Science* 84, pp. 153–162. ISSN: 00320633. DOI: 10.1016/j.pss.2013.05.021. URL: http://dx.doi.org/10.1016/j.pss.2013.05.021.

Shebanits, O. et al. (2017). "Titan's ionosphere: A survey of solar EUV influences". In: *Journal of Geophysical Research: Space Physics* 122.7, pp. 7491–7503. ISSN: 21699402. DOI: 10.1002/2017JA023987.

Singh, S. et al. (2017). "Experimental determination of acetylene and ethylene solubility in liquid methane and ethane: Implications to Titan's surface". In: *Geochimica et Cosmochimica Acta* 208, pp. 86–101. ISSN: 00167037. DOI: 10.1016/j.gca.2017.03.007. URL: http://dx.doi.org/10.1016/j.gca.2017.03.007.

Sittler, E. C., K. W. Ogilvie, and J. D. Scudder (1983). "Survey of low-energy plasma electrons in Saturn's magnetosphere: Voyagers 1 and 2". In: *Journal of Geophysical Research* 88.A11, p. 8847. ISSN: 0148-0227. DOI: 10.1029/JA088iA11p08847. URL: http://doi.wiley.com/10.1029/JA088iA11p08847.

Sittler, E.C. et al. (2009). "Heavy ion formation in Titan's ionosphere: Magnetospheric introduction of free oxygen and a source of Titan's aerosols?" In: *Planetary and Space Science* 57.13, pp. 1547–1557. ISSN: 00320633. DOI: 10.1016/j.pss.2009.07.017. URL: http://www.sciencedirect.com/science/article/pii/S0032063309002268.

Smith, H. T., R. E. Johnson, and V. I. Shematovich (2004). "Titan's atomic and molecular nitrogen tori". In: *Geophysical Research Letters* 31.16, pp. 2–5. ISSN: 00948276. DOI: 10.1029/2004GL020580.

Snowden, D. et al. (2007). "Three-dimensional multifluid simulation of the plasma interaction at Titan". In: *Journal of Geophysical Research: Space Physics* 112.12, pp. 1–9. ISSN: 21699402. DOI: 10.1029/2007JA012393.

Snowden, D et al. (2013). "The thermal structure of Titans upper atmosphere, I: Temperature profiles from Cassini INMS observations". In: *Icarus* 226.1, pp. 552–582. ISSN: 0019-1035. DOI: 10.1016/j.icarus.2013.06.006. URL: http://dx.doi.org/10.1016/j.icarus.2013.06.006.

Solá Comas, José (1908). "Observations des satellites principaux de Jupiter et de Titan." In: *Astronomische Nachrichten* 179.18, p. 4290.

Srama, R. et al. (2004). "The Cassini cosmic dust analyzer". In: *Space Science Reviews* 114.1-4, pp. 465–518. ISSN: 00386308. DOI: 10.1007/s11214-004-1435-z.

Stiles, Paul L., Klaas Nauta, and Roger E. Miller (2003). "Dipole Moments of Molecules Solvated in Helium Nanodroplets". In: *Physical Review Letters* 90.13, p. 4. ISSN: 10797114. DOI: 10.1103/PhysRevLett.90.135301.

Strobel, D. F. (1982). "Chemistry and evolution of Titan's atmosphere". In: *Planetary and Space Science* 30.8, pp. 839–848. ISSN: 00320633. DOI: 10.1016/0032-0633(82)90116-7.

Strobel, Darrell F. (2008). "Titan's hydrodynamically escaping atmosphere: Escape rates and the structure of the exobase region". In: *Icarus* 202.2, pp. 632–641. ISSN: 00191035. DOI: 10.1016/j.icarus.2009.03.007.

Szopa, Cyril et al. (2006). "PAMPRE: A dusty plasma experiment for Titan's tholins production and study". In: *Planetary and Space Science* 54.4, pp. 394–404. ISSN:

00320633. DOI: 10.1016/j.pss.2005.12.012. URL: http://www.sciencedirect.com/science/article/pii/S003206330600002X.

Tanguy, Loic et al. (1990). "Stratospheric Profile of HCN on Titan from Millimeter Observations". In: 57.

Teanby, N. et al. (2009). "Dynamical implications of seasonal and spatial variations in Titan's stratospheric composition." In: *Philosophical transactions. Series A, Mathematical, physical, and engineering sciences* 367.1889, pp. 697–711. ISSN: 1364-503X. DOI: 10.1098/rsta.2008.0164.

Teanby, N. et al. (2012). "Active upper-atmosphere chemistry and dynamics from polar circulation reversal on Titan". In: *Nature* 491.7426, pp. 732–735. ISSN: 00280836. DOI: 10.1038/nature11611. URL: http://dx.doi.org/10.1038/nature11611.

Teanby, N. A. et al. (2007). "Vertical profiles of HCN, HC3N, and C2H2 in Titan's atmosphere derived from Cassini/CIRS data". In: *Icarus* 186.2, pp. 364–384. ISSN: 00191035. DOI: 10.1016/j.icarus.2006.09.024.

Teanby, N. A. et al. (2018). "THE Origin of Titans External Oxygen: Further Constraints From ALMA Upper Limits on CS and CH2NH". In:

Tennyson, J. et al. (2016). "The ExoMol database: molecular line lists for exoplanet and other hot atmospheres". In: *Journal of Molecular Spectroscopy*, pp. 1–68.

Thelen, Alexander E. et al. (2017). "Spatial variations in Titan's atmospheric temperature: ALMA and Cassini comparisons from 2012 to 2015". In: *Icarus* 0, pp. 1–11. ISSN: 10902643. DOI: 10.1016/j.icarus.2017.10.042.

Theule, P et al. (2011). "Hydrogenation of solid hydrogen cyanide HCN and methanimine CH2NH at low temperature". In: *Astronomy & Astrophysics* 534, A64. ISSN: 0004-6361. DOI: 10.1051/0004-6361/201117494.

Thissen, R. et al. (2006). "Laboratory experiments for Titan's ionosphere: the chemistry of N2+ , N+ , and N2++ nitrogen ions Laboratory experiments for Titans ionosphere : the chemistry of N+2 , N , and N2 nitrogen ions". In: January, pp. 2–4.

Thissen, Roland et al. (2009). "Laboratory studies of molecular growth in the titan ionosphere". In: *Journal of Physical Chemistry A* 113.42, pp. 11211–11220. ISSN: 10895639. DOI: 10.1021/jp9050353.

Thompson, W Reid et al. (1991). "Plasma discharge in N$_2$ + CH$_4$ at low pressures: Experimental results and applications to Titan". In: *Icarus* 90.1, pp. 57–73. ISSN: 0019-1035. DOI: http://dx.doi.org/10.1016/0019-1035(91)90068-5.

Tigrine, S et al. (2016). "A microwave plasma source for VUV atmospheric photochemistry". In: *Journal of Physics D: Applied Physics* 49.39, p. 395202. ISSN: 0022-3727. DOI: 10.1088/0022-3727/49/39/395202. URL: http://stacks.iop.org/0022-3727/49/i=39/a=395202?key=crossref.c271bf76ea98ba3609296eb0d3cc

Tokano, T (2002). "Tidal Winds on Titan Caused by Saturn". In: *International Journal of Solar System Studies* 158.2, pp. 499–515. ISSN: 00191035. DOI: 10.1006/icar.2002.6883. URL: http://linkinghub.elsevier.com/retrieve/pii/S0019103502968831.

Toublanc, D., J. Gautier D. Raulin F. Parisot P. Brillet, and C. P. McKay (1995). *Photochemical modelling of Titans atmosphere*.

Touvelle, M et al. (1987). "Plasma Chemical Synthesis. II. Effect of Wall Surface on the Synthesis of Ammonia". In: *Plasma Chemistry and Plasma Processing* 7.1, p. 101.

Trafton, L. (1972a). "On the possible detection of H2 in titan's atmosphere". In: *The Astrophysical Journal* 5.175, pp. 285–293. ISSN: 0004-637X. DOI: 10.1086/151556. URL: http://articles.adsabs.harvard.edu/cgi-bin/nph-iarticle_ query?bibcode=1972ApJ...175..285T&db_key=AST&page_ind=0&data_type=GIF&type=SCREEN_VIEW&classic=YES.

Trafton, L (1972b). "The bulk composition of Titan's atmosphere". In: *The Astrophysical Journal* Allen 1963, pp. 295–306.

Tyler, G L et al. (1981). "Radio Science Investigations of the Saturn System with Voyager 1: Preliminary Results." In: *Science (New York, N.Y.)* 212.4491, pp. 201–206. ISSN: 0036-8075. DOI: 10.1126/science.212.4491.201. URL: http://www.ncbi.nlm.nih.gov/pubmed/17783830.

Vance, Steven D. et al. (2017). "Geophysical tests for habitability in ice-covered ocean worlds". In: pp. 1–44. URL: http://arxiv.org/abs/1705.03999.

Vervack, Ronald J., Bill R. Sandel, and Darrell F. Strobel (2004). "New perspectives on Titan's upper atmosphere from a reanalysis of the Voyager 1 UVS solar occultations". In: *Icarus* 170.1, pp. 91–112. ISSN: 00191035. DOI: 10.1016/j.icarus.2004.03.005.

Vila, Fernando, Piotr Borowski, and Kenneth D. Jordan (2000). "Theoretical study of the low-lying electronically excited states of diacetylene". In: *Journal of Physical Chemistry A* 104.39, pp. 9009–9016. ISSN: 10895639. DOI: 10.1021/jp001969c.

Vinatier, Sandrine et al. (2007). "Vertical abundance profiles of hydrocarbons in Titan's atmosphere at 15^o S and 80^o N retrieved from Cassini/CIRS spectra". In: *Icarus* 188.1, pp. 120–138. ISSN: 00191035. DOI: 10.1016/j.icarus.2006.10.031.

Vinatier, Sandrine et al. (2009). "Analysis of Cassini/CIRS limb spectra of Titan acquired during the nominal mission I: Hydrocarbons, nitriles and CO2 vertical mixing ratio profiles". In: *Icarus* 210.2, pp. 852–866. ISSN: 00191035. DOI: 10.1016/j.icarus.2010.06.024. URL: http://dx.doi.org/10.1016/j.icarus.2009.08.013.

Vinatier, Sandrine et al. (2010). "Analysis of Cassini/CIRS limb spectra of Titan acquired during the nominal missionI. Hydrocarbons, nitriles and CO2 vertical mixing ratio profiles". In: *Icarus* 205.2, pp. 559–570. ISSN: 00191035. DOI: 10.1016/j.icarus.2009.08.013. URL: http://linkinghub.elsevier.com/retrieve/pii/S0019103509003558.

Vinatier, Sandrine et al. (2015). "Seasonal variations in Titan's middle atmosphere during the northern spring derived from Cassini/CIRS observations". In: *Icarus* 250, pp. 95–115. ISSN: 10902643. DOI: 10.1016/j.icarus.2014.11.019. URL: http://dx.doi.org/10.1016/j.icarus.2014.11.019.

Vuitton, V., R. V. Yelle, and V. G. Anicich (2006). "The Nitrogen Chemistry of Titan's Upper Atmosphere Revealed". In: *The Astrophysical Journal* 647.2, pp. L175–L178. ISSN: 0004-637X. DOI: 10.1086/507467. URL: http://iopscience.iop.org/article/10.1086/507467.

Vuitton, V., R. V. Yelle, and M. J. McEwan (2007). "Ion chemistry and N-containing molecules in Titan's upper atmosphere". In: *Icarus* 191.2, pp. 722–742. ISSN: 00191035. DOI: 10.1016/j.icarus.2007.06.023.

Vuitton, V. et al. (2006). "Experimental and theoretical study of hydrocarbon photochemistry applied to Titan stratosphere". In: *Icarus* 185.1, pp. 287–300. ISSN: 00191035. DOI: 10.1016/j.icarus.2006.06.002.

Vuitton, V. et al. (2009). "Negative ion chemistry in Titan's upper atmosphere". In: *Planetary and Space Science* 57.13, pp. 1558–1572. ISSN: 00320633. DOI: 10.1016/j.pss.2009.04.004. URL: http://dx.doi.org/10.1016/j.pss.2009.04.004.

Waite, J H et al. (2004a). "The Cassini Ion and Neutral Mass Spectrometer (INMS) Investigation". In: *Space Science Reviews*, pp. 113–231.

Waite, J. H. et al. (2004b). "The Cassini Ion and Neutral Mass Spectrometer (INMS) investigation". In: 114.1-4, pp. 113–231. ISSN: 00386308. DOI: 10.1007/s11214-004-1408-2.

Waite, J. H. et al. (2005). "Ion Neutral Mass Spectrometer Results from the First Flyby of Titan". In: *Science* 85.2, pp. 195–209. ISSN: 00224073. DOI: 10.1016/S0022-4073(03)00225-5.

Waite, J. H. et al. (2007). "The Process of Tholin Formation in Titan's Upper Atmosphere". In: *Science* 870.2007. DOI: 10.1126/science.1139727.

Waite, J Hunter et al. (2017). "Cassini finds molecular hydrogen in the Enceladus plume: Evidence for hydrothermal processes". In: *Science* 356.6334, pp. 155–159.

Wang, Chia C., Sushil K. Atreya, and Ruth Signorell (2010). "Evidence for layered methane clouds in Titan's troposphere". In: *Icarus* 206.2, pp. 787–790. ISSN: 00191035. DOI: 10.1016/j.icarus.2009.11.022. URL: http://dx.doi.org/10.1016/j.icarus.2009.11.022.

Wang, Yicheng and J. K. Olthoff (1999). "Ion energy distributions in inductively coupled radio-frequency discharges in argon, nitrogen, oxygen, chlorine, and their mixtures". In: *Journal of Applied Physics* 85.9, p. 6358. ISSN: 00218979. DOI: 10.1063/1.370138. URL: http://link.aip.org/link/JAPIAU/v85/i9/p6358/s1&Agg=doi.

Wattieaux, G et al. (2015). "Transient phenomena during dust formation in a N ₂ CH ₄ capacitively coupled plasma". In: *Plasma Sources Science and Technology* 24.1, p. 015028. ISSN: 0963-0252. DOI: 10.1088/0963-0252/24/1/015028. URL: http://stacks.iop.org/0963-0252/24/i=1/a=015028?key=crossref.c0350fef26eea5c69b4714e0fbc95b20.

Wellbrock, A. et al. (2013). "Cassini CAPS-ELS observations of negative ions in Titan's ionosphere: Trends of density with altitude". In: *Geophysical Research Letters* 40.17, pp. 4481–4485. ISSN: 00948276. DOI: 10.1002/grl.50751.

West, R. A. et al. (2016). "Cassini Imaging Science Subsystem observations of Titan's south polar cloud". In: *Icarus* 270, pp. 399–408. ISSN: 10902643. DOI: 10.1016/j.icarus.2014.11.038. URL: http://dx.doi.org/10.1016/j.icarus.2014.11.038.

West, Robert A. et al. (2018). "The seasonal cycle of Titan's detached haze". In: *Nature Astronomy* 162.Figure 1. ISSN: 2397-3366. DOI: 10.1038/s41550-018-0434-z. URL: http://www.nature.com/articles/s41550-018-0434-z.

Westlake, J H et al. (2011). "Titans thermospheric response to various plasma environments". In: 116.December 2010, pp. 1–12. DOI: 10.1029/2010JA016251.

Westlake, J. H. et al. (2012). "Titan's ionospheric composition and structure: Photochemical modeling of Cassini INMS data". In: *Journal of Geophysical Research E: Planets* 117.1, pp. 1–21. ISSN: 01480227. DOI: 10.1029/2011JE003883.

Westlake, J. H. et al. (2014). "The role of ion-molecule reactions in the growth of heavy ions in Titan's ionosphere". In: *Journal of Geophysical Research: Space Physics* 119.7, pp. 5951–5963. ISSN: 21699402. DOI: 10.1002/2014JA020208.

Wilson, E. H. and S. K. Atreya (2003). "Chemical sources of haze formation in Titan's atmosphere". In: *Planetary and Space Science* 51.14-15, pp. 1017–1033. ISSN: 00320633. DOI: 10.1016/j.pss.2003.06.003.

— (2004). "Current state of modeling the photochemistry of Titan's mutually dependent atmosphere and ionosphere". In: *Journal of Geophysical Research E: Planets* 109.6. ISSN: 01480227. DOI: 10.1029/2003JE002181.

Woeller, F. and Cyril Ponnamperuma (1969). "Organic synthesis in a simulated Jovian atmosphere-II". In: *Icarus* 15.1, pp. 39–44. ISSN: 10902643. DOI: 10.1016/0019-1035(71)90031-5.

Yelle, Roger V et al. (2010). “Formation of NH3 and CH2NH in Titan’s upper atmosphere”. In: *Faraday Discussions* 147, p. 31. ISSN: 1359-6640. DOI: `10.1039/c004787m`. URL: `http://xlink.rsc.org/?DOI=c004787m`.

Young, D. T. (2004). “Cassini Plasma Spectrometer Investigation”. In: *Space Science Reviews*, pp. 1–112.

Yung, Yuk L. (1987). “An update of nitrile photochemistry on Titan”. In: *Icarus* 72.2, pp. 468–472. ISSN: 10902643. DOI: `10.1016/0019-1035(87)90186-2`.

Yung, Yuk L., Mark Allen, and Joseph Pinto (1984). “Photochemistry of the atmosphere of Titan: Comparison between model and observations”. In: *The Astrophysical Journal* 212.1981, pp. 465–506.

Žabka, Ján et al. (2012). “Anion chemistry on Titan: A possible route to large N-bearing hydrocarbons”. In: *Icarus* 219.1, pp. 161–167. ISSN: 00191035. DOI: `10.1016/j.icarus.2012.02.031`.

Zhou, Li, Ralf I Kaiser, and Alan T Tokunaga (2009). “Infrared spectroscopy of crystalline and amorphous diacetylene (C4H2) and implications for Titans atmospheric composition”. In: *Planetary and Space Science* 57, pp. 830–835. DOI: `10.1016/j.pss.2009.02.003`.

List of Figures

List of Tables

List of Reactions

Appendix A

Titan Flybys

TABLE A.1: List of all Titan flybys from the Prime through the Solstice Mission. Altitudes are given in km. *SOI* stands for Saturn Orbit Insertion.

Flyby	Date	Altitude	Mission	Orbit
T0	July 3, 2004	341500	Prime	SOI Probe Release
TA	October 26, 2004	1174	Prime	SOI Probe Release
TB	December 13, 2004	1192	Prime	SOI Probe Release
TC	January 13, 2005	60000	Prime	SOI Probe Release
T3	February 15, 2005	1579	Prime	SOI Probe Release
T4	April 1, 2005	2404	Prime	Occultations
T5	May 16, 2005	1027	Prime	Occultations
T6	August 22, 2005	3660	Prime	Occultations
T7	September 7, 2005	1027	Prime	Occultations
T8	October 28, 2005	1353	Prime	Petal Rotations/Megnetotail Petals
T9	December 26, 2005	10411	Prime	Petal Rotations/Megnetotail Petals
T10	January 15, 2006	2043	Prime	Petal Rotations/Megnetotail Petals
T11	February 27, 2006	1812	Prime	Petal Rotations/Megnetotail Petals
T12	March 19, 2006	1949	Prime	Petal Rotations/Megnetotail Petals
T13	April 30, 2006	1856	Prime	Petal Rotations/Megnetotail Petals
T14	May 20, 2006	1879	Prime	Petal Rotations/Megnetotail Petals
T15	July 2, 2006	1906	Prime	Petal Rotations/Megnetotail Petals
T16	July 22, 2006	950	Prime	Petal Rotations/Megnetotail Petals
T17	September 7, 2006	1000	Prime	Petal Rotations/Megnetotail Petals
T18	September 23, 2006	960	Prime	Petal Rotations/Megnetotail Petals
T19	October 9, 2006	980	Prime	Petal Rotations/Megnetotail Petals
T20	October 25, 2006	1030	Prime	Petal Rotations/Megnetotail Petals
T21	December 12, 2006	1000	Prime	Petal Rotations/Megnetotail Petals
T22	December 28, 2006	1300	Prime	180-degree Transfer
T23	January 13, 2007	1000	Prime	180-degree Transfer
T24	January 29, 2007	2631	Prime	180-degree Transfer
T25	February 22, 2007	1000	Prime	180-degree Transfer
T26	March 10, 2007	980	Prime	180-degree Transfer
T27	March 26, 2007	1010	Prime	180-degree Transfer
T28	April 10, 2007	990	Prime	180-degree Transfer
T29	April 26, 2007	980	Prime	180-degree Transfer
T30	May 12, 2007	960	Prime	180-degree Transfer
T31	May 18, 2007	2300	Prime	180-degree Transfer
T32	June 13, 2007	975	Prime	180-degree Transfer
T33	June 29, 2007	1948	Prime	180-degree Transfer

T34	July 19, 2007	1322	Prime	Icy Sats
T35	August 31, 2007	3302	Prime	Icy Sats
T36	October 2, 2007	975	Prime	High Inclination Sequences
T37	November 19, 2007	1000	Prime	High Inclination Sequences
T38	December 5, 2007	1300	Prime	High Inclination Sequences
T39	December 20, 2007	970	Prime	High Inclination Sequences
T40	January 5, 2008	1010	Prime	High Inclination Sequences
T41	February 22, 2008	1000	Prime	High Inclination Sequences
T42	March 25, 2008	1000	Prime	High Inclination Sequences
T43	May 12, 2008	1000	Prime	High Inclination Sequences
T44	May 28, 2008	1360	Prime	High Inclination Sequences
T45	July 31, 2008	1614	Equinox	High Inclination Sequences
T46	November 3, 2008	1105	Equinox	High Inclination Sequences
T47	November 19, 2008	1023	Equinox	High Inclination Sequences
T48	December 5, 2008	971	Equinox	High Inclination Sequences
T49	December 21, 2008	971	Equinox	High Inclination Sequences
T50	February 7, 2009	967	Equinox	High Inclination Sequences
T51	March 27, 2009	963	Equinox	High Inclination Sequences
T52	April 4, 2009	4147	Equinox	Saturn Equinox Viewing
T53	April 20, 2009	3599	Equinox	Saturn Equinox Viewing
T54	May 5, 2009	3242	Equinox	Saturn Equinox Viewing
T55	May 21, 2009	966	Equinox	Saturn Equinox Viewing
T56	June 6, 2009	968	Equinox	Saturn Equinox Viewing
T57	June 22, 2009	955	Equinox	Saturn Equinox Viewing
T58	July 8, 2009	966	Equinox	Saturn Equinox Viewing
T59	July 24, 2009	956	Equinox	Saturn Equinox Viewing
T60	August 9, 2009	971	Equinox	Saturn Equinox Viewing
T61	August 25, 2009	961	Equinox	Saturn Equinox Viewing
T62	October 12, 2009	1300	Equinox	Icy Satellite Flybys
T63	December 12, 2009	4850	Equinox	Icy Satellite Flybys
T64	December 28, 2009	955	Equinox	Icy Satellite Flybys
T65	January 12, 2010	1073	Equinox	Icy Satellite Flybys
T66	January 28, 2010	7490	Equinox	Icy Satellite Flybys
T67	April 5, 2010	7462	Equinox	Icy Satellite Flybys
T68	May 20, 2010	1400	Equinox	Inclined - 0
T69	June 5, 2010	2044	Equinox	Inclined - 0
T70	June 21, 2010	880	Equinox	Inclined - 0
T71	July 7, 2010	1005	Solstice	Inclined - 0
T72	September 24, 2010	8175	Solstice	Inclined - 0
T73	November 11, 2010	7921	Solstice	Inclined - 0
T74	February 18, 2011	3651	Solstice	Equatorial - 1
T75	April 19, 2011	1005	Solstice	Equatorial - 1
T76	May 8, 2011	1873	Solstice	Equatorial - 1
T77	June 20, 2011	1359	Solstice	Equatorial - 1
T78	September 12, 2011	5821	Solstice	Equatorial - 1
T79	December 13, 2011	3586	Solstice	Equatorial - 1
T80	January 2, 2012	2914	Solstice	Equatorial - 1
T81	January 30, 2012	3113	Solstice	Equatorial - 1
T82	February 19, 2012	3803	Solstice	Equatorial - 1
T83	May 22, 2012	955	Solstice	Equatorial - 1
T84	June 6, 2012	959	Solstice	Inclined - 1

T85	July 24, 2012	1012	Solstice	Inclined - 1
T86	September 26, 2012	956	Solstice	Inclined - 1
T87	November 13, 2012	973	Solstice	Inclined - 1
T88	November 29, 2012	1014	Solstice	Inclined - 1
T89	February 17, 2013	1978	Solstice	Inclined - 1
T90	April 5, 2013	1400	Solstice	Inclined - 1
T91	May 23, 2013	970	Solstice	Inclined - 1
T92	July 10, 2013	964	Solstice	Inclined - 1
T93	July 26, 2013	1400	Solstice	Inclined - 1
T94	September 12, 2013	1400	Solstice	Inclined - 1
T95	October 14, 2013	961	Solstice	Inclined - 1
T96	December 1, 2013	1400	Solstice	Inclined - 1
T97	January 1, 2014	1400	Solstice	Inclined - 1
T98	February 2, 2014	1236	Solstice	Inclined - 1
T99	March 6, 2014	1500	Solstice	Inclined - 1
T100	April 7, 2014	963	Solstice	Inclined - 1
T101	May 17, 2014	2994	Solstice	Inclined - 1
T102	June 18, 2014	3659	Solstice	Inclined - 1
T103	July 20, 2014	5103	Solstice	Inclined - 1
T104	August 21, 2014	964	Solstice	Inclined - 1
T105	September 22, 2014	1400	Solstice	Inclined - 1
T106	October 24, 2014	1013	Solstice	Inclined - 1
T107	December 10, 2014	980	Solstice	Inclined - 1
T108	January 11, 2015	970	Solstice	Inclined - 1
T109	February 12, 2015	1200	Solstice	Inclined - 1
T110	March 16, 2015	2275	Solstice	Inclined - 1
T111	May 7, 2015	2722	Solstice	Equatorial - 2
T112	July 7, 2015	1095	Solstice	Equatorial - 2
T113	September 28, 2015	1036	Solstice	Equatorial - 2
T114	November 13, 2015	1192	Solstice	Equatorial - 2
T115	January 16, 2016	3817	Solstice	Inclined - 2
T116	February 1, 2016	1400	Solstice	Inclined - 2
T117	February 16, 2016	1018	Solstice	Inclined - 2
T118	April 4, 2016	990	Solstice	Inclined - 2
T119	May 6, 2016	971	Solstice	Inclined - 2
T120	June 7, 2016	975	Solstice	Inclined - 2
T121	July 25, 2016	976	Solstice	Inclined - 2
T122	August 10, 2016	1600	Solstice	Inclined - 2
T123	September 27, 2016	1737	Solstice	Inclined - 2
T124	November 14, 2016	1581	Solstice	Inclined - 2
T125	November 29, 2016	3223	Solstice	Inclined - 2
T126	April 22, 2017	979	Solstice	F

Appendix B

Résumé substantiel

Je présente ici mes travaux de thèse que j'ai réalisé ces trois dernières années au sein du Laboratoire ATMosphères et Observations Spatiales (LATMOS) de l'Université de Versailles St-Quentin-en-Yvelines (UVSQ) et du Jet Propulsion Laboratory (JPL). Pendant ces 3 ans je me suis intéressé à la réactivité chimique des composés organiques en phase gaz et solide, en utilisant des expériences de laboratoire simulant les conditions de l'ionosphère et de la basse atmosphère de Titan, le plus gros satellite de Saturne (Figure B.1). Titan est la seule lune du Système Solaire qui possède sa propre atmosphère. Cette atmosphère est principalement composée d'azote moléculaire (N_2). Le méthane (CH_4) forme le gaz secondaire.

FIGURE B.1: Titan, vu par Cassini le 29 Mai 2017 à une distance de 2 millions de km, par la caméra ISS. La luminosité provient de derrière Titan, permettant ainsi à Cassini de voir la structure de l'atmosphère illuminée par le soleil. Crédit: NASA/JPL-Caltech/Space Science Institute (PIA21625)

D'une part, j'ai analysé les composés neutres et les composés chargés (ions) présents dans des mélanges gazeux simulant la haute atmosphère de Titan. Ces composés, comme détaillé ci-après, sont considérés comme précurseurs chimiques de la brume organique observée autour de Titan. C'est-à-dire qu'ils forment les premières étapes d'une succession de réactions chimiques de plus en plus élaborées formant plus bas dans l'atmosphère des particules solides complexes. La nature de ces particules dans l'atmosphère de Titan reste encore à élucider complètement. La mission Cassini-Huygens (2004-2017) a permis de déceler un certains nombre de ces composés organiques, concentrant une chimie basée sur la présence du carbone, de l'azote et de l'hydrogène. L'environnement de Titan est sans cesse soumis à l'arrivée de photons solaires UV plus ou moins énergétiques, ainsi que de particules énérgétiques issues du plasma magnétosphérique de Saturne. L'ensemble de ces particules forme une source d'énergie intense qui arrive dans la haute atmosphère de Titan, et ainsi dissocie et ionise les molécules de N_2 et CH_4. Ces réactions s'opèrent à plus de $\sim$900 km d'altitude. Ainsi, les premiers produits hydrocarbonés et azotés (neutres et chargés positivement et négativement) sont formés, et une longue cascade de réactions entre ces produits s'initie. Ces réactions sont diverses (Figure B.2) et aboutissent à la formation de molécules complexes qui diffusent puis sédimentent dans la bass atmosphère jusqu'à se déposer en surface. La brume opaque qui entoure le globe de Titan est consituée de ces composés organiques, ou aérosols, qui se forment dans la haute et moyenne atmosphère. Ces aérosols recouvrent la surface de Titan, elle-même présentant des lacs d'hydrocarbures, notamment proche du pôle nord. L'atmosphère est régulée par des saisons ainsi que par un cycle d'évaporation, condensation et précipitation basé sur le méthane.

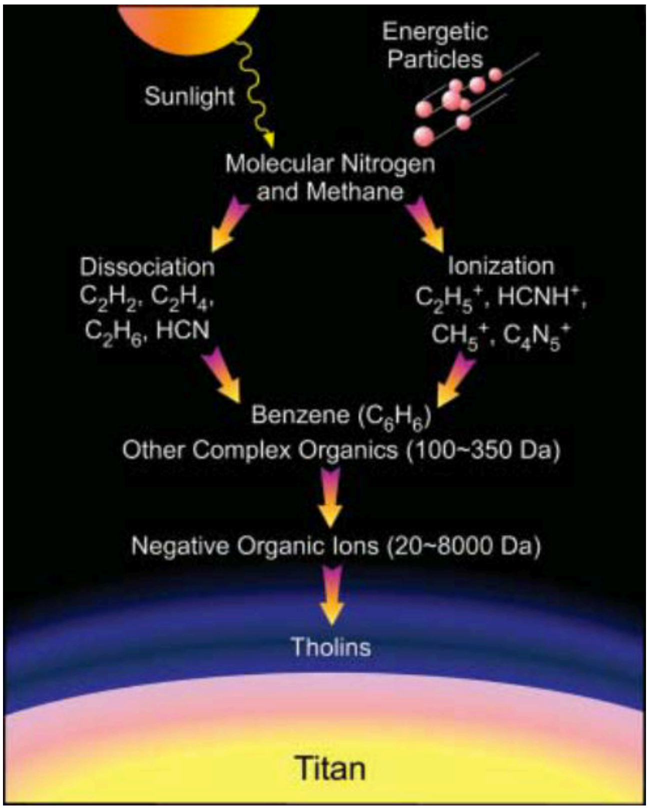

FIGURE B.2: Schéma résumant l'évolution chimique de la haute atmospère de Titan, qui commence par la dissociation et l'ionization des deux composés majoritaires, N_2 et CH_4. Les réactions chimiques se poursuivent plus bas dans l'atmosphère jusqu'à la formation d'aérosols, aussi nommés *tholins*.

La mission Cassini-Huygens a notamment montré le couplage qu'il existe dans la haute atmosphère entre les espèces chimiques (neutres, ions, radicaux, électrons) et qui précède la formation d'aérosols. Pour comprendre la nature de ces aérosols solides, il faut d'abord comprendre leurs mécanismes de formation, c'est-à-dire les précurseurs gazeux les précédents. La suite d'instruments à bord de Cassini-Huygens (Figure B.3) a pu sonder l'atmosphère de la haute atmosphère (ionosphère) jusqu'à la surface. Ces instruments ont pu mettre en évidence la richesse en produits formés par la photodissociation de N_2 et CH_4. Ces produits se composent d'hydrocarbures, dont les plus légers sont par exemple le C_2H_2 et C_2H_4, ainsi que de composés azotés, tel HCN. Ce dernier est la molécule azotée la plus abondante, après N_2 (Figure B.4). Cassini a aussi dévoilé la présence d'ions chargés positivement et négativement dans l'ionosphère, dont les masses vont de quelques centaines pour les ions positifs, à plus de 10000 unités de masses pour les ions négatifs. Ces composés participent probablement à l'évolution chimique de la haute atmosphère, ainsi qu'à leur incorporation dans les aérosols, aidant ainsi à leur croissance.

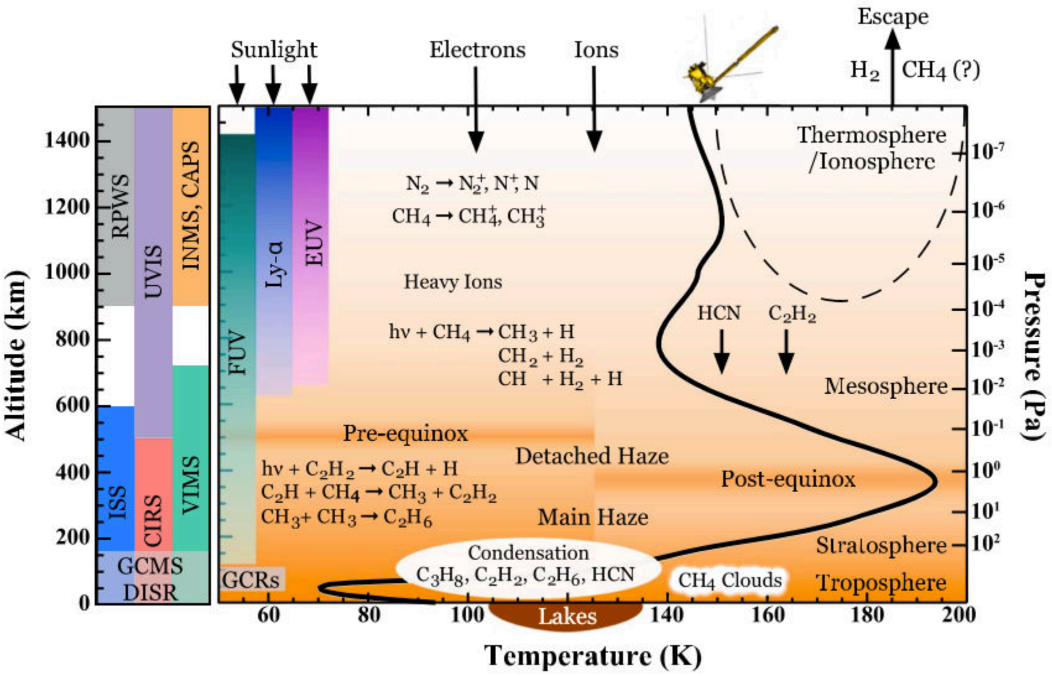

FIGURE B.3: Schéma présentant la colonne atmosphérique de Titan, avec son profil de température (courbe noire) en fonction de l'altitude et de la pression (Hörst, 2017). Certaines réactions cléfs de photodissociation sont présentées, en fonction de la couche atmosphérique. Les instruments à bord de Cassini-Huygens sont également présentés en fonction de leur sondage dans l'atmosphère.

Les limites de ces instruments (masses, résolution, suivi des mesures...) requierent la participation de modèles numériques se basant sur les observations, ainsi que de simulations en laboratoire. Depuis les premières investigations de l'atmosphère de Titan (Chapter 1) avant même la présence de satellites explorant l'environnement de Titan, les modèles numériques et simulations de laboratoire ont travaillé ensemble pour contraindre la famille d'espèces chimiques présentes dans l'atmosphère, l'éfficacité de certaines réactions, la possibilité de former certaines molécules prébiotiques, ainsi que d'examiner la nature des tholins, les analogues d'aérosols de Titan.

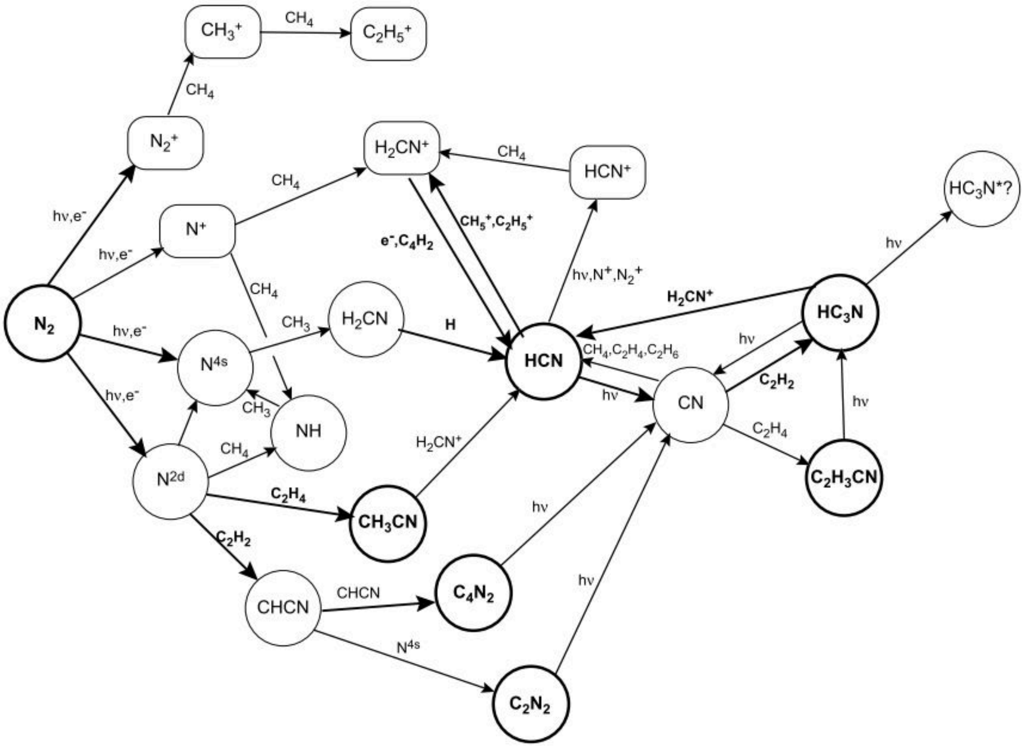

FIGURE B.4: Schéma représentant la chimie azotée de la haute atmosphère issu du modèle photochimique de Wilson and Atreya (2004). Les espèces stables sont indiquées en gras, et les ions positifs and rectangle. On remarque l'importance des réactions ions-molécules impliquant HCN, le nitrile majeur de l'atmosphère de Titan.

Mon travail pendant cette thèse a été d'utiliser des expériences de laboratoire pour investiguer la réactivité chimique en phase gaz, précurseure à la formation d'aérosols, ainsi que le vieillissement de ces composés plus bas dans l'atmosphère lorsqu'ils forment les premiers condensats de nucléation à la formation de nuages.

La réactivité en phase gaz

Pour pouvoir simuler la haute atmosphère de Titan en laboratoire, il faut d'abord comprendre le milieu qui contrôle cet environnement. Cette haute atmosphère est soumise à un flux de photons solaires UV ainsi que de particules énergétiques venant de la magnétosphère de Saturne impactant le N_2 et CH_4. Plusieurs techniques de laboratoire permettent de simuler ces sources d'énergie (Chapter 1) nécessaires pour dissocier et ionizer N_2 et CH_4. Dans cette étude, j'ai utilisé un réacteur à plasma poudreux à décharge radio-fréquences (13.56 MHz). Cette technique, qui permet de simuler les conditions énergétiques des particules chargées de la magnétosphère de Saturne et celle des photons solaires, produit aussi efficacement des *tholins* dont les propriétés peuvent être analyzées en laboratoire et comparées aux observations de Cassini-Huygens. Avec cet outil, j'ai pu étudier la composition en espèces neutres et ioniques au sein du plasma.

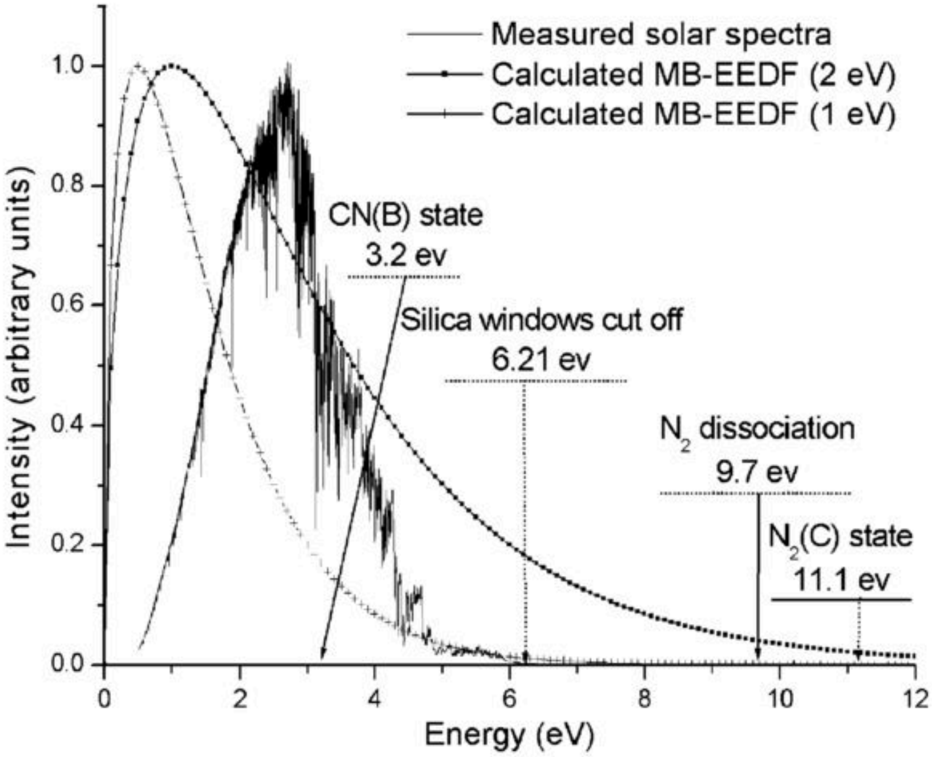

FIGURE B.5: Distributions en énergie des électrons issus de la décharge plasma (Szopa et al., 2006), avec le spectre solaire.

Le Chapitre 3 présente nos résultats sur une étude portée sur les espèces neutres majoritaires et considérées comme précurseures à la formation des *tholins*. Cette étude a été effectuée en couplant un piège cryogénique interne au réacteur avec un spectromètre de masse et infrarouge permettant d'analyzer les produits avec une approche quantitative. Les produits formés ont été piégés *in situ*, puis quantifiés par spectroscopie infrarouge. HCN, NH_3, C_2H_2 et C_2H_4 sont quantifiés, dans des mélanges N_2:CH_4 90:10 et 99:1%. Les analyzes complémentaires par spectrométrie de masse et infrarouge suggèrent une forte présence de C_2H_4 et HCN notamment à forte concentration de CH_4. Par ailleurs, ces résultats confirment aussi des études antérieures montrant des schémas de polymérization de précurseurs de tholins se basant sur HCN$-C_2H_4$.

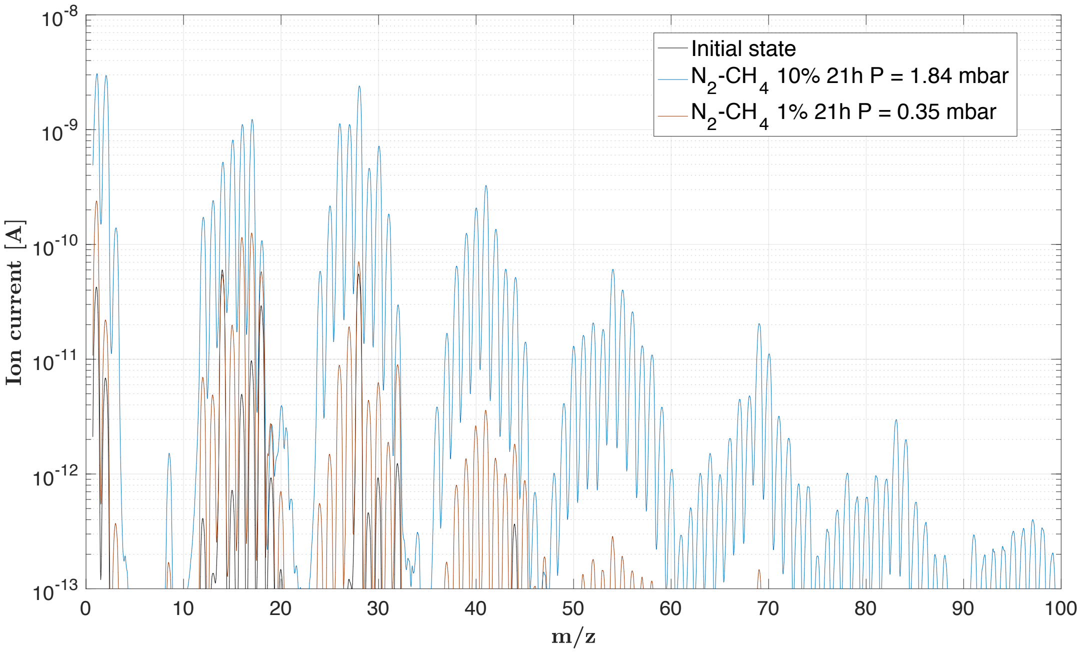

FIGURE B.6: Spectres de masses des produits obtenus avec 1% et 10% de CH_4 relargués après avoir été piégés par le système cryogénique. (Chapitre 3).

Dans le plasma, les espèces neutres sont en interactions avec les ions. C'est pourquoi pour comprendre la contribution des ions, il faut aussi étudier le couplage ions-neutres. Ceci a été possible grâce à un spectromètre de masse ions/neutres couplé au réacteur à plasma pour des analyzes *in situ* (Figure B.7). Cette étude est présentée dans le Chapitre 4. En étudiant les ions majoritaires dans trois conditions de méthane 1%, 5% et 10%, j'ai pu couvrir trois conditions particulières présentant des spectres différents. Dans des conditions propices à la formation de tholins, les ions majoritaires CH_5^+, $HCNH^+$ et $C_2H_5^+$ sont détéctés pour la première fois *in situ* dans notre réacteur (Table B.1). À faibles concentrations en méthane, l'ion NH_4^+ semble aussi contribuer significativement à l'ensemble des spectres. L'importance de ces ions et la richesse des spectres indiquent que la chimie des ions positifs précurseurs est significative et permettra de contraindre de futurs modèles simulant ce type de plasma. Dans le Chapitre 4 je compare aussi ces résultats avec les produits neutres. Par ailleurs, les spectres expérimentaux sont globalement en accord avec ceux de Cassini-INMS dans le Chapitre 4, indiquant que la chimie des ions positifs par PAMPRE est comparable aux observations faites dans l'ionosphère de Titan par INMS (Figure B.8).

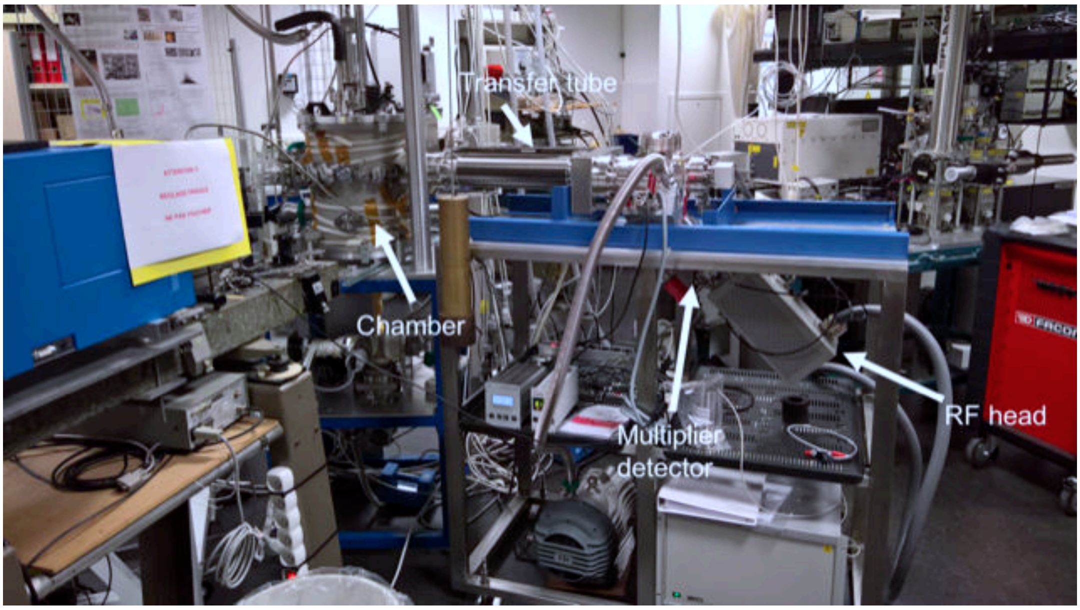

FIGURE B.7: Montage expérimental du réacteur à plasma PAMPRE, couplé à un spectromètre de masse ionique, permettant de détecter les ions positifs et négatifs dans la décharge.

L'étude des ions négatifs a aussi été commencée, mais n'est pas présentée dans ce manuscript. Les détections d'espèces d'ions négatifs à plus de 10000 masse arbitraire par Cassini-CAPS sont uniques, et méritent une investigation en laboratoire pour contraindre ces espèces avec une meilleure résolution en masse (Chapter 1). En effet, aucune autre étude de laboratoire actuelle ne porte sur l'étude des ions négatifs dans un plasma poudreux en simulation de l'ionosphère de Titan. Le champ d'étude reste donc large.

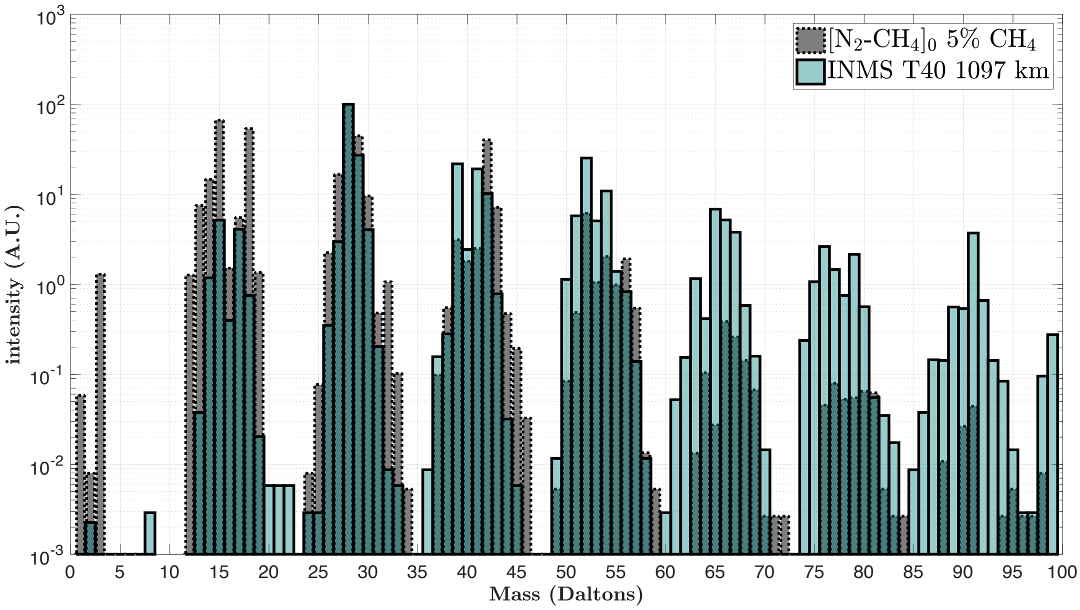

FIGURE B.8: Mass spectrum taken during the outbound leg of the T40 flyby (in blue), at 1097 km, compared with our experimental averaged spectra taken in 5% CH_4. The mass plot is separated in 1 Da. bins.

TABLE B.1: Diagrammes circulaires illustrant la variabilité des ions positifs présents dans des décharges plasma à 1%, 5% et 10% de CH_4, en fonction des massifs C_{1-4} (Chapitre 4). Chaque diagramme représente la contribution de chacun des ions (parties colorées), normalisée sur l'ensemble du spectre (partie grise).

	1%	5%	10%
C_1	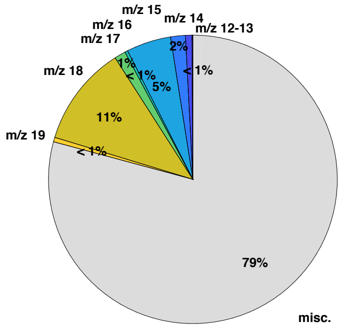	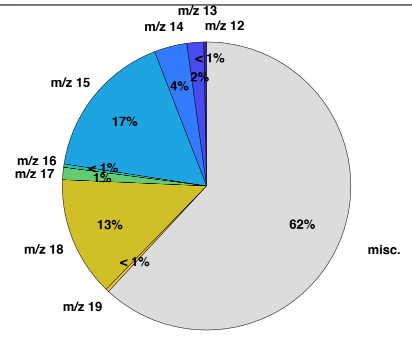	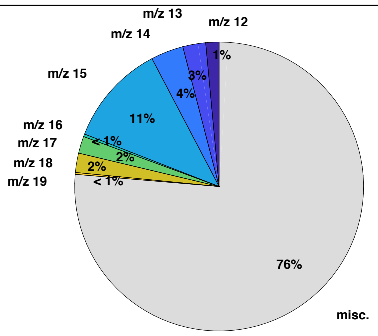
C_2	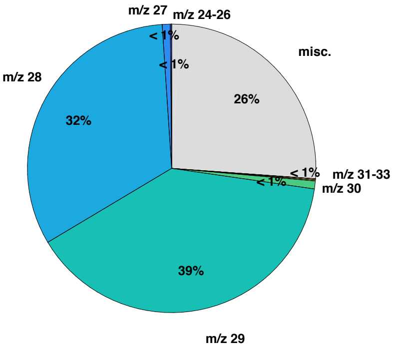	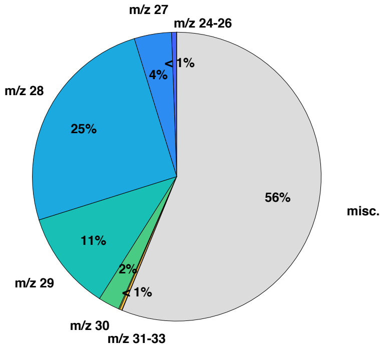	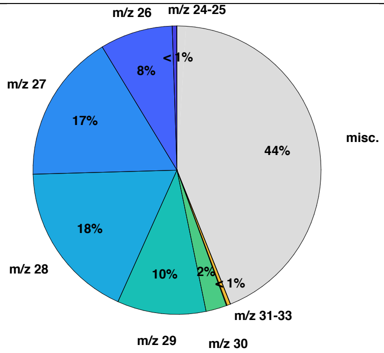
C_3	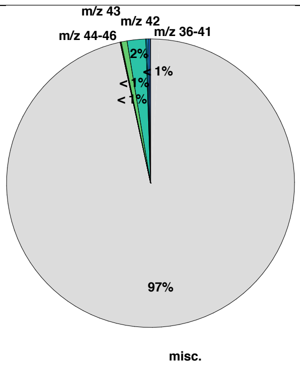	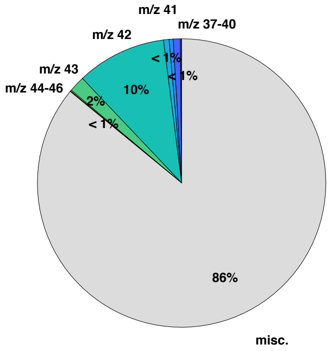	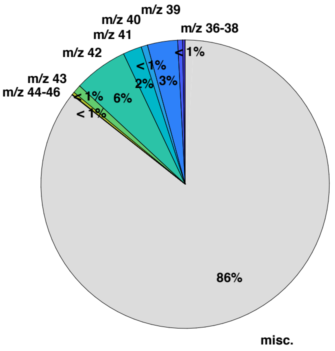
C_4	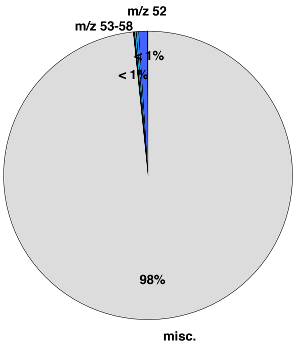	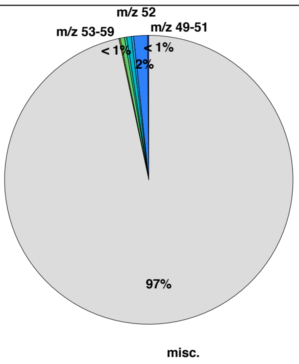	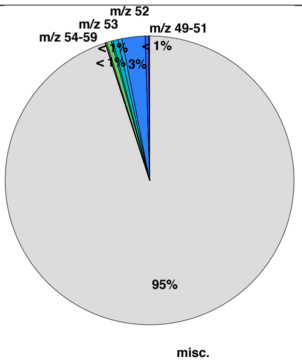

La photochimie des glaces

La majorité des produits photochimiques condensent dans la basse atmosphère proche de la tropopause, au point le plus froid (∼70 K). Cette region de l'atmosphère est souvent considérée comme relativement inerte, du fait que seulement les photons moins énergétiques parviennent jusqu'à la basse atmosphère, réduisant ainsi la possibilité d'initier une photochimie en phase glace à plus basse altitude. Simuler ces conditions nécessite de (i) pouvoir contrôler des conditions de basses température et (ii) de pouvoir condenser des espèces chimiques en conditions de basse atmosphère. C'est pourquoi utiliser un système cryogénique couplé avec un système d'irradiation s'avère nécessaire pour irradier des glaces qui, sur Titan, peuvent subir des radiations UV lorsque ces nuages se forment. Ces expériences que j'ai menées au Jet Propulsion Laboratory (JPL) se sont focalisées sur des glaces de HCN et HCN-C_4H_2 (Chapitre 5 et Figure B.9). J'ai irradié des glaces à plusieurs longueurs d'ondes dans le proche UV. Les glaces ont été étudiées par absorption infrarouge et UV.

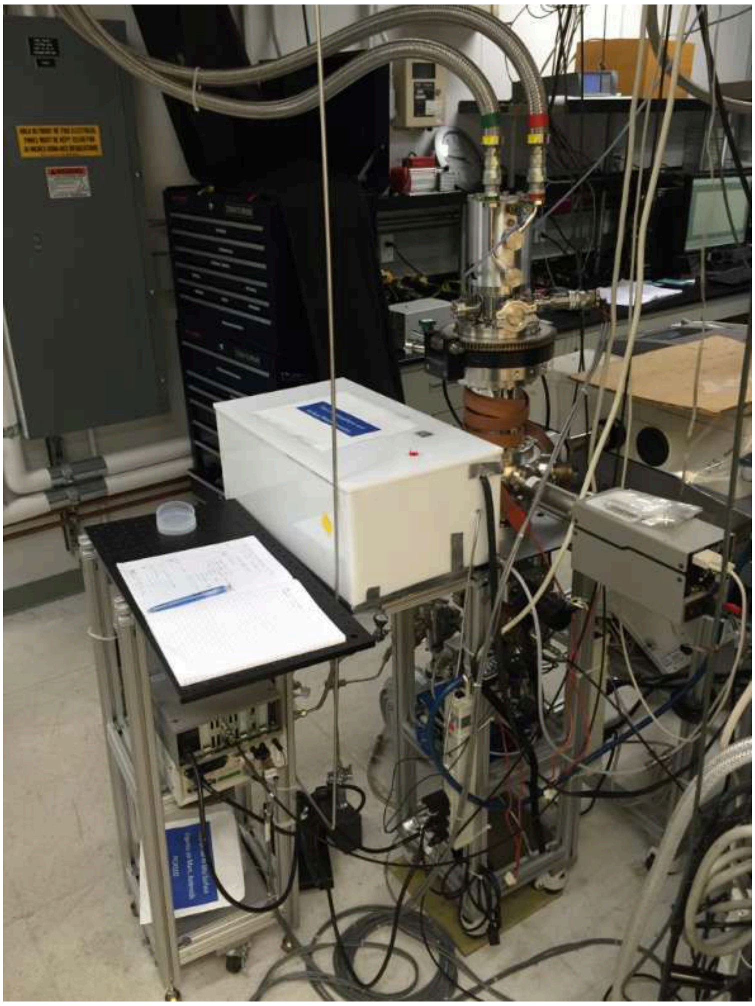

FIGURE B.9: Expérience Acquabella, utilisée pour simuler l'irradiation de glaces à faible température et l'absorption infrarouge de celles-ci.

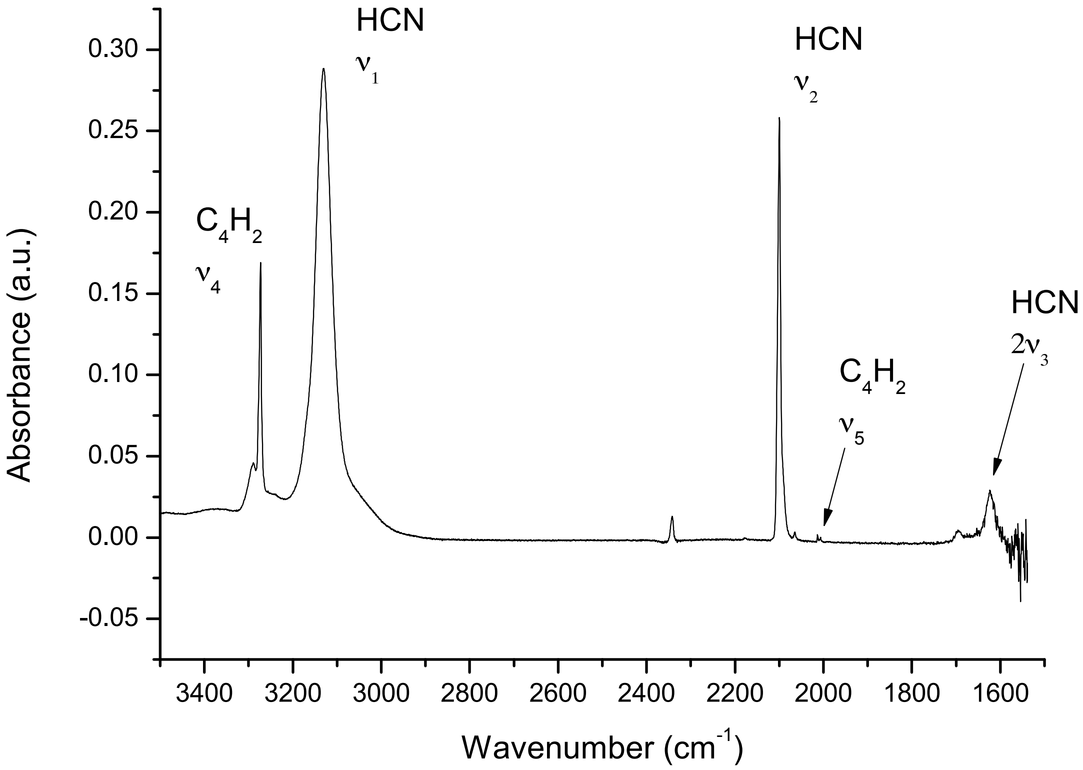

FIGURE B.10: Spectre infrarouge d'une glace de HCN-C_4H_2 pris à une température de 80K. HCN est principalement représentée par ses deux modes d'absorption ν_1 et ν_2. On peut aussi voir son overtone $2\nu_3$. C_4H_2 est visible par sa fréquence d'absorption ν_4 qui correspond à la vibration stretch de la liaison C−H, et de manière moins importante, la ν_5 qui est la stretch de la liaison C≡C.

Des glaces de HCN pures seules ou déposées sur des films de tholins irradiées à λ>300 nm ne présentent aucune modifications ni de produits formés par la photochimie. Ceci souligne le charactère relativement inerte de glace de HCN face à des irradiations dans le proche UV. De la même manière, nos résultats ne montrent par de réactions particulières entre les tholins et HCN pur après irradiations. Cependant, dans un mélange plus complexe où HCN est mélangée avec un hydrocarbure insaturé comme C_4H_2 (Figure B.10), la photochimie est initiée. En effet, nous observons une consommation de molécules de HCN par réaction avec C_4H_2 en phase solide accompagnée de la formation d'un produit de type nitrile. Ces expériences préliminaires montrent une réactivité de glace de HCN qui est catalysée par une photochimie couplée du C_4H_2. La présence d'un hydrocarbure insaturé semble donc nécessaire pour amorcer la réactivité de glace de HCN sous l'effet d'UV proches.

Perspectives

En continuité et complément du travail que j'ai effectué durant cette thèse, au moins trois points de perspectives ressortent:

- Étudier la chimie des ions négatifs dans une décharge plasma qui seraient potentiellement des précurseurs gazeux importants dans la formation et croissance des tholins. Jusqu'à présent, l'étude des anions n'a pas encore été effectuée dans notre décharge plasma. Nous nous attendons en effet, notamment grâce à la mission Cassini, de découvrir une chimie des ions négatifs complexe et avancée en phase gaz. Je viens récemment d'initier ce travail qui est actuellement en cours.
- Implémenter des mesures en phase gaz dans des mélanges incorporant des espèces traces, et voir leur effet potentiel sur la distribution des ions (et des neutres) au sein du plasma.
- Étendre les irradiations de glaces de HCN-C_4H_2 sur une plus grande gamme de longueurs d'onde. Il serait en effet intéressant de voir l'effet de la longueur d'onde du proche-UV au visible sur nos glaces, et en quoi la chimie HCN est différente, si elle a lieu.
- Un point reliant le précédent concerne la composition des glaces, qui peut être de nature variée. D'autres mélanges seraient à envisager, notamment quant à la présence d'autres hydrocarbures en mélange avec HCN.

Substantial abstract

I present in this thesis my thesis work, started three years ago in October 2015. I carried out this project at the Laboratoire ATMosphères et Observations Spatiales (LATMOS) at the University of Versailles St-Quentin (UVSQ) and at the Ice Spectroscopy Laboratory (ISL) at the Jet Propulsion Laboratory (JPL).

During the last 3 years, I studied the gas and solid phase chemical reactivity of organic compounds found in Titan's atmosphere. Titan being the only moon in the Solar System to possess its own dense and gravitationally-bound atmosphere (Figure B1), and is even larger than planet Mercury. Titan’s atmosphere is mostly made up of two dominant molecules: molecular nitrogen N_2 and methane CH_4.

Figure B1: Titan, as seen by Cassini on May 29, 2017, 2 million km away. Picture taken by the ISS camera. In this image, Titan is backlit, revealing the atmospheric structure. Credit: NASA/JPL-Caltech/Space Science Institute (PIA21625).

Firstly, I analyzed neutral species and charged (ion) compounds present in various gas mixtures using the PAMPRE experiment, simulating Titan's upper atmosphere conditions. These chemical species are the outcome of processes resulting from energetic radiation reaching Titan’s upper atmosphere, breaking apart the initial N_2 and CH_4. A cascade of subsequent reactions at altitudes >900 km will trigger the formation of new and larger gas phase products (Figure B2). Eventually, these products mainly containing hydrogen, carbon and nitrogen atoms will form large fractal aggregates composing the opaque haze enshrouding the surface of Titan. This haze is what gives Titan such a unique brownish hue. Most of the photochemically-produced volatiles will eventually condense in the lower atmosphere, where they may aggregate to form micrometer-sized icy particles and clouds.

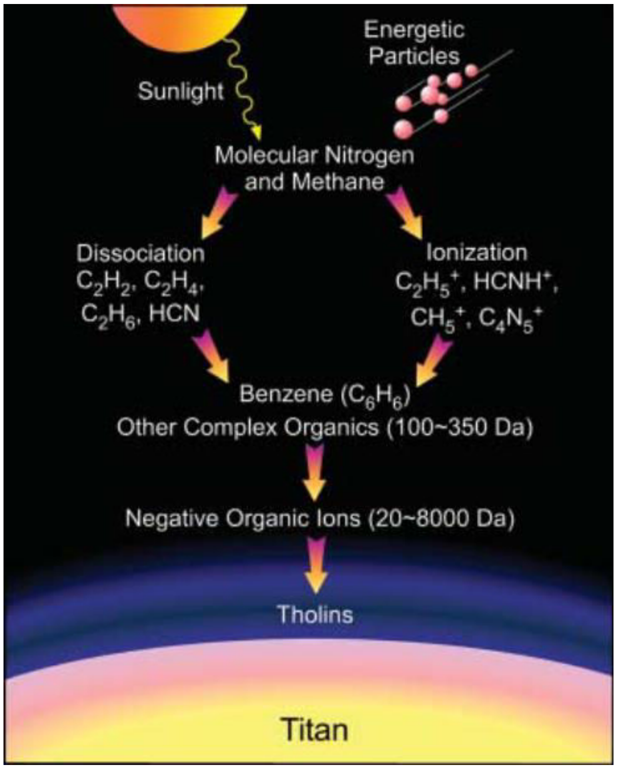

Figure B2: Schematic diagram showing the chemical evolution and some reactions leading to the formation of larger organic compounds in Titan's upper atmosphere.

The Cassini-Huygens mission revealed the chemical complexity which starts at high altitudes (>900 km) coupling neutrals, radicals and ions, preceding the formation of aerosols. To understand the composition of these aerosols, one must first understand the mechanisms leading to their formation. The Cassini instruments (Figure B3) probed deep into Titan's atmosphere; from the ionosphere to the surface. Dissociative and ionizing processes form the first ions and radicals, thus enabling the formation of larger organics such as C_2H_2, C_2H_4 or HCN (Figure B4).

Instrumental limitations (mass resolution, measurements…) require support from numerical models and laboratory work. Even before the first spacecraft explorations of Titan's atmosphere (Chapter 1), laboratory and numerical simulations worked together to characterize the organic chemistry, certain reactions, the formation of prebiotic molecules and the nature of analogous aerosols called *tholins*.

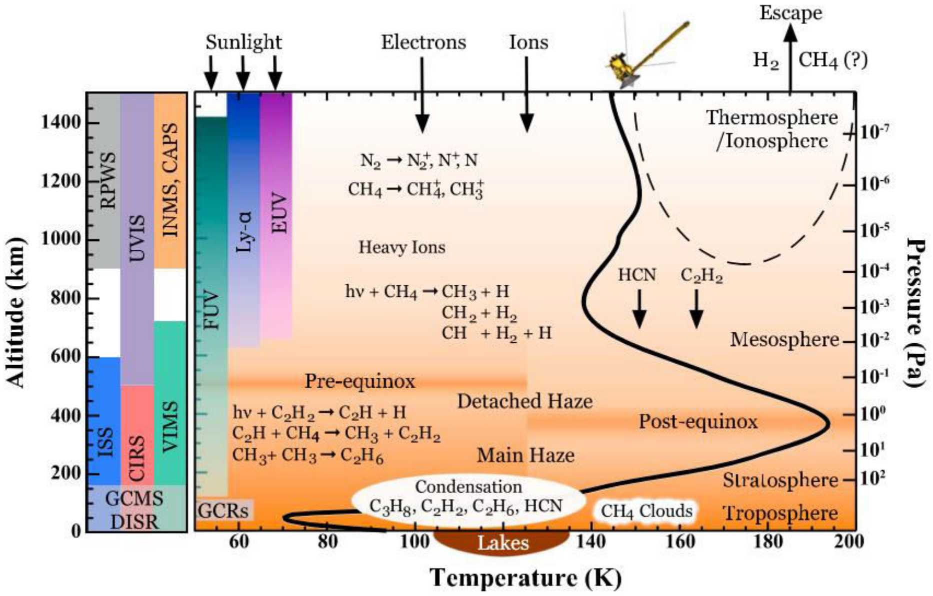

Figure B3: Diagram showing Titan's atmospheric profile (black curve) with respect to altitude and pressure. Some key reactions are displayed, as well as the Cassini instruments suite (Horst 2017).

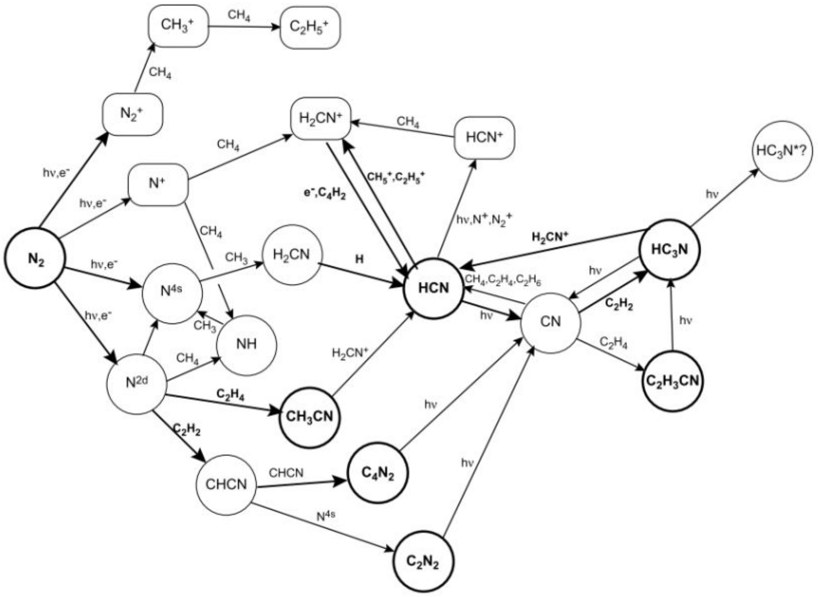

Figure B4: Reaction diagram from Wilson and Atreya (2004) indicating major pathways to the formation of the major neutral and nitrogen-bearing species and positive ions.

My work during this thesis was to carry out experiments in the laboratory to investigate the gas phase reactivity of ions and neutrals which are precursors to the formation of *tholins*.

Furthermore, at JPL, I studied how icy organic condensates photochemically evolve lower down in the atmosphere. These ices can form condensation nuclei to larger organic clouds in the lower stratosphere.

Gas phase reactivity

In order to simulate Titan's upper atmosphere, one must understand the processes taking place. The upper atmosphere (mostly N_2 and CH_4) undergoes intense solar UV photons and energetic particles coming from Saturn's magnetosphere. In Chapter 1, I present the context of my object of interest and several experimental techniques simulating these energy sources which are required to dissociate and ionize N2 and CH4. In this part of my PhD, I used a plasma reactor named PAMPRE with a radio-frequency discharge (13.56 MHz). Such an apparatus reproduces the energetic conditions of the energetic particles and solar photons impacting Titan's upper atmosphere (Figure B5). PAMPRE can also produce *tholins* whose optical properties can be further analyzed in the laboratory and compared with observations made by Cassini-Huygens. Using PAMPRE I studied neutral and ion species within the plasma in N_2-CH_4 conditions relevant to Titan's upper atmospheric composition.

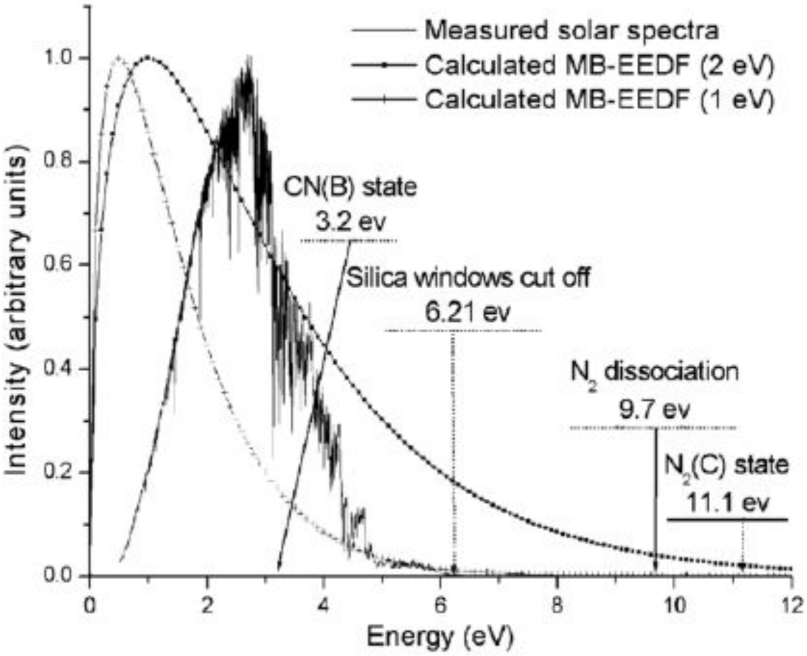

Figure B5: Energetic distribution of the electrons delivered by the discharge compared with the solar spectrum (Szopa et al., 2006).

A brief past and current review of laboratory experiments aimed at reproducing gas and solid phase processes is given in Chapter 2, accompanied with the two experiments that I used during this PhD.

Chapter 3 consists of an investigation of the neutral precursors to tholins present in the PAMPRE plasma discharge. In this chapter I present results using coupled mass spectrometry and an infrared analysis on the main neutral precursors. These measurements were made possible thanks to a cryotrap system developed inside the reactor. The first intermediate gas phase products trapped *in situ*, were measured by mass spectrometry and infrared spectroscopy using a quantification approach. These products, HCN, NH_3, C_2H_2 and C_2H_4 were studied in two N_2:CH_4 90:10 and 99:1 mixtures. Our results indicate a relatively strong presence of HCN and C_2H_4 with increasing methane, which are also in agreement with previous studies showing HCN-C_2H_4 patterns in *tholin* growth.

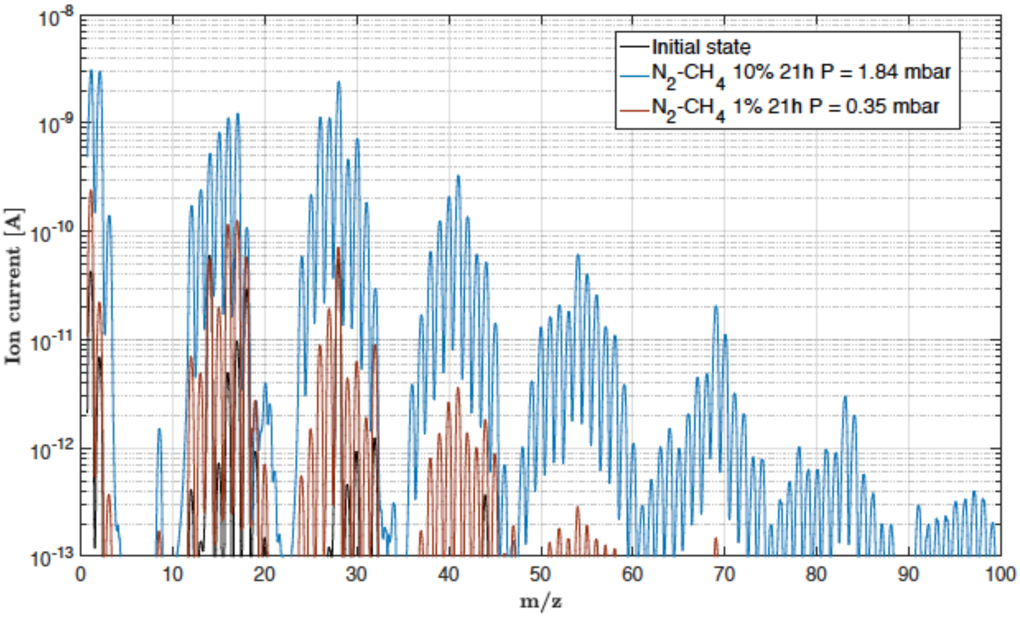

Figure B6: Mass spectra obtained in 1% and 10% CH4 concentrations, at the end of release after the cryogenic trapping (Chapter 3).

In the plasma, neutral interact with ions. Therefore, it is necessary to understand the ion-neutral coupling.

For the first time using our PAMPRE experiment, is was possible to probe inside the plasma and measure the positive ion compounds (Figure B7). Their coupling to neutral species is indeed important (Chapter 1). These results are detailed in Chapter 4. By studying the major ions in three different methane concentrations 1%, 5% and 10%, compounds such as CH_5^+, $HCNH^+$ and $C_2H_5^+$ are revealed to be important precursors. In low methane concentrations, NH4+ appears to also be a significant species (Table 1). These detections of ions up to *m/z* 100 suggest a significant role of these cation precursors to the formation of *tholins*. I also compared these results with the neutral chemistry of Chapter 3. Moreover, I compared these first results with spectra taken by the INMS instrument onboard Cassini (Figure B8).

Negative ions were also analyzed but the results are not presented in this manuscript, and is part of ongoing work.

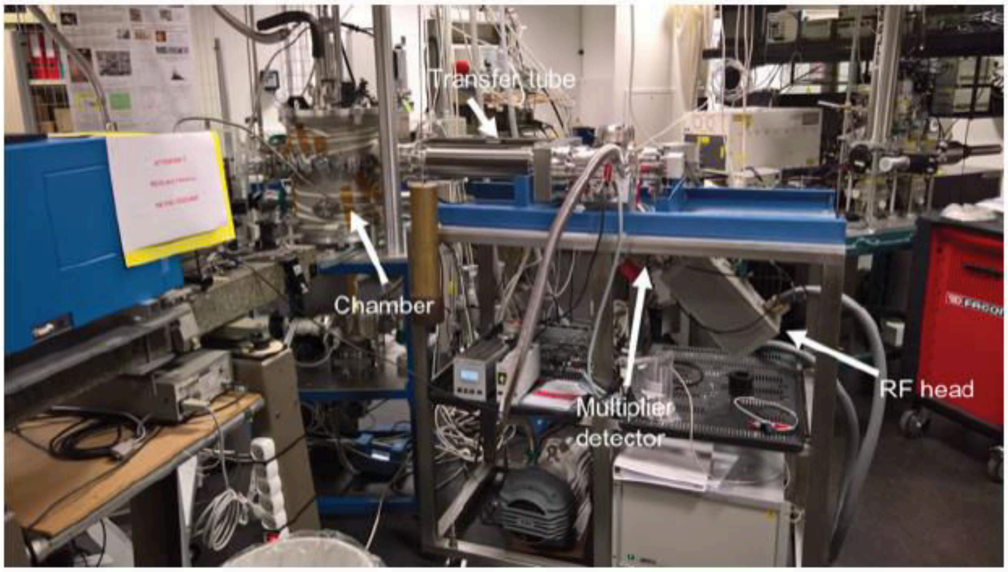

Figure B7: Experimental setup of the PAMPRE plasma reactor, coupled with a mass spectrometer (neutrals and ions).

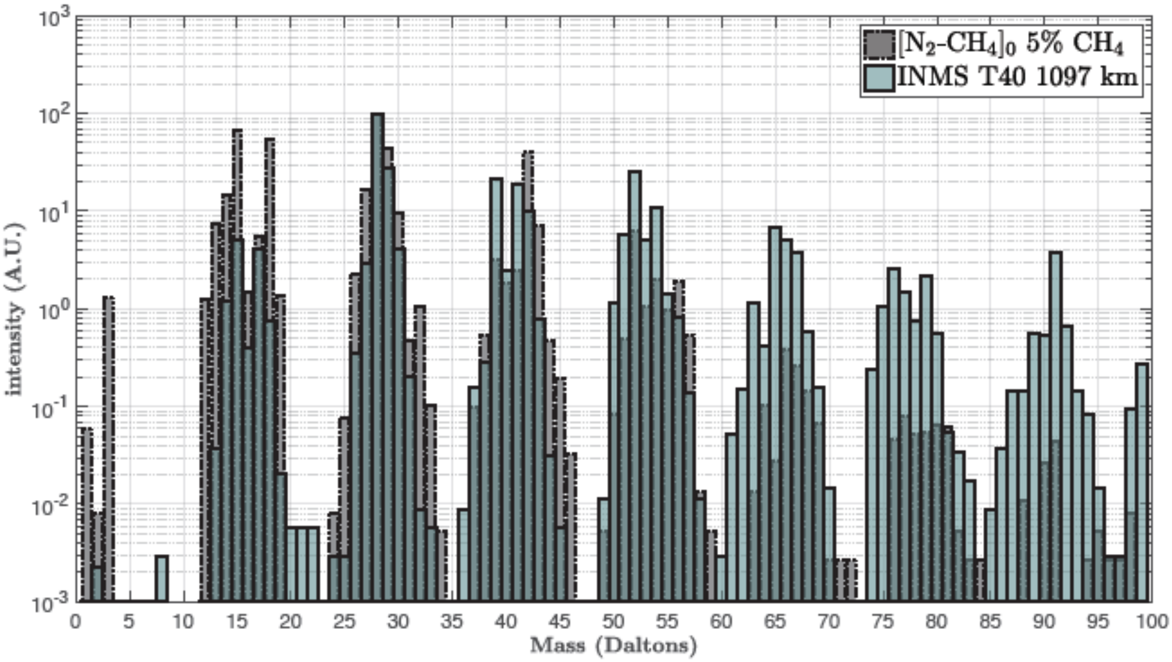

Figure B8: Mass spectrum taken during the outbound leg of the T40 flyby (in blue), compared with our experimental averaged spectrum taken in an N2:CH4 99:1 % gas mixture. The mass plot is separated in 1 u bins.

	1%	5%	10%
C_1	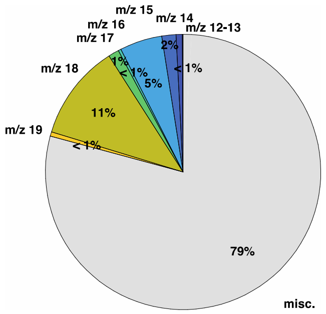	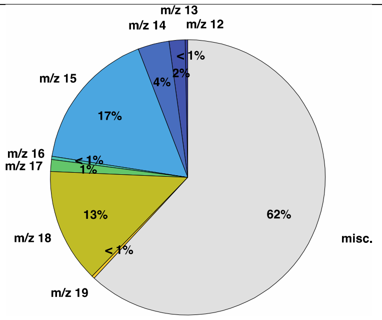	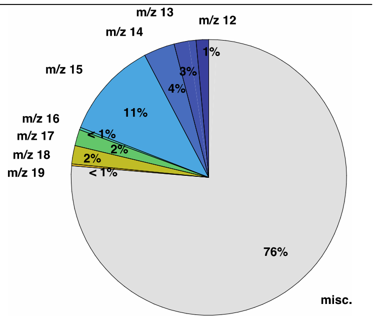
C_2	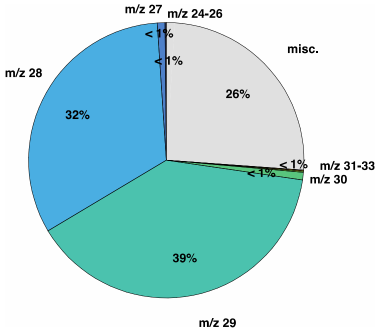	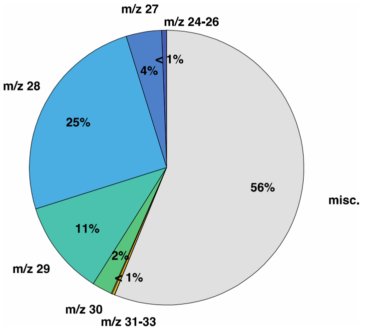	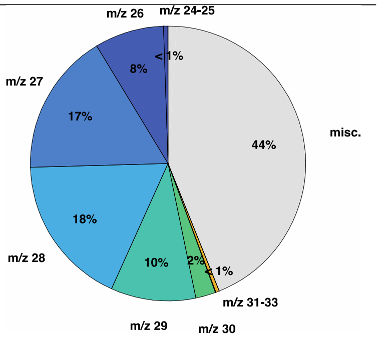
C_3	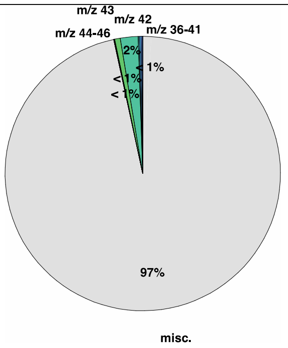	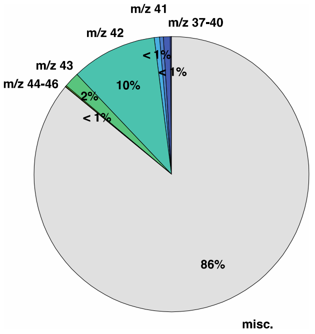	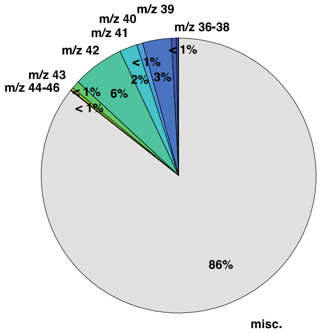
C_4	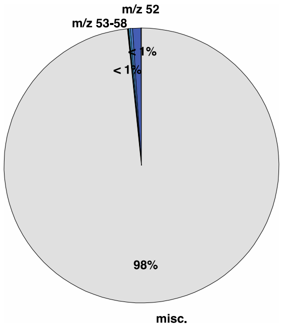	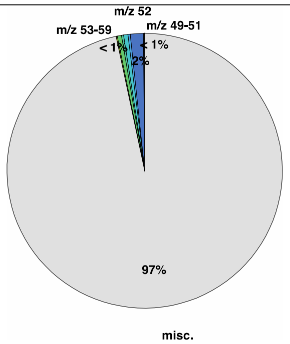	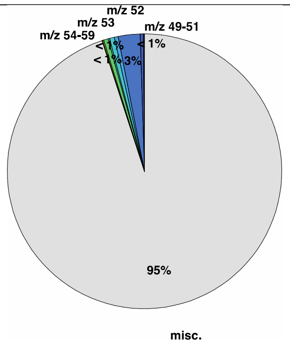

Table 1: Pie charts showing the ion contributions up to C4 species. Columns correspond to methane concentrations; rows to Cx groups. Colored slices correspond to normalized intensities over the entire spectra.

Ice photochemistry

In complement to these gas phase study, I had the opportunity of carrying out ice spectroscopy experiments in conditions analogous to Titan's lower atmosphere. Near the tropopause, most of the volatiles undergo a gas-solid phase change and icy particles rich in hydrocarbons and nitrogenous species may form. In particular, HCN clouds have been detected and monitored, and spectral signatures of other more complex icy particles likely to be nitrogen-rich are still not fully understood. Our current understanding of how these particles evolve in the lower atmosphere and how they interact with near-UV-vis wavelengths is relatively limited. This project, led at the Jet Propulsion Laboratory, focused on HCN and HCN-C_4H_2 ice mixtures which I irradiated at near-UV wavelengths (Figure B9 for the experiment). The spectral evolutions of these ices are presented in Chapter 5 and put in context of what these results suggest in characterizing the potential solid-state photochemistry in Titan's lower atmosphere. Over the centuries, our understanding of Titan's atmosphere has drastically expanded, with the help of observations, laboratory measurements and theoretical modeling. The exploration of Titan will certainly flourish over the decades to come, hopefully aided by future robotic missions probing further into its atmosphere, surface and liquid hydrocarbon lakes.

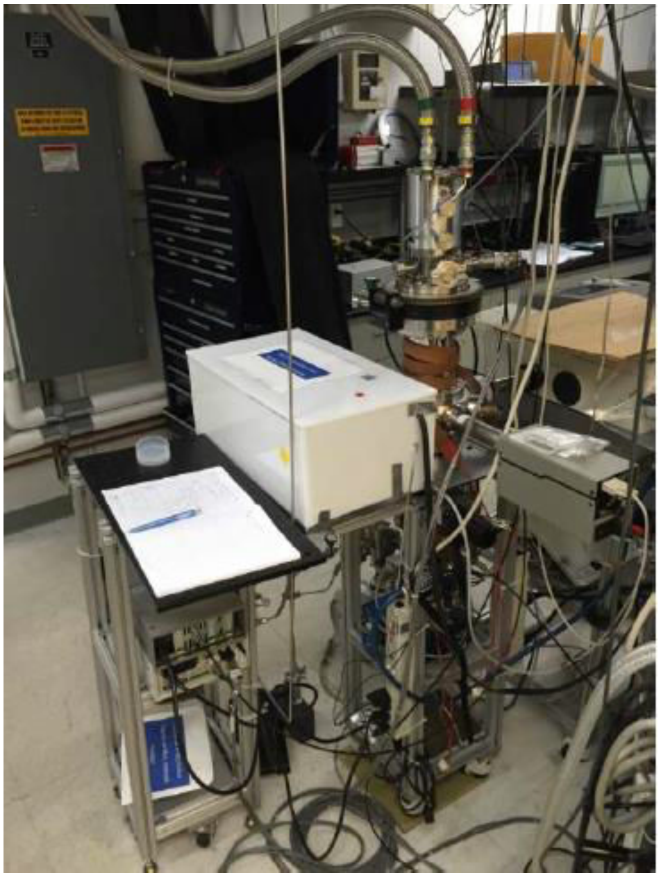

Figure B9: The Acquabella Experiment (ISL-JPL) that I used to irradiate organic ices at low-controlled temperatures.

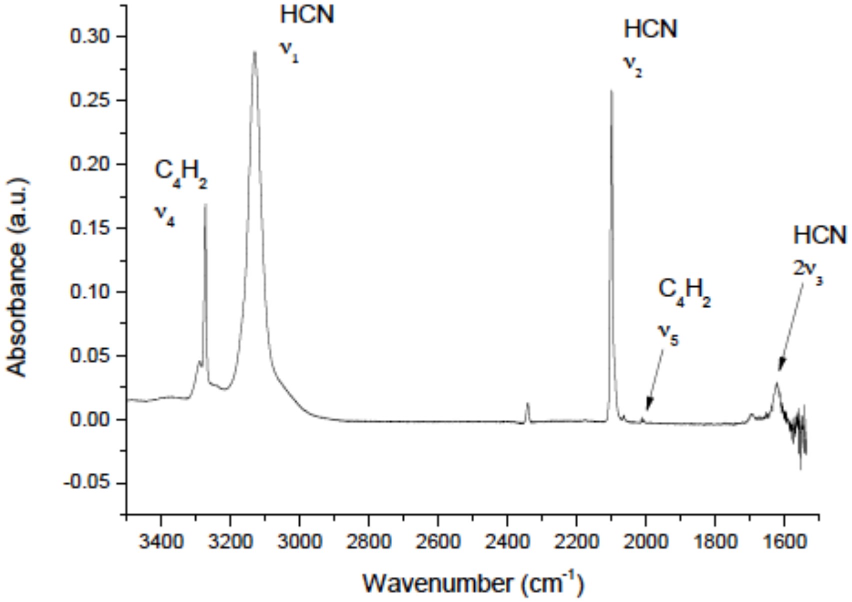

Figure B10: Infrared spectrum of an HCN-C4H2 ice mixture taken at 80K. We can see two absorption modes of HCN v1 and v2 and the 2 v3 overtone. C4H2 is also visible with the v4 absorption frequency, corresponding to the C-H stretching band, and to a lesser extent, the C-C stretching band.

At JPL, I studied pure HCN ices, deposited on *tholins* films and irradiated at wavelengths greater than 300 nm, which showed no significant reactivity. HCN alone or with *tholins* appears to be inert and does not absorb in the near-UV. However, when co-added with C_4H_2 ice (Figure B10 and Chapter 5), photochemistry is initiated given the UV-sensitivity of C_4H_2. Consumption of the nitrile band of HCN and C-H stretch of C_4H_2 simultaneously forms a product with a positive absorption in the nitrile region. The presence of an insaturated hydrocarbon such as C_4H_2 seem to be required to initiate HCN photochemistry at these low temperatures.

Perspectives

Ongoing and future work should focus on the following points:

- Study the anion chemistry and evaluate their impact as gas phase precursors in the formation of tholins. Cassini revealed a large quantity of anions (*m/z* up to 14,800).
- Study the effect of trace gases (O, N…) on the tholin composition
- Irradiate HCN-based ices on a longer UV range.
- Study other mixtures
- Submillimeter observations using advanced radiotelescopes, improving the characterization of neutral (and ion) species
- Modeling effort to constrain the negative ion chemistry and reactions based on laboratory data

université
PARIS-SACLAY

ÉCOLE DOCTORALE
Sciences mécaniques et énergétiques, matériaux et géosciences (SMEMAG)

Titre: Etude de la chimie de la haute et basse atmosphère de Titan: approche expérimentale

Mots clés: Titan, Chimie atmosphérique, Simulations expérimentales, Ionosphères, Photochimie des glaces

Résumé: Je présente ici mes travaux de thèse que j'ai réalisé ces trois dernières années au sein du Laboratoire ATMOsphères et Observations Spatiales (LATMOS) de l'Université de Versailles St-Quentin-en-Yvelines (UVSQ) et du Jet Propulsion Laboratory (JPL), California Institute of Technology. Pendant ces 3 ans je me suis intéressé à la réactivité chimique des composés organiques en phase gaz et solide, en utilisant des expériences de laboratoire simulant les conditions de l'ionosphère et de la basse atmosphère de Titan, le plus gros satellite de Saturne. Titan est la seule lune du Système Solaire qui possède sa propre atmosphère. Cette atmosphère est principalement composée d'azote moléculaire (N_2). Le méthane (CH_4) forme le gaz secondaire. D'une part, j'ai analysé les composés neutres et les composés chargés (ions) présents dans des mélanges gazeux simulant la haute atmosphère de Titan. Ces composés sont considérés comme précurseurs chimique à la brume organique observée entourant Titan. C'est-à-dire qu'ils forment les premières étapes d'une succession de réactions chimiques de plus en plus élaborées formant plus bas dans l'atmosphère des particules solides complexes. La nature de ces particules dans l'atmosphère de Titan reste encore à élucider complètement. Mon travail pendant cette thèse a été d'utiliser des expériences de laboratoire pour investiguer la réactivité chimique en phase gaz (Chapitres 3 & 4), précurseurs à la formation d'aérosols, ainsi que le vieillissement de ces composés plus bas dans l'atmosphère lorsqu'ils forment les premiers condensats de nucléation à la formation de nuages (Chapitre 5).

Title: Study of Titan's Upper and Lower Atmosphere: An Experimental Approach

Keywords: Titan, Atmospheric chemistry, Experimental simulations, Ionospheres, Ice photochemistry

Abstract: Titan is the only moon in the Solar System to possess its own dense and gravitationally bound atmosphere, and is even larger than planet Mercury. Its rocky diameter is a mere 117 km shy of Ganymede's. If we were to scoop up a 1 cm^3 sample from Titan's upper atmosphere, we would find two dominant molecules: molecular nitrogen N_2 and methane CH_4. Should we look a bit more carefully, we would find many neutral molecules and positive and negative ion compounds. These chemical species are the outcome of processes resulting from energetic radiation reaching Titan's upper atmosphere, breaking apart the initial N_2 and CH_4. A cascade of subsequent reactions will trigger the formation of new gas phase products more and more complex. Eventually, these products mainly containing hydrogen, carbon and nitrogen will form large fractal aggregates composing the opaque haze enshrouding the surface of Titan. This haze is what gives Titan such a unique brownish hue. Most of the photochemically-produced volatiles will eventually condense in the lower atmosphere, where they may aggregate to form micrometer-sized icy particles and clouds. During my PhD, I have focused my studies on (i) the gas phase reactivity of aerosol precursors in experimental conditions analogous to Titan's upper atmosphere (Chapters 3 & 4), and (ii) the end of life of some of the products as they condense in the lower and colder atmosphere (Chapter 5). I used two experiments to address these respective issues: the PAMPRE plasma reactor, located at LATMOS, UVSQ, Guyancourt, France, and the Acquabella chamber at the Jet Propulsion Laboratory, California Institute of Technology, Pasadena, USA. In this manuscript, I present my work on the neutral and positive ion reactivity in the PAMPRE plasma discharge, as well as ice photochemistry results using laser irradiation in near-UV wavelengths.

Université Paris-Saclay
Espace Technologique / Immeuble Discovery
Route de l'Orme aux Merisiers RD 128 / 91190 Saint-Aubin, France